Probing the Strangeness Content of the Proton and the Neutron Radius of ^{208}Pb using Parity-Violating Electron Scattering
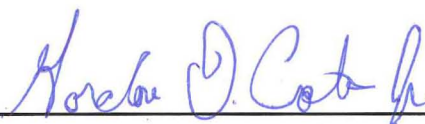
Rupesh Silwal
Sanepa, Lalitpur-2, Nepal

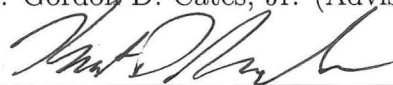B.A. in Physics, Lawrence University, 2006

A Dissertation presented to the Graduate Faculty
of the University of Virginia in Candidacy for the Degree of
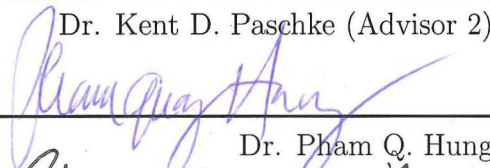Doctor of Philosophy

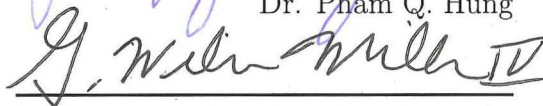Department of Physics

University of Virginia
May 2012

_____

Dr. Gordon D. Cates, Jr. (Advisor 1)

_____

Dr. Kent D. Paschke (Advisor 2)

_____

Dr. Pham Q. Hung

_____

Dr. G. Wilson Miller IV

Abstract

Precision measurement of the parity-violating asymmetry in electron-hadron scattering has been an extremely useful tool to study the structure of the hadrons. This thesis reports work on two such measurements: the measurement of the strange form-factors (FFs), G_E^s and G_M^s, by the Hall A Proton Parity Experiment (HAPPEX)-III collaboration, and the first direct measurement of the nucleon skin thickness in a heavy nucleus by the Lead (^{208}Pb) Radius Experiment (PREX) collaboration.

In HAPPEX-III, the parity-violating cross-section asymmetry in the elastic scattering of polarized electrons from unpolarized protons was measured at an average four-momentum transfer squared, $\langle Q^2 \rangle$, of 0.624 GeV^2. A parity-violating asymmetry, A_{PV}, of $-23.80 \pm 0.78(\text{stat}) \pm 0.36(\text{syst})$ parts-per-million (ppm) was measured, which corresponds to a linear combination of the strange FFs, $G_E^s + 0.517 G_M^s = 0.003 \pm 0.010(\text{stat}) \pm 0.004(\text{syst}) \pm 0.009(\text{ff})$. The errors stat and syst are experimental statistical and systematic errors respectively. The error ff arises due to limits on precision of the electromagnetic FFs and radiative corrections. This result is consistent with zero contribution from the strange quarks to the proton FFs. Combined with the existing data on strange FFs, this result constrains the contribution of the strange FFs to the nucleon FFs to a few percent of the nucleon FFs.

In PREX, the parity-violating asymmetry in the elastic scattering of polarized electrons from unpolarized ^{208}Pb was measured at an average $\langle Q^2 \rangle$ of 0.0088 GeV^2. A parity-violating asymmetry, A_{PV}, of $656 \pm 60(\text{stat}) \pm 14(\text{syst})$ parts-per-billion (ppb) was measured, which corresponds to a difference between the neutron and proton distribution radii in the ^{208}Pb nucleus of $R_n - R_p = 0.33 \, ^{+0.16}_{-0.18}$ fm. This result is the first electroweak evidence supporting the existence of a neutron skin in a neutron-rich nucleus.

One class of systematic uncertainty that both of these experiments were sensitive to is the non-parity violating asymmetries that resulted from the helicity-correlated (pulse-to-pulse) differences in the electron beam parameters. Therefore, considerable effort was invested to understand, and suppress the asymmetries arising from these effects. Although both HAPPEX-III and PREX benefited from this effort, the result of this work was much more important for PREX due to its much higher precision goal compared to that of HAPPEX-III.

Acknowledgments

I would like to start by thanking Gordon for accepting me as his advisee. I would most likely have been doing something other than nuclear physics had it not been for the opportunity that he offered me to work with him. I also thank him for being a terrific advisor, always with plentiful of ideas and suggestions, and for offering me much to learn. Most importantly, I thank him for providing me with the opportunity to work with Kent, who has been a tireless mentor.

Kent has been an extremely resourceful advisor, and has taught me much of what is presented in this thesis. From root, data-acquisition systems, analysis software, charged-particle detectors etc. to the physics of precision parity-violating measurements, Kent has taught me a great deal. I thank him for all that he has taught me, and for being such an incredible advisor.

I would also like to thank Bob Michaels, Krishna Kumar and Paul Souder for being exemplary physicists. Their excitement for physics was very contagious, and together with Gordon and Kent, they have taught me to think like a physicist, and inspired me to continue doing physics.

I would also like to thank the following people for their help at various stages of the work presented in this thesis, as well as for making my stay in Newport News manageable: Abdurahim Rakhman, Bryan Moffit, Chun Min Jen (Mindy), Diancheng Wang, Dustin McNulty, Jon Wexler, Kai Pan, Luis Mercado, Mark Dalton, Megan Friend, Ramesh Subedi, Zafar Ahmed, and Xiaoyan Deng.

Lastly, I would like to thank my parents, Ramesh Silwal and Sarita Silwal, my siblings, Rupak Silwal and Roopa Silwal, and my grandparents, for their unwavering encouragement and support of my pursuit of a Ph.D. In particular, I thank my mother for laying the foundation of my successes: she instilled in me the discipline and

patience, and taught me to face the challenges of life and strive for success, without which I would not have been where I am today.

Dedication

To my loving and ever so supportive parents, Ramesh Silwal and Sarita Silwal, siblings, Rupak Silwal and Roopa Silwal, and grandparents.

Contents

List of Figures

List of Tables

1

Introduction

Parity-violation is a phenomenon in which an interaction between two particles occurs differently depending on whether one looks at a particular reaction or a mirror image of the reaction. Historically, parity-violation has played an important role in the development of weak interaction theory. A fundamental shift in the understanding of the weak interaction occurred with the suggestion in the mid-1950s of Yang and Lee that the weak interaction might violate the law of conservation of parity [LY56]. Wu and collaborators in 1957 experimentally confirmed this [Wu57], leading to a reformulation of the weak interaction theory in terms of a vector axial-vector weak charged-current which is maximally parity-violating (PV). The pursuit of this theory further (and independently) by Weinberg [We67], Glashow [Gl61], and Salam [Sa68] led to the development of the Wienberg-Glashow-Salam (WGS) theory, also referred to as the electroweak theory, which describes the electromagnetic interaction and the weak interaction as two different aspects of a single theory. The existence of charged massive weak bosons ($W^{\pm}$), a neutral massive weak boson (Z^0) and a neutral massless boson of the electromagnetic interaction (γ) naturally comes out of this theory. Soon thereafter, the Gargamelle collaboration at CERN first discovered the neutral

currents of the weak interaction in 1973 in neutrino scattering experiments [Ha73]. The landmark SLAC-122 experiment in 1978 tested the suggested PV nature of the weak neutral interaction by measuring the PV asymmetry in the scattering cross-section of longitudinally polarized electrons scattered off a deuteron target [Pr78]. The results of SLAC-122 experiment put the electroweak theory of WGS-theory on much firmer ground by demonstrating parity-violation in the neutral weak current, consistent with appropriate coupling in WGS-theory, and ruling out other theories with a high degree of significance. Since then, several PV experiments such as ^{12}C at MIT-Bates [So90], ^{9}Be at Mainz [He89] and SLAC-158 at SLAC [An05] have further tested and restrained the parameters of the WGS electroweak theory.

More recently, PV experiments at intermediate energies (a few GeV) have been extremely useful as a tool to probe the structure of the nucleon. The strange-quark programs, such as HAPPEX [An04, AnH06, AnHe06, Ac07], A4 [Ma04, Ma05, Ba09], G0 [Ar05, An10] and SAMPLE [Sp04, It04, Be05], with their measurements of the nucleon strange electric and magnetic form-factors (FFs), G_E^s and G_M^s, have been instrumental in studying the extent of the "sea" contribution to the static and dynamic properties of the nucleon. The FFs describe the modification in the scattering from a point source when the source has some structure. The Lead Radius Experiment (PREX) collaboration recently provided the first direct measurement of the nucleon skin thickness confirming the existence of neutron skin in a heavy nucleus [Ab12]. These measurements are unique in that at energy scales other than the few GeV, the sensitivity to the nucleon structure is suppressed and cannot be accessed via processes such as purely electromagnetic or hadron-nucleus scattering. However, at the energy scale of these PV experiments, QCD becomes a strong-coupling theory, and hadronic degrees of freedom such as mesons, nucleons and nuclei have to be considered explicitly, allowing access to nucleon structure parameters.

An important feature that makes these PV experiments possible is the interference of the coupling amplitudes of γ-boson of the electromagnetic interaction to the Z^0-boson of the weak interaction. The pure weak neutral-current scattering amplitude is $\sim 10^{-4}$ of the electromagnetic scattering amplitude. So, without the interference term, a measurement of 10^{-8} effect would have to be made. But the interference term allows access to the weak neutral-currents with a measurement of the 10^{-4} effect.

The focus of this thesis is on the measurement of the nucleon strange electric and magnetic FFs, G_E^s and G_M^s, by the Hall A Proton Parity Experiment (HAPPEX) III collaboration with particular emphasis on the aspects of the experiment that the author was heavily involved in such as the source setup and helicity-correlated (HC) effects suppression, and data analysis. An entire chapter is devoted to the discussion of the development of techniques to suppresses HC beam systematics. The discussion of this chapter is not of critical importance to HAPPEX-III, but is extremely important for PREX due to its requirement of a very stringent control of beam systematics. However, HAPPEX-III did benefit from this study in that the beam systematics were extremely well suppressed (perhaps much more than they needed to be) and the corrections due to beam systematics were negligible. Measurement of the neutron skin thickness by the PREX collaboration is also briefly discussed in this thesis.

1.1   Strangeness in the Nucleon

With the establishment of the notion that a complete characterization of nucleon substructure must go beyond three valence quarks and include the $q\bar{q}$ sea and gluons, there has been considerable interest in studying the strangeness contribution to the nucleon properties to determine the extent of "sea" contribution to the static and dynamic properties of the nucleon. In deep inelastic scattering, for example, sea

quarks are known to dominate interactions in certain kinematic regimes. With the discovery by the EMC collaboration [As88] that quark spins are not the dominant contribution to nucleon spin, the role of sea quarks, and especially strange quarks, has been scrutinized. In addition, the bare masses of the valence quarks account for only about 1% of the nucleon mass, and the nucleon momentum distribution cannot be explained in terms of the valence quarks alone [Ba95, La97]. So a better understanding of the role of gluons and sea quarks in nucleon substructure is imperative. Cleanly isolating the effects of the quark sea is typically difficult with one notable exception being the extraction of the vector strange matrix elements $\langle \overline{s} \gamma_\mu s \rangle$ in semi-leptonic neutral weak scattering [KM88]. Following the recognition that PV electron scattering can measure the neutral weak form factors and hence the vector strange-quark matrix elements [Mc89], numerous experiments have been performed. $A4$ at Mainz [Ma04, Ma05, Ba09], G0 at Jlab [Ar05, An10], HAPPEX at Jlab [An04, AnH06, AnHe06, Ac07] and SAMPLE at MIT-Bates [Sp04, It04, Be05] have measured strange FFs at various four-momentum transfer squared (Q^2), clarifying the sea contribution to the properties of the nucleon.

Although these experiments mostly suggest a zero strangeness contribution to the nucleon properties at low Q^2, G0 results [Ar05] at higher $Q^2 (\sim> 0.5$ GeV$^2)$ are suggestive of non-zero strange FFs. However, these results have significant systematic uncertainties, making it difficult to draw any concrete conclusions. The only other datum in the region is from HAPPEX-I [An04] which is consistent with both the G0 data and zero strange FFs. Extrapolation to this region from the low Q^2 region data is unreliable due to both G_E^s and G_M^s being functions of Q^2, which are not *a priori* known. Hence, HAPPEX-III was proposed to measure the strange FFs at Q^2 of 0.62 GeV^2 with high statistical accuracy and small systematic uncertainties.

HAPPEX-III ran at the Thomas Jefferson National Accelerator Facility, also re-

ferred to as Jefferson Lab (JLab), from Aug-Oct 2009, and measured nucleon strange FFs of zero within uncertainty. This result is consistent with each of the previous HAPPEX measurements of zero strangeness at various values of Q^2 [An04, AnH06, AnHe06, Ac07].

1.2 Neutron Radius

The neutron radius, R_n, is a fundamental property of the neutron, but it is still relatively poorly known. This is in contrast to the proton radius, R_p, which has been cleanly measured, for instance, by electron scattering or the spectroscopy of muonic atoms [Vr87]. The accepted value of R_n is primarily based on estimates, which are plagued by model assumptions, uncertainties in corrections that are difficult to quantify theoretically and uncertainties in analysis [Ho01]. In a heavy nucleus such as ^{208}Pb, a number of relativistic mean-field-theory models have predicted R_n to be $0 - 0.4$ fm larger than R_p (~ 5.45 fm) [Ab12]. This difference is attributed to the presence of a neutron skin. But significant model dependence in the interpretation of existing experimental data has made it difficult to refute or verify the presence of the neutron skin, and left a considerable uncertainty in the estimate of R_n. At present, the uncertainty in R_n is estimated to be $\sim 5\%$ [Ab12].

A clean direct measurement of R_n to $\sim 1\%$ has the potential to benchmark the neutron size and shape, with implications in several areas of physics. In the study of stellar explosions, for instance, determination of fundamental parameters of bulk nuclear matter called symmetry energy and its density dependence is affected by the uncertainty in R_n. Knowledge of R_n of ^{208}Pb is required in order to calibrate the equation of state for neutron rich nuclear matter, which is an important input parameter for modeling and studying the structure of neutron stars. Atomic PV (APV) exper-

iments that measure the ratios of the APV amplitudes between isotopes in order to avoid the uncertainties due to difficult atomic structure calculations have enhanced sensitivity to the uncertainty in R_n. Hence, a clean and precise R_n measurement would have important implications in several areas of physics.

PREX proposed to measure R_n to 1%, by measuring the PV electroweak asymmetry in the elastic scattering of polarized electrons off ^{208}Pb. ^{208}Pb has 44 more neutrons than protons, and some of these extra neutrons are expected to be found in the surface where they form a neutron-rich skin. As a result, the A_{PV} measurement from ^{208}Pb is sensitive to the existence of this neutron skin. The first run of PREX was performed at JLab from March-July 2010, and R_n was measured to $\sim 3\%$, providing evidence for the existence of neutron skin to 1.8σ-level [Ab12].

1.3   Source Setup and Future Experiments

The landmark SLAC-122 [Pr78] experiment in 1978 pioneered the technique of precision PV experiments, laying the groundwork for future PV experiments. SLAC-122 set a benchmark for the precision achievable at the time by implementing techniques and developing technologies that were new or untested at the time such as the development of an intense source of longitudinally polarized electrons, use of magnetic spectrometers to momentum analyze the scattered electrons and suppress the backgrounds, integration of the scattered flux rather than counting the individual electrons, and suppression of HC beam systematics sufficient to allow desired precision. Building upon these achievements of SLAC-122, successive generations of PV experiments such as ^{12}C at MIT-Bates [So90], ^{9}Be at Mainz [He89], SLAC-158 at SLAC [An05], and PREX [Ab12] and QWEAK [Arm07] at JLab have increasingly pushed for higher precision and smaller asymmetry measurements. Recently, building

on the successes of HAPPEX-II [AnH06, AnHe06, Ac07], PREX [Ab12] achieved extremely good control over the beam systematics for precision PV measurements. Like in the previous generations of experiments, the control of beam systematics during PREX has further refined our techniques and demonstrated that the precision goals of future experiments such as MØLLER [Be08] and PVDIS [Ar07, Bo09] at 12 GeV are achievable.

2

Theory

2.1 Parity-Violating (PV) Asymmetry

The fundamental couplings of the electron with the photon (γ) and Z^0 are given as [Mu94]

$$ic_e g_Q^e \gamma_\mu, \qquad i(c_Z M_Z/4M_W)\gamma^\mu(g_V^e + g_A^e \gamma_5) \tag{2.1.1}$$

where c_e and c_Z are the electromagnetic and weak coupling strengths respectively. g_Q^e, g_V^e and g_A^e are the electromagnetic, weak vector and weak axial-vector charges of the electron respectively. M_Z and M_W are the masses of the Z^0 and W bosons respectively. The scattering amplitudes for one-boson-exchange (γ or Z^0) of an electron with a hadron, as illustrated in Figure 2.1.1, can be expressed as [Mu94]

$$\mathcal{M}^\gamma = (4\pi\alpha/Q^2)g_Q^e l^\mu J_\mu^{EM} \tag{2.1.2a}$$

$$\mathcal{M}^Z = -(G_F/2\sqrt{2})(g_V^e l^\mu + g_A^e l^{\mu 5})(J_\mu^{NC} + J_{\mu 5}^{NC}) \tag{2.1.2b}$$

where $Q \equiv K_\mu - K'_\mu$ is the four-momentum transfer imparted by an electron with initial(final) four-momentum of $K_\mu(K'_\mu)$. α is the fine-structure constant and G_F is

(a) γ-exchange   (b) Z^0-exchange
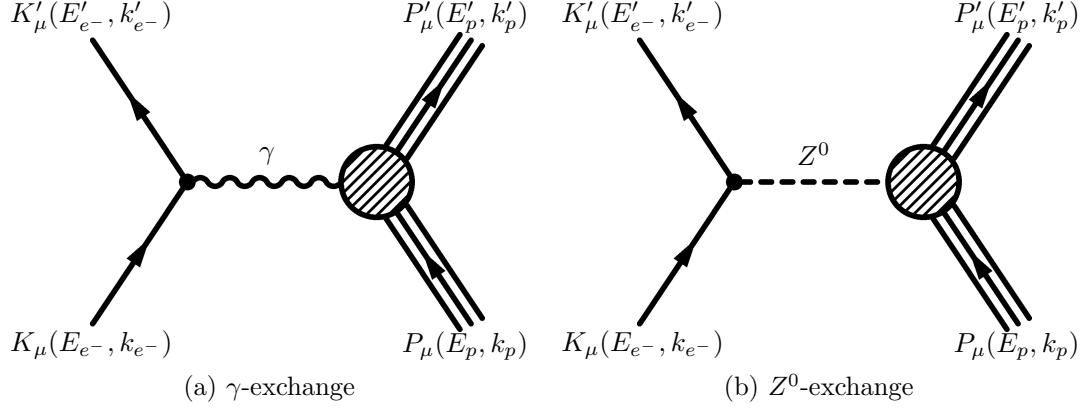
Figure 2.1.1: One-boson-exchanges in electron hadron scattering. $K_\mu(K'_\mu)$ is the four-momentum of the initial(final) state of the electron, and $P_\mu(P'_\mu)$ is the four-momentum of the initial(final) state of the hadron. For each of the electron and the hadron, $E(E')$ is the initial(final) state energy and $k(k')$ is the initial(final) state momentum.

the weak interaction Fermi constant. At tree-level $G_F = \pi\alpha/\sqrt{2}M_W^2 \sin^2\theta_W$ where θ_W is the weak mixing angle defined as $\sin^2\theta_W \equiv 1 - M_W^2/M_Z^2$ in the on-shell renormalization scheme. l^μ and $l^{\mu 5}$ are the electron's vector and axial-vector currents given as [Mu94]

$$l^\mu \equiv \bar{u}_e \gamma^\mu u_e, \qquad l^{\mu 5} \equiv \bar{u}_e \gamma^\mu \gamma^5 u_e \tag{2.1.3a}$$

where u_e is the electron spinor with implicit dependence on the momentum ($\bar{u}_e = \bar{u}_e(k')$, $u_e = u_e(k)$). Analogous to the electron's currents, the hadronic currents J_μ^{EM}, J_μ^{NC} and $J_{\mu 5}^{NC}$ can be expressed as

$$J_\mu^{EM} \equiv g_Q^H \bar{u}_H \gamma_\mu u_H, \quad J_\mu^{NC} \equiv g_V^H \bar{u}_H \gamma_\mu u_H, \quad J_{\mu 5}^{NC} \equiv g_A^H \bar{u}_H \gamma_\mu \gamma_5 u_H \tag{2.1.3b}$$

where u_H's are the hadron spinor with implicit dependence on the momentum ($\bar{u}_H = \bar{u}_H(k')$, $u_H = u_H(k)$). g_Q^e, g_V^e and g_A^e are the electromagnetic, weak and axial-vector charges of the hadron. Since the hadrons are composed of quarks, the hadronic

currents can also be expressed as the matrix elements of the electromagnetic, weak and axial-vector current operators as [Mu94]

$$J_\mu^{EM} \equiv \langle H | \hat{J}_\mu^{EM} | H \rangle, \quad J_\mu^{NC} \equiv \langle H | \hat{J}_\mu^{NC} | H \rangle, \quad J_{\mu 5}^{NC} \equiv \langle H | \hat{J}_{\mu 5}^{NC} | H \rangle \qquad (2.1.3c)$$

where $|H\rangle$ is any hadronic state and

$$\hat{J}_\mu^{EM} \equiv \sum_q g_Q^q \bar{u}_q \gamma_\mu u_q, \quad \hat{J}_\mu^{NC} \equiv \sum_q g_V^q \bar{u}_q \gamma_\mu u_q, \quad \hat{J}_{\mu 5}^{NC} \equiv \sum_q g_A^q \bar{u}_q \gamma_\mu \gamma_5 u_q \qquad (2.1.3d)$$

with the sum confined to the three light quarks (u, d, s) and the heavy quarks (t, b, c) ignored due to their negligible contribution to the nucleon static EM structure at low Q^2 (~ 1 GeV^2) [KM88]. As in Eqs. 2.1.3a and 2.1.3b, the u's are the spinor operators with implicit dependence on the momentum. g_Q^q, g_V^q and g_A^q are the electromagnetic, weak and axial-vector charges of the quarks. The Q^2 dependence of the Z^0 propagator has been ignored in Eq. 2.1.2b since $|Q^2| \ll M_Z^2$ at the kinematics discussed in this thesis.

The electron-hadron (eH) scattering amplitude is simply the sum of the scattering amplitudes from above:

$$\mathcal{M}^{eH} = \mathcal{M}^\gamma + \mathcal{M}^Z. \qquad (2.1.4)$$

The scattering probability, $d\sigma$, is proportional to the total scattering amplitude:

$$d\sigma \propto |\mathcal{M}^{eH}|^2 = |\mathcal{M}^\gamma|^2 + 2(\mathcal{M}^\gamma)^*(\mathcal{M}^Z) + |\mathcal{M}^Z|^2 \qquad (2.1.5)$$

where * denotes the complex conjugate. Assuming that the contributions from l's and J's in the scattering amplitudes given by Eqs. 2.1.2 are comparable, the ratio of the scattering amplitudes at $Q^2 = 1$ GeV^2 and $G_F = 1.17e^{-5}$ GeV^{-2} has a magnitude

given by [Ze59]

$$|\mathcal{M}^{\gamma}|^2 : 2(\mathcal{M}^{\gamma})^*(\mathcal{M}^Z) : |\mathcal{M}^Z|^2 \sim \frac{4\pi\alpha}{Q^2} : 2\left(\frac{4\pi\alpha}{Q^2}\right)\left(\frac{G_F}{2\sqrt{2}}\right) : \left(\frac{G_F}{2\sqrt{2}}\right)^2 \sim 1 : 2e^{-4} : 9e^{-9}.$$

The electromagnetic scattering amplitude, $\mathcal{M}^{\gamma}$, dominates eH scattering. Thus, any absolute cross-section measurement would be a measurement of $\mathcal{M}^{\gamma}$. However, the weak neutral current scattering amplitude, $\mathcal{M}^Z$, interferes with $\mathcal{M}^{\gamma}$, and this term is only a factor of $\sim 10^{-4}$ smaller than $\mathcal{M}^{\gamma}$, making $\mathcal{M}^Z$'s measurement accessible to precision experiments. Since the axial-vector component of the weak neutral current maximally violates parity, $\mathcal{M}^Z$ can be cleanly isolated via a differential cross-section measurement as

$$A_{PV} = \frac{d\sigma^R - d\sigma^L}{d\sigma^R + d\sigma^L} = \frac{2(\mathcal{M}^{\gamma})^*(\mathcal{M}^{Z,PV})}{|\mathcal{M}^{eH}|^2} \sim \frac{2(\mathcal{M}^{\gamma})^*(\mathcal{M}^{Z,PV})}{|\mathcal{M}^{\gamma}|^2}, \qquad (2.1.6)$$

where $d\sigma^{R(L)}$ is the scattering probability of a right(left) circularly polarized electron with the hadron, and $\mathcal{M}^{Z,PV}$ is the PV component of $\mathcal{M}^Z$ given as

$$\mathcal{M}^{Z,PV} = -(G_F/2\sqrt{2})(g_V^e l^{\mu} J_{\mu 5}^{NC} + g_A^e l^{\mu 5} J_{\mu}^{NC}). \qquad (2.1.7)$$

Since J_{μ}^{NC} and $J_{\mu 5}^{NC}$ contain information about the extended structure of the hadron, PV A_{PV} measurement provides a clean means of studying the hadron properties.

A_{PV} for eH scattering to discrete states (in the Standard Model) is often expressed as [Do89]

$$A_{PV} = A_{PV}^0 \frac{W^{PV}}{F^2} \qquad (2.1.8)$$

with

$$A_{PV}^0 \equiv -\frac{G_F |Q^2|}{4\pi\alpha\sqrt{2}} \qquad (2.1.9)$$

where W^{PV} contains the PV response and F^2 contains the parity-conserving response. Both W^{PV} and F^2 are expressed in terms of form-factors(FFs).

2.2 Form Factors (FFs)

The hadronic matrix elements of the current operators of the hadrons from Eq. 2.1.3c cannot be evaluated. But symmetry arguments can be used to constrain these matrix elements in terms of FFs. FFs describe the deviation of the hadrons from point-particle like scattering objects and parametrize the extended structure of the hadrons. The hadronic matrix elements of the current operators from Eq. 2.1.3c for a proton (spin 1/2 hadron) is given as

$$J_\mu^{EM} = \bar{p}(k') \left[\gamma^\mu F_1^{\gamma,p}(Q^2) + \frac{i\sigma^{\mu\nu}q_\nu}{2M_p} F_2^{\gamma,p}(Q^2) \right] p(k) \tag{2.2.1a}$$

$$J_\mu^{NC} = \bar{p}(k') \left[\gamma^\mu F_1^{Z,p}(Q^2) + \frac{i\sigma^{\mu\nu}q_\nu}{2M_p} F_2^{Z,p}(Q^2) \right] p(k) \tag{2.2.1b}$$

$$J_{\mu5}^{NC} = \bar{p}(k') \left[\gamma^\mu \gamma_5 G_A^{Z,p}(Q^2) \right] p(k) \tag{2.2.1c}$$

where F_1, F_2 and G_A are the Dirac, Pauli and axial-vector FFs, $\sigma^{\mu\nu} = \frac{i}{2}[\gamma^\mu, \gamma^\nu]$ and $q^2 = -Q^2 < 0$. $\bar{p}(k')$ and $p(k)$ are the proton Dirac spinors for the final and initial momenta k' and k respectively. M_p is the proton mass.

At $Q^2 = 0$, the electromagnetic FFs, $F_1^{\gamma,p}$ and $F_2^{\gamma,p}$ are normalized as

$$F_1^{\gamma,p}(0) = Q_p = 1, \qquad F_2^{\gamma,p}(0) = \kappa_p = +1.79 \tag{2.2.2}$$

where Q_p is the electric charge of the proton in units of the electron charge $|e|$ and κ_p is the anomalous magnetic moment of the proton in units of the Bohr magneton μ_N.

In terms of the constituent quarks, Eqs. 2.2.1 can be expressed as

$$J_\mu^{EM} = \bar{p}(k') \left[\sum_{j=quarks} g_Q^j \left(\gamma^\mu F_1^{j,p}(Q^2) + \frac{i\sigma^{\mu\nu}q_\nu}{2M_j} F_2^{j,p}(Q^2) \right) \right] p(k) \qquad (2.2.3a)$$

$$J_\mu^{NC} = \bar{p}(k') \left[\sum_{j=quarks} g_V^j \left(\gamma^\mu F_1^{j,p}(Q^2) + \frac{i\sigma^{\mu\nu}q_\nu}{2M_j} F_2^{j,p}(Q^2) \right) \right] p(k) \qquad (2.2.3b)$$

$$J_{\mu5}^{NC} = \bar{p}(k') \left[\sum_{j=quarks} g_A^j \gamma^\mu \gamma_5 G_A^{j,p}(Q^2) \right] p(k) \qquad (2.2.3c)$$

where $F_{1(2)}^{j,p}$ refer to the jth-quark contribution to the Dirac(Pauli) FFs of the proton. The underlying quark *vector* currents are identical for the electromagnetic and weak neutral currents in Eqs. 2.2.3 because the charges have been factored out. Thus $F_1^{j,p}$ and $F_2^{j,p}$ appearing in Eqs. 2.2.3a and 2.2.3b are identical.

Analogous to the electromagnetic FFs normalization, the Dirac quark FFs of a proton at $Q^2 = 0$ are given as

$$F_1^{u,p}(0) = 2, \qquad F_1^{d,p}(0) = 1, \qquad F_1^{s,p}(0) = 0 \qquad (2.2.4a)$$

so as to yield the normalization of 2(1) for the u(d)-quark distributions in the proton. The normalization of the Pauli FFs for the proton at $Q^2 = 0$ are given as

$$F_2^u(0) \equiv 2\kappa_p + \kappa_n = +1.67 \qquad (2.2.4b)$$

$$F_2^d(0) \equiv \kappa_p + 2\kappa_n = -2.03 \qquad (2.2.4c)$$

$$F_2^s(0) = \kappa_s \qquad (2.2.4d)$$

where $\kappa_{p(n)} = +1.79(-1.91)$ are the anomalous magnetic moment of the proton(neutron) and κ_s is the anomalous magnetic moment of the strange quark in units of the Bohr magneton μ_N.

2.2.1 Sachs Form Factors

The Dirac and Pauli FFs, F_1 and F_2, are usually expressed in terms of the Sachs FFs [Sa62], G_E and G_M, which are defined as

$$G_E \equiv F_1 - \frac{Q^2}{4M^2}F_2, \qquad G_M \equiv F_1 + F_2 \qquad (2.2.5)$$

Here, all the FFs have implicit Q^2 dependence. G_E is referred to as the electric FF and G_M is referred to as the magnetic FF. The advantage of the Sachs FFs over Dirac and Pauli FFs is that in the center-of-mass frame (also referred to as the Breit frame), G_E^γ and G_M^γ are simply the Fourier transforms of the electric and magnetic charge densities of the nucleon [Sa62]. Despite this advantage, the Sachs FFs do have some limitations. The Sachs FFs depend on Q^2 leading to a variation of the Breit frame with Q^2. As a result, the nucleon charge distributions vary with Q^2. There are also relativistic corrections that need to be applied before the Sachs FFs can be interpreted as charge distributions. Though small, these corrections also depend on Q^2, complicating the interpretability of the Sachs FFs.

The hadronic matrix elements of the currents in Eqs. 2.2.1a-2.2.1b and Eqs. 2.2.3a-2.2.3b for a proton can be compared to express $F_{1,2}^{\gamma,p}$ and $F_{1,2}^{Z,p}$ in terms of the quark Dirac and Pauli FFs as

$$\begin{aligned}
F_{1,2}^{\gamma,p} &= g_Q^u F_{1,2}^u + g_Q^d F_{1,2}^d + g_Q^s F_{1,2}^s \\
&= \frac{2}{3}F_{1,2}^u - \frac{1}{3}(F_{1,2}^d + F_{1,2}^s) \qquad (2.2.6a) \\
F_{1,2}^{Z,p} &= g_V^u F_{1,2}^u + g_V^d F_{1,2}^d + g_V^s F_{1,2}^s \\
&= (1 - \frac{8}{3}\sin^2\theta_W)F_{1,2}^u - (1 - \frac{4}{3}\sin^2\theta_W)(F_{1,2}^d + F_{1,2}^s) \qquad (2.2.6b)
\end{aligned}$$

		Tree-Level
g_V^p	$2g_V^u + g_V^d$	$1 - 4\sin^2\theta_W$
g_V^n	$g_V^u + 2g_V^d$	-1
$g_V^{(0)}$	$g_V^u + g_V^d + g_V^s$	-1
$g_A^{T=1}$	$\frac{1}{2}(g_A^u - g_A^d)$	-1
$g_A^{T=0}$	$\sqrt{3}(g_A^u + g_A^d)$	0
$g_A^{(0)}$	$g_A^u + g_A^d + g_A^s$	1

Table 2.1: The vector and axial-vector charges of Eqs. 2.2.8 and 2.2.11 expressed in terms of the constituent quark charges, and the corresponding Standard Model values at tree-level.

or, equivalently in terms of the Sachs FFs as

$$G_{E,M}^{\gamma,p} = g_Q^u G_{E,M}^u + g_Q^d G_{E,M}^d + g_Q^s G_{E,M}^s$$
$$= \frac{2}{3}G_{E,M}^u - \frac{1}{3}(G_{E,M}^d + G_{E,M}^s) \tag{2.2.7a}$$

$$G_{E,M}^{Z,p} = g_V^u G_{E,M}^u + g_V^d G_{E,M}^d + g_V^s G_{E,M}^s$$
$$= (1 - \frac{8}{3}\sin^2\theta_W)G_{E,M}^u - (1 - \frac{4}{3}\sin^2\theta_W)(G_{E,M}^d + G_{E,M}^s). \tag{2.2.7b}$$

Here $g_Q^u = \frac{2}{3}$ and $g_Q^d = g_Q^s = -\frac{1}{3}$ are the electric charges of the individual quarks. $g_V^u = (1 - \frac{8}{3}\sin^2\theta_W)$ and $g_V^d = g_V^s = -(1 - \frac{4}{3}\sin^2\theta_W)$ are the vector charges of the individual quarks in the Standard Model.

The charge symmetry of the strong interaction can be used to write Eqs. 2.2.7a-2.2.7b equivalent for neutron as

$$G_{E,M}^{\gamma,n} = \frac{2}{3}G_{E,M}^d - \frac{1}{3}(G_{E,M}^u + G_{E,M}^s) \tag{2.2.7c}$$

$$G_{E,M}^{Z,n} = (1 - \frac{8}{3}\sin^2\theta_W)G_{E,M}^d - (1 - \frac{4}{3}\sin^2\theta_W)(G_{E,M}^u + G_{E,M}^s) \tag{2.2.7d}$$

Charge symmetry asserts the invariance under a set of exchanges $p \iff n$ and $u \iff d$ and is only broken at the level of $\sim 1\%$ or less [Mi98].

The two equations, Eqs. 2.2.7a and 2.2.7c, have three unknown quantities: $G_{E,M}^u$, $G_{E,M}^d$ and $G_{E,M}^s$. $G_{E,M}^{\gamma,p(n)}$ is taken to be known from previous measurements. In order to extract the strange FFs $G_{E,M}^s$, Eq2. 2.2.7a- 2.2.7c are used to express the neutral current interaction term $G_{E,M}^{Z,p}$ as

$$G_{E,M}^{Z,p} = g_V^p G_{E,M}^{\gamma,p} + g_V^n G_{E,M}^{\gamma,n} + g_V^{(0)} G_{E,M}^s \qquad (2.2.8a)$$

In the above equation, the only unknown quantity is $G_{E,M}^s$. Here, the vector charges, g_V^j, are derived by using the electric charges, $g_Q^u = \frac{2}{3}$ and $g_Q^d = g_Q^s = -\frac{1}{3}$. An analogous expression for $G_{E,M}^{Z,n}$ can be derived (for completeness) using Eqs. 2.2.7a,2.2.7c and 2.2.7d as

$$G_{E,M}^{Z,n} = g_V^n G_{E,M}^{\gamma,p} + g_V^p G_{E,M}^{\gamma,n} + g_V^{(0)} G_{E,M}^s. \qquad (2.2.8b)$$

The tree-level vector charges, g_V^j, of Eqs. 2.2.8 given in Table 2.1.

The nucleon Sachs FFs are normalized at $Q^2 = 0$, analogous to the Dirac and Pauli FFs normalization, as

$$G_E^{\gamma,p}(0) = F_1^{\gamma,p}(0) = 1, \qquad G_M^{\gamma,p}(0) \equiv \mu_p = F_1^{\gamma,p}(0) + F_2^{\gamma,p}(0) = +2.79 \qquad (2.2.9a)$$

$$G_E^{\gamma,n}(0) = F_1^{\gamma,n}(0) = 0, \qquad G_M^{\gamma,n}(0) \equiv \mu_n = F_1^{\gamma,n}(0) + F_2^{\gamma,n}(0) = -1.91 \qquad (2.2.9b)$$

where the electric FFs are expressed in units of the electron charge $|e|$ and the magnetic FFs are expressed in units of the Bohr magneton μ_N. The γ superscript indicates that these are FFs characterizing the electromagnetic interaction via a photon (γ) exchange. $\mu_{p(n)}$ is the anomalous magnetic moment of the proton(neutron) in units of the Bohr magneton μ_N.

The normalization of the quark FFs at $Q^2 = 0$ follows a similar prescription.

The electric quark Sachs FFs for a proton at $Q^2 = 0$ yield the normalized quark distributions in the proton as

$$G_E^u(0) = 2, \qquad G_E^d(0) = 1, \qquad G_E^s(0) = 0 \tag{2.2.10a}$$

The quark magnetic Sachs FFs at $Q^2 = 0$ are defined as the individual quarks magnetic moment as

$$G_M^u(0) \equiv \mu_u, \qquad G_M^d(0) \equiv \mu_d, \qquad G_M^s(0) \equiv \mu_s \tag{2.2.10b}$$

and expressed in terms of the nucleon magnetic moments via Eqs. 2.2.7a and 2.2.7c as

$$G_M^{\gamma,p}(0) = \frac{2}{3}\mu_u - \frac{1}{3}\mu_d - \frac{1}{3}\mu_s \tag{2.2.10c}$$

$$G_M^{\gamma,n}(0) = \frac{2}{3}\mu_d - \frac{1}{3}\mu_u - \frac{1}{3}\mu_s \tag{2.2.10d}$$

2.2.2 Axial-Vector FFs

The extraction of the weak neutral axial-vector FFs usually begins with the comparison of Eqs. 2.2.1c and 2.2.3c to write the proton axial-vector FF (for elastic ep scattering) in terms of the constituent quark axial-vector FFs. The quark axial-vector FFs are then rewritten in terms of the isovector $(G_A^{(3)})$, isoscaler $(G_A^{(8)})$ and strange (G_A^s) axial-vector FFs as [Mu94]

$$\tilde{G}_A^{Z,p} = g_A^{T=1} G_A^{(3)} + g_A^{T=0} G_A^{(8)} + g_A^{(0)} G_A^s. \tag{2.2.11}$$

Expressing the proton axial-vector FF in this form facilitates contact with experimental and theoretical observations. Here,

$$G_A^{(3)} = G_A^u - G_A^d \tag{2.2.12a}$$

$$G_A^{(8)} = \frac{1}{2\sqrt{3}}(G_A^u + G_A^d - 2G_A^s) \tag{2.2.12b}$$

where all the FFs have implicit Q^2 dependence and the tree-level axial-vector charges, g_A^j, are given in Table 2.1.

The axial-vector FFs appearing in Eq. 2.2.11 are generally parameterized with a dipole form [BeF05, Ga71] as

$$G_A^j(Q^2) = G_A^j(0)G_A^D(Q^2) \tag{2.2.13a}$$

$$G_A^D(Q^2) = \frac{1}{(1 + Q^2/\Lambda_A^2)^2} \tag{2.2.13b}$$

where $\Lambda_A = 1.001 \pm 0.020\,\text{GeV}$ [Bu03] is the axial-vector dipole mass parameter.

Since the weak neutral axial-vector current is not conserved (unlike the electromagnetic and weak neutral vector currents), $Q^2 = 0$ values of the axial-vector FFs are not constrained by any symmetry or nucleon quantum numbers. Instead, they are normalized at $Q^2 = 0$ as the spin contribution of each FF term in Eq. 2.2.11 to the net nucleon spin and expressed as

$$G_A^{(3)}(0) = \Delta u - \Delta d \tag{2.2.14a}$$

$$G_A^{(8)}(0) = \frac{1}{2\sqrt{3}}(\Delta u + \Delta d - 2\Delta s) \tag{2.2.14b}$$

$$G_A^s(0) = \Delta s \tag{2.2.14c}$$

where Δq is the net contribution of the individual quark to the nucleon spin. $\Delta u -$

$\Delta d = 1.2695(29)$ is determined from Gamow-Teller β-decay rates with the assumption that the nucleon is in a state of good isospin [Na11]. $\Delta u + \Delta d - 2\Delta s = 0.585(25)$ is determined from hyperon β-decay by imposing an additional constraint of good SU(3) symmetry for the eight lowest-lying baryons in an extension of the SU(2) isospin [Go00]. $\Delta s = -0.084(40)$ is determined from polarized deep inelastic scattering data, and the large uncertainty arises from the model dependency of analysis [Li06]. All the axial-vector normalizations at $Q^2 = 0$ are given in the $\overline{\text{MS}}$-scheme.

At tree-level $g_A^{(T=0)} = 0$, and Eq. 2.2.11 reduces to

$$\tilde{G}_A^{Z,p} = g_A^{T=1} G_A^{(3)} + g_A^{(0)} G_A^s. \tag{2.2.15}$$

2.3 HAPPEX-III

The PV response, W^{PV}, and the parity-conserving FFs in the expression of the PV asymmetry from Eq. 2.1.8 for an electron-proton (ep) scattering are given as [Do88]

$$W^{PV}(\tau, \epsilon) = \frac{1}{\epsilon(1+\tau)} \left[g_A^e \left\{ \epsilon G_E^{\gamma,p} G_E^{Z,p} + \tau G_M^{\gamma,p} G_M^{Z,p} \right\} + g_V^e \epsilon' G_M^{\gamma,p} \tilde{G}_A^{Z,p} \right] \tag{2.3.1a}$$

$$F^2(\tau, \epsilon) = \frac{1}{\epsilon(1+\tau)} \left[\epsilon (G_E^{\gamma,p})^2 + \tau (G_M^{\gamma,p})^2 \right] \tag{2.3.1b}$$

where the electric vector and axial-vector charges, $g_V^e = -(1 - 4\sin^2\theta_W)$ and $g_A^e = 1$ in the Standard Model. $\tau = Q^2/4M_p$, $\epsilon = [1 + 2(1+\tau)\tan^2(\Theta/2)]^{-1}$ where Θ is the central scattering angle.

The PV asymmetry from Eq. 2.1.8 then becomes

$$A_{PV} = A_{PV}^0 \times \{g_V^p + \frac{(\epsilon G_E^p G_E^n + \tau G_M^p G_M^n)g_V^n}{\epsilon(G_E^p)^2 + \tau(G_M^p)^2} +$$
$$\frac{\epsilon G_E^p (G_E^s + \eta G_M^s)g_V^{(0)}}{\epsilon(G_E^p)^2 + \tau(G_M^p)^2} - \frac{\epsilon'(1 - 4\sin^2\theta_W)G_M^p \tilde{G}_A^{Z,p}}{\epsilon(G_E^p)^2 + \tau(G_M^p)^2}\} \qquad (2.3.2)$$
$$= A_V + A_S + A_A$$

with

$$A_V = A_{PV}^0 \left[g_V^p + \frac{(\epsilon G_E^p G_E^n + \tau G_M^p G_M^n)g_V^n}{\epsilon(G_E^p)^2 + \tau(G_M^p)^2} \right] \qquad (2.3.3a)$$

$$A_S = A_{PV}^0 \left[\frac{\epsilon G_E^p (G_E^s + \eta G_M^s)g_V^{(0)}}{\epsilon(G_E^p)^2 + \tau(G_M^p)^2} \right] \qquad (2.3.3b)$$

$$A_A = -A_{PV}^0 \left[\frac{\epsilon'(1 - 4\sin^2\theta_W)G_M^p \tilde{G}_A^{Z,p}}{\epsilon(G_E^p)^2 + \tau(G_M^p)^2} \right] \qquad (2.3.3c)$$

where the vector, axial-vector and the strange content in the asymmetry expression have be separated for clarity, following the notational convention of [Ma05]. Here, $\eta = \frac{\tau G_M^p}{\epsilon G_E^p}$. In Eqs. 2.3.2 and 2.3.3, the superscript γ is dropped from the FFs of the electromagnetic interaction for convenience ($G_{E(M)}^{\gamma,p(n)} \to G_{E(M)}^{p(n)}$).

If the nucleon electromagnetic and axial-vector FFs are considered known, a measurement of the PV asymmetry, A_{PV}, at a specific kinematic yields a linear combination of G_E^s and G_M^s. The choice of kinematics determines the amount of contribution from each of the terms that appear in the expression of A_{PV}. At forward (small scattering) angles, both η and ϵ' are small. Thus, a forward angle A_{PV} measurement yields a linear combination of G_E^s and G_M^s, with small contributions (and uncertainties) from the axial-vector terms because they are highly suppressed (as a consequence of ϵ' being small). At backward (larger scattering) angles, η gets drastically bigger while ϵ' increases by a much smaller amount. As a result, the backward angle A_{PV}

measurements are primarily sensitive to G_M^s, and also have larger contributions (and uncertainties) arising from the axial-vector terms.

HAPPEX-III measured a linear combination of G_E^s and G_M^s at forward angle, meaning that the uncertainties arising from the axial-vector terms were highly suppressed.

2.4   HAPPEX-III Radiative Corrections

So far, only the lowest level (tree-level) contributions in the ep scattering that correspond to the one-boson-exchange (γ or Z^0) with one quark at a time have been considered. However, ep scattering can also proceed via the exchange of both the γ and Z^0 boson in the same scattering channel, or via the exchange of γ or Z^0 with more than one quark at a time in the same scattering channel. This leads to "higher-order" or "radiative" corrections in the ep scattering tree-level contributions. Corrections arising from the assumptions such as ignoring the heavy quarks (c, t, b) are also loosely considered radiative corrections.

Radiative corrections to the PV asymmetry, A_{PV}, are performed via the vector and axial-vector charges, $g_{V,A}^j$, that appear in the expression of A_{PV}. These charges, corrected for the radiative effects, are given in Table 2.2. The R-factors contain the radiative corrections, and the tree-level charges of Table 2.1 can be obtained from the charges (corrected for the radiative effects) of Table 2.2 by setting $R = 0$. In the Standard Model, R-factors primarily arise from three factors [Mu94]: heavy quark contributions, "one-quark" electroweak interactions and "many-quark" or "anapole" electroweak interactions.

$$R = \Delta_{\text{heavy}} + R_{\text{one-quark}} + R_{\text{anapole}} \tag{2.4.1}$$

	Tree-Level	Rad. Corr. Included
g_V^p	$1 - 4\sin^2\theta_W$	$(1 - 4\sin^2\theta_W)(1 + R_V^p)$
g_V^n	-1	$-(1 + R_V^n)$
$g_V^{(0)}$	-1	$-(1 + R_V^{(0)})$
$g_A^{T=1}$	-1	$-(1 + R_A^{(T=1)})$
$g_A^{T=0}$	0	$\sqrt{3}R_A^{(T=0)}$
$g_A^{(0)}$	1	$1 + R_A^{(0)}$

Table 2.2: The vector and axial-vector charges at the tree level ($R_{V,A} = 0$) and with the radiative correction R-factors in the Standard Model.

Δ_{heavy} is the correction arising from the effects of the heavy quarks (c, b, t) to the hadronic neutral current couplings. This effect has been bound to be $\sim 10^{-4}$ for the vector term and $\sim 10^{-2}$ for the axial term [KM88], and is therefore neglected in our radiative corrections. $R_{\text{one-quark}}$ and R_{anapole} corrections are discussed in separate sections below.

2.4.1 One-Quark Corrections

The one-quark corrections are the corrections to the tree-level ep scattering contributions arising from the scattering channel that involves both the γ and Z^0 propagators but only a single quark (or equivalently a $q\bar{q}$ loop). Typical one-quark radiative correction diagrams are shown in Figures 2.4.1: $\gamma - Z^0$ mixing diagram is on the left and $\gamma - Z^0$ box diagram is on the right. The $\gamma - Z^0$ mixing diagram is also referred to as the vacuum polarization correction, analogous to a similar concept in quantum-electrodynamics (QED), because the γ and Z^0 couple to a $q\bar{q}$ loop. One-quark corrections are the lowest order corrections, and are reliably calculable in the Standard Model with little theoretical uncertainty, apart from that arising from a gentle dependence of the corrections on the Q^2 [Mu94, Zh00]. This dependence, however, can be ignored without significantly affecting the results of HAPPEX-III because of

(a) $\gamma - Z^0$ mixing diagram. (b) $\gamma - Z^0$ box diagram.
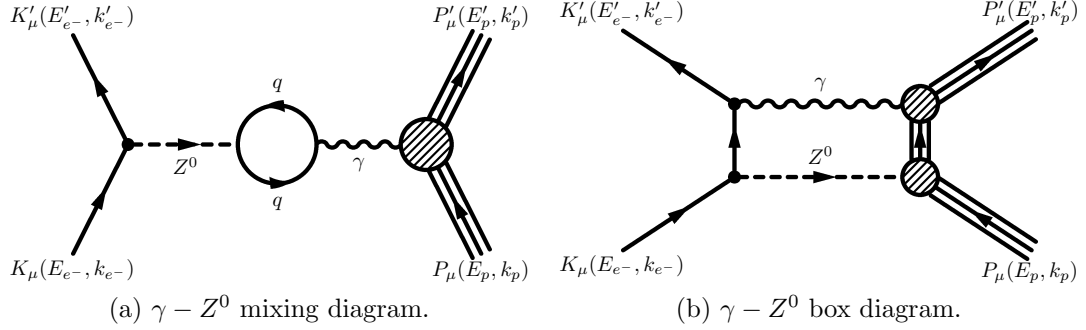
Figure 2.4.1: Two representative one-quark processes that lead to corrections in the tree-level variables. On the left is the $\gamma - Z^0$ mixing diagram where a γ and Z^0 couple to a $q\bar{q}$ loop. On the right is the $\gamma - Z^0$ box diagram.

	Tree Level	One-Quark
ρ	1	1.0006
ρ'	1	0.9877
κ'	1	1.0026
κ	1	1.0299
λ'	0	-1.8e-5
λ_u	0	-0.0118
λ_d	0	0.0029

Table 2.3: Tree level and one-quark corrections in the Standard Model in the $\overline{\text{MS}}$-scheme [Na11]. In this scheme, $\sin^2 \theta_W = 0.23116(13)$ [Na11].

low Q^2 of 0.6 GeV^2.

The one-quark corrections are usually presented in the literature in terms of the Standard Model neutral-current parameters $\rho, \rho', \kappa, \kappa', \lambda', \lambda_u$ and λ_d as given in Table 2.3 [Na11]. These neutral-current parameters are parameterized in terms of the R-factors in order to perform the one-quark radiative corrections. This parameterization is discussed below.

The effective coupling constants that characterize the weak interaction, C_1 and C_2, can be expressed in terms of the neutral-current parameters of Table 2.3 as [Na11]

$$C_{1\mu} = \rho'(-\frac{1}{2} + \frac{4}{3}\kappa' \sin^2\theta_W) + \lambda' \qquad (2.4.2a)$$

$$C_{1d} = \rho'(\frac{1}{2} - \frac{2}{3}\kappa' \sin^2\theta_W) - 2\lambda' \qquad (2.4.2b)$$

$$C_{2\mu} = \rho(-\frac{1}{2} + 2\kappa \sin^2\theta_W) + \lambda_\mu \qquad (2.4.2c)$$

$$C_{2d} = \rho(\frac{1}{2} - 2\kappa \sin^2\theta_W) + \lambda_d \qquad (2.4.2d)$$

where C_1's relate to the PV vector(electron) axial-vector(quark) couplings and C_2's relate to the PV axial-vector(electron) vector(quark) couplings of the weak neutral current (via Z^0) of ep scattering (analogous to the PV scattering amplitude of Eq. 2.1.7). These coupling constants are related to the vector and axial-vector charges, $g_{V,A}^j$, of Table 2.2 as

$$g_V^{u,c,t} = -2C_{1\mu} \qquad\qquad g_V^{d,s,b} = -2C_{1d} \qquad (2.4.3a)$$

$$g_A^{u,c,t} = \frac{2C_{2u}}{1 - 4\sin^2\theta_W} \qquad g_A^{d,s,b} = \frac{2C_{2d}}{1 - 4\sin^2\theta_W} \qquad (2.4.3b)$$

The prescription for extracting the R-factors of one-quark corrections is to use the neutral-current parameters published in the particle data book [Na11] (and presented in Table 2.3) to calculate the coupling constants C_1s and C_2s via Eqs. 2.4.2. Using these coupling constants, the constituent quark's weak vector and axial-vector charges $g_{V,A}^j$'s are calculated using Eqs. 2.4.3. The weak vector and axial-vector charges that relate to the R-factors are then calculated using the expressions in Table 2.1. The R-factors can then be extracted by using the expressions for these charges in terms of the R-factors from Table 2.2.

The coupling constants C_1s and C_2s, quark weak vector and axial-vector charges

	Tree Level	One-Quark
C_{1u}	-0.191787	-0.188654
C_{1d}	0.345893	0.341279
C_{2u}	-0.03768	-0.0356709
C_{2d}	0.03768	0.0267709

Table 2.4: Tree-level and one-quark C-parameters of Eqs. 2.4.2 in $\overline{\text{MS}}$-scheme of the Standard Model evaluated using the values of Table 2.3.

	Tree Level	One-Quark
$g_V^{u,c,t}$	0.383573	0.377308
$g_V^{d,s,b}$	-0.691787	-0.682558
$g_A^{u,c,t}$	-1	-0.94668
$g_A^{d,s,b}$	1	0.710482

Table 2.5: Tree-level and one-quark g-charges of Eqs. 2.4.3 in $\overline{\text{MS}}$-scheme of the Standard Model.

	Tree-Level	One-Quark
g_V^p	0.07536	0.0720586
g_V^n	-1	-0.987808
$g_V^{(0)}$	-1	-0.987808
$g_A^{T=1}$	-1	-0.828581
$g_A^{T=0}$	0	-0.40911
$g_A^{(0)}$	1	0.474282

Table 2.6: The vector and axial-vector charges at the tree-level and with one-quark corrections in the $\overline{\text{MS}}$-scheme of the Standard Model.

	Tree-Level	One-Quark
R_V^p	0	-0.0438087
R_V^n	0	-0.012192
$R_V^{(0)}$	0	-0.012192
$R_A^{T=1}$	0	-0.171419
$R_A^{T=0}$	0	-0.2362
$R_A^{(0)}$	0	-0.525718

Table 2.7: The R-factors at the tree-level and with one-quark corrections in the $\overline{\text{MS}}$-scheme of the Standard Model.

$g_{V,A}^j$s, composite weak vector and axial-vector charges that relates to the R-factors and the associated R-factors at tree-level and with one-quark corrections are presented in Tables 2.4, 2.5, 2.6 and 2.7.

2.4.2 Anapole Corrections

The anapole corrections arise due to axial-vector coupling of the photon to the nucleon [Zh00]. The coupling of the ep electromagnetic scattering (via γ-boson exchange) can be modified by the interaction among the quarks inside the nucleon via the exchange of weak bosons ($Z^0, W^\pm$). One such process is depicted in Figure 2.4.2 in which the weak interaction between the quarks generates a parity-violating (PV) pion (π) emission, followed by a parity-conserving (PC) π absorption through the
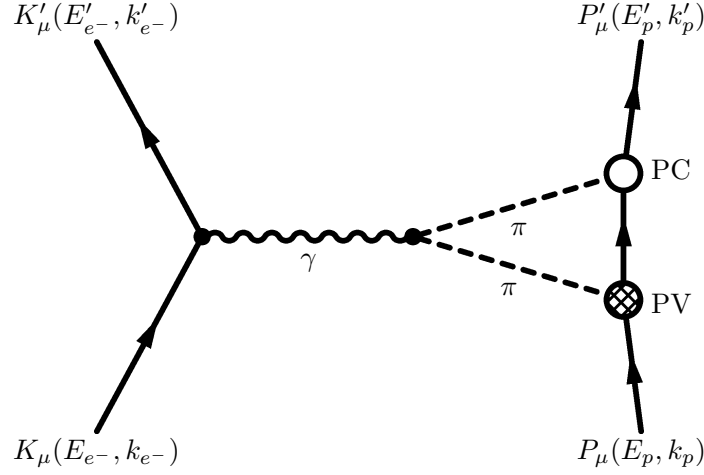
Figure 2.4.2: A representative multi-quark process of the electron proton scattering: quarks inside the proton interact via the generation of a parity-violating (PV) pion (π) followed by a parity-conserving (PC) π absorption via the strong interaction.

strong interaction. The anapole corrections are purely axial-vector, and do not affect the vector couplings of the weak neutral current interactions.

HAPPEX-III used the anapole corrections published by Zhu et al. [Zh00]. The authors presented their results in the on-shell renormalization-scheme (OSR), and their results are recast in the $\overline{\text{MS}}$-scheme to make these corrections compatible with the one-quark corrections as

$$\frac{R_{\overline{MS}}}{R_{OSR}} = \frac{1 - 4s_W^2}{1 - 4s_Z^2} = 1.44 \tag{2.4.4}$$

where $s_Z^2 = \sin^2 \theta_W = 0.23116(13)$ in $\overline{\text{MS}}$-scheme and $s_W^2 = \sin^2 \theta_W = 0.22292(28)$ in OSR-scheme [Na11]. The anapole corrections are presented in Table 2.8.

$R_A^{T=1}$	$R_A^{T=0}$	$R_A^{(0)}$
0.086 ± 0.34	0.014 ± 0.20	N/A

Table 2.8: The anapole corrections in the $\overline{\text{MS}}$-scheme [Zh00].

A large number of virtual hadronic states can give rise to the anapole effects. But

only a few of the dominant contributions have been considered in the corrections of Table 2.8, so the authors assign considerable amount of theoretical uncertainties in these corrections to reflect this. While the authors suggest that the anapole corrections can be as large as 30% of the axial-vector FF, the net effect at HAPPEX-III kinematics is suppressed by the small $\epsilon'(1 - \sin^2 \theta_W)$ term that multiplies the axial-vector term in the expression of A_{PV}. Yet, the anapole correction uncertainties are amongst the dominant sources of uncertainty in the strange FFs extraction from A_{PV} (the other dominant source of uncertainty is the uncertainty in the proton and neutron FFs themselves). The uncertainty in these corrections, as a fraction of the axial-vector FF, is assumed in this work to be constant with Q^2.

Additional radiative corrections involving two-photon exchange, expected to be at the level of 0.03% [AS07], are neglected.

2.5   PREX

In the Born approximation, the PV cross-section asymmetry for longitudinally polarized electrons elastically scattered from an unpolarized ^{208}Pb nucleus, A_{PV}, is expressed as

$$A_{PV} = A_{PV}^0 [g_V^p + g_V^n \frac{F_n(Q^2)}{F_p(Q^2)}] \tag{2.5.1a}$$

with $g_V^p = 1 - 4\sin^2\theta_W$, $g_V^n = -1$ as given in Table 2.2 and

$$F_n(Q^2) = \frac{1}{4\pi} \int dx j_0(qx)\rho_n(x), \tag{2.5.1b}$$

$$F_p(Q^2) = \frac{1}{4\pi} \int dx j_0(qx)\rho_p(x). \tag{2.5.1c}$$

$F_{n(p)}$ is the neutron(proton) FF and is expressed as the Fourier transform of the neutron(proton) charge density $\rho_{n(p)}$. j_0 is the zero'th order spherical Bessel function. At tree level, $g_V^p = 0.07536$ (in the $\overline{\text{MS}}$-scheme, Table 2.6). So A_{PV} measurement of Eq. 2.5.1a is almost a direct measurement of the (Fourier transform of) the neutron density; the Fourier transform of the proton density occurring in the denominator of Eq. 2.5.1a is determined via unpolarized electron scattering experiments.

The Born approximation, however, is not valid for a heavy nucleus such as ^{208}Pb, and Coulomb distortion effects must be included. These effects have been accurately calculated [Lal97, RP05, Be75, Ch98, Va72], and many other details relevant for a practical parity-violation experiment to measure neutron densities have been discussed in a publication by Horowitz et al. [Ho01].

3

HAPPEX-III Experimental Setup

This chapter discusses the experimental apparatus of HAPPEX-III, which was performed in experimental Hall A of Thomas Jefferson National Accelerator Facility [Le01], also referred to as Jefferson Lab (JLab). The apparatus included equipment that was fairly standard to JLab including the accelerator itself, as well as the equipment that was standard to experimental Hall A. Instruments specific to HAPPEX-III, which were not part of the standard JLab equipments are also discussed in this chapter.

Most of the experimental apparatus used by HAPPEX-III were also used by PREX. Thus, most of what is discussed in this chapter also applies to PREX. However, any PREX specific instruments, not shared by HAPPEX-III, are discussed in the following chapter.

3.1 Overview

HAPPEX-III used 100 μA continuous-wave (cw) electron beam that was longitudinally polarized, and had an average energy of 3.481 GeV. These electrons were generated at the polarized electron source, also referred to as the injector, accelerated

in the linear-accelerators (linacs) of JLab [Le01], and transported to experimental Hall A. A schematic of HAPPEX-III experimental setup is presented in Figure 3.1.1. The electrons elastically scattered from a 25 cm liquid hydrogen (LH2) target located at the center of the hall. The two Hall A high-resolution spectrometers (HRSs) [Al04], which could be rotated about a pivot at the center of the hall, were placed symmetrically about the central beamline at an average polar angle of $\langle \theta \rangle \sim 13.7°$. Each HRS accepted electrons in the solid angle of 5 msr and transported them to the detectors. The HRSs were set to a momentum of 3.1415 GeV in order to transport only the elastically scattered electrons. The unscattered electrons were discarded at the beam dump.

The Compton polarimeter, located near the beamline entrance of the hall, provided continuous beam polarization measurement concurrently with data acquisition. The Møller polarimeter, located inside the hall, provided an independent beam polarization measurement, but its measurements were invasive and required dedicated measurements. Located between the polarimeters were the raster magnets that rastered the beam at the target. Beam position monitors (BPMs) and beam current monitors (BCMs) were located both inside the hall and along the beamline outside the hall. The BPMs monitored beam parameters such as the energy, intensity and trajectories, and the BCMs monitored the beam intensity. The integrated responses of the BPMs, BCMs, detector photo-multiplier tubes (PMTs), and other diagnostic instruments were digitized by various analog-to-digital converters (ADCs) and recorded for each helicity-window by a centralized data acquisition system (DAQ). A helicity-quartet $(+--+$ or $-++-)$ pattern, with each helicity-window held constant for 33.83 ms was used during HAPPEX-III. The helicity patterns are described below in Section 3.4.
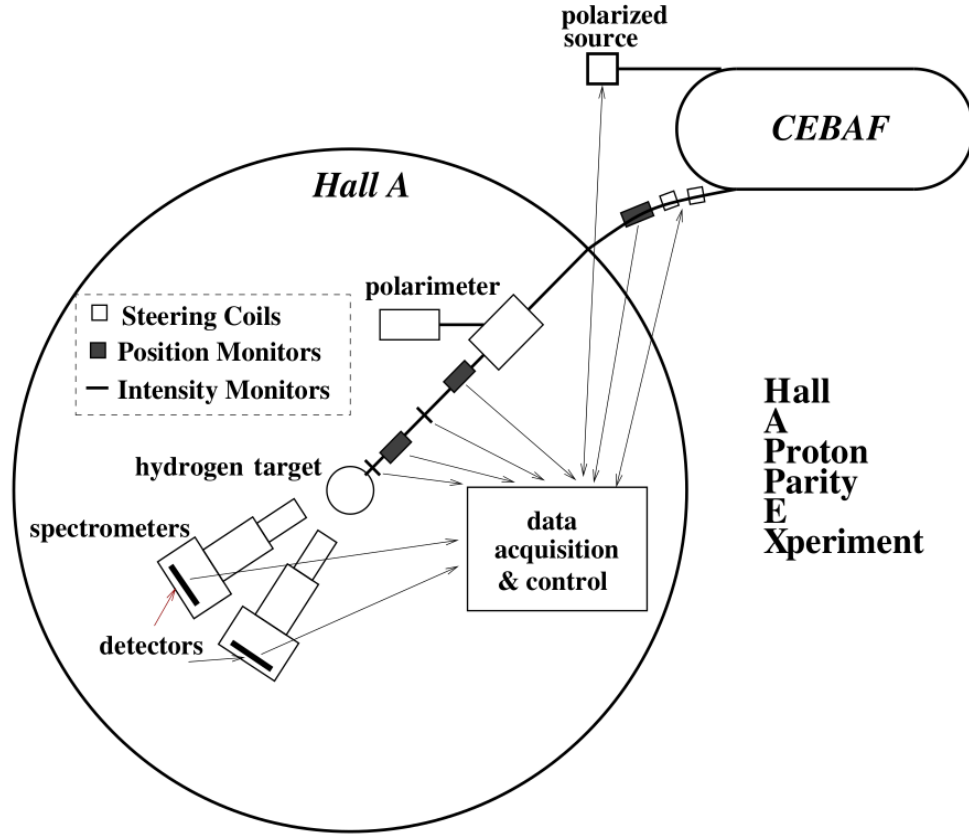
Figure 3.1.1: An overview of the experimental setup of HAPPEX-III. The electrons were generated at the polarized electron source, also referred to as the injector, accelerated to high energies, and transported into experimental Hall A. The electrons elastically scattered from a target located at the center of the hall, and the Hall A high-resolution spectrometers (HRSs) focused them onto detectors. The beam polarization was monitored by two independent polarimeters: Compton and Møller polarimeters. The beam current monitors (BCMs) monitored the beam intensity, and the beam position monitors (BPMs) monitored the beam energy, intensity and trajectories. The responses of the BCMs, BPMs, detectors and other diagnostic instruments were read out by a centralized data acquisition system (DAQ). Reproduced from [An04].

3.2 Jefferson Lab

A schematic of Jefferson Lab (JLab) is displayed in Figure 3.2.1. The longitudinally polarized cw electrons were generated at the injector and transported into the north linac where they acquired $\sim 1.1\,\mathrm{GeV}$ of energy. Each of the north and south linac
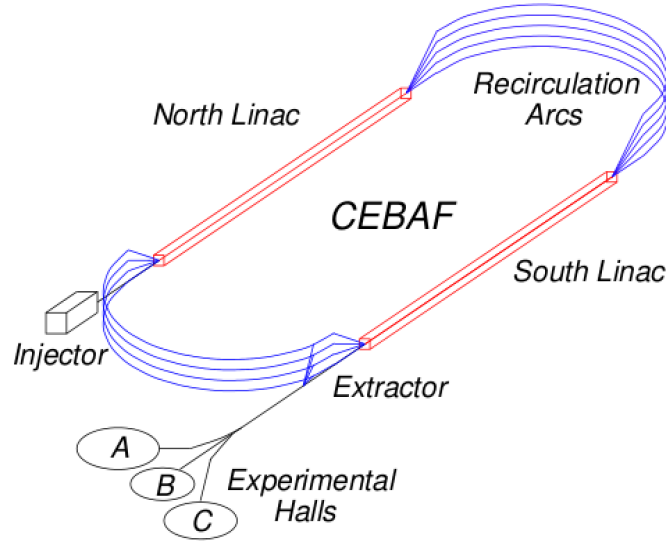
Figure 3.2.1: A schematic of Continuous Electron Beam Accelerator Facility (CE-BAF), also referred to as Jefferson Lab (JLab). The longitudinally polarized electrons were generated at the injector, accelerated to high energies at the linear-accelerators (linacs), and transported to experimental halls A, B and C. Reproduced from [Mo07].

provided up to 1.1 GeV energy to the electrons. The electrons were then bent at the recirculating arcs and transported into the south linac. The electrons exiting the south linac could either be transported into one of the three experimental halls, or be fed back into the north linac through the recirculating arcs for additional acceleration. During HAPPEX-III, the electrons exiting the south linac were fed back into the recirculating arcs and into the linacs for additional acceleration: the electrons traversed through each of the north and south linac twice and acquired 3.481 GeV of energy before being transported into experimental Hall A. During HAPPEX-III, JLab delivered 100 μA cw electron beam with an average polarization of 89.4%.

3.3 Polarized Electron Source (Injector)

The polarized electrons were generated at the injector. The injector consisted of a laser table and a GaAsP photocathode as illustrated in Figure 3.3.1. On the laser
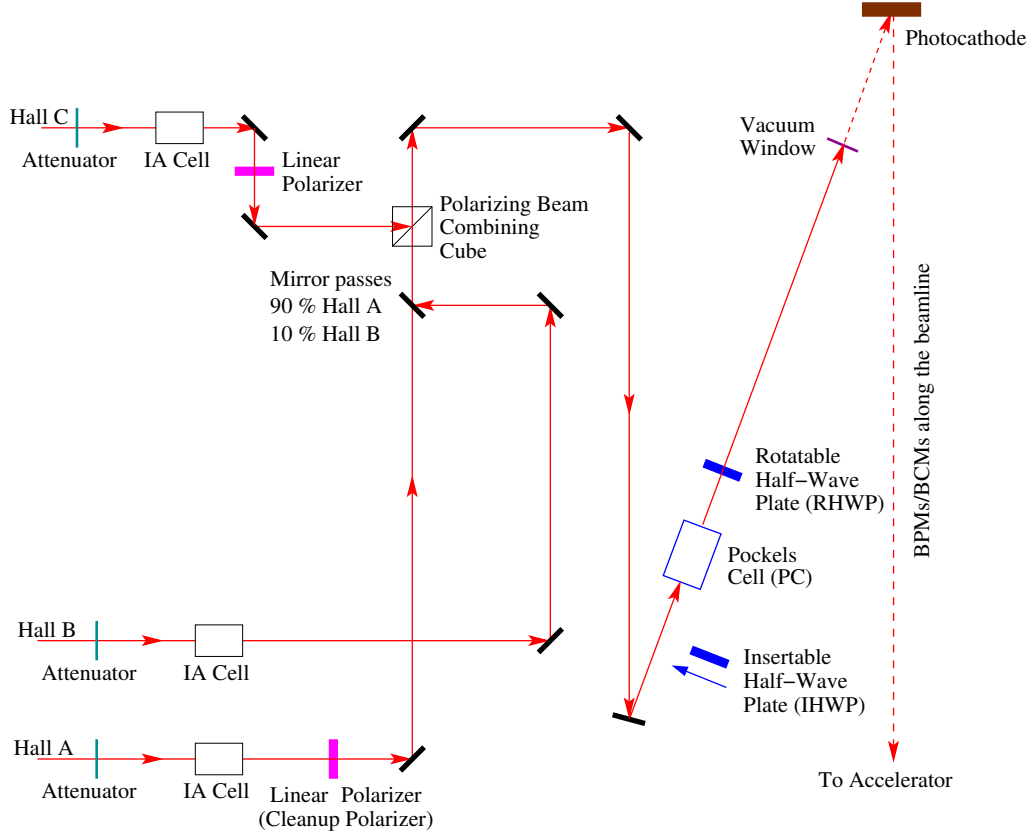
Figure 3.3.1: The schematic of polarized source (injector) at JLab. The laser light was circularly polarized by the Pockels Cell (PC) operated at its quarter-wave voltage. This laser light generated circularly polarized electrons from a GaAsP photocathode, with the polarization state determined by the laser light's polarization.

table were 780 nm lasers that propagated through a series of optical elements and acquired circular polarization. The laser circular polarization was generated using a "Pockels Cell (PC)" that was operated at its quarter-wave voltage. A PC is a uniaxial crystal which becomes triaxial, and behaves like a retardation plate when appropriate voltage is applied along its symmetry axis. The polarity of this voltage was modulated rapidly in complementary pairs to generate laser light of complementary helicity pairs.

An insertable half-wave plate (IHWP) was inserted and retracted from the laser light's path at regular intervals during the experiment. The IHWP, along with a rotatable half-wave plate (RHWP) were used to minimize uncertainties arising from

imperfect laser light circular polarization. The use of IHWP and RHWP to suppress the uncertainties arising from imperfect laser light circular polarization is described in Chapter 6.

The three experimental halls had their own lasers, each a gain-switched diode laser modulated at 499 MHz. These lasers generated circularly polarized electrons from a GaAsP photocathode, with the polarization state determined by the incident laser light's polarization. The three lasers were interleaved to produce electron bunches with a frequency of 1497 MHz [Le01]. So the electron beam could be arbitrarily split into three 499 MHz bunches, and variable amounts of current delivered into each experimental hall.

3.4   Helicity Generator (HG)

The helicity generator (HG) [Fl10] generated pulses that controlled the generation of the electron beam helicity and the operation of the "parity" [1] data acquisition system (DAQ). Not all the pulses generated by the HG were used by HAPPEX-III. So the pulses unused by HAPPEX-III are ignored [2] and only the ones used by HAPPEX-III are discussed in this section. The HG was developed locally at JLab.

HAPPEX-III used four types of pulses: MPS, pair-sync, helicity and delayed helicity. During HAPPEX-III, individual window width of all these pulses were 33.83 ms. The schematic of these pulses are presented in Figure 3.4.1. Not shown in Figure 3.4.1 is delayed helicity, which was simply the helicity pulse delayed by 8 helicity windows.

The MPS determined the timing schematic of the parity DAQ. Each MPS window consisted of T_{Settle} and T_{Stable}. T_{Stable} marked the period during which the beam

---

[1]A detailed discussion of the "parity" DAQ is presented in Section 3.11.1.

[2]Detailed information on the HG and the pulses it generates can be found at [Fl10].
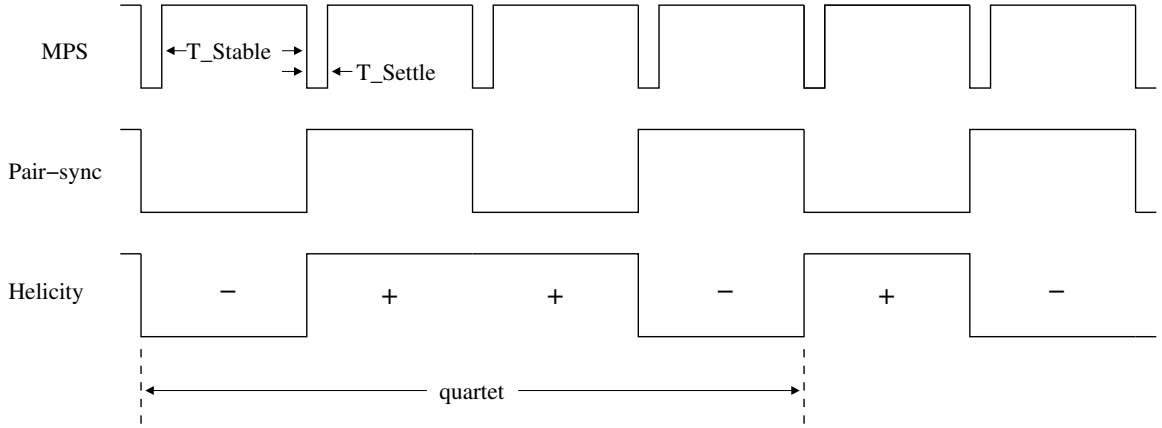
Figure 3.4.1: HAPPEX-III only used MPS, helicity, pair-sync and delayed helicity (which is simply just the helicity pulse delayed by 8 helicity widows, and is not shown here). The MPS determined the timing schematic of the parity DAQ. The helicity determined the beam polarization state and the pair-sync simply kept track of the complementary pairs. During HAPPEX-III, each window in all these pulses were 33.83 ms wide. HAPPEX-III used a T_{Settle} of 500 μs, T_{Stable} of 33.33 ms and a quartet helicity pattern.

polarization state was acceptable. Its leading edge triggered the parity DAQ to begin data acquisition. T_{Settle} was the amount of time during which the beam polarization state was unacceptable. T_{Settle} extended to slightly greater than the time required to change between the helicity states in order to avoid instabilities associated with PC high-voltage (HV) change. HAPPEX-III used a T_{Settle} of 500 μs, and T_{Stable} of 33.33 ms.

The helicity signal determined the polarity of the PC HV, determining the helicity of the electron beam. Thus, the helicity signal contained information about the beam polarization state. The first window of a helicity-sequence was generated using a pseudo-random algorithm, and the rest determined by the choice of sequence: the second window of a helicity-pair was always the complement of the first $(+-$ or $-+)$, the helicity-quartet was always $+--+$ or $-++-$ and the helicity-octet was always $+--+-++-$ or $-++-+--+$. HAPPEX-III used the helicity-quartet sequence. At HAPPEX-III helicity window length of 33.83 ms, each window contained two full

60 Hz cycles of the power-line noise that averaged to zero.

The HG used a pseudo-random 32-bit algorithm to generate the helicity-sequence that repeated once every $2^{32} = 4.3 \times 10^9$ windows. During HAPPEX-III, the pseudo-random generator only generated a new helicity window every $33.83 \times 4 = 135.3$ ms. So, the pattern repeated once every ~ 18 years essentially making the HAPPEX-III helicity sequence random.

The pair-sync toggled at the helicity reversal frequency, and marked the complementary pairs of a helicity sequence. The start of each helicity, pair-sync and delayed helicity window always coincided with the leading edge of T_{Settle}.

The HG was completely ground-isolated from other equipments: it was operated by a stand-alone battery, and fiber optic cables transmitted all the output signals. The ground-isolation minimized the helicity-correlated (HC) electronics pickup and ground loops, which could contribute to the generation of false asymmetries and systematic errors. Any electronic pickups and crosstalks were further suppressed by transmitting only the delayed helicity information to the data stream, breaking any correlation with the current helicity.

3.5   Beam Monitors

HAPPEX-III used the standard JLab beam current monitors (BCMs) [Al04] and beam position monitors (BPMs) [Ba91] to monitor the beam current and position respectively. The beam monitors were located at appropriate locations throughout the accelerator and the experimental halls of JLab. Together, these monitors monitored the beam current, position and energy. During the experiment, the output from the monitors were constantly monitored for beam instabilities. Automated feedback systems also used the monitors to maintain beam stability. Figure 3.5.1 displays the
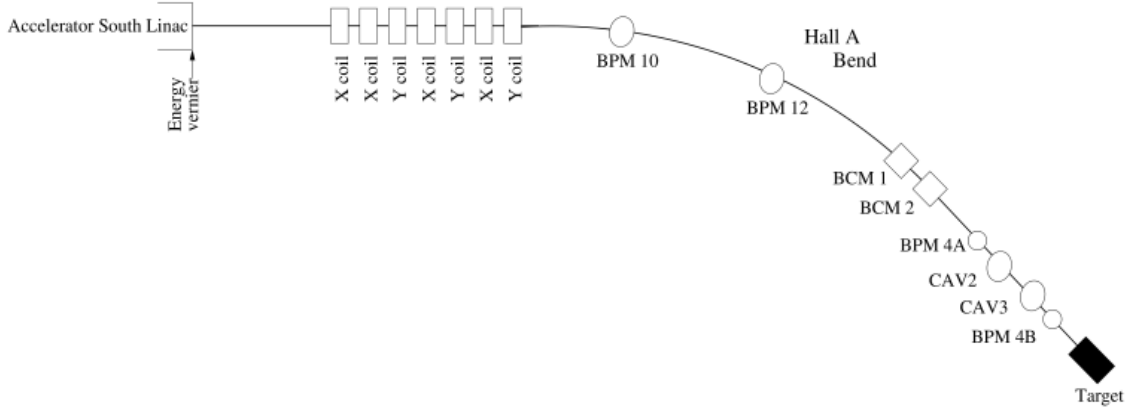
Figure 3.5.1: Locations of the BPMs and BCMs, along with the beam modulation (BM) coils used during HAPPEX-III. BPM4b and BPM4a were located 1.3 and 7.5 m upstream of the target. BCM1 and BCM2 were separated by ~ 3 m. Reproduced from [Ka07].

locations of the BPMs and BCMs inside and at the entrance of Hall A that were used by HAPPEX-III.

3.5.1 Beam Current Monitor (BCM)

HAPPEX-III used the BCMs developed locally at JLab [Al04] to monitor beam intensity. The BCMs were resonant radio-frequency (RF) cylindrical high-Q (~ 3000) waveguide cavities tuned to the frequency of the beam (1497 GHz) [Al04]. These BCMs provided non-interfering low-noise stable beam current measurements. The BCMs had a precision of 3.8 ppm at 100 μA beam current over an integration length of 33.0 ms ($\sim 2.06 \times 10^{19}$ electrons). In addition to the excellent resolution of the BCMs, the precision was in part due to the low-noise high-resolution analog-to-digital converters (ADCs) [1].

HAPPEX-III also used the Unser [Un81, Al04] to quantify the linearity of the beam monitors, and determine pedestals. The Unser was a parametric current trans-

---
[1]See Section 3.11.1 for discussion of the ADCs.

former with its nominal response to current well determined by its transformer. It was calibrated by passing a known current through a wire inside the beam pipe, and measuring its response. The Unser provided an absolute beam current measurement. However, its output drifted significantly on a time scale of several minutes [Al04]. So it was not used as the primary beam current monitor.

HAPPEX-III read out two BCMs immediately upstream of the target, BCM1 and BCM2 on Figure 3.5.1, and a BCM at the 5 MeV region of the accelerator. The BCMs immediately upstream of the target provided independent measurements of the beam currents close to the target. One of these BCMs normalized the detector signals for beam current fluctuations. The 5 MeV region BCM was primarily used in dedicated source studies performed with the electron beam. The BCMs were also used to monitor intrinsic beam noise by studying the differences in the beam asymmetry measured by different BCMs.

3.5.2   Beam Position Monitor (BPM)

The BPMs were wire stripline monitors composed of four antennas, X^+, X^-, Y^+ and Y^-, placed symmetrically around the beam pipe. Each antenna provided a signal proportional to the beam position as well as intensity. In asymmetry analysis, the output from these stripline antennas were used to calculate the beam position as

$$x = \frac{X^+ - X^-}{X^+ + X^-} \times 18.76; \qquad y = \frac{Y^+ - Y^-}{Y^+ + Y^-} \times 18.76$$

where 18.76 was the distance from the stripline axis center to the base of the antennas in mm.

The stripline antennas were situated at $\pm 45°$ to the horizontal/vertical [Ba91] except for those in the 100 KeV region of the accelerator, where they were situated along

the horizontal/vertical. Those at $\pm 45°$ were projected along the horizontal/vertical during analysis to determine the beam positions in the corresponding directions.

HAPPEX-III read out numerous BPMs from inside the hall, arc and the injector into the data stream. Most of these BPMs were in the data stream for diagnostics during online and offline data analysis. The injector BPMs were primarily used in dedicated injector studies with the electron beam, and during online data analysis to monitor the quality of the beam at the injector. The most important of the BPMs for HAPPEX-III were BPM4a, BPM4b and BPM12x. BPM4b and BPM4a were located 1.3 and 7.5 m upstream of the target. Together these BPMs provided a projection of the beam position and angular fluctuations at the target. BPM12x was located at the arc and was used to monitor beam energy fluctuations. The arc was located at the entrance of Hall A where the beam was bent. So any beam energy fluctuations show up as horizontal beam position changes in the BPMs at the arc.

3.6   Target

HAPPEX-III used the Hall A cryo-target system, Figure 3.6.1, which consisted of liquid hydrogen (LH2) "production" target and targets for optics, alignment and backgrounds studies that were mounted onto a target ladder in a vertical stack.

HAPPEX-III used two production targets: a 25 cm cell in loop 3 (L3) and a 20 cm cell in loop 1 (L1). The loop 2 (L2) in the target ladder, Figure 3.6.1, was empty and unused. The LH2 cells were racetrack shaped, Fig 3.6.2, and made of aluminum (Al) walls. Each cell was 2 cm in diameter. The thickness of the entrance and exit windows of the 25 cm cell were $0.117 \pm 0.005 \pm 0.002$ and $0.150 \pm 0.005 \pm 0.002$ mm respectively [Me09]. The thickness of the entrance and exit windows of the 20 cm cell on L2 were $0.126 \pm 0.011 \pm 0.003$ and $0.100 \pm 0.008 \pm 0.003$ mm respectively [Me09].
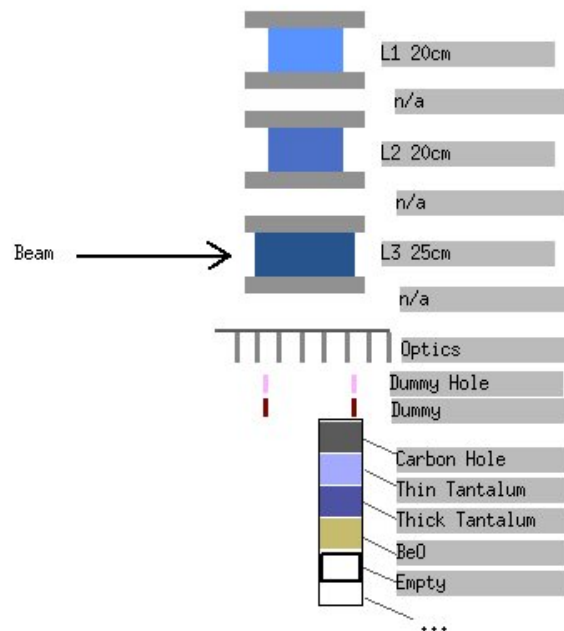
Figure 3.6.1: HAPPEX-III used the Hall A target ladder system. The top three targets are liquid-hydrogen (LH2) production targets. The optics target had foils located at different points mapping the length of the LH2 target, and was used for acceptance studies. Rest of the targets were used for beam alignment.

The first error is due to the deviation of the multiple measurements, while the second one is a systematic error arising from the instrument calibrations. The 25 cm cell was used for most of the experiment until the failure of a pump on this cell loop, after which the 20 cm cell was used. A site-wide power outage at JLab resulted in the failure of the L3 pump. About 1.2% [1] of the production data was acquired with the 20 cm cell.

The LH2 cryo-target was operated at 19 K and $\sim$ 28 psiA. The target was cooled using 15 K ^{4}He from the End Station Refrigerator (ESR) and 4 K ^{4}He from the Central Helium Liquifier (CHL) for a total cooling power of $\sim$ 1 KW. This amount of cooling power was necessary because beam heating at 100 μA, heat load from a fan that circulated the LH2 inside the target loop and an additional small heater

---

[1] Of the total 19262 mA collected, only 2282 mA was collected with the 20 cm cell on L3.

Figure 3.6.2: HAPPEX-III used cryogenic liquid-hydrogen (LH2) targets contained in a race-track shaped aluminum (Al) cells. The target ladder contained three such cells, but only two were used during HAPPEX-III. The bottom cell on loop 3 (L3) was 25 cm long, and the top two cells on loops 1 (L1) and 2 (L2) were each 20 cm long. The L3 cell was used for majority of the run, until it malfunctioned due to a power outage. Then, HAPPEX-III ran with the L1 cell for about 1 week before the end of the experiment. The electron beam propagated into the scattering chamber through the hole towards the center and to the left of the target above.

that stabilized the target temperature generated a total heat load of ~ 1 KW. A high power heater with the capacity to deliver up to 1 KW of heat was connected to the cryo-target. Its load, along with the cryogen flow rate were regulated via an automated proportion, integral, derivative (PID) feedback loop [Al04] in order to prevent big target temperature fluctuations. The feedback, in addition to regulating the target temperature during beam intensity fluctuations, critically ensured that the target did not freeze. LH2 freezes at ~ 14 K at 28 psiA, and freezing was a possibility due to the use of 4 K ^{4}He coolant in the cryo-target loop. The flow of both the 4 K and 19 K ^{4}He could be manually controlled via a Joule-Thompson valve either remotely via the target control interface or locally from inside the hall. Appropriate coolant flow rate was established during target commissioning by the Hall A target expert. The 19 K flow rate was adjusted by tiny amounts as necessary by the target operator during the experiment. The 4 K coolant flow rate was left largely untouched, and

only adjusted by the Hall A target expert as necessary. LH2 was circulated transverse to the direction of beam propagation at the maximum allowed rate of 72 Hz during HAPPEX-III in order to minimize LH2 density fluctuations due to localized beam heating.

Located below the LH2 targets were the optics, dummy hole, dummy, carbon hole, thin Tantalum (Ta), thick Ta, and BeO targets, as shown in Figure 3.6.1. The dummy hole, carbon hole and BeO targets were used for beam alignment. The hole in the dummy and carbon targets were used to center the beam about the target. The BeO was florescent when the beam was incident on it, and was used to visually inspect the location of the beam at the target. A camera located outside the scattering chamber and focused at the scattering point fed real-time video of the beam location at the target.

The optics target was a multi-foil Al target with foils of different radiation lengths of the LH2 target. These foils were located at different points along the length of the LH2 target and mapped the LH2 target's length. The optics target was used for HRS and detector acceptance studies.

The tantalum target was extremely thin, and resulted in very low energy losses in the electrons that scattered off it. Therefore, it was used for HRS central angle determination. A water-cell target that consisted of 5 mm water contained in a steel cell of 0.001" thick walls at beam entry and exit faces was also used for HRS central angle determination. The water-cell target was incorporated into the target ladder system, at the location of the "empty" target in Figure 3.6.1 during the HRS angle determination data acquisition. The HRS central angle determination is described in Section 7.7.3.1. The water-cell target was removed after the HRS angle determination data was acquired.

The dummy target consisted of Al foils at the location of entry and exit walls of

Target	Description	Thickness (g/cm^2)
Loop 1 Cell	20 cm Cryo LH2	–
Loop 2 Cell	20 cm Cryo LH2	–
Loop 3 Cell	25 cm Cryo LH2	–
Optics	^{12}C Multi-Foil (@ 0, $\pm$7.5, $\pm$15 cm)	0.042 ± 0.001
Dummy Hole	Aluminum Foils (2 mm hole)	
Dummy	Aluminum Foils (@ $\pm$12.5 cm)	-12.5 cm: 0.401 ± 0.00022
		+12.5 cm: 0.378 ± 0.00021
Carbon Hole	Carbon Foil (2 mm hole)	0.08388 ± 0.00012
Thin Tantalum	Tantalum Foil	0.021487 ± 0.000078
Thick Tantalum	Tantalum Foil	0.12237 ± 0.000341
BeO	BeO	0.149 ± 0.001
Empty/H$_2$O Cell	No Target/$\sim$ 5 mm H$_2$O	–

Table 3.1: The thickness of various targets used during HAPPEX-III.

the 25 cm LH2 cell, and was used to study the amount of Al contamination in data. At the end of the experiment, the LH2 production target was emptied and dedicated background measurements of the Al data contamination was performed as well. The thickness of the target foils of the targets used during HAPPEX-III are summarized in Table 3.1.

The target ladder sat inside a vacuum scattering chamber, and was centered at the pivot of the hall spectrometers. The scattering chamber was 104 cm in diameter and maintained at 10^{-6} torr of vacuum. The window entrance and exits of the scattering chamber were made of $\sim$ 0.406 mm thick Al foils.

3.7 Raster

Beam rastering was necessary to prevent damage to the target due to beam heating, and to suppress non-statistical broadening of the asymmetry width resulting from target density fluctuations.
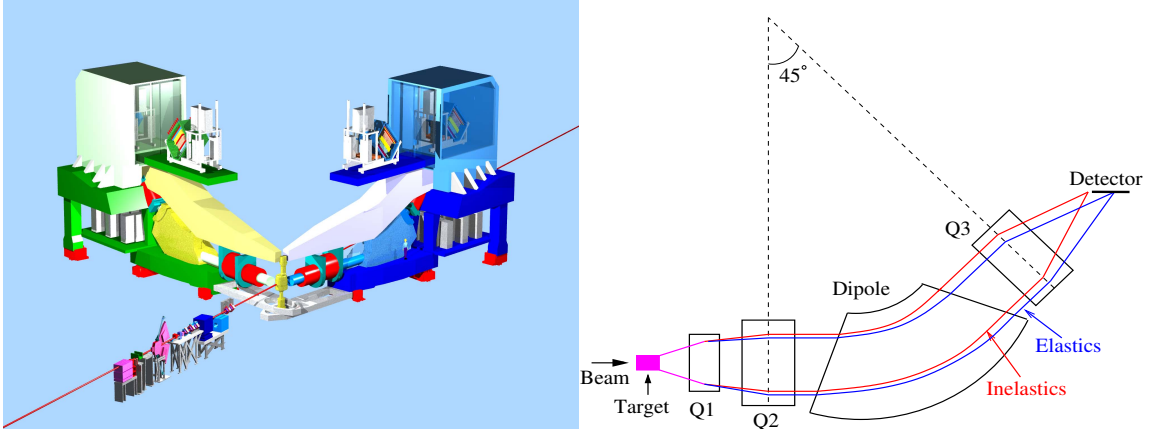
Figure 3.8.1: On the left is a cartoon of the Hall A high-resolution spectrometers (HRSs). On the right is a illustration of the physical separation of the elastically scattered electrons from the inelastically scattered electrons, and the focusing of the elastically scattered electrons onto the detector. Q1, Q2 and Q3 on this illustration are the quadrupole magnets. These quadrupoles are displayed in red at appropriate locations in the cartoon of the HRSs on the left.

HAPPEX-III used the standard Hall A raster system which consisted of two dipole magnets, one vertical and one horizontal, modulated with a triangular waveform at ~ 24.96 and ~ 25.08 KHz respectively, at a phase difference of 120 Hz [Mi05]. These magnets were located about 23 m upstream of the target, and rastered the beam to image a rectangular cross-sectional area at the target. The raster size was varied by adjusting the amplitudes of modulation of the dipole magnets.

HAPPEX-III used a beam raster size $\sim 5 \times 6$ mm which was the maximum size achievable at the HAPPEX-III beam optics configuration. The raster size is maximized to suppress target density fluctuations.

3.8 High-Resolution Spectrometer (HRS)

HAPPEX-III used the twin Hall A high-resolution spectrometers (HRSs). Each HRS was composed of a set of superconducting magnets: two quadrupoles, one dipole
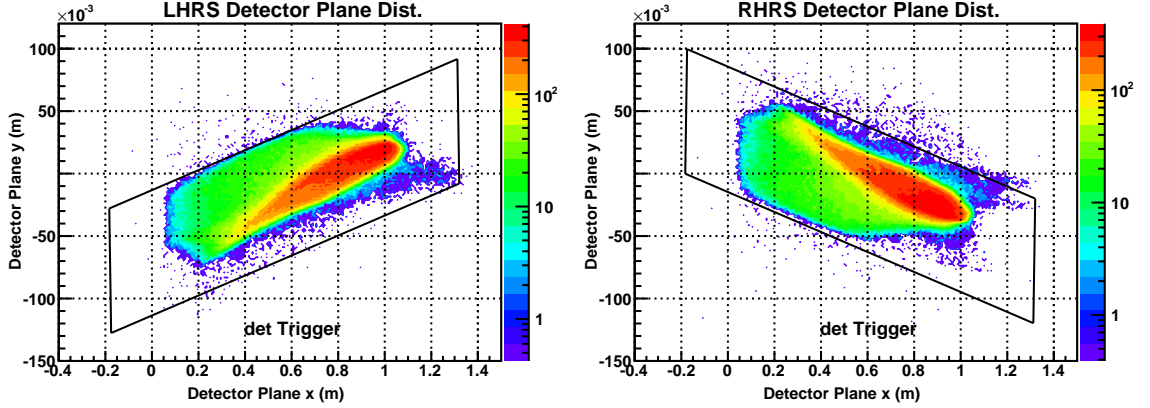
Figure 3.8.2: The elastically scattered electrons are cleanly separated form the in-
elastically scattered electrons, and focused onto the detectors by the HRSs as shown
above. The plot on the left refers to data acquired on the focal plane detectors on
the LHRS and the one on the right refers to those acquired on the RHRS focal plane
detectors. The xy-plane is the focal plane where the detector is located. The outline
of the detector are shown on each of the plots, overlapping the electron distribution.
The axes are scaled to reflect true detector dimensions. The electrons are incident at
about 45° to the x-axis and 90° to the y-axis, coming out of the xy-plane.

and one quadrupole (QQDQ) constituted in the order presented as illustrated in
Figure 3.8.1. The quadrupoles focused or defocused the beam, while the dipole bent
the beam vertically by 45°. The first two quadrupoles focused the beam onto the
dipole, while the third quadrupole focused the beam onto a plane, referred to herein
as the focal plane. The detector was located at the focal plane.

The HRSs provided very high momentum resolution (10^{-4}) over momentum range
of 0.8-6.0 GeV, a large acceptance in angle and momentum, good position and angu-
lar resolution in the scattering plane, extended angular acceptance and a large angular
range [Al04]. As a result, the elastically scattered electrons from across the length
of the target were transported onto the detectors by the HRSs. In addition, these
elastically scattered electrons were physically separated from any inelastically scat-
tered electrons at the focal plane which allowed detectors of appropriate dimensions
to collect the elastically scattered electrons without much inelastics contamination,
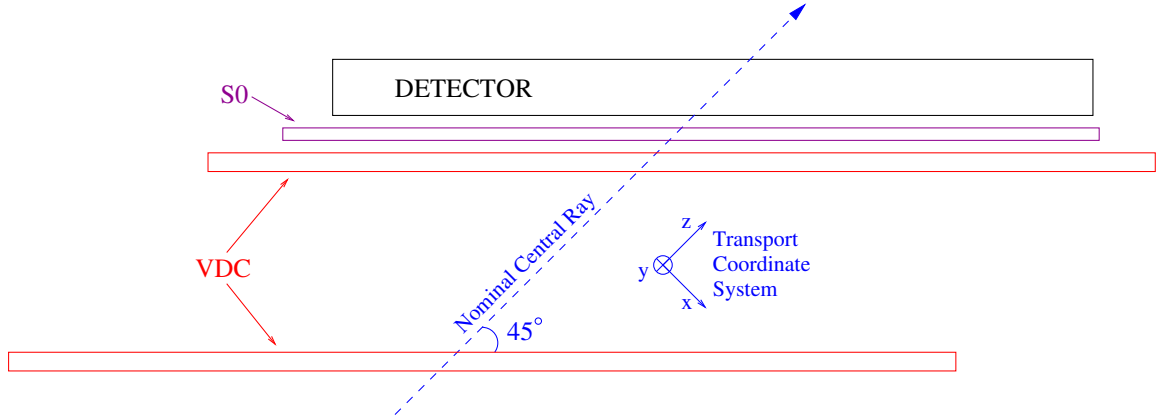
Figure 3.9.1: The position of the HAPPEX-III detectors relative to the S0 scintillator and the vertical drift chambers (VDCs) are shown above. The dimensions of the VDC in the xy-plane formed by rotating the "transport" coordinate system by $+45°$ about y-axis is larger than that of S0. Similarly, the dimension of S0 in this plane is larger than that of the detector. As a result, in the above setup, the electrons incident on the detectors necessarily pass through both the VDCs and the S0.

as shown in Figure 3.8.2. The HRSs are discussed in further details at [Al04].

The HRSs are positioned symmetrically at $\langle \theta \rangle \sim 13.7°$ about the central beam axis, with a solid angle acceptance of about 5 msr during HAPPEX-III. Both the HRSs were set to a momentum of 3.14159 GeV.

3.9   Detectors

HAPPEX-III used the standard Hall A detector package along with dedicated calorimeter detectors. The calorimeter detectors were located at the focal plane, and referred to herein as the focal plane detectors. They were used to acquire asymmetry data while the standard Hall A detector package was used in dedicated low current runs for optics, backgrounds and Q^2 measurements.

3.9.1   Focal Plane Detector

HAPPEX-III used two identical focal plane detectors, one in each HRS. These were
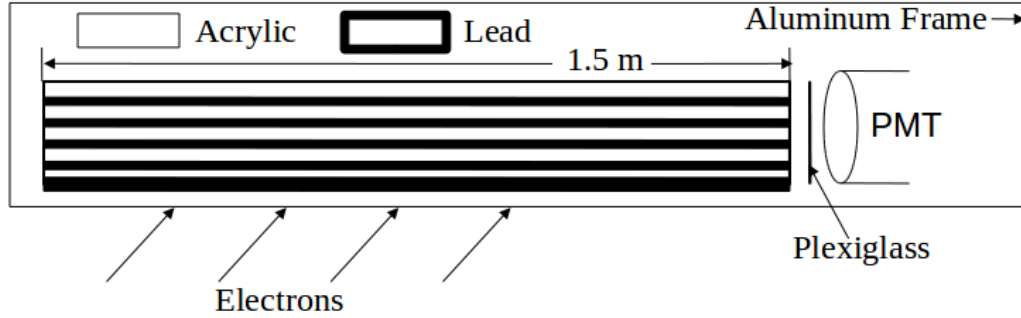
Figure 3.9.2: HAPPEX-III focal plane detectors were made of lead-acrylic sandwich calorimeters. Electrons incident on the lead generated electron showers. These electrons generated Čherenkov radiation in the acrylic scintillator. A single 5-inch diameter Burle 8854 photomultiplier tube (PMT) located at one end of the detector collected the Čherenkov radiation. The Plexiglass filtered UV radiation present in the Čherenkov radiation in order to decrease sensitivity to electron's energy variations along the detector's length.

the primary detectors that acquired the production data. Each detector was composed of alternate layers of lead and acrylic, sandwiched together to form a calorimeter as shown in Figure 3.9.2. Electrons incident on the lead generated an electron shower, which then produced Čherenkov radiation in the acrylic. The Čherenkov radiation propagated inside the acrylic, along the length of the detector via internal reflections, and was collected at one end by a single 5-inch diameter Burle 8854 photomultiplier tube (PMT). The detector was located at the focal plane with the lead-acrylic layers parallel to the focal plane, and the electrons incident at $\sim 45°$ along its length. Its position and pitch-yaw orientation were optimized in dedicated studies in order to focus part of the Čherenkov cone towards the PMT for maximal light collection.

The sandwich calorimeters were 10 cm wide and 150 cm long, with the dimensions chosen in order to collect the elastically scattered electrons while at the same time avoid most of the inelastically scattered electrons that made it to the focal plane. There were 4 lead layers sandwiched between 5 acrylic (Bicron BC-800 UVT Lucite) layers. Each lead sheet was 6.4 mm thick and the acrylic sheet was 1.27 cm thick.

These thickness were chosen to provide sufficiently good energy resolution. The detector energy resolution affected the error in the parity-violating asymmetry, Eq. 2.1.8, measured by the detector as

$$\sigma_A = \frac{1}{\sqrt{N}}\sqrt{1 + \left(\frac{\Delta E}{\langle E \rangle}\right)^2}. \qquad (3.9.1)$$

$\frac{\Delta E}{\langle E \rangle}$ was measured to be $\sim 14\%$ for HAPPEX-III, which broadened the statistical width of the asymmetry measurement by $\sim 1\%$, a negligible amount. At the bottom of the calorimeter stack were two layers of 6.4 mm lead sheets that acted as preradiators. The acrylic was wrapped in teflon to preserve the internal reflection of the Čherenkov radiation in acrylic; the teflon does not adhere to the acrylic surface, and created an acrylic-air interface that was conducive to total internal reflection.

A piece of Plexiglass was placed between the calorimeters and the PMT to reduce sensitivity to energy variations along the length of the calorimeter. Without the Plexiglass, the Čherenkov radiation was attenuated by as much as 50%/m. This was because the acrylic attenuated light of wavelengths shorter than ~ 350 nm strongly, and the Čherenkov light had considerable amount of UV-radiation. The Plexiglass filtered this UV-radiation, and decreased the signal attenuation to $\sim 15.4\%$/m [1]. Although the Plexiglass also reduced the total signal size, the signals were still large enough that the use of Plexiglass was preferable.

The calorimeters and the PMT were mounted in a light-tight Al box. Al was chosen because any magnetic materials in the periphery of the detector could lead to false asymmetry: any magnetized material present in or around the detector could potentially be polarized due to its proximity to the HRS magnets, and the elastically scattered electrons that arrive at the detector could Møller scatter with the polarized

---

[1]The LHRS detector attenuation was $\sim 11.7\%/m$ and the RHRS detector attenuation was $\sim 19.1\%/m$ resulting in an average detector attenuation of $\sim 15.4\%/m$.
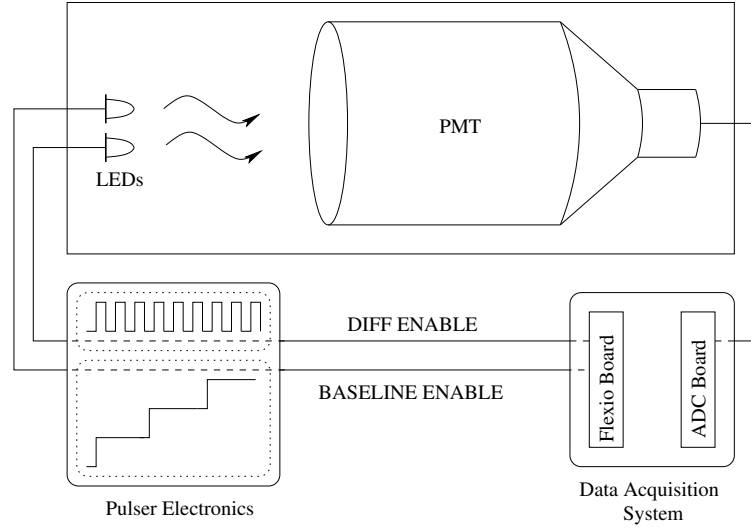
Figure 3.9.3: The schematic of the detector linearity bench test is presented above. The two light-emitting diodes (LEDs) were driven by the flexio board connected to data-acquisition system (DAQ). The DIFF LED was toggled every 30 ms. The DIFF LED was operated at a constant frequency of ~ 20 KHz, while the BASELINE LED was operated at variable frequencies in the range of 0-500 KHz. The BASELINE LED was operated at each frequency for about 4.5 secs. Both the DIFF and BASELINE LED amplitudes were adjusted to match the size of signal observed with individual electrons during the experiment. At this amplitude, the BASELINE LED operated at 500 KHz generated integrated signal sizes of about the same size as those observed with 100 μA electron beam.

electrons from these magnetized materials introducing false asymmetry.

The PMT voltage divider was optimized for linearity. These detectors were designed and first used during HAPPEX-I [An04, Ru01]. More information on these detectors is available at [Ru01].

3.9.1.1 Detector Non-Linearity

HAPPEX-III detector non-linearity was measured via *in-situ* tests during the experiment and bench tests after the experiment. The *in-situ* detector non-linearity tests were performed with light emitting diodes (LEDs) placed inside the focal plane de-

tectors, at the end of the acrylic calorimeter opposite to the PMT [1]. The bench tests were performed with the LEDs immediately in front of the PMT, without anything in between as illustrated in Figure 3.9.3. The bench tests used the same sets of ADCs and the twinax cables to read out the PMT signal into the DAQ. During the bench tests, the PMT voltages and ADC gains were set to those used during the experiment. All the non-linearity tests were performed with blue LEDs because the acrylic in the focal plane detectors generated Čherenkov radiation spectrum centered at blue radiation's wavelength.

The detector non-linearity tests used two LEDs at a time: the baseline LED and the difference (diff) LED. The diff LED was pulsed at a constant frequency of ~ 20 KHz, and was toggled between ON and OFF every 30 msec. The baseline LED was pulsed at variable frequencies in the range of 0-500 KHz, with the LED pulsed at each frequency for 900 msec. Between the successive frequency changes, the baseline frequency was set to 500 KHz for ~ 4.5 sec to emulate the signal sizes observed at the detectors during the experiment that was produced by elastically scattered electrons. The difference of diff ON and diff OFF was studied at each of the baseline frequencies to determine the extent of the detector non-linearity. All the tests used HAPPEX-III helicity window length of 33.83 ms.

The LED pulse width and amplitude were adjusted at the beginning of the tests to replicate the pulse signal size generated by the electrons in the detector during the experiment. This was achieved by modulating the LED ~ 500 KHz, which was the total elastically scattered rate observed in the two focal plane detectors, and adjusting the LED pulse width and amplitude to match the total ADC signal size obtained with the electron beam.

The LED frequency and timing parameters were set via a programmable input-

---

[1]A schematic of the focal plane detector is presented in Figure 3.9.2
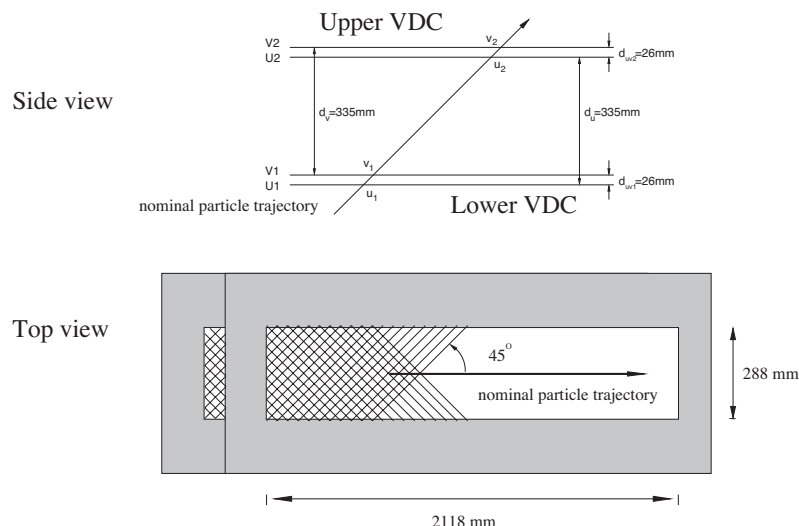
Figure 3.9.4: Each Hall A HRSs used two VDCs to reconstruct the trajectories of the electrons propagating through the VDCs and onto the detectors. Each VDC contained two wire planes with the wires between the planes oriented at 90° to each other. The VDCs were located at the focal plane with the wire planes parallel to the focal plane. The electrons were incident on the wires at 45°. Reproduced from [Al04].

output programmable board located in the DAQ crate, and the tests run by the parity DAQ. The LED width and amplitude were set manually via digital-to-analog controller (DAC) output on the custom HAPPEX timing board (HTB). The HTB is discussed in Section 3.11.1.

3.9.2   Hall A Standard Detector Package

HAPPEX-III used the Vertical Drift Chambers (VDCs) and S0 scintillators of the Hall A standard detector package [Al04].

3.9.2.1 Vertical Drift Chambers (VDCs)

There were two VDCs in each of the HRSs. Each of the VDCs detected the location of the electrons passing through them. Together, the two VDCs were used to reconstruct the trajectories of the electrons propagating through the VDCs and onto the detectors. The schematic of the VDCs are displayed in Figure 3.9.4, and are described in detail at [Fi01].

Each VDC chamber measured 2118×288 mm and had two wire planes in the standard UV configuration: the wires from these planes were oriented at $90°$ to each other. The VDCs were filled with a mixture of argon and methane, and operated at a potential difference of -4 KV. There VDC wire planes were parallel to the focal plane, and the scattered electrons were incident wire planes at $45°$.

3.9.2.2 S0 Scintillator

There was one S0 scintillator in each of the HRS. The schematic of the S0 scintillator is illustrated in Figure 3.9.5. Each S0 scintillator was made of $0.01 \times 1.85 \times 0.25$ m^3 plastic scintillator. A wavelength shifter bar with a single PMT attached to its one end was attached along the 25 cm sides of the scintillator [Mo07]. The light from the plastic scintillator was absorbed by these wavelength shifters and re-emitted into the PMT. Any electron incident on the plastic scintillator caused emission of radiation towards both the wavelength shifters simultaneously. So signals detected simultaneously in the two PMTs indicated electron hits. These coincidence signals were used to select the elastically scattered electron events from backgrounds during data acquisition (the standard Hall A DAQ used the S0 coincidence signals as triggers during some runs) and analysis.

The S0 was situated on top of the VDCs and under the focal plane detectors, with the plane containing the plastic scintillator and the PMT parallel to the focal plane.
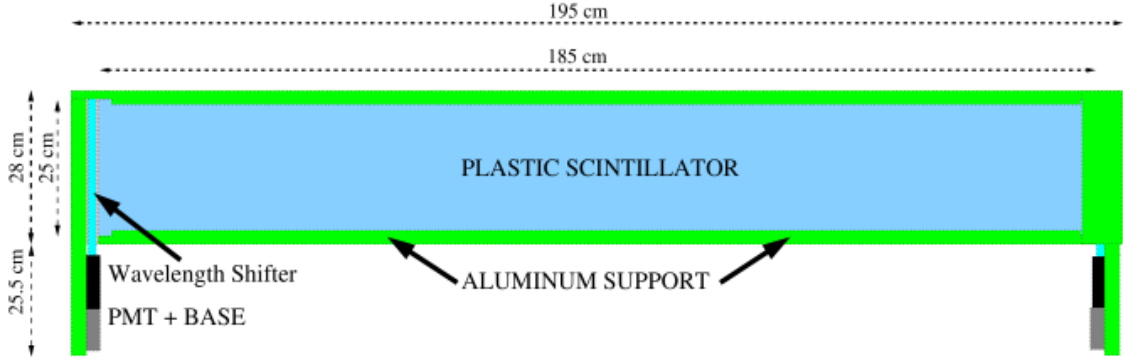
Figure 3.9.5: HAPPEX-III used one S0 scintillator in each of the HRS. The scintillation radiation generated by each electron were detected in both the PMTs simultaneously. So the coincidence signals of the S0 PMTs were used to select the elastically scattered electron events from backgrounds. The S0 was situated on top of the VDCs and under the focal plane detectors, with the plane containing the plastic scintillator and the PMT parallel to the focal plane. Reproduced from [Mo07].

The electrons were incident on the S0 at 45°. Being larger than the detector, the S0 was placed to such that all the electrons incident on the focal plane detector passed through the S0 scintillators.

3.10 Luminosity Monitor

The luminosity monitor (lumi) measured the electron beam luminosity. The lumi was made of quartz calorimeter that was fused to a cylindrical light-guide. An R7723 PMT was attached at the other end of the light-guide, with a filter-box situated immediately in front of the PMT. The filter-box contained a slot for an optical filter that could be to used to attenuate signals when the electron rates were extremely high. The filter was necessary in such instances in order to avoid PMT saturation. Al foils were wrapped around the light-guide to make it light-tight. The Čherenkov radiation generated by the electrons incident on the quartz propagated through the light-guide, and into the PMT.
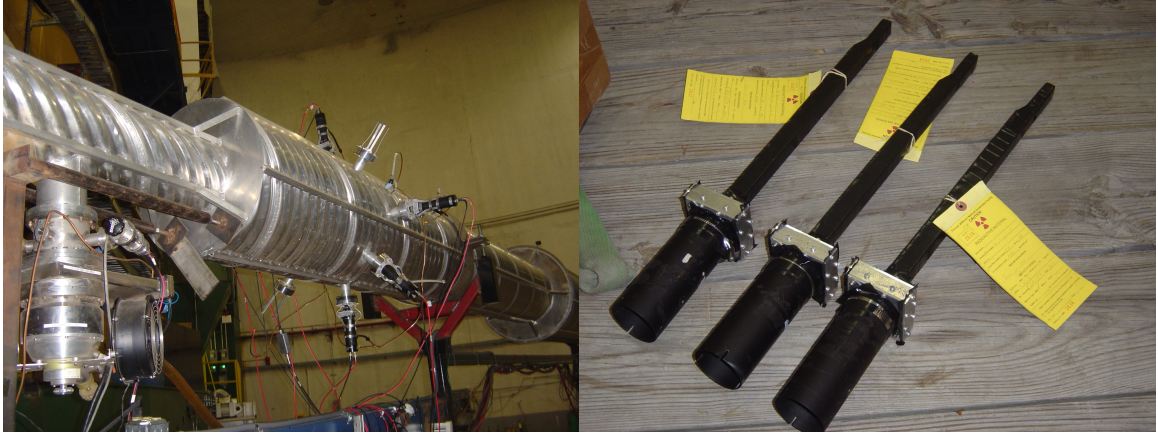
Figure 3.10.1: HAPPEX-III used the luminosity monitors (lumis) to monitor target density fluctuations. The were a total of 8 lumis situated symmetrically around the beamline immediately downstream of the target. Each lumi consisted of a quartz calorimeter that was fused to a cylindrical light guide. The electrons incident on the quartz generated Čherenkov radiation that propagated through the light guide and into a PMT.

There were a total of 8 lumis, situated symmetrically about the central beam axis as shown in Figure 3.10.1. They were located ~ 7 m downstream of the scattering chamber along the beam dump. The lumis, being located immediately downstream of the target, needed ability to handle extremely high rates. So quartz, which is sufficiently radiation hard, was used as the calorimeter. The quartz was located on the electrons' path and provided sensitivity to the electrons scattered in the range of $0.5 - 0.8°$.

Due to extremely high rates, the lumis had small asymmetry widths, and were sensitive to target density fluctuations. So HAPPEX-III used the lumis to monitor the extent of target density fluctuations.

3.11   Data Acquisition System

HAPPEX-III used two different data acquisition systems (DAQs), the Integrating

DAQ, referred to herein as the parity DAQ, and the Counting DAQ, with each system operating in the mode implied by its name. The parity DAQ acquired the asymmetry data, while the counting DAQ was used in dedicated, low-current measurements of backgrounds, optics, HRS central angle and Q^2. Both the DAQs were designed based on the DAQ system developed at JLab. The DAQ utilized the CODA architecture [Wa94] that integrated and allowed control of multiple systems and processes running simultaneously via a Linux interface. It also facilitated slow controls for experimental parameter adjustments concurrently with data acquisition.

The DAQ typically consisted of Versa Module European (VME) crates integrated together by CODA. Each VME crate consisted of VME digitization devices [ADCs, time-to-digital converters(TDCs), scalers], a single-board VME computer, an ethernet network card and ethernet connection. The DAQ was accessed via Linux workstations, and had the capability to write to a mass storage tape silo (MSS) for data storage. A trigger supervisor (TS) supplied a single trigger to all the crates, and synchronized the operation of these crates. The Run Control interface of CODA allowed for the selection of different crate configurations, start and end of data acquisition runs, and the monitoring and resetting of CODA components. CODA also allowed for online data access for diagnostics and monitoring, as well as insertion of data into the data stream from other user processes such as Experimental Physics and Industrial Control System (EPICS) [1] variables and beam modulation (BM) parameters.

3.11.1 Integrating (Parity) DAQ

The parity DAQ acquired the production (asymmetry) data. The MPS pulse [2] generated by the HG board triggered this DAQ. Thus, the data accumulation rate was

---

[1] EPICS documentation, www.aps.anl.gov/epics.
[2] MPS pulse is discussed in Section 3.4.

independent of the scattering rate, and this DAQ could handle extremely high scattering rates with minimal DAQ dead time. However, this DAQ integrated the signal over a helicity window, and saved it as an event. Any contaminants that might present in the data were also integrated. Therefore, the signals had to be extremely clean, with sources of backgrounds well suppressed for unambiguous interpretation of data.

The HAPPEX-III parity DAQ consisted of four VME crates: Counting House (CH), Left HRS (LHRS), Right HRS (RHRS) and Injector crate. These crates were located at the locations implied by their names. The crates were scattered at various locations throughout the accelerator and experimental Hall A of JLab in order to minimize the noise and signal attenuation resulting from long cable lengths. Each of the crates contained VME digitization devices such as ADCs and scalers as necessary.

HAPPEX-III used two different kinds of custom ADCs: 16-bit and 18-bit, with the number referring to the size of the ADC bit register. The 16-bit ADCs were built and used during HAPPEX-I [An04], and could output signals up to $2^{16} = 6.55 \times 10^4$ ADC channels. The 18-bit ADCs were designed for PREX, and could output signals up to $2^{18} = 2.62 \times 10^5$ ADC channels. The 18-bit ADCs were designed to accommodate faster data acquisition rates, and decrease the susceptibility to pedestal drifts and non-linearity [1]. However, there was no substantial gain in signal-to-pedestal noise ratio in the 18-bit ADC over the 16-bit ADC for HAPPEX-III [Me12]. All the beam monitors and detectors were read out via ADCs during HAPPEX-III.

HAPPEX-III used the scaler to read out the BM system parameters. The scaler was essentially a pulse counter. Any BM system frequencies were directly connected to the scaler. The signals in the form of voltages were converted into frequencies by using a Voltage-to-Frequency (V2F) converter and read out in the scaler. The V2F converted a voltage (usually in the range of $0-10$ V) into a pulse train with frequency

---

[1]See Chapter 5 Section 5.5 for effects of pedestal drifts and non-linearity.

proportional to the input voltage.
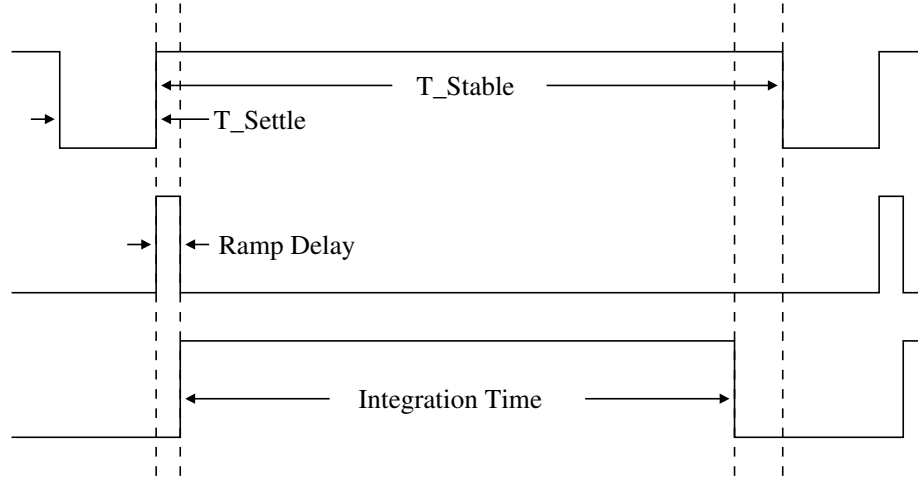
Figure 3.11.1: HAPPEX-III DAQ timing scheme was executed by the HAPPEX timing board (HTB). The leading edge of T_{Stable} triggered the HTB. The HTB generated the ramp delay (RD) and integration time (IT), with the length of these signals remotely programmable in units of 2.5 μs. HAPPEX-III used an RD of 0 and an IT of 33.0 ms. The IT ended 330 μs before the start of T_{Settle}, and 830 μs before the arrival of next T_{Stable}, providing ample time for the DAQ to clear the data buffer before next round of integration.

The timing scheme of the DAQ was executed by the HAPPEX timing board (HTB), which was located in the CH VME crate. The leading edge of T_{Stable} triggered the HTB which generated the ramp delay (RD) and integration time (IT) shown in Figure 3.11.1, with the length of these signals remotely programmable in units of 2.5 μs. The RD was the amount of delay between the arrival of trigger and the start of the IT. The IT was the length of integration period during each helicity window, and ended before the end of T_{Stable}. The DAQ generated error if either RD or IT did not start or end during the T_{Stable} window. The HTB relayed the timing information to the TS, which triggered the VME crates.

HAPPEX-III used an RD of 0 and an IT of 33.0 ms. The IT ended 330 μs before the start of T_{Settle}, and 830 μs before the arrival of next T_{Stable} providing ample time for the DAQ to clear the data buffer before next round of integration.

3.11.2   Counting DAQ

The counting DAQ was the standard Hall A DAQ [Al04]. Like the parity DAQ, the counting DAQ consisted of VME crates that contained VME digitization devices such as ADCs, TDCs and scalers. Unlike the parity DAQ, however, the counting DAQ did not utilize a timing board for triggers. Instead, the trigger system consisted of the S0 scintillator coincidence signals, focal plane detector signals, and a 1024 Hz pulser. Each of these triggers could be selected or prescaled remotely without access to the hall. Appropriate triggers were chosen depending on the objective of the data being acquired. This method of data acquisition was sensitive to instrument dead times, and could only handle low scattering rates. A dead time of $\sim 20\%$ was measured at a trigger rate of 2 KHz [Al04]. The counting DAQ read out the VDCs, S0, focal plane detectors and the target BPMs into the data stream during HAPPEX-III.

3.12   Beam Modulation (BM)

HAPPEX-III used a BM system similar to the one used during HAPPEX-I [An04]. The BM system was designed to modulate the beam independently in position (x and y), angle (θ_x and θ_y) and energy (ΔE), spanning a space of five independent variables. A set of seven air-core corrector coils in the Hall A beamline upstream of the dispersive arc was used for position and angle modulation. Dispersive arc is the region at the entrance of the hall where the beam was bent. The modulation coils relative to the BPMs are shown in Figure 3.5.1. The energy modulation was performed via a vernier input on a cavity in the accelerator's south linac. The corrector coils and the vernier were operated by control voltages supplied by a VME digital-to-analog converter (DAC) module controlled by the parity DAQ.

The beam position and angle fluctuations at the target were extracted via mea-

surements of the beam positions at the target BPMs, BPM4b and BPM4a, which were located 1.3 and 7.5 m upstream of the target respectively in a field free region. The beam energy fluctuations were extracted from beam position fluctuations measured by BPM12x. BPM12x was located at the point of highest dispersion of the arc (about 4 m), and sensitive to beam energy fluctuations. The location of these BPMs relative to the target and modulation coils and the vernier, is shown in Figure 3.5.1.

HAPPEX-III BM cycles consisted of a sequence in which each of the seven coils and the cavity were modulated by a sawtooth wave. Each coil and the cavity was modulated for 5.4 secs. At the start of the modulation cycle, a delay of 3.2 secs was set during which the beam position feedback was turned off. The "feed forward" system, which drove corrections based on the frequency spectrum of corrections averaged over the previous several minutes, remained active. Then the coils were modulated in succession without any delay between each successive coil modulation. At the end of the last coil modulation, a delay of 3.2 secs was set to turn off the beam energy lock, and get ready for the cavity modulation. After the cavity had been modulated, a delay of 6.5 secs was set during which the beam position feedback and energy lock were turned back on. The BM cycle ended at the end of this delay. One such cycle lasted 52.5 secs, and repeated once every 9 mins and 18 secs. Typical coil modulation amplitudes were ± 150 mA, that generated beam excursions of $300 - 400$ μm at the target BPMs. The amplitude of the energy vernier was set to ± 100 KeV that generated beam excursions of about ± 0.4 mm on BPM12x [1]. The responses of the BPMs during a BM cycles are shown in Figure 7.3.2 in Section 7.3.2.1.

The detectors response to BM was much smaller than the statistical window-to-window noise. Therefore, several BM cycles were averaged to extract the detector

---

[1] 100 KeV per pass resulted in a total of 300 KeV modulation of the cavity energy. This is consistent with 0.4 mm beam excursion observed at BPM12x: $0.4 \times 10^{-4}/(4 \times 3 \times 10^6) \sim 300$ KeV. Here, 4 is the dispersion length in meters, and 3×10^6 is the beam energy in KeV.

responses to beam parameter fluctuations. The small amplitude allowed that the BM cycle data to be used as good asymmetry data without significant loss in statistical precision.

3.13   Asymmetry Feedback

HAPPEX-III asymmetry feedback system continuously monitored the helicity-correlated (HC) beam intensity asymmetry, A_I, and initiated necessary adjustments to suppress it. A_I arose from the differences in the laser light circular polarization between the complementary helicity states that generated the electron beam. A_I is calculated as

$$A_I = \frac{I_R - I_L}{I_R + I_L} \tag{3.13.1}$$

where $I_{R(L)}$ is the beam intensity integrated over the right(left) helicity state. The complementary laser light helicities were generated by a PC as discussed in Section 3.3, and the effects of the imperfections in the laser light circular polarization are described in Chapter 6. The schematic of the feedback system is displayed in Figure 3.13.1.

The asymmetry feedback system was operated by the parity DAQ, and ran in a Linux system which had the HAPPEX parity-analyzer software (PAN) [PAN] installed. During a feedback cycle, PAN analyzed data collected by the DAQ, and used A_I and the PITA slope to evaluate the necessary PC voltage adjustments. The PITA slope relates the amount of PC voltage adjustment necessary to induce a ppm change in A_I, and is described in Chapter 6. The feedback system transmitted these voltages, in near real-time, to the PC HV control electronics via the EPICS interface. The feedback system performed this process concurrently with data taking.
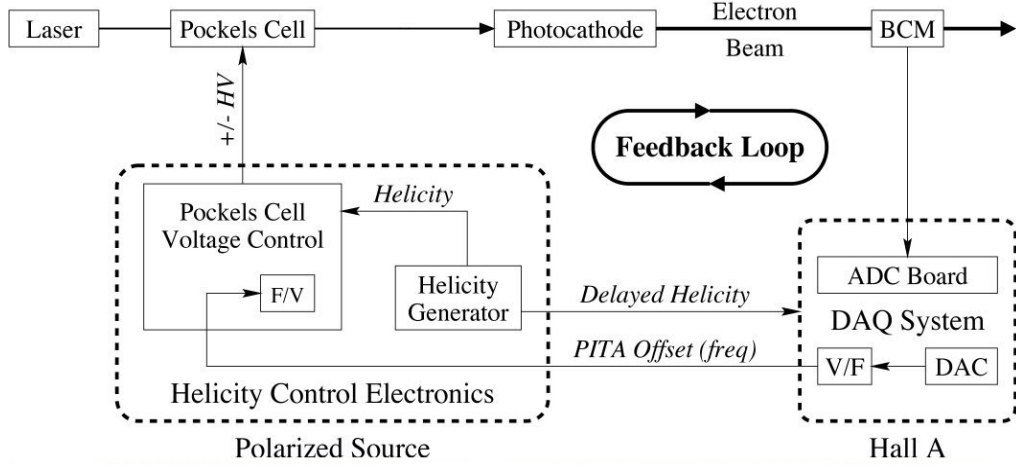
Figure 3.13.1: HAPPEX-III feedback system continuously monitored the false asymmetry (A_I) in the beam, and initiated necessary adjustments to keep it suppressed. During each feedback cycle, the DAQ system calculated and transmitted the necessary Pockels Cell (PC) voltage adjustments to the PC HV control electronics. The HV control electronics made these voltage adjustments to minimize A_I. During HAPPEX-III, the feedback cycle repeated every two minutes, with each cycle only using the data collected over the last two minutes.

The asymmetry feedback cycle length was adjustable and mostly chosen based on the precision achievable in A_I during each cycle. During HAPPEX-III, the feedback cycle repeated every two minutes, with each cycle only using the data collected over the last two minutes. At the HAPPEX-III helicity reversal rate of ~ 29.6 Hz (each helicity window was 33.83 ms long), ~ 3550 events (~ 1775 pairs) were collected during a two minute cycle, for which the typical statistical uncertainty was ~ 18 ppm while the A_I drifted between $\sim 0 - 50$ ppm.

The feedback system also had the capability to chose the monitor to be used as the feedback monitor. The feedback monitor's output was used for A_I evaluation. HAPPEX-III used the BCM closest to the target as the feedback monitor.

The PITA slopes, and the PC HVs were different between IHWP insertion and retraction [1]. So these parameters were stored in a text file, and read by the feedback

---

[1]See Figure 3.3.1 laser table schematic with the IHWP.

system to make necessary adjustments for each IHWP state.

3.14 Polarimeters

During HAPPEX-III, the beam polarization was measured by three different polarimeters: Mott, Møller and Compton. Each of these polarimeters provided an independent beam polarization measurement, and were used to cross-check each polarimeter's results with the others.

3.14.1 5 MeV Mott Polarimeter
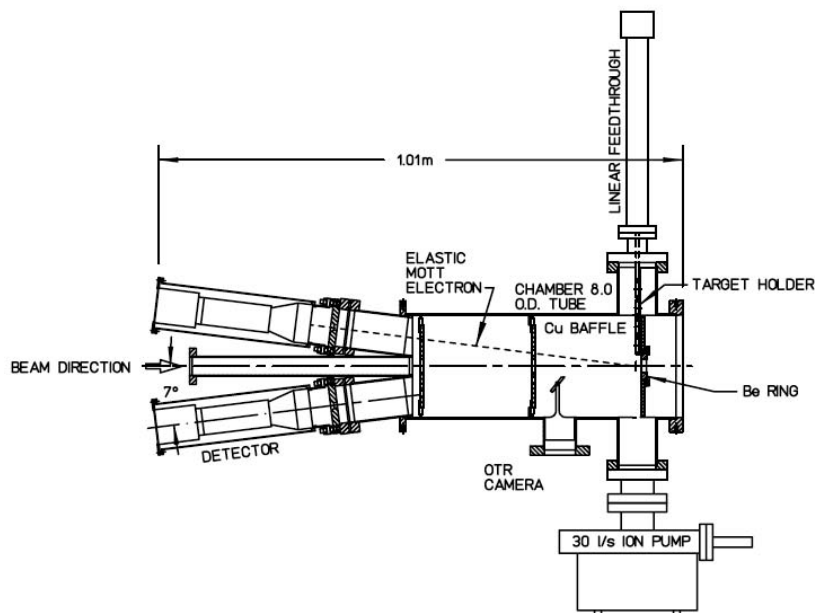
Figure 3.14.1: HAPPEX-III used the Mott polarimeter to measure the beam polarization at the 5 MeV region of the accelerator at JLab. The electron spin polarization was extracted by scattering the spin polarized electrons off gold foil targets, and measuring the right-left and up-down asymmetry in the back scattered electrons. HAPPEX-III used the results of Mott polarimeter to cross-check the beam polarization measurements inside the experimental hall, and to optimize the spin manipulation configuration in the injector. Figure reproduced from [Gr94].

The Mott polarimeter was located at the 5 MeV region of the accelerator at JLab. This polarimeter measured the beam polarization by scattering the 5 MeV longitudinally polarized electrons off gold foil targets at $\sim 172.6°$ (the "Sherman function" is maximum at this angle for gold at the kinetic energy of 5 MeV [Gr94]). Back scattered electrons were measured along horizontal and vertical directions by four detectors and the right-left and up-down asymmetry extracted, providing simultaneous transverse polarization measurements. The schematic of the Mott polarimeter at JLab is presented in Figure 3.14.1. A detailed description of the Mott polarimeter at JLab is presented in [Gr94].

The Mott beam polarization measurements were invasive, and were performed at regular intervals during beam studies by the accelerator group. HAPPEX-III did not use the results of the Mott polarimeter in the extraction of the final beam polarization. Nonetheless, results of the Mott polarimeter were important cross-checks on the beam polarization measured inside the experimental hall.

3.14.2 Møller Polarimeter

The Hall A Møller polarimeter [Al04] exploited the double-polarization spin asymmetry in Møller scattering of polarized electrons off a polarized target to measure the longitudinal component of the electron polarization. The left-right counting rate asymmetry was exploited to extract the beam polarization. The longitudinal beam polarization was calculated as

$$P_b = \frac{A_{Møller}}{P_{tgt} \cos \theta A_{zz}} \tag{3.14.1}$$

where $A_{Møller}$ was the left-right counting rate Møller asymmetry, P_{tgt} was the target polarization, θ was the angle subtended by the beam on the target, and A_{zz} was
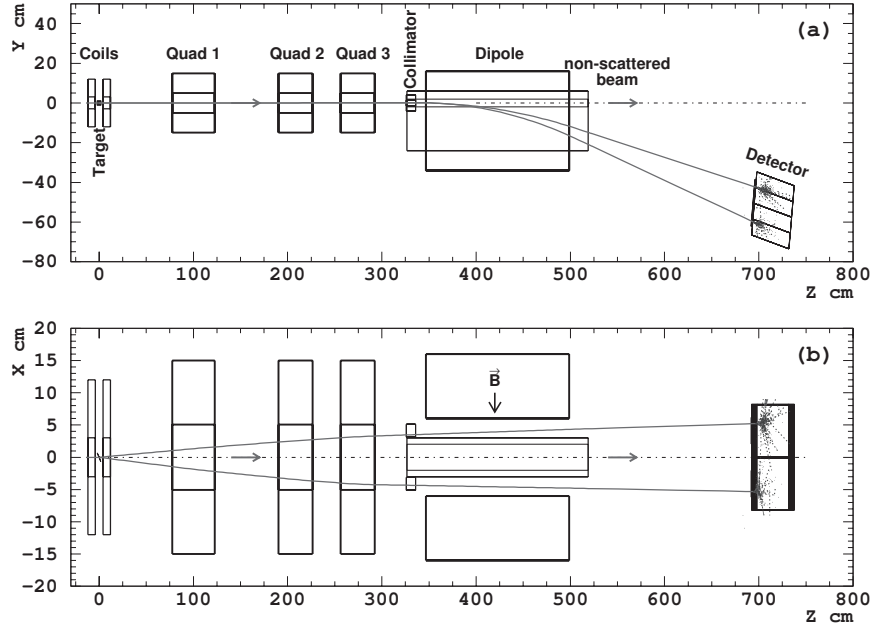
Figure 3.14.2: The Hall A Møller polarimeter scattered longitudinally polarized electrons off electrons polarized along the beam propagation direction in ferromagnetic target foils, and exploited the left-right counting rate asymmetry to extract the beam polarization. The quads adjusted the beam focus, and the dipole bent the beam vertically out of the scattering plane onto the detectors. Reproduced from Hall A NIM [Al04].

the analyzing power. HAPPEX-III used ferromagnetic foils that had $P_{tgt} \sim 7.6\%$ at the typical magnetic field strength of $\sim 24~mT$ present inside the Møller scattering chamber. The foil target polarizations were previously measured in dedicated measurements. The Møller magnet's magnetic fields were along the beam propagation direction, but the electrons in the targets were polarized along the foil. Beam polarization measurements with these foils at 20° and 160° (−20°) were taken and averaged during each measurement. This averaging suppressed systematic uncertainties in the polarization measurement arising from any transverse polarization that might be present in the beam as a result of precession in the accelerator and the extraction arc. At $\theta_{CM} = 90°$, the center of Møller polarimeter acceptance, $A_{zz} = 7/9$.

The Møller polarimeter was located inside Hall A, upstream of the target scatter-

ing chamber. The schematic of the Møller polarimeter is displayed in Figure 3.14.2. Longitudinal polarized electrons scattered off the polarized electrons from the Møller target into a spectrometer composed of three quads and a dipole. The spectrometer focused the scattered electron-pair onto two separate lead-glass calorimeter detectors that detected the electrons in coincidence. A vertical steel plate at the dipole mid plane, with a hole at the center to allowed the non-scattered electrons through, acted as a collimator for the scattered electrons and a magnetic shield for the non-scattered electrons in the beam.

Møller beam polarization measurements were invasive. Typically, each Møller measurement acquired one hour of data with a statistical precision of $\sim 0.2\%$. But each measurement took ~ 4 hrs in order to prepare and back out of the dedicated setup that was required for Møller measurement. The dominant error in the polarization measurement was systematic $\sim 1.7\%$, with this uncertainty dominated by the target foil polarization uncertainty of $\sim 1.5\%$.

3.14.3   Compton Polarimeter

The Hall A Compton polarimeter [Al04] utilized Compton scattering of the polarized electrons with a circularly polarized photon beam to measure the electron beam polarization. The beam polarization, P_b, was extracted as [Fr11]

$$P_b = A_{exp}/P_\gamma A_{th} \tag{3.14.2}$$

where P_γ is the photon polarization, A_{th} is the theoretical Compton scattering rate asymmetry at 100% photon and electron polarizations, and A_{exp} is the experimental
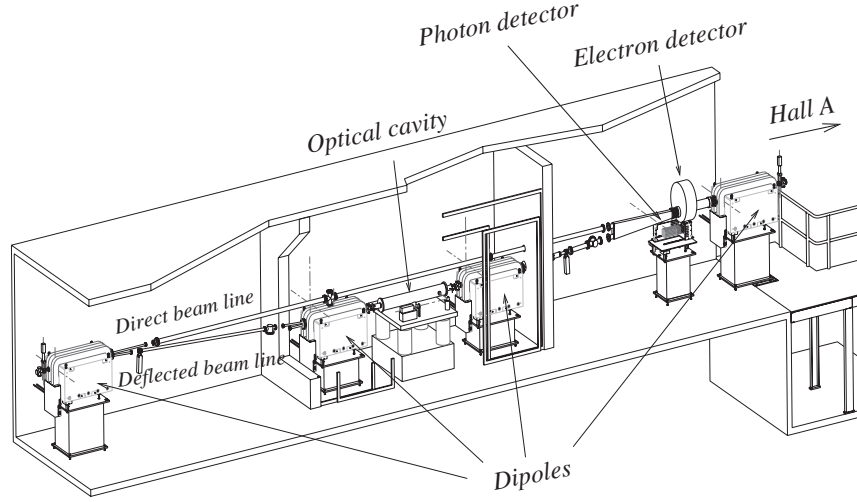
Figure 3.14.3: The Hall A Compton polarimeter scattered polarized electrons off a circularly polarized photon beam, and measured the left-right counting rate asymmetry to extract the electron beam polarization. The dipoles direct the beam through the optical cavity where the Compton scattering occurred. The electron detector detected the Compton scattered electrons and the photon detector detected the γ-radiation generated during the Compton scattering. Reproduced from Hall A NIM [Al04].

Compton scattering rate asymmetry measured as

$$A_{exp} = \frac{S^+ - S^-}{S^+ + S^-}. \tag{3.14.3}$$

$S^{+(-)}$ is the scattering rate flux of the right(left) helicity state.

The Hall A Compton polarimeter was located towards the beamline entrance of the hall, and consisted of a magnetic chicane, a photon source, a photon detector, and an electron detector, Figure 3.14.3. The dipoles direct the electron beam through the chicane. In the chicane was a mode locked Fabry-Perot cavity that typically contained ~ 1.5 KW circulating power when working well. The electron beam crossed the photon beam at an angle of 23 mrad [Al04] and some fraction of the electrons Compton scattered with the photons in the cavity. The crossing angle of the electron

beam with the photon beam was minimized to maximize the luminosity. The γ-rays generated by the Compton scattering in the cavity was detected by a photon detector while an electron detector detected the Compton scattered electrons. The circular polarization state of the photon beam, P_γ, was determined by a quarter-wave plate (QWP) located outside the cavity on the photon beam line.

The Compton polarimeter used a dedicated DAQ that was triggered by either single photons, single electrons or coincidences. The Compton polarimeter was extremely sensitive to backgrounds, so the photon beam was toggled on and off during beam polarization measurements to measure the backgrounds. The Compton polarimeter measured the beam polarization concurrently with data taking, and was non-invasive.

During HAPPEX-III, the Compton data was acquired in the integrated mode [Fr11]. In this mode, several systematic uncertainties associated with the traditional method of data acquisition in counting mode are avoided, and beam polarization measurements made with better than $\sim 1\%$ accuracy [Fr11]. The electron detector was not functional during HAPPEX-III, so all the Compton beam polarization measurements were performed with the photon detector alone.

4

PREX Experimental Setup

PREX utilized most of the experimental apparatus utilized by HAPPEX-III. This apparatus included equipment that was fairly standard to Jefferson Lab (JLab) including the accelerator itself, the equipment that was standard to experimental Hall A, and some instruments specific to HAPPEX-III, all of which is discussed in Chapter 3. Therefore, only apparatus that was specific to PREX or any apparatus used during HAPPEX-III that required significant upgrades for PREX are discussed in this chapter.

4.1 Overview

The experimental overview of PREX is similar to the one illustrated in Figure 3.1.1 for HAPPEX-III, albeit with some modifications. PREX used 50 to 70 μA longitudinally polarized 1.06 GeV continuous-wave (cw) electron beam. The electrons were generated at the injector, and accelerated through the linear-accelerators (linacs) [Le01] and into the experimental Hall A, very much like during HAPPEX-III. During PREX, these electrons elastically scattered from a ^{208}Pb target located at the center of the

hall. The electrons elastically scattered at an average polar angle of $\langle \theta \rangle \sim 5°$ were detected using a new septum magnet and the twin Hall A high-resolution spectrometers (HRSs) [Al04] that were placed symmetrically about the central beamline. As was the case during HAPPEX-III, the elastically scattered electrons were focused onto detectors specifically constructed for PREX, that were placed at the focal plane [1].

During PREX, the beam polarization was measured by two independent polarimeters, the Compton polarimeter and the Møller polarimeter, very much like during HAPPEX-III. The electron beam was rastered at the target, and the beam intensity, energy, and trajectory on target were inferred from the response of beam monitoring devices such as the beam position monitors (BPMs) and beam current monitors (BCMs). The integrated responses of these beam monitors and the detector photo-multiplier tubes (PMTs) were digitized by 18-bit analog-to-digital converters (ADCs) and recorded for each helicity-window by a centralized data acquisition system (DAQ). PREX used a helicity-quartet $(+--+ \text{ or } -++-)$ pattern, and each helicity-window was held constant for 8.33 ms.

4.2   Double Wien

PREX used a double Wien filter, in addition to the IHWP used during HAPPEX-III, for slow helicity reversal. Slow helicity reversal refers to a technique in which the electron beam helicity is reversed relative to both the electronic helicity control signals and the voltage applied to the PC. The slow helicity reversal is described in Section 5.6.2. The double Wien spin manipulation is potentially better at canceling helicity-correlated (HC) beam systematic effects compared to the IHWP.

The PREX double Wien filter consisted of two solenoids and two Wien filters as

---

[1]The focal plane is described in Section 3.8.
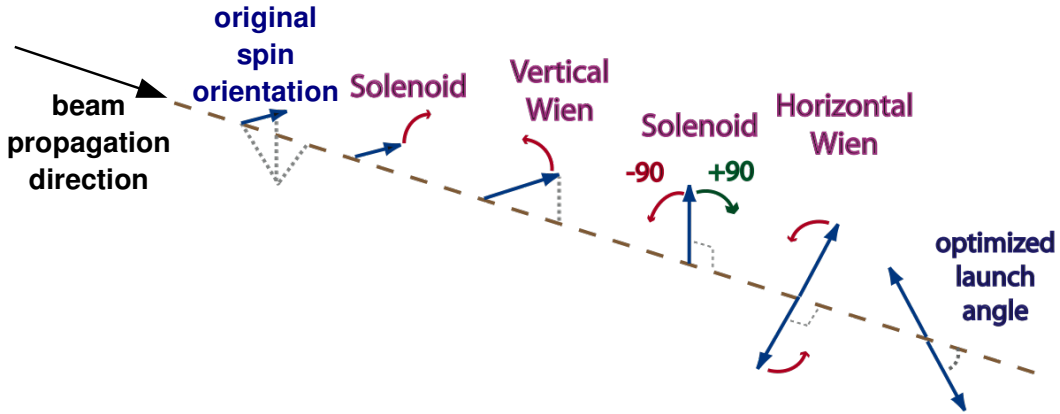
Figure 4.2.1: The double Wien filter used during PREX. Only the second solenoid and the horizontal Wien filter were added for PREX. The set of solenoids and Wien filters were used for slow helicity reversal to provide enhanced suppression of HC systematic uncertainties. The horizontal Wien also optimized the beam polarization inside the experimental hall. Adopted from [RM].

illustrated in Figure 4.2.1. The double Wien slow reversal was performed in three steps in which, 1) the first solenoid and the Vertical Wien filter were used to orient the beam polarization vertically, 2) the second solenoid was used for $\pm 90°$ polarization rotation, and 3) the Horizontal Wien filter finally optimized the beam polarization for maximal longitudinal polarization inside the experimental hall. During the experiments that preceded PREX, the beamline only contained the first solenoid and the Horizontal Wien.

During PREX, the slow helicity reversal via the double Wien filter was used to cancel any second-moment systematic uncertainties, in addition to the *non-polarization* effects present in the beam. The non-polarization effects, and the higher-moment HC effects are described in Chapter 6. The second-moment systematics cancellation is possible because the solenoids reverse the beam helicity without affecting its focusing: the solenoidal magnetic field direction only affects the electron beam helicity while the beam optics depends on the square of these fields. Therefore, the double Wien slow

helicity reversal only reversed the sign of the zeroth-moment (HC charge asymmetry) and the first-moment (HC position differences) HC effects, without affecting the second-moment HC effects such as the HC beam spot-size and shape differences. This allowed the cancellation of any HC second-moment effects in the beam on averaging the data with complementary helicity and Wien states.

4.3   Beam Modulation (BM)

PREX used a modified version of the BM system used during HAPPEX-III. The BM system used during PREX had the capability to modulate two coils simultaneously, while the BM system used during HAPPEX-III could only modulate one coil at a time. PREX BM system used VME-4145 waveform generators to generate sine waveforms that modulated the beam, unlike the BM system used during HAPPEX-III that used a VME DAC module to generate triangle waveforms to modulate the beam. The VME-4145 waveform generators were connected to the same set of seven air-core corrector coils and the vernier input on the accelerator cavity used during HAPPEX-III. The BM system used during HAPPEX-III is described in Section 3.12. The cavity and the modulation coil location on the Hall A beamline is show in Figure 3.5.1 in Section 3.12. These coils and the cavity were modulated by the waveforms generated by the VME-4145 waveform generators, which in turn were operated by the control voltages supplied by a VME DAC module controlled by the parity DAQ.

The BM system was upgraded due to the possibility that the single coil modulation system might not provide sufficient orthogonality of the BM parameters (beam position (x and y), angle (θ_x and θ_y) and energy (ΔE)) at the kinematics of PREX. This orthogonality is required to evaluate the false asymmetry arising from the fluctuations in these parameters, A_{Fb}, given by Eq. 7.3.5, and correct the raw asymmetry,

A_{raw}, for A_{Fb}. However, initial tests with only one coil modulated at a time demonstrated sufficient orthogonality in the space of these variables. Therefore, the BM system modulated the beam with only one coil at a time during PREX, very much like during HAPPEX-III.

During PREX, the BM cycles consisted of a sequence in which each of the seven coils and the cavity were modulated by 15 Hz sine waveforms that were generated by the VME-4145 waveform generator. As a result, the modulation was not constant in time during the integration period, unlike during HAPPEX-III modulation for which the modulation amplitude was constant during the integration period. Therefore, the phase of the modulating waveform for each integrating period was recorded during PREX.

A complete BM cycle lasted about 85.68 secs, and comprised of individual coils and the energy cavity modulation for 4.23 secs each. Each coil modulation was preceded by a delay of 5.28 secs during which the parameters of the sine waveform such as the modulation amplitude and duration were set in VME-4145. The beam position feedback was also turned off during the delay preceding the first coil modulation, although the "feed forward" system continued to operate. The cavity modulation was preceded by a delay of 6.48 secs, during which the parameters of the sine waveform for the cavity modulation were set. The lock on the beam energy was also turned off during this delay. The end of the cavity modulation was followed by 8.38 secs delay before the end of the BM cycle. The VME-4145 waveform generation was disabled during this delay. The beam position feedback and the energy lock were also turned back on during this delay. The BM cycle repeated once every 9 mins and 36 secs. The coils were modulated to generate beam excursions of $0.3 - 0.5$ μm at the target BPMs, and the cavity was modulated to generate beam excursions of about 0.75 mm on BPM12x.
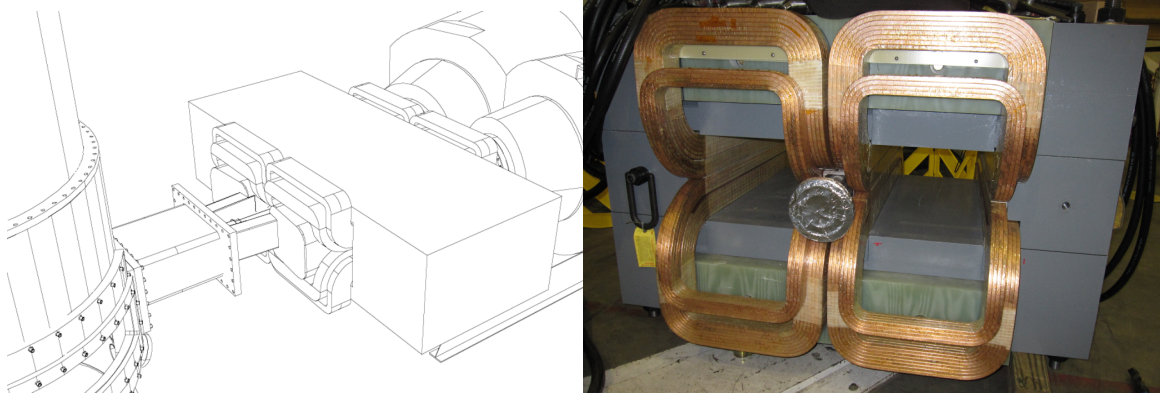
Figure 4.4.1: PREX used septum magnets to transport the elastically scattered electrons at 5° into the HRSs. The use of septum was necessitated by the inaccessibility of the HRSs to scattering angles smaller than 12.5°. The septum was located between the target scattering chamber and the first quadrupoles of the HRSs as shown in the figure on the left. The right picture shows the central beam line (for the passage of unscattered electrons) and a set of separate coils that generated magnetic fields to transport the electrons onto each of the HRSs. Reproduced from [PREXWeb].

Very much like during HAPPEX-III, the response of the detectors to BM was much smaller than the statistical window-to-window noise during PREX. As a result, several BM cycles were averaged to extract the detector responses to beam parameter fluctuations, and the BM data were used as good asymmetry data without significant loss in statistical precision.

4.4   Septum

PREX used septum magnets to bend elastically electrons scattered at 5° into the HRSs. The septum was necessary because the HRSs cannot be set to scattering angles smaller than 12.5°. The septum was located between the target scattering chamber and the first quadrupole of the HRSs. The PREX septum is shown in Figure 4.4.1.

4.5   PREX Collimator
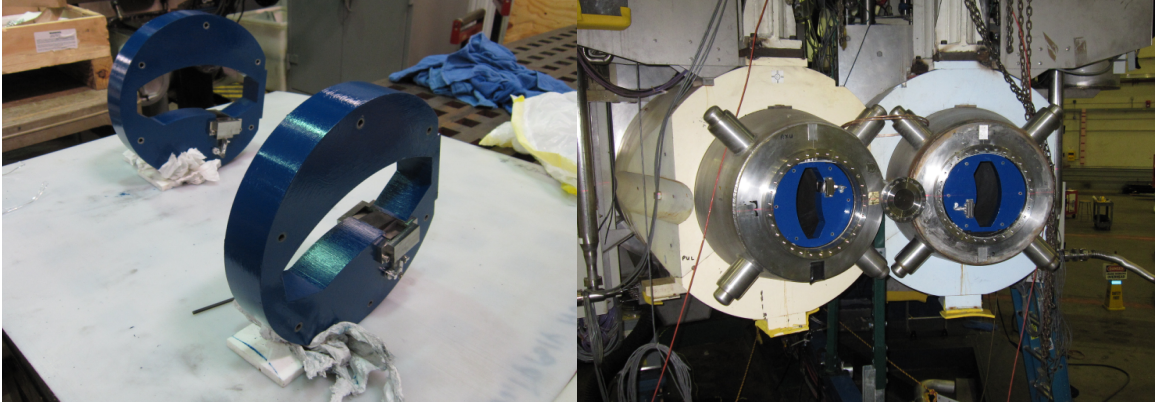
Figure 4.5.1: The lead collimators for PREX facilitated constant monitoring of the transverse beam asymmetry, A_T, and also suppressed the data contamination from unwanted electrons by blocking them from reaching the focal plane. The picture on the right illustrates the orientation of each of the collimators at the entrance of the first quadrupole of each HRS. The large semi-circle opening inside the collimator and the "notch" on the inside edge of the semi-circle transmitted elastically scattered electrons to the focal plane. The notch, however, contained Beryllium, and induced energy losses in the elastically scattered electrons. As a result the trajectories of the electrons transmitted through the notch separated from the trajectories of the elastically scattered electrons transmitted through the semi-circle opening, and were incident at a different location on the focal plane. A dedicated A_T detector located appropriated to collect the electrons transmitted through the beryllium monitored A_T, concurrently with asymmetry data acquisition by the focal plane detectors. Reproduced from [PREXWeb].

A lead collimator, designed specifically to facilitate the measurement of the transverse asymmetry, A_T, and to suppress backgrounds by blocking unwanted electrons from entering the HRSs, was used during PREX. This collimator is illustrated in Figure 4.5.1. The semi-circular opening and a notch at the edge of the inner semi-circle transmitted elastically scattered electrons onto the focal plane. The electrons incident on other parts of the collimator were completely blocked by the collimator.

The notch contained Beryllium (Be), and induced energy losses in the elastically scattered electrons. As a result, the electrons transmitted through the notch followed

a slightly different trajectory inside the HRSs than the elastically scattered electrons transmitted through the semi-circle opening, and were incident at a different physical location on the focal plane. The intention was to exploit this separation to monitor A_T with a dedicated A_T detector, and simultaneously acquire the asymmetry data with the focal-plane detectors. However, a superior location for the dedicated A_T monitor was found in the radiative tail, and signal from the Be notch was not used. The detector setup is shown in Figure 4.8.2.

The notches were located in a region of high scattering rates, and a big scattering angle, ϕ. The notch was located towards the top of the collimator in one HRS, and towards the bottom in another in order to achieve symmetry of A_T sign. The collimators were carefully designed and positioned to select identical acceptance angles for both the HRSs.

4.6 Low Current Cavity Monitors

PREX used low-current cavity monitors to monitor beam position and current during four-momentum transfer squared (Q^2) measurements. These cavity monitors were necessary for the following reasons:

- The standard Hall A DAQ and components of detector packages that were essential for Q^2 determination lost reliability at the extremely high rates generated at beam currents of $> 1~\mu A$ with the PREX ^{208}Pb target. The scattering rate for this target was ~ 20 MHz/μA. But the standard Hall A DAQ had typical dead times of $\sim 20\%$ at 2 KHz trigger rates, and the VDCs of the standard Hall A detector package could only operate reliably below 200 KHz. Therefore, PREX Q^2 determination needed to be performed at extremely low currents of $\ll 1~\mu A~(\sim 50$ nA).
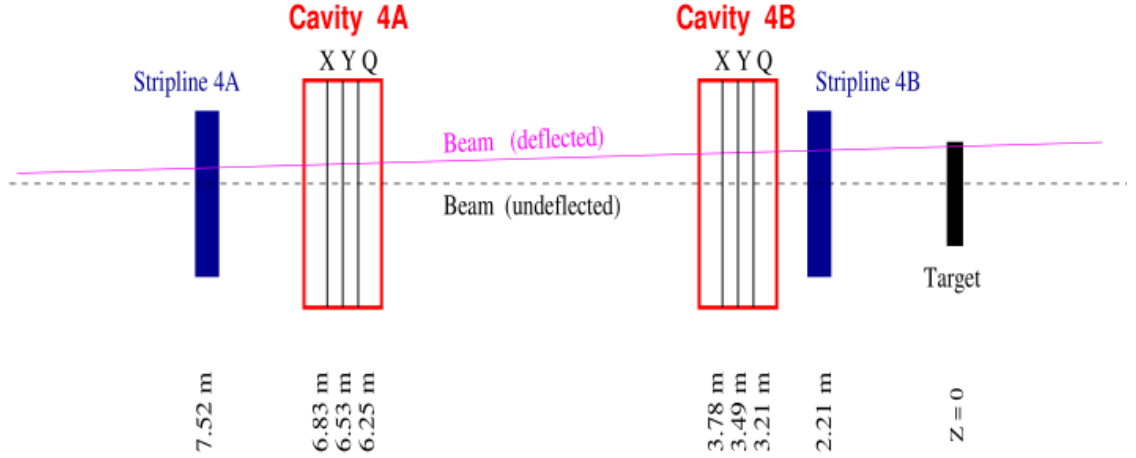
Figure 4.6.1: PREX low-current cavity monitors provided reliable beam position and current measurements from 10 nA to 100 μA. These were essential during PREX Q^2 measurements because at the extremely high rates of ~ 20 MHz/μA achieved with the PREX ^{208}Pb target, the standard Hall A detector package and DAQ could not operate reliably even at beam currents of 1 μA, and the Hall A BPMs and BCMs were unreliable at beam currents of < 1 μA. Adopted from [Bo08].

- But, at the low currents needed for PREX Q^2 determination, the existing Hall A monitors lost reliability: the BPMs were not reliable below beam currents of 1 μA [Al04], and the BCMs were highly non-linear below 5 μA [Al04].

Therefore, these low-current cavities were essential for beam position and current determination during PREX Q^2 measurements. These cavities provided reliable beam current and position measurements from 10 nA to 100 μA [Bo08].

Each of these cavity-monitor assemblies was a triplet of cavities that measured the beam current and position along x and y. Two monitor assemblies were located near the target between the stripline BPMs 4a and 4b as illustrated in Figure 4.6.1. These cavities are described in [Bo08].
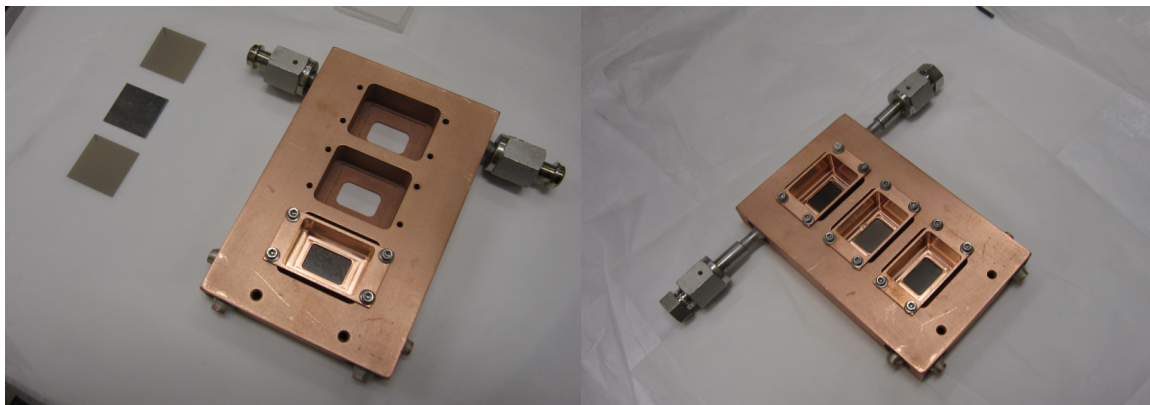
Figure 4.7.1: PREX used three lead-diamond sandwich targets, each made of a 0.5 mm thick isotopically pure lead (^{208}Pb) (the dark foil in the middle of the two light foils in the picture on the left) sandwiched between two 0.15 mm thick diamond foils (the two light foils on either side of the dark foil in the picture on the left). All three lead-diamond sandwiches were mounted onto a copper frame. 20 K cryogenic ^{4}He circulated around the edges of the lead-diamond sheets inside the copper frame to keep the ^{208}Pb from melting due to beam heating. Both the pictures present target beam entry view. Reproduced from [PREXWeb].

4.7   Target

PREX used a lead (^{208}Pb) target as the primary target to acquire asymmetry data. The ^{208}Pb target was made of a 0.5 mm thick isotopically pure ^{208}Pb foil sandwiched between two 0.15 mm thick diamond sheets [1]. A thin layer of "vacuum grease" was applied at the interface between the lead and diamond sheets. The lead-diamond target was clamped onto a copper frame by screwing a copper sleeve that made a tight fit with the frame as shown in Figure 4.7.1. A silver-based paste was applied at the interface between the copper and diamond sheet to improve thermal conductivity.

An important consideration that went into designing the PREX target was the susceptibility of ^{208}Pb in the target to melting due to beam heating. The lead has a low melting point of $\sim$ 600 K, and a poor thermal conductivity of only $\sim$ 35 W/m/K. As a result, at the nominal PREX operating currents of $\sim$ 50 μA, the

---

[1]A complete measurement of the lead and diamond sheet thickness is documented at [Mi10]

target temperature would easily exceed 600 K without a medium to transport the heat away from the target. Therefore, the diamond sheets which made contact with the ^{208}Pb in the target (and have excellent thermal conductivity (> 900 W/m/K)), and cryogenic ^{4}He at 20 K circulating around the edges of the lead-diamond sheets inside the copper frame were used to transport heat away from ^{208}Pb. During PREX, the ^{208}Pb target temperature was held at ~ 96 K at 50 μA beam current [1].

PREX had a total of three [2] lead-diamond targets, all of which were mounted on a single copper frame as shown in Figure 4.7.1. The copper frame was mounted on a target ladder that also contained a Beryllium Oxide (BeO), Tantalum (Ta), thin lead (0.05 mm thick), thick ^{12}C (2 mm thick), thin ^{12}C (0.15 mm thick), super-thin ^{12}C (0.075 mm thick), and "holey" carbon target (carbon target with a circular hole at its center), as illustrated in Figure 4.7.2a. The target-ladder setup was different during the calibration phase of the experiment. At the beginning of PREX, the copper frame was mounted in the configuration presented in Figure 4.7.2b which contained an optics ^{12}C-foil, BeO, Ta, thin ^{12}C and the water-cell target for calibrations. The optics ^{12}C-foil target consisted of 5 carbon foils at $-15.0, -7.5, 0.0, 7.5, 15.0$ cm along the beam propagation axis, with 0.0 being the center of the lead-diamond target. The water-cell target consisted of 5 mm water contained in a steel cell of 0.001" thick walls at beam entry and exit faces. The water-cell runs were used in the HRS central angle determination in a procedure similar to the one discussed in Section 7.7.3.1.

---

[1]Despite the mechanisms to transport the heat away from ^{208}Pb in the target, the ^{208}Pb uniformity degraded nevertheless, with the extent of degradation proportional to the amount of beam exposure time. The effects of ^{208}Pb uniformity degradation are discussed in Section 4.11.

[2]Multiple lead-diamond targets were built as a precaution against thermal failure of one or more of these targets. By the end of PREX all three lead-diamond targets were used and each of these targets had degraded in uniformity substantially.

(a) PREX production target

(b) PREX optics target
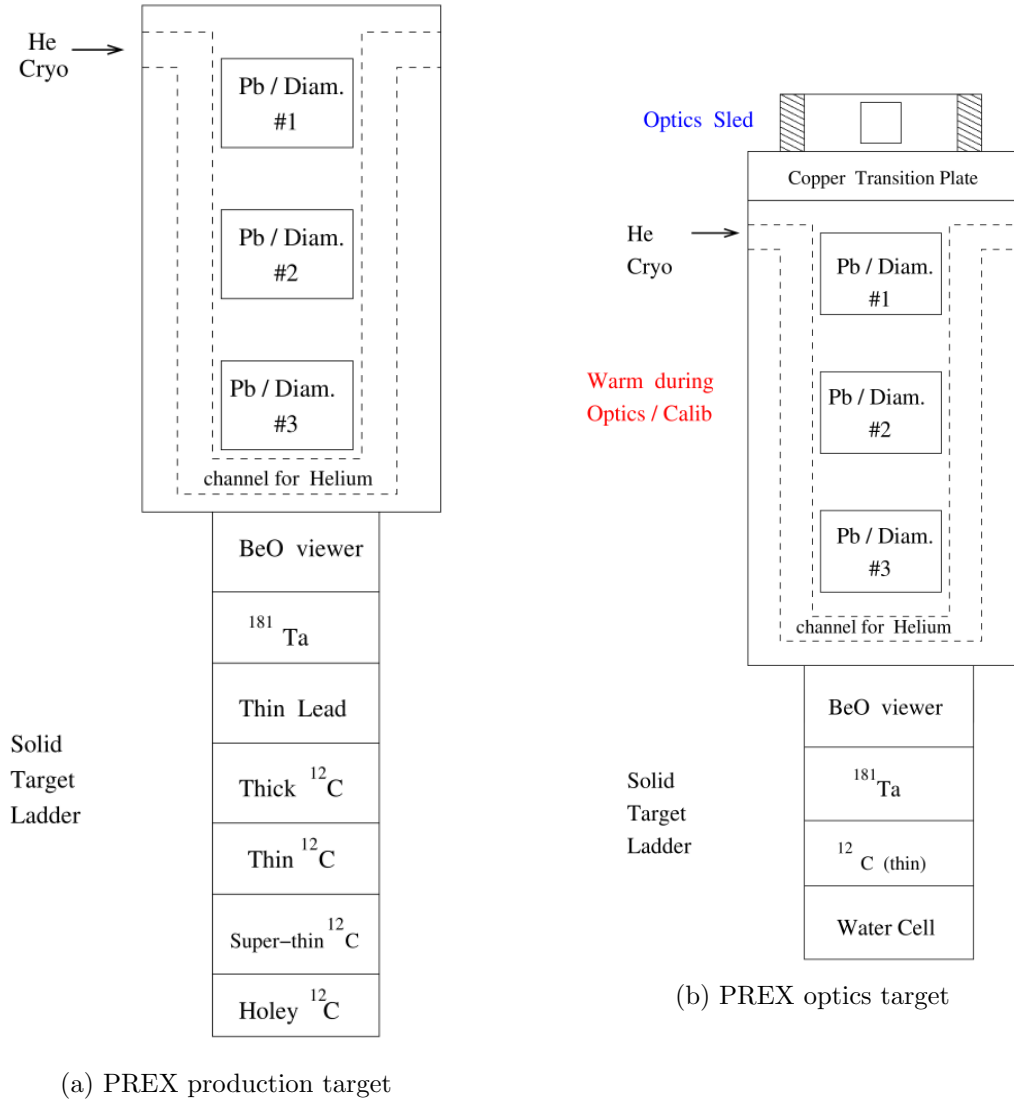
Figure 4.7.2: On the left is the PREX production target ladder that contained three lead-diamond sandwiches, Beryllium Oxide (BeO), Tantalum (Ta), thin lead (0.05 mm thick), thick ^{12}C (2 mm thick), thin ^{12}C (0.15 mm thick), super-thin ^{12}C (0.075 mm thick), and a "holey" carbon (carbon target with a circular hole at its center) mounted in a vertical stack. On the right is the PREX optics target ladder that contained some of the same targets from the production target ladder, in addition to the "optics sled" and the water-cell target. The optics target was used during the "commissioning" phase towards the start of PREX, and replaced by the production target ladder during asymmetry data acquisition. The lead-diamond targets were used to acquire the asymmetry data, while the rest were used either for diagnostics, beam alignment, background measurements or central scattering angle determination. Reproduced from [PREXWeb].

4.8 Focal Plane Detectors

The PREX focal plane detector package consisted of three detectors in each of the HRSs: two primary detectors that acquired the asymmetry data, and an A_T detector that monitored the transverse asymmetry, A_T, during the experiment. Each detector consisted of 3.5×14.0 cm^2 quartz scintillators connected to air light guide that transported the Čherenkov radiation generated by the electrons incident on the quartz onto a 2-inch quartz-window R7723 PMTs. The detectors were able to withstand the radiation damage caused by the high signal flux and also provided a sufficiently uniform response to the electrons. The detectors were mounted on a motorized platform that could be maneuvered along a set of tracks, and remotely allowed detector alignment about a plane.

The primary detectors measured the elastically scattered electron flux, and were stacked on top of each other along the beam propagation path as depicted in Figure 4.8.1. These detectors were mounted with the quartz parallel to the VDCs so that the elastically scattered electrons were incident on the quartz at $45°$. This orientation optimized the generation of the Čherenkov radiation in the quartz and its collection into the PMTs. The detector on the bottom of the stack, and closer to the VDCs, had a 5 mm thick quartz, and the one above it had a 1 cm thick quartz. The quartz scintillator's dimensions ensured that only elastic events (and a negligible fraction of electrons inelastically scattered at the first nuclear excited state of 2.6 MeV) were accepted by the quartz detectors.

The A_T detector, also located at the focal plane, measured the transverse asymmetry, A_T, arising from any residual transverse polarization (at the scattering vertex) present in the beam. Like the primary detectors, the A_T detector was also positioned such that the electrons were incident on the quartz scintillators at $\sim 45\%$. The A_T
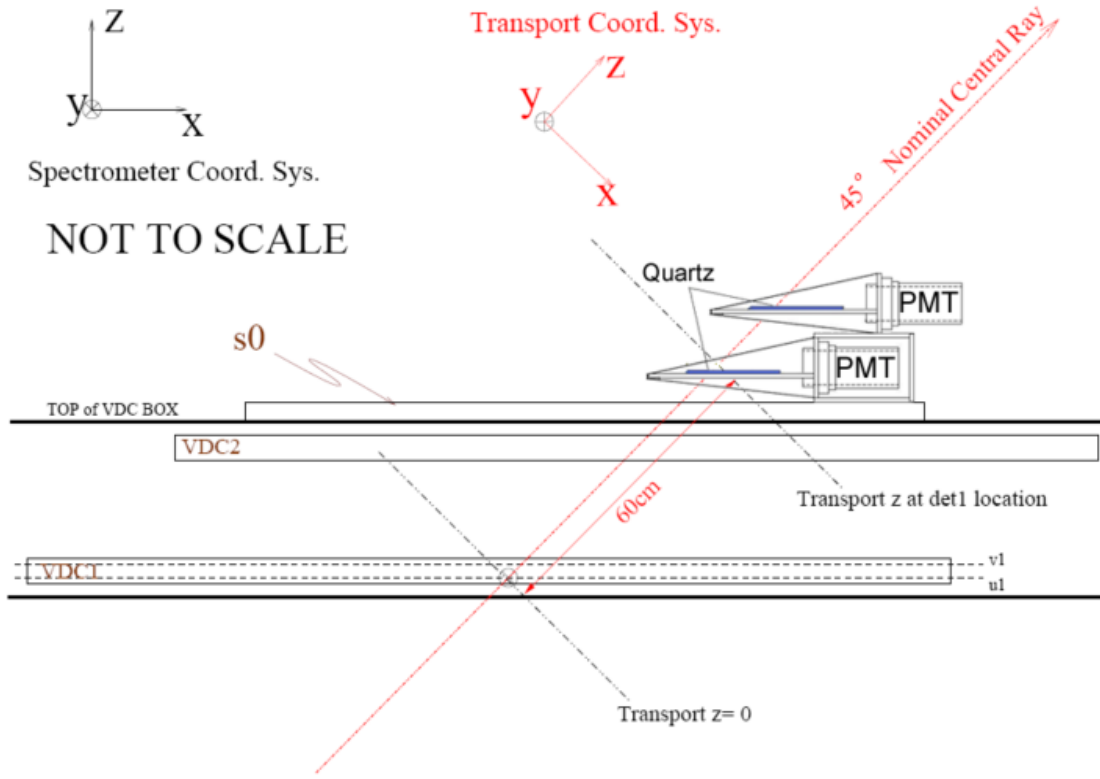
Figure 4.8.1: The primary detectors for PREX were stacked on top of each other along the beam propagation path. The electrons were incident on these detectors at about 45° that ensured optimal collection of the Čherenkov radiation generated in the quartz into the PMTs. The bottom detector had a $3.5 \times 14.0 \times 0.5$ cm^3 quartz, and the top detector had $3.5 \times 14.0 \times 1$ cm^3 quartz. The quartz scintillator's dimensions ensured that electrons accepted by the quartz detectors were dominantly elastic electrons. Adopted from [Me12].

detector was located in a region in the ^{208}Pb radiative tail which had a reasonably large average Q^2, as discussed in Section 4.5. The detector assembly in one of the HRSs, with the two primary detectors and the A_T detector, is shown in Figure 4.8.2.

All the detectors were equipped with non-linearity test systems that characterized the detector's non-linearity *in-situ* during the experiment, when the experiment was not taking beam. This system consisted of two LEDs fitted near the PMT's base,
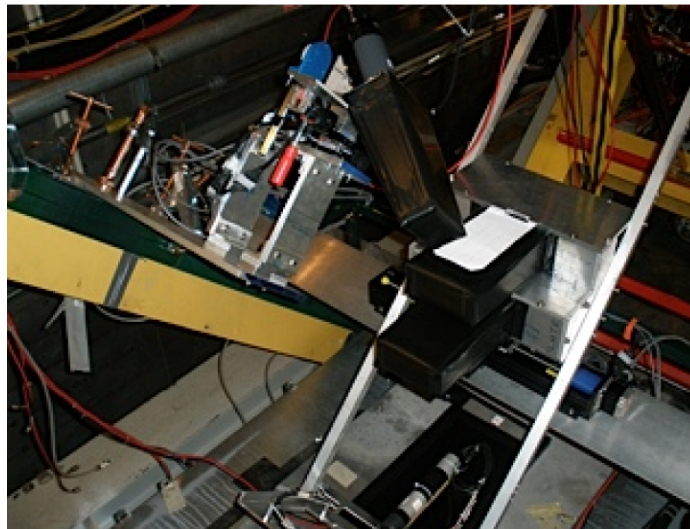
Figure 4.8.2: The detector assembly in one of the HRSs. All three detectors are sealed with black tapes, and appears as black rectangular objects in the picture. At the center and towards the top is the A_T detector. Immediately below it are the two primary detectors that acquired the asymmetry data. Adopted from [Me12].

with the LEDs operated using a technique similar to the one used during HAPPEX-III detector non-linearity tests. The detector non-linearity setup schematic, tests and results of the PREX detectors are described in [Me12].

4.9   Compton Polarimeter

The standard Hall A Compton polarimeter was designed for $\sim$ 100 nA to 100 μA electrons at JLab beam energies of 1-6 GeV [Al04]. As described in Section 3.14.3, this polarimeter had a typical circulating power of $\sim$ 1.5 KW inside the Fabry-Perot cavity (when working well) where the photon beam interacted with the electron beam, and provided 1% statistical precision with $\sim$ 25 minute's data for 4.6 GeV 40 μA electrons [Es05]. However, at PREX energy of 1 GeV, the statistical precision in its beam polarization measurement could be as large as 2% for similar beam current and acquisition period. There were other difficulties in achieving the precision required by
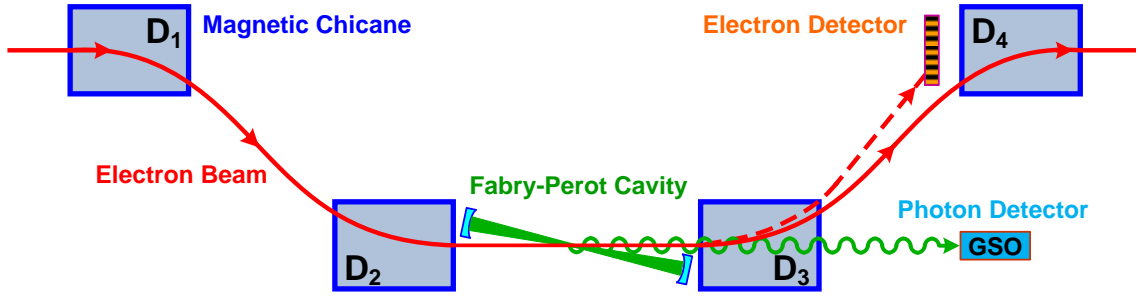
Figure 4.9.1: PREX used a new Compton polarimeter with a schematic similar to the old Hall A Compton polarimeter. However, PREX Compton used a 532 nm (2.33 eV) laser instead of the 1054 nm (1.16 eV) used by the old Hall A Compton, and its Fabry-Perot cavity contained a circulating power of $\sim$ 3.5 KW instead of the $\sim$ 1.5 KW of the old Hall A Compton. With these modifications, PREX Compton polarimeter measured beam polarization to 1% statistical precision with 6 minutes of data for 1 GeV 50 μA electron beam at 100% photon detector efficiency [Ra11]. Figure adopted from [Ra11].

PREX with this polarimeter. This polarimeter used 1064 nm (1.16 eV) laser as its photon source. At this photon energy, and the nominal photon-electron beam crossing angle of 23.5 mrad, the Compton scattered 1 GeV electrons remained very close to the primary electron beam (the maximum separation of the Compton scattered electrons from the primary electron beam was $\sim$ 4.1 mm at the standard dipole settings [Ra11]) rendering the detection of these electrons extremely difficult. The left-right Compton asymmetry was also only 0.88% for 1 GeV electrons, requiring excellent signal-to-noise ratio, which degraded significantly for beam energies below 2 GeV. As a result, the standard Hall A Compton polarimeter could not achieve the 1% precision in beam polarization measurement as required by PREX.

PREX used a new Compton polarimeter with a 532 nm (2.33 eV) laser that contained a typical circulating power of $\sim$ 3.5 KW in its Fabry-Perot cavity. The schematic of the PREX Compton polarimeter was similar to the standard Hall A Compton polarimeter, and is illustrated in Figure 4.9.1. The 1 GeV Compton scat-

tered electrons were separated from the primary electron beam by about a maximum of 8.3 mm (about twice that of 1064 nm photons) at the nominal dipole settings and photon-electron beam crossing angle of 23.5 mrad, and the left-right Compton asymmetry was about 1.7% (also twice the asymmetry achieved with 1064 nm photons) [Ra11]. As a result, this new Compton polarimeter avoided most of the difficulties associated with the beam polarization measurements by the old Hall A Compton polarimeter. A detailed description of this polarimeter, along with the PREX beam polarization measurements are discussed in [Ra11].

Like during HAPPEX-III, PREX also used the integrating detection technique of the back-scattered photons using custom Flash ADCs. Integration eliminated systematic uncertainty arising from thresholds and deadtime that affected the older counting method. Integration also had the advantage of being able to handle significantly more backgrounds than during HAPPEX-III, reducing sensitivity to beam tuning. PREX Compton polarimeter measurements were indeed very clean, and measured the beam polarization with a total systematic error of 1.2% at 1 GeV [Pa11].

The electron detector was not functional during PREX. Thus, all the Compton beam polarization measurements were acquired with the photon detector.

4.10   Møller Polarimeter

The standard Hall A Møller polarimeter was modified for PREX because of stringent requirements on the beam polarization requirements of PREX. The standard Hall A Møller polarimeter measured beam polarization with a 1.7% systematic uncertainty during HAPPEX-III, which fell short of the 1% precision required by PREX. The 1.7% uncertainty was dominated by the uncertainty in the magnetized target foil polarization measurement, which was as big as 1.5%. Therefore, suppression of

the uncertainty in target foil polarization measurement was the focus of the Møller polarimeter upgrade for PREX.

The upgraded Møller polarimeter used a high-field magnet that provided a magnetic field of up to 4 T, although only 3 T was used during PREX. This was very large compared to the low-field magnet used by the standard Hall A Møller system that typically provided $\sim$ 24 mT. At such high fields, the electrons in the ferromagnetic target foil are 100% polarized, and the foil saturated. Therefore, the target polarization could be determined with much greater precision. During PREX, the target foil polarization was inferred with an uncertainty of $\sim$ 0.25% [Sa11].

Other upgrades to the standard Hall A Møller polarimeter included reducing the target foil thickness from 7-30 μm to 1-10 μm for beam polarization measurements at currents of up to 50 μA, introduction of a beam duty cycle in order to reduce target heating at high beam currents, new data acquisition system (DAQ) based on Flash ADCs (FADCs) to handle higher scattering rates and the introduction of segmented detectors to handle higher scattering rates [Sa10]. These upgrades are described in [Sa10].

4.11 Raster

During PREX, beam rastering was necessary to prevent thermal damage to the target due to beam heating, and to suppress non-statistical broadening of the asymmetry width resulting from spatial target inhomogeneity. However, the standard Hall A rastering system could only synch at frequencies lower than those required to sufficiently suppress the asymmetry width broadening during PREX. Therefore, the standard Hall A raster system was customized and operated in a different configuration than the one used during HAPPEX-III. In the standard configuration, the raster orbits

were determined by complementary waveforms of ~ 24.96 and ~ 25.08 KHz, with a phase difference of 120 Hz between them [Mi05]. The raster waveform frequencies were not synched to the helicity waveforms that triggered the parity DAQ. As a result, each helicity window sampled the target area covered by the raster pattern differently. This difference in sampling did not introduce any noticeable variation in the asymmetry widths during HAPPEX-III because the target density variations were negligible. However, during PREX, the target non-uniformity due to localized beam heating was substantial, and resulted in luminosity fluctuations that increased the asymmetry width by as much as $\sim 40\%$. So the raster pattern frequency was locked to a multiple of the helicity frequency to eliminate noise arising from target non-uniformity. Locking the raster to a multiple of the helicity frequency forced the raster to execute the same orbit between any two adjacent helicity cycles. PREX raster synched schematic is illustrated in Figure 4.11.1.

PREX used Agilent frequency generators to generate triangular raster waveforms of frequencies similar to the ones generated by the standard Hall A raster system. The advantage of using these Agilent frequency generators were that they could be tuned to generate frequencies with arbitrary phase differences unlike the Hall A raster system. PREX used phase differences of 240, 480 and 960 Hz over the course of the run. Typically, a phase difference of 240 Hz provided effective suppression of the noise arising from target non-uniformity. But as the target degradation progressed, increasing the phase differences to 480 and then to 960 provided greater noise suppression.

The extent of target degradation can be inferred from the correlation plots of the asymmetries measured between the two HRSs. Typical correlation plots with and without the raster synch are presented in Figure 4.11.2. The plot on the left was acquired without the raster synch, while the plot on the right was acquired with the

Setup for Agilent-based raster synchronization
If the scope is triggered on the 30 Hz signal from Riad's box, and the two Agilents
are set to the frequencies shown below, the signals from the Agilents should appear
stationary on the screen. If they appear to drift slowly to the left or the right, both
frequencies should be adjusted by the same amount up or down until they appear
motionless. Changes in the exact frequencies needed are presumably due to small
drifts in difference between what Riad's box considers to be 10 MHz, and what the
two Agilents consider to be 10 Mhz.

From Riad's Box

10 MHz
signal
from
optical
fiber

30 Hz

10 MHz output from Agilent

Agilent 33220a
Nominal 25.08 kHz
Actual: 25.079950 kHz
for 120 Hz repeat freq.
or 25.19995 kHz
for 240 Hz repeat freq.

Agilent 33250a
Nominal 24.96 kHz
Actual: 24.959950 kHz
for 120 Hz repeat freq.
same for 240 Hz
repeat frequency

Scope
(necessary for setting
frequencies on
Agilents)

Channel
#1 #2   #3   #4

Output, pulse
mode, 200 ns
pulse width,
2.5 V p-to-p

Output, square
wave mode, 20%
duty factor,
2.5 V p-to-p

Make certain that the correct
frequencies (25.08 and 24.96 kHz)
are fed to the correct cables
(they are labeled).

To raster box downstairs   To raster box downstairs

Figure 4.11.1: PREX raster was synched to a multiple of the helicity frequency that
forced the raster to execute the same orbit between any two adjacent helicity cycles.
This was performed by synching the Agilent frequency generator boxes to the 10 MHz
signal originating in the helicity-generator, referred to above as "Riad's Box". The
differences between the waveform frequencies generated by the Agilent boxes were set
to a multiple of the helicity reversal frequencies. Triangular waveforms generated by
the Agilent boxes modulated the raster orbit.

raster synched, with other conditions unchanged. A strong correlation indicates a

large spatial non-uniformity in the target, with the correlation getting stronger as the

target non-uniformity increases. With the raster synched, however, the effects of the

target non-uniformity is suppressed, as reflected in the plots of Figure 4.11.2.

A typical raster scan of the ^{208}Pb-target after exposure to ~ 50 μA beam for 2-3

weeks is presented in Figure 4.11.3. The "hole" at the center of the target is due to
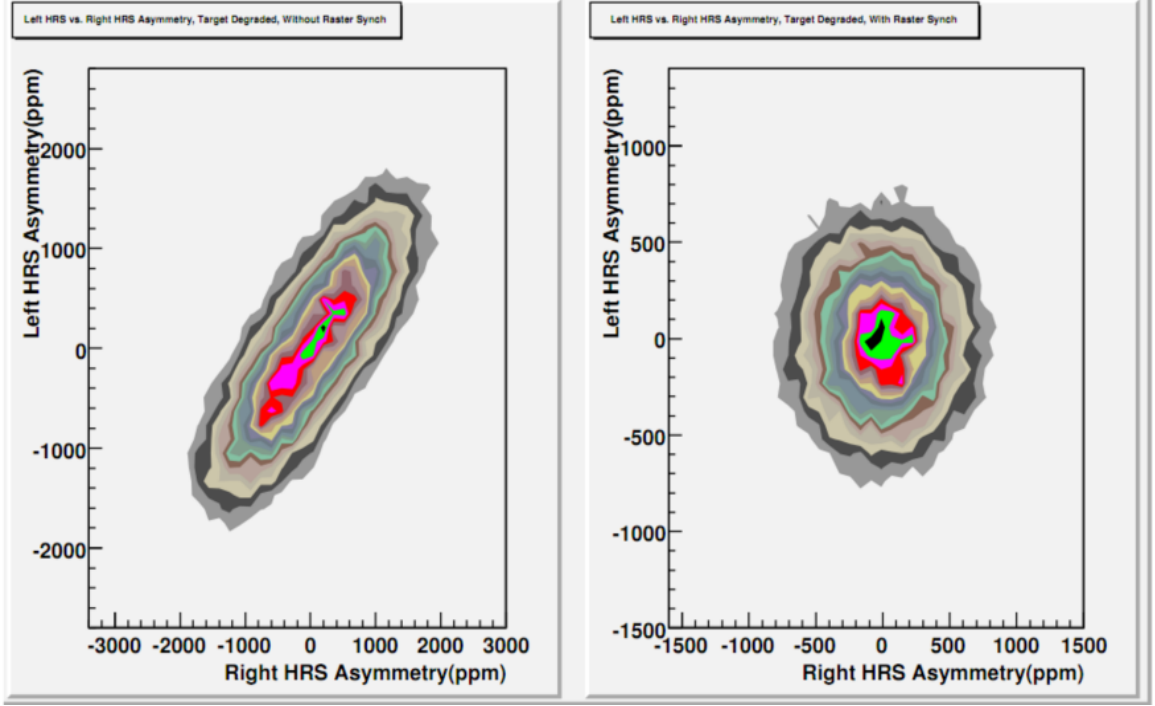
Figure 4.11.2: The effects of the target non-uniformity can be mitigated by synching the raster to the helicity signals. The target non-uniformity are observed as correlation between the parity-violating asymmetries measured between the HRSs because the parity-violating asymmetry is sensitive to the scattering angle. The plot on the left was acquired without the raster synched to helicity signals, and shows a strong correlation between the asymmetries measured between the HRSs. The plot on the right was acquired with identical conditions, but with the raster synched to the helicity signals. This plots shows close to no correlation. Adopted from [Me12].

lower rates at the target center, indicating that the amount of ^{208}Pb at the center of the target is much lower than at the target peripheries. The target was no longer used after the hole appeared on it. The raster scans were acquired with low beam currents on the standard Hall A DAQ with the scattered electrons used as triggers.

PREX rastered the beam over a 4×4 mm^2 area of the target.
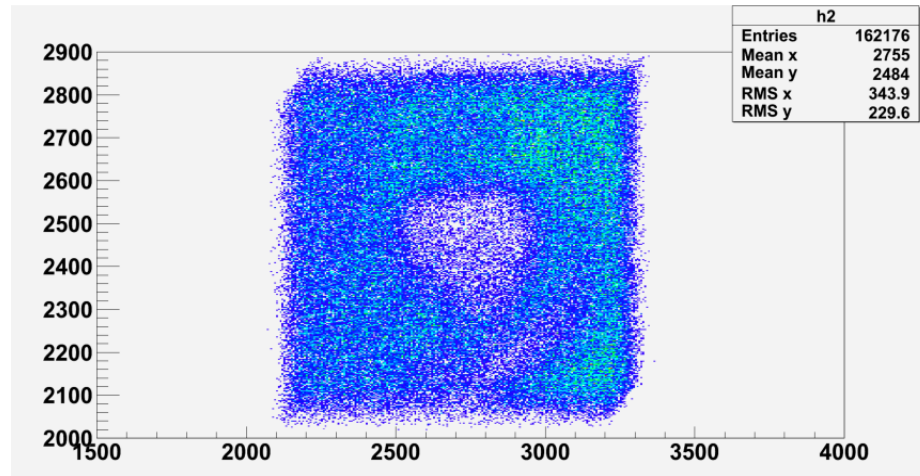
Figure 4.11.3: PREX raster scan acquired on the ^{208}Pb target after exposure to ~ 50 μA beam for 2-3 weeks. The "hole" at the center of the target is due to lower rates at the target center, indicating a much lower fraction of ^{208}Pb at the center of the target compared to the peripheries. Adopted from [Me12].

5

Experimental Method

The experimental techniques used in high-precision parity-violating (PV) experiments have increasingly been refined through successive generations of PV experiments. While some of the techniques pioneered in the early PV experiments have become ubiquitous in the present-day PV experiments, newer techniques have also been developed to achieve much higher precisions required by the next generation of PV experiments. This chapter gives an overview of the experimental methods employed in two such high-precision PV experiments, HAPPEX-III and PREX, and discusses the considerations that drove the employment of these techniques.

HAPPEX-III proposed to measure the PV asymmetry, A_{PV}, to an absolute statistical precision of 550 parts per billion (ppb) and an absolute systematic precision of 310 ppb. These were $\sim 2.5\%$ and $\sim 1.4\%$ relative statistical and systematic precisions respectively on the expected asymmetry of ~ 23.5 ppm. For HAPPEX-III, the A_{PV} is calculated as

$$A_{PV} = \frac{K}{P_b} \frac{(A_{raw} - A_F)}{1 - \sum_i f_i} - \frac{\sum_i A_i f_i}{1 - \sum_i f_i} \qquad (5.0.1)$$

where K is the kinematic (finite) acceptance correction and P_b is the beam polarization. A_F is the helicity-correlated (HC) false asymmetry arising from random fluctuation in the beam trajectory and energy, along with the HC false asymmetry arising from any transverse beam polarization. f_i is the fractional background, and A_i the asymmetry associated with the background. The parameters of Eq. 5.0.1 are discussed further in this chapter, and their measurements and extraction for HAPPEX-III are discussed in Chapter 7.

PREX proposed to measure an A_{PV} of 510 ppb with a statistical precision of 3% (15 ppb) and a systematic uncertainty of 1.1% (5 ppb) for a total uncertainty of $\sim 3.2\%$ (16.3 ppb). For PREX, the A_{PV} is calculated from Eq. 5.0.1 by setting $K = 1$. The measurements and extraction of parameters of Eq. 5.0.1 during PREX, and corresponding A_{PV} evaluation is discussed in Chapter 8. During PREX the finite acceptance correction is not performed via K, because for PREX, unlike for HAPPEX-III, the precise interpretation of A_{PV} requires nuclear model-dependent calculations averaged over the experimental acceptance. Therefore, during PREX, the finite acceptance of the HRSs was carefully characterized by a finite acceptance function, which is described in Section 8.5.

The HAPPEX-III precision requirements were demanding, but PREX precision requirements were much more stringent. Extremely good control of almost all facets of the experiment was required to meet the precision requirements of PREX. Therefore, considerable effort was invested to improve the apparatus and measurement techniques to minimize the uncertainty arising from the terms in the expression of A_{PV}. These techniques and the considerations that drove them are discussed in this chapter.

5.1 Experimental Overview

As described in Chapter 3, the longitudinally polarized electrons were generated at the injector, accelerated to high energies, and transported into experimental Hall A. The electrons were generated in pairs of complementary (right and left) circular polarization (helicity) states, and each helicity-state held constant for the duration of the "helicity-window". The electrons scattered from unpolarized targets located at the center of the experimental hall, and the scattering rate asymmetry between the helicity-states was measured as

$$A_{raw} = \frac{\sigma_R - \sigma_L}{\sigma_R + \sigma_L} \tag{5.1.1}$$

where $\sigma_{R(L)}$ was the right(left) scattering cross-section proportional to the scattering rate corresponding to the right(left) helicity state. The electrons scattered onto two identical high resolution spectrometers (HRSs) that were situated symmetrically about the central beamline. The HRSs focused the elastically scattered electrons 45° vertically out of the scattering plane onto the calorimeter detectors.

The beam parameters such as the intensity, energy, polarization and trajectory at the target were inferred from the responses of various monitoring devices. The beam position monitor (BPM) monitored the beam intensity, energy and trajectory, while the beam current monitor (BCM) monitored the beam intensity. Møller and Compton polarimeters, both located inside the experimental Hall A, monitored the beam polarizations independently of each other. A Mott polarimeter, located at the injector, also provided an independent beam polarization measurement. These monitoring devices are described in Chapter 3, and their measurements discussed in Chapter 7.

As discussed in Section 3.11.1, the asymmetry data were acquired by integrating

the responses of the monitoring devices over each helicity-window. The variables in Eq. 5.0.1 were either directly measured or inferred from previous measurements. The four-momentum transfer, Q^2, which is proportional to A_{PV} as described in Section 2.1, was determined in dedicated measurements. Any uncertainties in the A_{PV} were quantified via dedicated studies. The determination of A_{PV}, and the associated uncertainties are described in Chapters 7 for HAPPEX-III and 8 for PREX.

The asymmetry data were analyzed with a "blinded" analysis, and the data "unblinded" only after data quality was verified. The blinded analysis is discussed later in this chapter in Section 5.14, and the data quality verification is discussed in Section 7.2.1.

5.2 Statistical Uncertainty

The raw asymmetry of each helicity pair, $(A_{raw})_i$, is calculated as

$$(A_{raw})_i = \left(\frac{D_R/I_R - D_L/I_L}{D_R/I_R + D_L/I_L} \right)_i \tag{5.2.1}$$

where $(D_{R(L)})_i$ is the detector signal integrated over the right(left) helicity-window, and $(I_{R(L)})_i$ is the beam intensity integrated over the right(left) helicity-window of the ith helicity-pair. The raw helicity-pair asymmetries are histogrammed, and a raw arithmetic mean, A_{raw}, evaluated. The statistical precision of A_{raw} is limited by the counting statistics as

$$\sigma_{\mathrm{RMS}} = 1/\sqrt{\mathrm{N_{pair}}} \tag{5.2.2}$$

where $\mathrm{N_{pair}}$ ($= \mathrm{N_R} + \mathrm{N_L}$) is the total number of electrons integrated during a helicity pair. The *observed* statistical precision of A_{raw}, $\sigma_{A_{raw}}$, however, is larger than the σ_{RMS} determined by the counting statistics. σ_{RMS} can be broadened by sources of

window-to-window fluctuations such as beam monitor instrument noise, analog-to-digital converter (ADC) bit-resolution, detector pedestal fluctuations, detector energy resolution, and target density fluctuations. So the observed statistical precision of A_{raw} is

$$\sigma_{A_{raw}} = \sigma_{\text{RMS}} + \sigma_{\text{other}} \tag{5.2.3}$$

where σ_{other} is the RMS broadening due to window-to-window fluctuations mentioned above.

The σ_{other} increases the uncertainty in A_{raw}. Therefore, the experimental parameters are optimized to minimize σ_{other}. For instance, the helicity modulation frequency is determined via a combination of target density fluctuations studies and noise studies. The target density fluctuations get smaller relative to counting statistics with increasing modulation frequency because the beam duty cycle is smaller at higher modulation frequencies, resulting in reduced localized beam heating of the target. However, the reduced duty factor also reduces the duty factor of data integration. In addition, random fluctuations get larger at higher modulation frequencies due to counting statistics. Therefore, an optimum modulation frequency with acceptable tradeoff between the target density fluctuations and other noise pickups is established.

It is also desirable to increase the electron flux rate to obtain greater statistical precision in A_{raw} in a reasonably short period of time.

5.3   Data Integration

The method of data acquisition using counting techniques was traditional in nuclear and particle physics experiments. However, at the extremely high scattering rates

desired for precision PV experiments [1], this technique posed unique experimental challenges especially in a precise control of deadtime and pile-up effects in a counting data-acquisition system (DAQ). Using analog integration at a very linear detector signal, as described in Section 3.11.1, circumvents these challenges.

In this integrated mode of data acquisition, the flux at the detector is integrated over a specified length of time during each helicity window. This technique has the advantage that fairly simple detectors such as Čherenkov calorimeters, as described in Sections 3.9.1 and 4.8, can be used. In addition, the data acquisition rate is insensitive to the scattering rates because the DAQ uses an external periodic trigger. As a result, this technique is free of deadtime issues that plague high rate counting experiments. The integrating technique, however, is sensitive to ADC pedestal drifts, detector photo-multiplier tube (PMT) non-linearities, non-linearities in the beam intensity monitor that normalizes the detector signals, and any background contamination of the data.

5.4   Target Non-Uniformity and Density Fluctuations

The extremely high scattering rates in high-precision PV experiments are achieved by increasing the beam intensity and the length of the target along the beam propagation axis. So, during these PV experiments, the beam deposits an enormous amount of heat on the target; the heat load on the target during HAPPEX-III was about 1 KW, while it was much less during PREX. As a result, localized beam heating led to target density fluctuations and non-uniformities despite best efforts to uniformly drain the

---

[1]The cumulative scattering rate at the detectors for HAPPEX-III was ~ 500 KHz at 100 μA beam, and for PREX was ~ 1.0 GHz at 70 μA beam.

heat away from the target via cryogenic cooling. The HAPPEX-III and PREX targets cooling mechanisms are described in Sections 3.6 and 4.7.

The target non-uniformities and density fluctuations increase the window-to-window width of the measured asymmetry, A_{raw}, as described by Eq. 5.2.3, and limit the precision in A_{raw}. During HAPPEX-III, bubbles formed in the cryogenic target due to localized beam heating, altering the density of the target. Therefore, in addition to the cryogenic cooling, the target density fluctuations and non-uniformities were suppressed by optimizing the beam raster size, and maximizing target cryogen flow rate and pressure to suppress these effects. During PREX, thermal damage to the target resulted in a spatially non-uniform target. A raster pattern asynchronous with the helicity window effectively randomized the target thickness between the complementary helicity pairs, and increased the window-to-window of A_{raw}. Therefore, the raster was synchronized with the electronic helicity control signals in order to force the raster to cover precisely the same region of the target between the complementary helicity windows, and mitigate the effects of the thermal damage to the target during PREX.

The raster configurations used during HAPPEX-III and PREX are described in Sections 3.7 and 4.11 respectively.

5.5   Pedestal Fluctuations and Non-linearities

The total integrated signal at the detector, D_{raw}, can be expressed as

$$D_{raw} = D_{flux} + D_{other} \tag{5.5.1}$$

where D_{flux} is the signal resulting from the electron flux at the detector alone, and D_{other} arises due to sources other than the electron flux such as non-linearities in the ADCs and PMTs, ADC pedestal drifts, etc. If $D_{other} \ll D_{flux}$, the asymmetry measured by the detector, A_{raw}, can be expressed as

$$A_{raw} \simeq A_{flux} \left(1 - \left(\frac{D_{other}}{D_{flux}} \right)_{avg} \right). \tag{5.5.2}$$

D_{other}, in addition to modifying the value of A_{raw}, also increases its systematic uncertainty. Only by minimizing the ratio D_{other}/D_{flux} can the effects of D_{other} be suppressed.

D_{other} was minimized via extensive studies of the PMTs and ADCs for non-linearities and pedestal drifts leading up to the experiment. Only those PMTs and ADCs that exhibited these characteristics minimally were used during the experiment. The results of such studies were used to determine the optimal PMT-base combination, and the PMT operating voltage. The ADCs were also operated at the gain settings at which they were minimally non-linear and exhibited minimal pedestal drifts. During the experiment, the data were constantly monitored for non-linearities and pedestal drifts, and necessary adjustments made. Routine opportunistic measurements were also performed during the experiment to measure these effects.

D_{flux} was maximized by operating the PMTs and ADCs in a region where the readout signal was maximum, yet not saturated.

An analogous argument can be made for the monitors with the total integrated signal measured by each monitor given as

$$M_{raw} = M_{flux} + M_{other} \tag{5.5.3}$$

where M_{flux} results from the electron flux alone, and M_{other} arises due to sources other

than the electron flux such as non-linearities in the monitor and readout electronics, pedestal drifts on the ADCs that read out the monitors, etc. M_{other} arising from the ADCs was suppressed by employing techniques similar to the ones discussed above for the ADCs.

5.6 Helicity-Correlated (HC) Beam Parameters

The scattering cross-section depends on the beam parameters such as the beam intensity, energy, position and angle. Therefore, any window-to-window fluctuations in these beam parameters result in helicity-correlated (HC) differences in the scattering rates at the detector, leading to non-zero HC false asymmetries. The HC fluctuations in the beam arise due to differences in the electron beam parameters between the complementary states of the helicity pairs, related the laser light circular polarization used to generate the electrons. The complementary states of laser light polarization were generated by a Pockels Cell (PC). This is discussed in Section 3.3.

The HC false asymmetries potentially contribute a false asymmetry in the measured scattering asymmetry, A_{raw}. Therefore, the HC false effects in the beam, such as the HC false beam intensity asymmetry, A_I, described in Section 3.13, and the HC false beam-position and spot-size differences, described in Chapter 6, were minimized. Methods such as asymmetry feedback, discussed in Section 5.6.1 and slow helicity reversal, discussed in Section 5.6.2 were employed to further suppress or cancel HC beam asymmetries.

5.6.1 Beam Intensity Asymmetry Feedback

The HC beam intensity asymmetry, A_I, as discussed in Section 3.13, is given as

$$A_I = \frac{I_R - I_L}{I_R + I_L} \tag{5.6.1}$$

where $I_{R(L)}$ is the beam intensity integrated over the right(left) helicity window. A_I can be a source of significant systematic uncertainty if left unchecked: the systematic errors due to non-linearities and pedestal drifts in A_I (discussed in Section 5.5), along with the higher-moment HC effects namely HC position and spot-size differences (discussed in Chapter. 6), scale with the magnitude of A_I. Therefore, suppression of A_I is necessary to achieve the precision goals of high-precision PV experiments [1] such as HAPPEX-III and PREX.

A_I was suppressed in source studies at the beginning of both HAPPEX-III and PREX. The asymmetry feedback system provided additional suppression of A_I beyond what was achieved by the source studies. The asymmetry feedback system is described in Section 3.13.

One useful feature of the feedback system is that it not only causes the central value of A_I to converge to zero, but does so faster than one would naively expect them to based solely on the knowledge of the beam jitter and A_I statistics. The A_I scales as $1/N$ instead of the normal statistical $1/\sqrt{N}$ scaling expected in the absence of feedback [Hu04], where N is the number of feedback cycles. Therefore, the feedback mitigates the effects of beam intensity noise even as it protects against significant systematic shifts in A_I.

---

[1] There are techniques such as the use of second Pockels Cell (PC) along the laser's path to directly correct the intensity asymmetry, A_I [Hu04]. However, these techniques does not correct the underlying effects that give rise to HC position and spot-size differences.

5.6.2 Slow-Helicity Reversal

Slow-helicity reversal is a technique that is used to suppress the HC effects arising from the *non-polarization effects*. These are effects that are independent of the laser light polarization such as the HC beam steering that arise due to the PC acting as a voltage activated lens, and are discussed in Section 6.3.1.

During slow-helicity reversal, the helicity of the beam, relative to both the PC HVs and the electronic helicity control signals, are reversed either by inserting an insertable half-wave plate (IHWP) immediately upstream of the PC or via double Wien filter [1]. The schematic of the IHWP and PC setup is described in Sections 3.3 and 6.3. The Wien filter is described in Section 4.2. The slow-helicity reversal changes the sign of A_{PV} relative to the helicity control signals and PC HVs along with the sign of the HC beam parameters that are dependent on the beam polarization. However, the non-polarization effects do not change sign, and these effects can be canceled by averaging data with opposite helicity-reversal states.

The slow-helicity reversal is typically performed multiple times during the experiments, and data evenly divided between the opposite helicity-reversal states.

5.7 Random Rapid Helicity Reversal

During the source studies, HAPPEX-III and PREX, the helicity of the beam is modulated rapidly either at 30, 120 or 240 Hz in order to mitigate the effects of the 60 Hz power-line noise. As is illustrated in Figure 5.7.1, integration at these frequencies cancels the effects of the 60 Hz power-line noise. At 30 Hz helicity reversal rate, two complete 60 Hz cycles are contained in each helicity window, which averages out

---

[1]The double Wien filter was installed after HAPPEX-III for PREX. So the slow helicity reversal via double Wien filter was performed only during PREX. The double Wien filter is discussed in detail in Section 4.2.
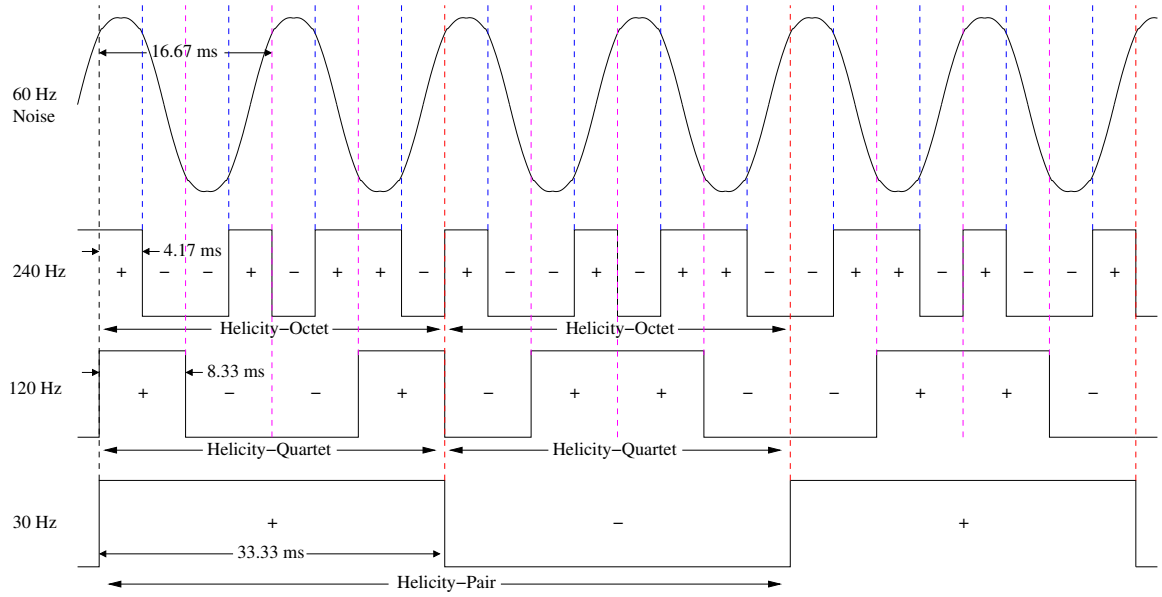
Figure 5.7.1: 60 Hz power-line noise is cancelled with appropriate choice of helicity sequence. At 30 Hz helicity reversal rate, two complete 60 Hz cycles are contained in each helicity window, which averages out on integration. At 120 or 240 Hz reversal rates, only a fraction of the 60 Hz cycle is contained in each helicity window. Therefore, helicity-quartet is used for 120 Hz, and helicity-octet for 240 Hz. These octets and quartets contain complementary measurements at the same phase relative to the 60 Hz noise. As a result, the 60 Hz noise averages out in the helicity-pairs formed from the octets and quartets.

on integration. At 120 or 240 Hz reversal rates, only a fraction of the 60 Hz cycle is contained in each helicity window. Therefore, helicity-quartet is used for 120 Hz, and helicity-octet for 240 Hz, and helicity-pairs formed by averaging the integrated responses over the individual helicity-windows of each quartet and octet. The helicity sequence are discussed in Section 3.4. Since the octets and quartets contain complementary measurements at the same phase relative to the 60 Hz noise, the 60 Hz noise averages out in the helicity-pairs formed from the octets and quartets. Helicity reversal frequencies higher than 240 Hz can also be used with appropriate choice of the helicity-sequence.

The helicity sequence is randomized because a random helicity sequence sup-

presses sensitivities to periodic background noise: randomness avoids locking onto any systematic periodic noise and helps avoid engaging feedback locks that integrate a frequency spectrum over long periods of time. Randomness also minimizes sensitivities to the "history" effects which are known to exist for non-random helicity sequences [Ka07]. For instance, helicity pattern of the preceding windows have been observed to affect the amount of circular polarization of the current helicity state. Randomizing helicity sequence essentially nullifies these effects; they still exist but average to zero [1].

The helicity reversal rate is determined based on the experimental scattering rates and the noise suppression requirements. In general, higher scattering rates yield smaller asymmetry distribution widths, and higher reversal rates yield larger asymmetry distribution widths [2]. Thus, if the scattering rates are extremely high then a higher reversal rate is preferred in order to keep the asymmetry distribution width large enough that the sensitivities to sources of RMS width broadening from sources other than the counting statistics, discussed in Section 5.2, are suppressed. However, at higher reversal rates, one would expect the random noise to increase the RMS width broadening. But the random noise is better suppressed at higher reversal rates, allowing higher reversal rates with well suppressed random noise, and suppressed sensitivity to the non-statistical sources of RMS broadening. A rapid helicity reversal rate also minimizes sensitivities to slow drifts such as changes in temperature which can increase the systematic uncertainties in A_{PV}.

---

[1] The history effects can also be nullified by using periodic helicity patterns or by grouping the helicity windows into appropriately patterns during analysis.

[2] The duty factor of each integration window decreases at higher reversal rates. The counting statistics $(1/\sqrt{N})$ increases the width of measurement, but more measurements are acquired at higher reversal rate. The real gains are in target non-uniformities, and in ADC noise. The noise from the ADC conversion decreases with higher reversal rate because a constant noise is added every integration period.

5.8   Beam Modulation (BM) and Regression

As discussed in Section 5.6, HC asymmetries in beam parameters such as the beam energy (ΔE), position (x and y) and angle (θ_x and θ_y) at the target result in HC false asymmetries, A_{Fb}, due to the sensitivity of the scattering cross-section to these parameters. These can arise due to systematic effects in the polarized electron source, or from random noise, and have to be minimized. Despite best efforts, however, some amount of fluctuations in these beam parameters are unavoidable, leading to a non-zero A_{Fb}. Therefore, the effects of these beam parameter fluctuations were continuously monitored during the experiments, and A_{raw} corrected via two independent techniques: beam modulation (BM) and beam regression.

The BM system performs controlled excursion of the beam in x, y, θ_x, θ_y and ΔE, and measures the responses at the monitors and detectors. These responses, along with the appropriate modulation amplitudes and the HC beam effects are then used to calculate the A_{Fb} correction to A_{raw}. The BM system is described in detail in Section 3.12, and BM corrections discussed in Section 7.3.2.1.

Regression uses a linear regression algorithm that minimizes the correlation of the detector responses to the "natural" beam motion inferred from the responses of the beam monitors, and corrects A_{raw} for A_{Fb}. Regression corrections to A_{raw} are discussed in Section 7.3.2.2.

5.9   Backgrounds

As discussed in Section 3.11.1, the technique of integrating all the flux at the detector results in data contamination, also referred to as the backgrounds in the data. The backgrounds are the detector responses to everything but the electrons that scatter elastically from the target and do not rescatter on its transport path to the detector.

The Hall A HRSs provide excellent suppression of backgrounds, and are described in Section 3.8. Despite this suppression, however, some amount of data contamination is unavoidable. Therefore, the sources of the backgrounds, along with the extent of contamination and its effects on A_{PV} are investigated in dedicated measurements, and A_{PV} corrected. The backgrounds determination, and associated A_{PV} corrections for HAPPEX-III are described in Section 7.6.2, and in Section 8.4.2 for PREX.

5.10   Beam Polarization

The parity-violating asymmetry, A_{PV}, needs to be normalized by the beam polarization, P_b, as given in Eq. 5.0.1. This normalization is necessary because P_b is usually less than 100%, and as a result, any systematic uncertainties in the determination of P_b increases the systematic uncertainty in A_{PV}. Therefore, considerable effort is spent to accurately measure P_b with high precision.

P_b was measured with three independent polarimeters during HAPPEX-III and PREX. Møller and Compton polarimeters, both located inside Hall A, measured P_b close to the target. The Mott polarimeter, located at the injector, measured P_b at the injector. Results from the Møller and Compton polarimeters were used to calculate A_{PV} for HAPPEX-III and PREX. The Mott polarimeter was used to configure and optimize beam polarization state in the injector.

The Mott, Møller and Compton polarimeters are described in Section 3.14. The beam polarization measurements during HAPPEX-III are discussed in Section 7.6.1, and during PREX are discussed in Section 8.4.1.

5.11 Transverse Asymmetry

As mentioned in Section 5.1, longitudinally polarized electrons were used to form the scattering rate asymmetry between the helicity-states, A_{raw}. Any transverse polarization present in the electrons results in a transverse asymmetry, $A_T \cos \phi$ where ϕ is the HRSs angle. For HRSs aligned symmetrically about the central beamline, this azimuthally dependent asymmetry is about the same size, but of opposite sign between the two HRSs. However, imperfections in the HRS symmetry results in imperfect cancellation of $A_T \cos \phi$ between the two HRSs, resulting in a false asymmetry, A_{FT}.

$A_T \cos \phi$ was measured in dedicated studies with a fully transverse beam during PREX, and estimates of the geometric cancellation were used to place an upper limit on the A_{FT}. During HAPPEX-III, A_{FT} was estimated by extrapolating earlier measurements performed during HAPPEX-II and G0 to provide an upper limit for this effect. The results of A_{FT} for HAPPEX-III are discussed in Section 7.3.3, and for PREX is discussed in Section 8.2.4.

5.12 Four-Momentum Transfer Squared (Q^2)

As described by Eqs. 2.1.8 and 2.1.9 in Section 2.1, A_{PV} is proportional to the four-momentum transfer squared, Q^2, and interpretation of A_{PV} requires knowledge of Q^2. Therefore, Q^2 was measured in dedicated low current runs at regular intervals during HAPPEX-III and PREX. Due to the Q^2 dependence of A_{PV}, the uncertainties in Q^2 increases the systematic uncertainty in A_{PV}. Therefore, considerable effort was made to suppress the systematic uncertainties in Q^2. The Q^2 measurements, and the associated systematic uncertainties are discussed in Section 7.7 for HAPPEX-III, and in Section 8.6 for PREX.

5.13   Finite Acceptance

The scattering cross-section and the corresponding A_{PV} vary across the finite-acceptance of the HRSs, and the detector measures an average of the flux across this acceptance (weighted by the extent of acceptance at each point along the acceptance). In addition to this, energy losses such as ionization and Bremsstrahlung losses in the electrons convolute the experimental asymmetry, A_{raw}, over a range of Q^2 even at a particular HRS acceptance. Thus, any measurement of A_{raw} is effectively a measurement of A_{raw} averaged over a range of Q^2. These finite-acceptance effects on A_{raw} need to be appropriately accounted for in order to extract a theoretically interpretable value for A_{PV}.

During HAPPEX-III, A_{raw} was normalized with a kinematic acceptance factor, K, to correct for the effect of finite-acceptance. The dominant Q^2 behavior of A_{PV} lies in a leading factor of Q^2, and in the well known electromagnetic form-factors (FFs) of the proton and neutron. Over the small range of acceptances, it is possible to de-convolute these effects with negligible model dependence. K is the ratio of A_{PV} evaluated at the finite-acceptance averaged Q^2 measured by the detector to A_{PV} averaged over the finite-acceptance but evaluated at the Q^2 at the scattering vertex. The finite-acceptance correction for HAPPEX-III is described in Section 7.6.3.

During PREX, A_{PV} is sensitive to proton and neutron distributions in the nucleus, and the behavior over the HRS acceptance is potentially significantly model dependent. The finite-acceptance effects were accounted for as following: the HRS acceptance was characterized with an acceptance function $\epsilon(\theta)$ that provided the probability for an electron to reach the detector after elastically scattering from ^{208}Pb as a function of scattering angle θ. The quoted A_{PV} was not corrected for kinematics. The theoretical asymmetry in any model can be integrated over the HRS acceptance

using this acceptance function, in order to compare it to the A_{PV} measured during PREX, and extract the neutron radius, R_n [1]. The finite-acceptance correction for PREX is described in Section 8.5.

5.14 Blinded Asymmetry Analysis

A "blinded" analysis of the raw asymmetry, A_{raw}, is performed in which the true value of A_{raw} is hidden by introducing a finite randomly selected offset:

$$A_{\text{blind}} = A_{raw} + (\pm 1)A_{\text{offset}} \tag{5.14.1}$$

where A_{offset} is a random offset whose value is bounded to within $\pm 5\sigma$ of the expected A_{raw} precision. The $\pm$ sign adjusts the sign reversal in A_{raw} resulting from slow-helicity reversal discussed in Section 5.6.2. A blinded analysis hides the true value of A_{raw}, and prevents introduction of biases during data quality verification, and analysis.

During HAPPEX-III and PREX, the blinding was initiated before the beginning of asymmetry data acquisition. The blinding was performed via the parity-analyzer software (PAN) [PAN]. All the raw data was recorded without any manipulation for blinding; only the output of the asymmetry values from the analysis code were reported as blinded values. The asymmetry data were unblinded only after the data quality verification and analysis were completed.

---

[1]In fact, the extraction of R_n over the acceptance is only weakly model dependent, but this is an empirical observation based on the existing models. The possibility that other models would predict very different behavior of A_{PV} with Q^2 requires this approach to minimize the model-dependence in the way results from PREX are quoted.

6

Polarized Electron Source

6.1   Introduction

HAPPEX-III and PREX proposed the measurement of parity-violating asymmetries of $10^{-5} - 10^{-6}$ up to an accuracy of 10^{-8}. To achieve this accuracy, the polarized electron source needs to produce electrons in the right- and left-helicity polarization states with minimal right-left helicity-correlated (HC) asymmetries, A_{LR}^{beam}, that result from right-left differences in beam parameters such as the beam intensity, position, angle, spot-size and shape, and energy. The polarized electrons were generated from a GaAsP photocathode by using circularly polarized laser light, with the electron polarization state determined by the laser light's polarization state. Therefore, the generation and transport of the circularly polarized light through a carefully designed optical system were investigated in dedicated source studies, and several mechanisms that generate A_{LR}^{beam}'s identified. This chapter discusses these studies.

The source studies were performed by making measurements on both the laser light and the electron beam. The initial phase of the studies was performed with the laser light alone on the laser table. The primary objectives of the laser-table

studies were Pockels Cell (PC) alignment and optimization of the PC voltages. A PC is a uniaxial crystal which behaves like a retardation plate when appropriate voltage is applied along its birefringent axis. The circularly polarized laser light that generated the polarized electrons was generated using a PC operated at its quarter-wave voltage. Therefore, any misalignment in the position and voltages of the PC resulted in imperfect circular polarization that typically lead to a significant A_{LR}^{beam}. Mechanical effects associated with rapidly switching the high-voltage (HV) on the PC could also result in A_{LR}^{beam}.

The electron beam source studies were performed after the laser-table source studies, with the PC voltages and position well determined. The electron beam source studies facilitated further suppression of the effects of down-stream optical elements in the laser's path, as well as effects related to the photocathode itself. These studies primarily involved further optimization of the PC positions and the optical elements in the laser's path down-stream of the PC.

6.2 Polarized Electron Source (Injector) Setup

The schematic of the polarized electron source (injector) setup at JLab is presented in Figure 6.2.1, and is discussed in some detail in Section 3.3. Thus, only details relevant to the source studies are discussed in this section.

The injector setup included three different lasers, one for each experimental hall. The source studies, however, were performed with only the Hall A laser because both HAPPEX-III and PREX were performed in experimental Hall A. The Pockels Cell labeled in Figure 6.2.1 as the IA cell was unplugged from its power source, and not operational for the majority of these studies, nor during HAPPEX-III and PREX. Some of the initial electron beam data, however, were acquired with the IA operational
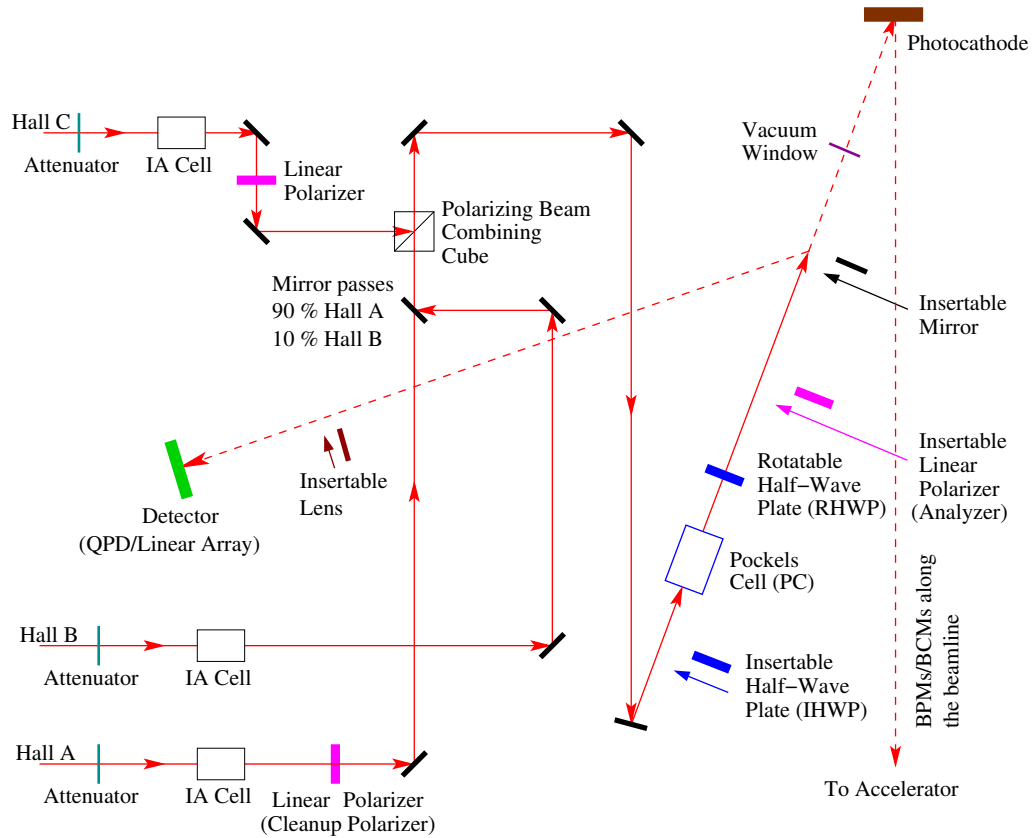
Figure 6.2.1: The schematic of the injector setup at JLab. The Pockels Cell (PC) was used to convert linearly polarized light into circularly polarized light. The insertable mirror was used to guide the beam onto a quad-photodiode (QPD) or a linear array-photodiode (LAPD) detector during laser table studies. The insertable lens and the insertable linear polarizer were only used during laser table studies. The insertable mirror and the insertable linear polarizer were retracted during the electron beam source studies and the experiments. The insertable half-wave plate (IHWP) was inserted and retracted during laser table studies, electron beam source studies and the experiments.

(more on this later).

The Hall A laser passed through a "cleanup polarizer" (a linear polarizer) that ensured that the laser light polarization was either horizontal or vertical. The laser light was then guided onto the PC by a series of dielectric mirrors that were minimally sensitive to the laser light polarization. The PC was mounted with its longitudinal axis along the direction of beam propagation with its fast (or slow) axis at 45° to the

analyzing axis of the cleanup polarizer. In this orientation, the polarization vector of the laser light was incident at 45° to the fast (or slow) PC axis. The PC was operated at its quarter-wave voltage ($V_{\lambda/4}$) that was modulated between $+V_{\lambda/4}$ and $-V_{\lambda/4}$, by helicity logic pulses, to generate circularly polarized laser light in complementary helicity states. The helicity pulses were generated by the helicity generator (HG), as is described in Section 3.4. In general, the light emerging from the PC is slightly elliptic in character, and one can describe such light as containing a small amount of *residual linear polarization.* A rotatable half-wave plate (RHWP), immediately downstream of the PC, was used to rotate the polarization axis of the residual linear polarization.

Again referring to Figure 6.2.1, the dielectric insertable mirror, insertable linear polarizer (referred to herein as the analyzer), insertable lens, quad-photodiode (QPD) detector and the linear-array photodiode (LAPD) detector were only used during the laser-table studies. The QPD and LAPD detectors are described in Appendix C.1 and C.2. The insertable mirror guided the laser light onto the QPD or LAPD detector. The analyzer amplified the effects of any residual linear polarization present in the laser light because it transmitted 100% of linearly polarized laser light along one axis and 0% along the complementary axis. The photocathode's "analyzing power" was only $\sim 4\%$ compared to 100% of the analyzer [1]. The insertable lens was cylindrical and expanded the laser light across the array of photodiodes (arranged in a straight line) of the LAPD detector. The insertable lens was only used with the LAPD detector. The analyzer and the insertable mirror were retracted during the electron beam source studies and the experiments. The insertable half-wave plate (IHWP) was used to perform slow-helicity reversals, a process in which the sign of essentially all *polarization effects* on the laser light, discussed in Section 6.3, were reversed.

---

[1]The "analyzing power" is discussed further in Section 6.3.

The slow-helicity reversal is discussed in Section 5.6.2. The IHWP performed this reversal by rotating the polarization axis of the linear laser light incident on the PC by 90°. The IHWP did not affect the *non-polarization effects* present on the laser light. The polarization and non-polarization effects are discussed in Section 6.3. IHWP insertion and removal was a useful diagnostic tool, and was also used to cancel the *non-polarization effects* during the experiments.

Not shown in Figure 6.2.1 are the beam position monitors (BPMs) and beam cavity monitors (BCMs) present along the electron beam line that monitored various beam parameters during the electron-beam source studies and the experiments. The BPMs and BCMs are described in Section 3.5.

6.3 Formalism

6.3.1 Helicity-Correlated Beam Asymmetries (HCBAs)

Following the prescription of Humensky et al. [Hu04], the phase shift introduced by the PC on the laser light can be expressed as

$$\delta^R = -\left(\frac{\pi}{2} + \alpha\right) - \Delta; \qquad \delta^L = +\left(\frac{\pi}{2} + \alpha\right) - \Delta \qquad (6.3.1)$$

where $\delta^{R(L)}$ refers to the phase shift associated with the right(left) helicity light. The deviations in the phase shift from a perfect $\pi/2$ phase shift are parametrized by α and Δ. α is *symmetric* meaning that a nonzero α results in residual linear polarization along the same axis (x and y) for both helicity states. Δ is *anti-symmetric*, and results in residual linear polarization along complementary axes between the two helicity states light, as illustrated in Figure 6.3.1.

If an analyzer, with transmission coefficients T'_x and T'_y along some axes x' and
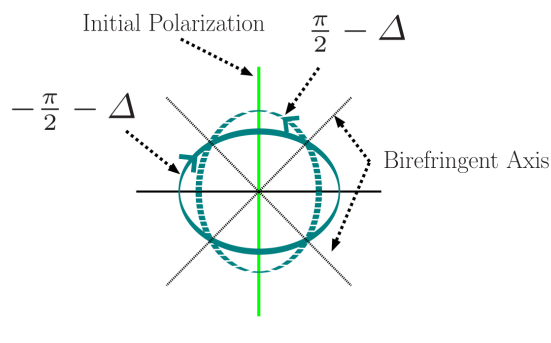
Figure 6.3.1: Δ-phase is *anti-symmetric*, and results in residual linear polarization along complementary axis between the two helicity states light. Reproduced from [Pa07].

y' [Hu04], is introduced immediately downstream of the PC in Figure 6.2.1, the intensity of transmitted light depends on the laser light phase shift as

$$I^{R(L)} \propto \epsilon T \cos(\delta^{R(L)}) \cos(2\psi) \qquad (6.3.2)$$

where $\epsilon = T'_x - T'_y$, $T = (T'_x + T'_y)/2$, and ψ is the angle subtended between x' and the horizontal axis. The difference in the transport efficiency along x' and y' is taken to be small ($\epsilon \ll T$). Due to differences in the phase shift introduced by the PC in the two helicity states light, an asymmetry in the intensity of transmitted light in the two helicity states, also referred to herein as the helicity-correlated beam intensity asymmetry (HCBA), arises. The HCBA can be expressed as

$$Aq = \frac{I^R - I^L}{I^R + I^L} = -\frac{\epsilon}{T}[\Delta \cos(2\psi)]. \qquad (6.3.3)$$

Here, it is assumed that $\Delta \ll 1$ and $\alpha \ll 1$. This assumption allows the use of small-angle approximation, and only first-order terms in phase shifts and ϵ are retained in the above equation [Hu04]. In the discussion that follows, $\frac{\epsilon}{T}$ is often referred to as the "analyzing power", and x'/y' as the "analyzing axes". Notice that the *symmetric*
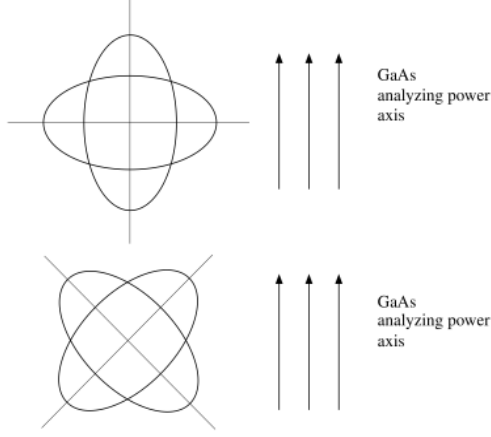
Figure 6.3.2: The rotatable half-wave plate (RHWP) located immediately down-stream of the Pockels Cell (PC) rotates any linear residual polarization present on the laser light. Therefore, RHWP is used to minimize the helicity-correlated beam intensity asymmetry (HCBA) arising from Δ-phase interaction with the analyzing-power of the photocathode. Reproduced from [Ka07].

phase shift, α, cancels and only the *anti-symmetric* phase shift, Δ, appears in the equation above.

If a half-wave plate (RHWP in this case) and an additional retardation plate downstream of the RHWP is inserted between the PC and the analyzer, the HCBA of Eq. 6.3.3 becomes [Hu04] [1]

$$Aq = -[\underbrace{\frac{\epsilon}{T}\beta\sin(2\rho - 2\psi)}_{\text{offset}} + \underbrace{\frac{\epsilon}{T}\gamma\sin(2\theta - 2\psi)}_{2\theta} + \underbrace{\frac{\epsilon}{T}(\Delta - \Delta^0)\cos(4\theta - 2\psi)}_{4\theta}]. \quad (6.3.4)$$

The parameter β is a small phase shift induced by the retardation plate present between the RHWP and the analyzer, and ρ is the retardation plate's orientation angle with respect to the horizontal. γ is the retardation due to the RHWP's deviation from perfect half-wave (π) retardation, and θ is the angle subtended by the RHWP's fast-axis to the horizontal. Δ^0 is introduced to account for phase shift deviations from

---

[1] θ and ψ in Eq. 6.3.4 are interchanged from the notation of Humensky et al [Hu04] to be consistent with the notation used in the fit equations presented in this chapter.

perfect $\pi/2$ phase shift arising from residual birefringence of the PC, due to latent stress in the crystal [Pa07][1]. The rotation of residual linearly polarized light by the RHWP is illustrated in Figure 6.3.2.

In the formalism presented so far, an insertable half-wave plate (IHWP), when inserted *upstream* of the PC with its fast-axis at 45° to horizontal in the setup of Figure 6.2.1, reverses the sign of each of the terms in Eq. 6.3.4. Therefore, the effects contained in Eq. 6.3.4 are referred to as the *polarization effects*: these are the HC effects that depend on the laser light polarization. The IHWP insertion rotates the polarization axis of the linear laser light incident on the PC by 90°, and effectively interchanges the HC effects between the right and left helicity states respectively, reversing the sign of the HCBA described by Eq. 6.3.4 [2]. This technique of reversing the sign of the polarization effects is referred to as the slow-helicity reversal. The slow-helicity reversal can also be performed via a Wien filter as discussed in Section 5.6.2.

In addition the polarization effects, the HCBAs also arise from *non-polarization effects*. These are effects that *do not* reverse sign upon IHWP insertion. These are static effects independent of the laser light polarization such as the HC beam steering that arises due to the PC acting as a voltage-activated lens as illustrated in Figure 6.3.3. This "lensing effect" arises because the PC, in addition to being an electro-optic device, is also piezoelectric in nature, and the HVs applied to the PC deforms its shape. As a result, the PC $\pm\lambda/4$-wave voltages that generate complementary states of the laser light helicity, also may generate accompanying shape changes in the PC crystals, steering the beam in a HC manner. Since the non-polarization

---

[1]In general, Δ^0 arises from the optical elements present between the Pockels Cell (PC) and the rotatable half-wave plate (RHWP) along the laser's path, including the PC itself. In the schematic of Figure 6.2.1, this optical element is the PC alone.

[2]The effects of imperfect linear polarization from upstream of the IHWP do not reverse sign, but with the use of cleanup polarizer, the input linear polarization is essentially perfect entering the system.
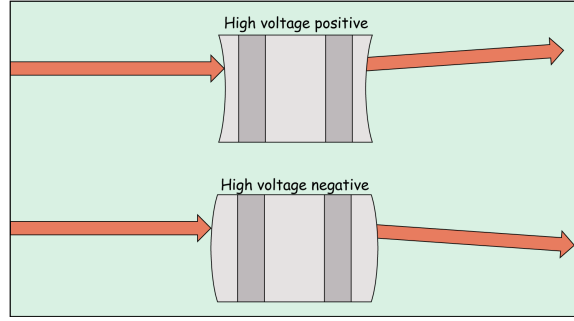
Figure 6.3.3: The high-voltage (HV) applied across the Pockels Cell (PC) causes the PC to steer the beam in a helicity-correlated (HC) manner. The $+ve/-ve$ HVs generate circularly polarized laser light in right/left helicity state. The PC beam steering is a *non-polarization effect* i.e. this effect is independent of the laser light polarization. The non-polarization effects also result in helicity-correlated beam asymmetry (HCBA).

effects are unaffected by IHWP reversal, these effects cancel when data with opposite IHWP states are averaged.

The formalism presented so far adequately characterizes the effects of residual linear polarization present in the laser light for the schematic presented in Figure 6.2.1. However, Figure 6.2.1 includes two different setups: the laser table source studies setup and the electron beam source studies setup, that were used during the laser table source studies and the electron beam source studies respectively. The individual terms of Eq. 6.3.4 resulted from effects specific to each setup. Therefore, the sources of some of these effects overlapped between the two setups due to the same experimental apparatus, while some of the effects contained in Eq. 6.3.4 resulted from different sources between the two setups. These terms, and their sources for the two setups are summarized in Table 6.1.

The parameters ϵ, T and ψ largely arise from the photocathode during electron beam studies; the photocathode itself acts in a manner analogous to an asymmetric transport element, albeit with a much weaker analyzing power of only $\sim 4\%$ compared to 100% when a polarizer was used as an analyzer. The determination of photocathode

	Electron Beam	Laser Table (Analyzer)	Laser Table (No Analyzer)
ϵ, T, ψ	Photocathode	Analyzer	Mirror, Lens, Photodiode
β, ρ	Vacuum Window	–	Mirror, Lens
γ, θ	RHWP	RHWP	RHWP
Δ, Δ^0	Pockels Cell (PC)	Pockels Cell (PC)	Pockels Cell (PC)

Table 6.1: The sources of various terms appearing in Eq. 6.3.4 for laser table studies performed with the analyzer in the laser's path (Laser Table (Analyzer)), without the analyzer in the laser's path (Laser Table (No Analyzer)), and the electron beam studies (Electron Beam) are presented above. The schematic of the source studies is presented in Figure 6.2.1. During the laser table studies, the insertable mirror was inserted in the laser's path, and the *laser light* was observed in either the quad-photodiode detector (QPD) or the linear-array photodiode detector (LAPD). The analyzer was inserted in the laser's path as needed, and the insertable lens was only used with the LAPD. During the electron beam studies, the insertable mirror was retracted, and laser light generates circularly polarized *electrons* that were observed via the beam monitors, beam current monitors (BCMs) and beam position monitors (BPMs).

analyzing power is discussed in Appendix C.4 and is related to the different quantum efficiencies for photoemission along different axes in the strained GaAsP crystals. The parameters ϵ, T and ψ arise from the analyzer during the laser table studies when the analyzer is present in the laser's path. The optical elements downstream of the PC (insertable mirror, insertable lens and photodiodes of QPD and LAPD) act as the analyzing elements during the laser table studies performed without the analyzer in the laser's path. The analyzing power of these elements, however, is negligible compared to that of the analyzer.

During the electron beam source studies, the parameters β and ρ arise from the vacuum-window, and are important during production running of our parity experiments. During the laser table studies performed with the analyzer in the laser's path, β is essentially zero because there is no optical element between the RHWP and the analyzer. During the laser table studies performed without the analyzer in the laser's path, β and ρ arise from the insertable mirror and insertable lens, with these terms

dominated by the insertable mirror effects.

The parameter Δ arises from the PC, and γ and θ arise from the RHWP for both the electron beam and laser table studies. In general, Δ^0 arises from the optical elements present between the PC and the RHWP, including the PC itself. In the schematic of Figure 6.2.1, this optical element is the PC alone.

6.3.2   PITA Effects

The phase shift induced by the PC in each of the helicity states can be expressed as

$$\delta^{R(L)} = \frac{\pi}{2V_{\lambda/4}^{R(L)}} V_{PC}^{R(L)} \tag{6.3.5}$$

where $V_{PC}^{R(L)}$ is the voltage applied across the PC to generate circularly polarized laser light in right(left) helicity state. The quantity $V_{\lambda/4}^{R(L)}$ is the voltage required for quarter-wave ($\lambda/4$) phase retardation of the laser light of wavelength λ, to generate right(left) circularly polarized light. The parameter Aq, using Eq. 6.3.3 and the above equation, can be expressed as

$$Aq = -\frac{\epsilon}{T}\frac{\pi}{2V_{\lambda/4}}\cos(2\psi)(\Delta V) = -k(\psi)(\Delta V). \tag{6.3.6}$$

where $V_{\lambda/4} = \frac{1}{2}(V_{\lambda/4}^R + V_{\lambda/4}^L)$, $\Delta V = \frac{1}{2}(\Delta V^R - \Delta V^L)$, and $\Delta V^i = (V_{PC}^i - V_{\lambda/4}^i)$ with i indicating either right(R) or left(L) helicity state. ΔV^i is zero only when the PC voltage, V_{PC}^i, is matched to the $\lambda/4$-voltage, $V_{\lambda/4}^i$. Eq. 6.3.6 is sometimes referred to as the Polarization Induced Transport Asymmetry (PITA) [Ca89] equation, and $k(\psi)$ as the PITA slope. The PITA equation characterizes the sensitivity of a given optical system and the analyzer to any residual linear polarization present in the laser light. At a given orientation of the analyzer, ψ, both Aq and V_{PC} are easily measurable,
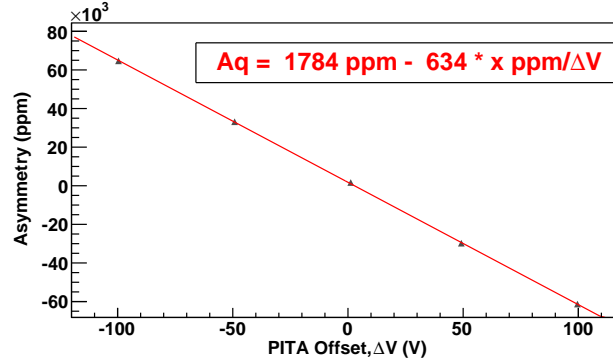
Figure 6.3.4: A typical PITA scan plot is presented above. The helicity-correlated beam intensity asymmetry (HCBA) is plotted on the y-axis, and PITA offset voltages are plotted on the x-axis. The data presented above were acquired at PITA offset voltages of 0, ±50 and ±100 V. A PITA offset voltage of +100 V is a change of +100 V in the helicity state corresponding to $+V_{PC}$ and -100 V in the helicity state corresponding to $-V_{PC}$. The slope of the straight line fit of the data points, as displayed above, is referred to in this work as the "PITA-slope". The y-intercept of this fit, along with the PITA-slope determine the PITA offset voltage at which the HCBA is zero. For the data presented above, the PITA offset voltage is $+1784/634 \sim +3$ V, meaning that the HCBA will be zero when $+3$ V is *added* to *both* $+V_{PC}$ and $-V_{PC}$.

allowing adjustments of Aq via PC voltage adjustments.

To determine the ideal voltage at which to run the PC, as well as the sensitivity of Aq to changes in the voltage, a "PITA scan" is performed in which Aq is measured as a function of V_{PC}. A typical PITA scan is shown in Figure 6.3.4. In a PITA scan, the PC voltages are adjusted *anti-symmetrically* and Aq measured at each of these voltages. An anti-symmetric voltage adjustment involves increasing the magnitude of the voltage for one helicity state and decreasing the magnitude of the voltage for the other helicity state by a similar amount. For instance, an anti-symmetric $+100$ V adjustment from $V_{\lambda/4} = \pm 2.4$ kilo-voltages (KVs), corresponding to the particular PC used during these studies, would be voltages of $+2.5$ KV for one helicity state and -2.3 KV for the other. These anti-symmetric voltage adjustments are referred to, herein, as the "PITA offset" voltages. The Aq and PITA offset voltages are plotted

along the y- and x-axes respectively in a PITA scan plot, and a straight line fit of the data points performed. The slope and offset of this fit are often referred to as the "PITA slope" and the "PITA offset" [Ca89]. The PITA slope and PITA offset can be used to calculate the PITA offset voltage where Aq will be zero.

In the laser table setup of Figure 6.2.1 with the analyzer present on the laser's path, when $\psi = 0°$, i.e. the analyzer's polarization axis is either along the horizontal or vertical (and at $45°$ to the PC fast/slow-axis), the PITA slope is ≈ 650 ppm. When the analyzer is present on the laser's path $\frac{\epsilon}{T} \approx 1$. If $\psi = 45°$, i.e. the analyzer's polarization axis is at $45°$ to the horizontal (and parallel to the PC fast/slow-axes), the PITA slope is 0 ppm.

6.3.3   Phase Gradients

The discussion so far has centered on non-zero phase-offsets that lead to various non-zero terms in the expression of HCBA in Eq. 6.3.4. Now, if these phase-offsets are spatial varying, then the HCBA will also have spatial dependence, resulting in, what are effectively, HC shifts in the beam centroid. The effect of a spatially varying Δ-phase on the phase across the beam spot is illustrated, with exaggeration, in Figure 6.3.5. The manner in which this leads to a HC shift in beam centroid is illustrated in Figure 6.3.6.

A spatially varying HCBA opens the possibility of higher-moment HC effects such as the HC position differences, and HC spot-size and shape differences. A linear Δ-phase gradient results in a shift of the beam centroids in opposite directions between the two helicity states, resulting in a HC position difference. This is the effect illustrated in Figure 6.3.6. The HC position difference is often referred to as the "first-moment" effect, similar to the moments of a statistical distribution [Hu04], because it arises from a linear Δ-phase gradient. A curvature in the Δ-phase gradient
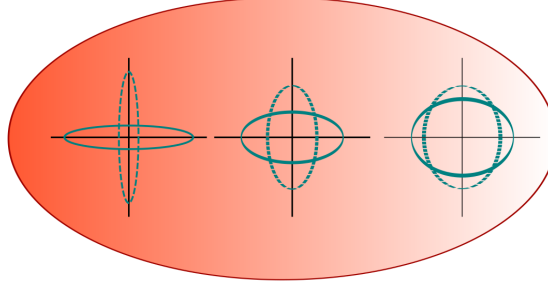
Figure 6.3.5: A phase gradient across the beam spot results from a spatially varying Δ-phase. The size of Δ-phase, and hence, the amount of residual linear polarization, is larger on the left relative to the right, resulting in a helicity-correlated (HC) shift in the beam centroid. Reproduced from [Pa07].

is related to the second-moment effects that result in HC beam spot-size and shape differences.

The relationship between the different moments of the HC effects are evident in the data presented in Figure 6.3.7. These are plots acquired by physically moving the PC across the laser beam. If there is a gradient in the Δ-phase along the face of the PC, we would expect, and indeed observe a change in Aq, as is seen in the top plot of Figure 6.3.7. The second and third plots represent the associated first- and second-moment effects along x, Dx and $Drms$ respectively. In these plots, Dx roughly tracks with the first-derivative of Aq: Dx is zero at the extrema of the Aq curve, and maximum when the slope of the Aq curve is maximum. Similarly, $Drms$ tracks with the first-derivative of Dx, with $Drms$ of ~ 0 corresponding to the extrema of Dx curve, and $Drms$ extrema corresponding to the maximum slopes of the Dx curve.

The HC position differences along x (Dx) and y (Dy) can be expressed as

$$Dx \propto \frac{\partial}{\partial x} Aq; \qquad Dy \propto \frac{\partial}{\partial y} Aq. \qquad (6.3.7)$$
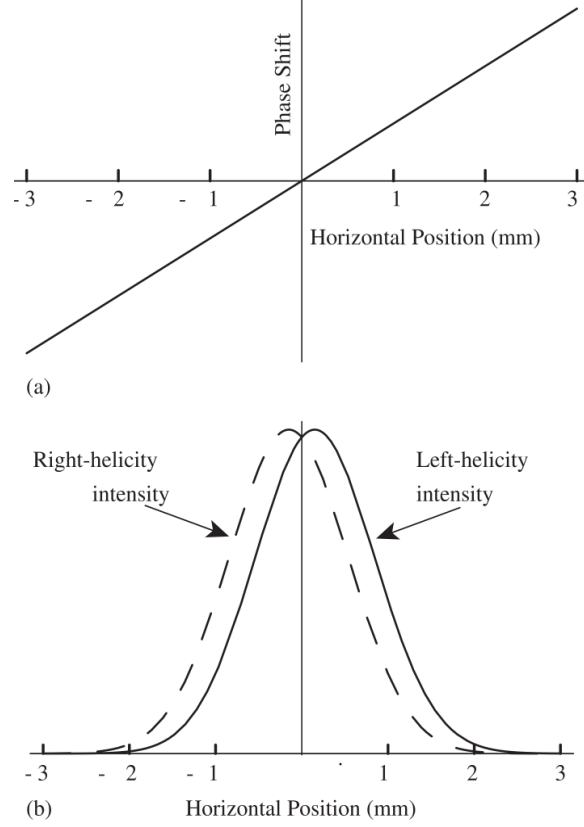
Figure 6.3.6: A spatially varying Δ-phase leads to a spatially varying helicity-correlated beam asymmetries (HCBA) in Eq. 6.3.4, which when analyzed, results in helicity-correlated (HC) shift of the beam centroid giving rise to HC position differences. A linear gradient in Δ-phase is presented on the top plot. The resulting intensity profiles, assuming a Gaussian profile, are presented for right-left helicity beams. Reproduced from [Hu04].

The associated HC spot-size and shape differences are given by

$$Drms_x \propto \left(\frac{\partial}{\partial x}\right)^2 Aq; \qquad Drms_y \propto \left(\frac{\partial}{\partial y}\right)^2 Aq. \qquad (6.3.8)$$

Analogous to the spatial variations in Δ-phases, $\frac{\epsilon}{T}$, β, γ and Δ^0 in Eq. 6.3.4 could also vary spatially across the beam spot, resulting in HC higher-moment effects as well.
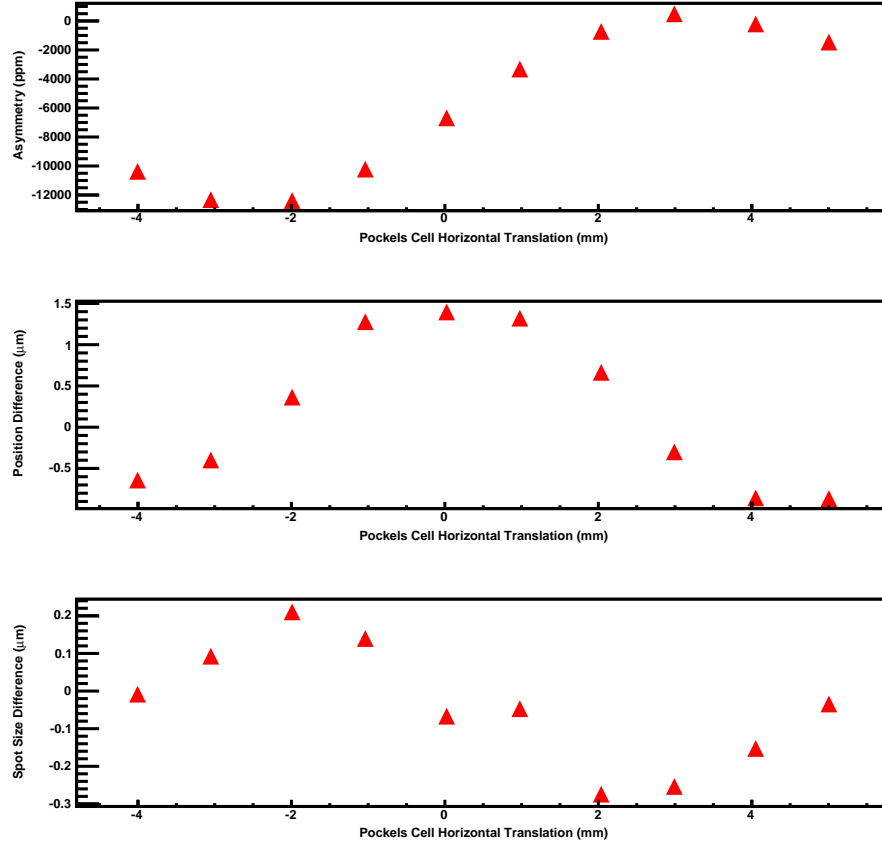
Figure 6.3.7: The data acquired by scanning the PC across the face of the beam is presented above, to illustrate the relationship between different moments of the HC effects. This data was acquired with the LAPD detector oriented vertically, and the analyzer present in the laser's path in Figure 6.2.1. The top plot represents the zero-moment effect: helicity-correlated beam asymmetry (HCBA), Aq. The second plot represents the first-moment effect along x: helicity-correlated (HC) position difference, Dx. The third plot represents the second-moment effect along the same axis: HC beam spot-size and shape differences, $Drms$. Dx tracks with the first-derivative of Aq and $Drms$ with the first-derivative of Dx (or equivalently, second-derivative of Aq). Dx ($Drms$) is zero at the extrema of the Aq (Dx) curve, and the extrema in Dx ($Drms$) correspond to the maximum slopes in the Aq (Dx) curve.

6.3.4   HCBA dependence on PC angular misalignment

The formalism presented so far assumes that the laser light is incident on the PC parallel to the symmetry axis (optic axis) of PC. However, the laser light is usually incident at an angle to the PC symmetry axis resulting in phase gradients. In fact,
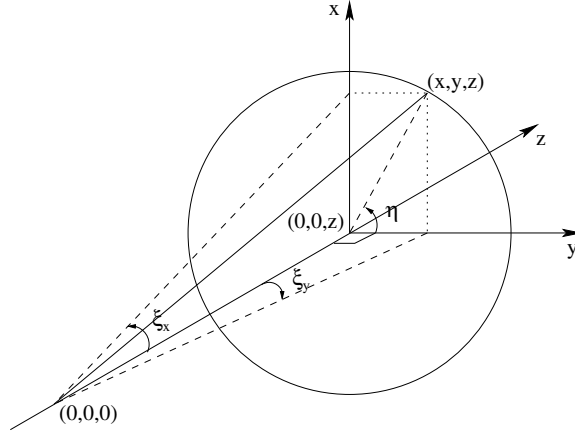
Figure 6.3.8: The ray of light incident on an optical material at an angle ξ. η is the orientation of the material's fast-axis from y-axis.

the angular misalignment of the PC relative to the laser light is the largest source of phase gradients, and results in large HC effects of all moments discussed in the previous section. In order to investigate the HCBA due to angular misalignment of the PC, I note that the HCBA arising from a retardation plate that induces a phase shift ζ, and has its fast-axis at an angle η from the horizontal can be expressed as

$$Aq = -\frac{\epsilon}{T}\zeta \sin(2\eta - 2\psi) \tag{6.3.9}$$

where ψ is the angle subtended by one of the analyzing axes, x', to the horizontal, as above. When a ray of light propagates along the optic axis of a PC in the absence of applied voltage, there are in principle, no birefringent effects. When the ray makes an angle with respect to the optic axis, however, it will be shown that the electric vector in the plane defined by the ray and the optic axis experiences a different index of refraction compared to the orthogonal electric vector. There is, thus, effectively a fast (or slow) axis at an angle η, where η is the angle of the ray-optic-axis plane with respect to the horizontal.

As illustrated in Figure 6.3.8, if the PC is located at $(0, 0, z)$ with its face along

the xy-plane, a ray of light propagating from a point source located at $(0,0,0)$ and incident at a point (x, y, z) subtends an angle ξ with the PC such that

$$\sin \xi_x = x/d_x; \qquad \sin \xi_y = y/d_y \tag{6.3.10}$$

where $d_x = \sqrt{x^2 + z^2}$ and $d_y = \sqrt{y^2 + z^2}$. For small angles ξ_x and ξ_y, $d_x \approx d_y \approx z$, $\sin \xi_x \approx \xi_x$, $\sin \xi_y \approx \xi_y$, and the equation above becomes

$$\xi_x \approx x/z; \qquad \xi_y \approx y/z. \tag{6.3.11}$$

Similarly, the angle of the effective fast-axis from horizontal, η, can be expressed in terms of x and y as

$$\sin \eta = x/\sqrt{x^2 + y^2}. \tag{6.3.12}$$

Using, Eq. 6.3.11, the equation above can be written as

$$\sin \eta = \xi_x/\sqrt{\xi_x^2 + \xi_y^2}. \tag{6.3.13}$$

In order to incorporate the above equation into the expression for HCBA of Eq. 6.3.9, the following expressions are evaluated:

$$\sin 2\eta = 2 \sin \eta \cos \eta \tag{6.3.14a}$$
$$= 2 \sin \eta \sqrt{1 - \sin^2 \eta}$$
$$= 2\xi_x \xi_y/(\xi_x^2 + \xi_y^2)$$
$$\cos 2\eta = 1 - 2 \sin^2 \eta \tag{6.3.14b}$$
$$= (1 - 2\xi_x^2/(\xi_x^2 + \xi_y^2))$$
$$= -(\xi_x^2 - \xi_y^2)/(\xi_x^2 + \xi_y^2)$$

Now, the HCBA of Eq. 6.3.9 is expressed as

$$Aq = -\frac{\epsilon}{T}\zeta \sin(2\eta - 2\psi) \tag{6.3.15a}$$

$$= -\frac{\epsilon}{T}\zeta(\sin 2\eta \cos 2\psi - \cos 2\eta \sin 2\psi)$$

and Eqs. 6.3.14 used to express Aq as

$$Aq = -\frac{\epsilon}{T}\zeta \left[2\frac{\xi_x \xi_y}{\xi_x^2 + \xi_y^2} \cos 2\psi + \frac{\xi_x^2 - \xi_y^2}{\xi_x^2 + \xi_y^2} \sin 2\psi \right]. \tag{6.3.15b}$$
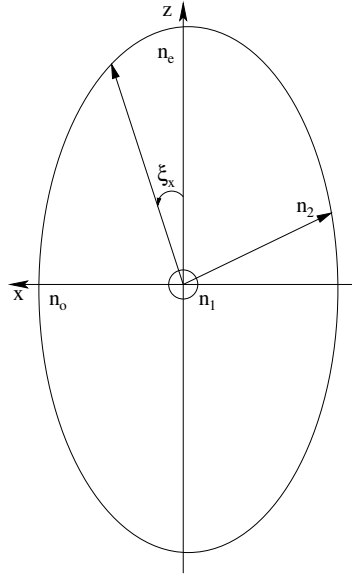
Figure 6.3.9: The light ray incident on an optical element on the xz-plane with an angle ξ_x to the z-axis, propagates along this plane with indices of refractions n_1 and n_2. n_1 is along yz-plane (perpendicular to the plane of the paper), and n_2 is along xz-plane. If the indices of the optical element along the x- and z-axes are n_o and n_e respectively, $n_1 = n_o$, and n_2 can be expressed in terms of n_o and n_e as given by Eq. 6.3.21c.

The phase shift, ζ, introduced by the PC in the above equation can also be expressed in terms of the angles ξ_x and ξ_y. This is discussed in what follows. If the PC has indices of refraction n_o along x- and y-axes, and n_e along z-axis, a ray of light

incident along the xz-plane at an angle of ξ_x with z-axis propagates with indices of refraction n_1 and n_2 given as

$$\frac{1}{n_1^2} = \frac{1}{n_o^2} \tag{6.3.16}$$

$$\frac{1}{n_2^2} = \frac{\cos^2 \xi_x}{n_o^2} + \frac{\sin^2 \xi_x}{n_e^2} \tag{6.3.17}$$

where n_1 is the resulting index refraction in the yz-plane, and n_2 is the resulting index refraction in the xz-plane, as is depicted in Figure 6.3.9. Eq. 6.3.17 can be rewritten as

$$n_2 = \left[\frac{\cos^2 \xi_x}{n_o^2} + \frac{\sin^2 \xi_x}{n_e^2}\right]^{-1/2} \tag{6.3.18}$$

$$= n_o \left[\cos^2 \xi_x + (\frac{n_o}{n_e})^2 \sin^2 \xi_x\right]^{-1/2}. \tag{6.3.19}$$

For small angles ξ_x and ξ_y,

$$\sin \xi_x \approx \xi_x \tag{6.3.20a}$$

$$\cos \xi_x = \sqrt{1 - \sin^2 \xi_x} \approx \sqrt{1 - \xi_x^2}. \tag{6.3.20b}$$

Using these small-angle approximations, n_2 can be expressed as

$$n_2 \approx n_o \left[1 - \xi_x^2 + (\frac{n_o}{n_e})^2 \xi_x^2\right]^{-1/2} \tag{6.3.21a}$$

$$\approx n_o \left[1 + (\frac{n_o^2 - n_e^2}{n_e^2}) \xi_x^2\right]^{-1/2} \tag{6.3.21b}$$

Furthermore, using $\frac{n_o^2 - n_e^2}{n_e^2} \ll 1$, the above expression for n_2 becomes

$$n_2 \approx n_o \left[1 - \frac{1}{2}(\frac{n_o^2 - n_e^2}{n_e^2}) \xi_x^2\right] \tag{6.3.21c}$$

Now, assuming that the PC has a thickness of D, the phase shift introduced by the PC on the light ray incident in the xz-plane is

$$
\begin{aligned}
\zeta_{xz} &= \frac{2\pi D}{\lambda}(n_1 - n_2) \\
&= \frac{\pi D}{\lambda}\left[\left(\frac{n_o^2 - n_e^2}{n_e^2}\right)\right]\xi_x^2
\end{aligned}
\tag{6.3.22a}
$$

where λ is the wavelength of the light, and n_1 and n_2 are given by Eqs. 6.3.16 and 6.3.21c respectively.

A similar argument can be made for light ray incident in the yz-plane at an angle of ξ_y with the z-axis, and the phase shift induced on this ray of light can be expressed as

$$
\zeta_{yz} = \frac{\pi D}{\lambda}\left[\left(\frac{n_o^2 - n_e^2}{n_e^2}\right)\right]\xi_y^2.
\tag{6.3.23}
$$

For a light ray, that traverses both xz- and yz-planes, subtending angles ξ_x and ξ_y to the z-axis along the respective planes, as is shown in Figure 6.3.8, the total phase shift introduced by the PC is

$$
\begin{aligned}
\zeta &= \zeta_{xz} + \zeta_{yz} \\
&= \frac{\pi D}{\lambda}\left[\left(\frac{n_o^2 - n_e^2}{n_e^2}\right)\right]\left[\xi_x^2 + \xi_y^2\right].
\end{aligned}
\tag{6.3.24}
$$

Now, substituting Eq. 6.3.24 into Eq. 6.3.15b, the HCBA, Aq, can be expressed as

$$
Aq = -\frac{\epsilon}{T}\frac{\pi D}{\lambda}\left[\left(\frac{n_o^2 - n_e^2}{n_e^2}\right)\right]\left[2\xi_x\xi_y\cos 2\psi + (\xi_x^2 - \xi_y^2)\sin 2\psi\right].
\tag{6.3.25}
$$

This equation expresses the HCBA in terms of the incidence angles, ξ_x and ξ_y, of the laser light. Only the orientation of the PC fast-axis (or equivalently slow-axis) in terms of these angle, as is given by Eq. 6.3.13 and 6.3.14, have been used to derive

this expression. Therefore, Eq. 6.3.25 applies only to those optical elements whose fast-axis *changes* depending on the incidence angle of the light rays. In the setup of Figure 6.2.1, only the PC exhibits this behavior. Thus, the HC effects contained in Eq. 6.3.25 is entirely due to the PC in this setup. The angular alignment of the PC is carefully optimized, as is discussed in the later sections of this chapter. The effects contained in Eq. 6.3.25 are sometimes referred to as the "Skew/Paschke" effects.

The dependence of the skew effects on PC misalignment in angle relative to the beam is evident in the data presented in Figure 6.3.10. The data presented in these plots are acquired by rotating the PC about its center in the range of ± 8 mrad along xz-plane, where z points along the direction of beam propagation. The HC effects, HCBA, HC position difference and HC spot-size and shape differences, all display large sensitivity to PC misalignment angle.

6.4   Controlling Helicity-Correlated (HC) Effects

For convenience, the rest of the chapter refers to the parts of Eq. 6.3.4 by the label assigned to them as the *offset*, 2θ or 4θ-*term*. For instance, the *offset-term* refers to $\frac{\epsilon}{T}\beta\sin(2\rho - 2\psi)$ and so on.

This section presents a brief discussion of the considerations that drove the source studies. The polarized source setup of the electron beam source studies was also used during HAPPEX-III and PREX. Therefore, this section focuses on the techniques employed to control the HC effects, relative to this configuration. In this configuration, the terms of Eq. 6.3.4 can be conceptually categorized based on their sources as

$$Aq = \text{Photocathode} \times [\text{Vacuum Window} + \text{RHWP} + \text{PC}]$$

where the Vacuum Window, RHWP and PC correspond to the *offset*, 2θ and 4θ-term
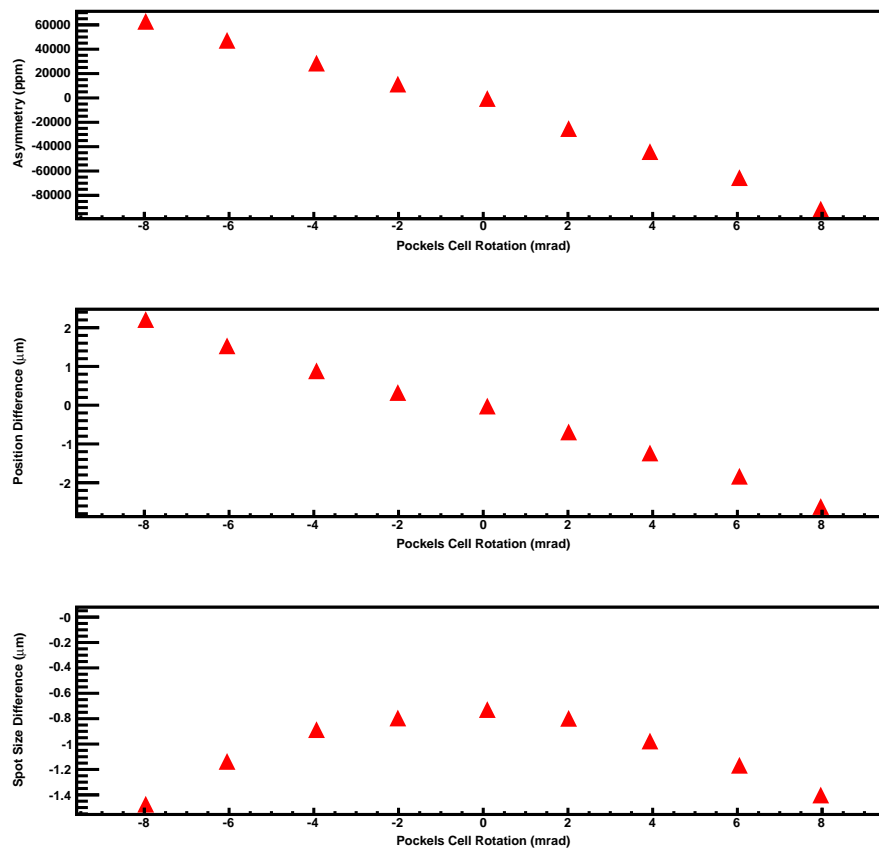
Figure 6.3.10: The Pockels Cell (PC) misalignment in angle relative to the beam propagation direction results in large HC effects, as is evident in these plots. These effects are contained in HCBA of Eq. 6.3.25. The plots presented above refer to data acquired with the PC rotated in the range of ± 8 mrad in the xz-plane about its center. These data were acquired with the LAPD detector oriented at 45° to the horizontal, and with the analyzer present in the laser's path in a setup similar to that of Figure 6.2.1. The top plot presents the HCBA as a function of the PC rotation angle. The middle and bottom plots present the HC position difference, and HC spot-size and shape differences measured along one of the PC birefringence axis (which is at 45° from the horizontal) as a function of the PC rotation angle.

respectively. Considering broadly, there are two ways to suppress Aq:

- Use a photocathode with no analyzing power ($\frac{\epsilon}{T} = 0$): When HAPPEX-III and PREX ran, $\frac{\epsilon}{T} = 0$ was only achievable with a photocathode that yielded electrons with a substantially reduced beam polarization of $\sim 35\%$. The very

feature of the photocathode that was responsible for the generation of highly polarized electrons (up to $\sim 90\%$) also introduced an analyzing power in the photocathode [Hu04]. Therefore, the choice was between using a photocathode with $\frac{\epsilon}{T} = 0$, albeit with much reduced beam polarization, or a photocathode that generated highly polarized beam but with a non-zero $\frac{\epsilon}{T}$, that had to be managed appropriately. Opting for the first choice would have solved the issues at the center of this study, but the figure-of-merit (FOM) would have taken an unacceptably big hit at the reduced beam polarization (FOM is proportional to the inverse of the beam polarization). Also, previous experiments such as HAPPEX-II have successfully demonstrated that $\frac{\epsilon}{T}$ could be judiciously managed [AnH06, AnHe06, Ac07]. So it was still preferable to use the photocathode that generated highly polarized electrons and contend with a non-zero $\frac{\epsilon}{T}$.

- Set offset-term + 2θ-term + 4θ-term = 0: This can be achieved either by setting the individual terms to 0 or by arranging their sum to be 0.

The first approach is more desirable because it minimizes the sensitivity to higher-moment effects namely the HC position, and beam spot-size and shape differences. But setting the individual terms to zero is not so straightforward. The 4θ-term can be zeroed by Δ-phase adjustments achieved via PC alignment and voltages adjustments. However, zeroing out the offset-term and the 2θ-term is much more difficult because they are independent of the Δ-phases. But the non-polarization effects are usually small compared to the polarization effects, whose suppression requires adjustments of the optical elements other than the PC. The offset-term depends on β, ρ and ψ, so it can be zeroed if $\beta = 0$, or if $\psi = \rho - n\pi/2$ where n is an integer. A perfect vacuum-window would result in $\beta = 0$. But the vacuum-window during our experiment was far from perfect. So the

offset-term was zeroed by adjusting ψ, which entailed appropriate adjustments of the photocathode orientation (the vacuum-window could not be rotated at JLab, so ρ was fixed). Similarly, the 2θ-term can be zeroed either by using a perfect RHWP (so that γ, the retardation deviation from perfect half-wave, is zero), or by adjusting the RHWP orientation appropriately to set $\theta = \psi$.

The second approach, of arranging the sum of offset-term, 2θ-term, and 4θ-term to be zero, is not ideal because the higher-moment HC effects present in the beam can lead to significant uncertainties in A_{PV}. Therefore, the first approach was initially adopted. Despite best efforts, however, individual terms in Eq. 6.3.4 were often non-zero for the reasons discussed above, and due to finite precision in the adjustments that could be made such as the limitation on the cathode's orientation adjustment precision. Thus, after practical limits on minimizing the individual terms were reached, the RHWP angle θ and the PC voltages (to adjust Δ) were selected to force the sum of Eq. 6.3.4 to zero.

6.5   Before PC Alignment (Electron Beam)

The data presented in the plots of Figure 6.2 were acquired with the electron beam before the laser table studies. These data are representative of the source parameters before dedicated studies and optimization were performed. Figure 6.2 represent scans of the RHWP rotated in the range of $\theta = [0, \pi]$. In each of the plots, Aq, Dx and Dy are plotted on the y-axis and RHWP angle is plotted on the x-axis. $Dx(Dy)$ is the HC position difference in x(y).

The expression for Aq displayed in the plots is a fit of the measured HCBA based

IHWP IN	IHWP OUT	
Aq = 496.42 + -1458.69 sin (2θ +38.68) + -523.19 sin (4θ +140.16)	Aq = -930.07 + 1476.42 sin (2θ +33.45) + 1221.30 sin (4θ +157.37)	PITA = 0 V
Dx = 1.29 + -0.29 sin (2θ +37.90) + 0.48 sin (4θ +158.91)	Dx = 1.07 + -0.10 sin (2θ +164.15) + 0.42 sin (4θ +27.82)	
Dy = 1.16 + -0.80 sin (2θ +33.22) + -0.65 sin (4θ +157.18)	Dy = 0.28 + 0.60 sin (2θ +18.60) + 0.96 sin (4θ +162.56)	
Aq = 533.34 + -1642.12 sin (2θ +16.13) + -4263.04 sin (4θ +169.76)	Aq = -909.36 + 1509.34 sin (2θ +58.19) + 2634.65 sin (4θ + 0.17)	PITA = ±120 V
Dx = 1.41 + -0.21 sin (2θ +101.43) + -0.35 sin (4θ +47.24)	Dx = 1.10 + 0.09 sin (2θ +19.72) + -0.64 sin (4θ +177.99)	
Dy = 1.19 + -0.75 sin (2θ +20.81) + -2.45 sin (4θ +166.58)	Dy = 0.35 + 0.63 sin (2θ +79.68) + -0.95 sin (4θ +178.87)	

Table 6.2: The plots of data acquired with the electron beam before any source studies were performed are presented above. These data are acquired by rotating the rotatable half-wave plate (RHWP) in the range of $\theta = [0, \pi]$, and are representative of the helicity-correlated (HC) parameters of the electron beam before the studies. The left and right column correspond to data acquired IHWP state IN and OUT respectively. The top and bottom row correspond to data acquired at PITA offsets of 0 V and ±120 V respectively. In each data set, the HC beam asymmetry (HCBA), HC position differences in x (Dx) and in y (Dy) are plotted against the RHWP angles in the first, second and third sub-plots respectively. The data plotted in each of the sub-plots are fitted to Eq. 6.3.4, parameterized in the form given by Eq. 6.5.1. These fits are drawn as solid curves, and the associated fit equations presented below each sub-plot. The dashed curves are fits of 2θ-term and 4θ-term alone, parameterized in similar forms.

on Eq. 6.3.4 and parameterized in the form

$$Aq = A + B\sin(2\theta + \phi) + C\sin(4\theta + \zeta) \qquad (6.5.1)$$

where A, B, C, ϕ and ζ are the fit-parameters, and θ is the fit-variable. Dx and Dy are parameterized in a form similar to that of Aq, with the assumption that these HC position differences arise due to the phase-gradients in Aq, and hence, have a form similar to that of Aq.

The set of plots such as the one presented in Figure 6.2 completely summarizes the source setup and the parity quality of the electron beam:

1. The offset-term for the Aq is expressed as $\frac{\epsilon}{T}\beta\sin(2\rho - 2\psi)$, Eq. 6.3.4. $\frac{\epsilon}{T}$ is a non-zero constant for the photocathode used to acquire these data. The same photocathode was used during much of the source studies, and during the experiments. β is the phase-shift due to the vacuum-window and ρ is the angle subtended by the fast-axis of the vacuum-window birefringence to the horizontal. Both β and ρ were more or less fixed since the vacuum-window could not be easily replaced or its orientation changed. ψ is the angle subtended by the analyzing axis of the photocathode to the horizontal. Unlike the vacuum-window, however, the photocathode's orientation could be adjusted, albeit to limited precision. Therefore, the only available handle to suppress the offset-term was to adjust the photocathode's orientation to set $\psi = \rho$.

   Large Aq, Dx and Dy offset-terms in all the plots indicate that the photocathode orientation had not been optimized. Large Dx and Dy offset-terms also indicate a significant phase-gradient in either one or both the vacuum-window and the photocathode.

2. The 2θ-term in Aq is given as $\frac{\epsilon}{T}\gamma\sin(2\theta - 2\psi)$, Eq. 6.3.4. γ is the phase-offset

due to the RHWP's retardation deviation from perfect half-wave retardation. θ is the angle subtended by its fast-axis to the horizontal.

γ is big in the plots, indicating large HC effects arising from the RHWP phase-shifts. Large Dx and Dy 2θ-terms (of up to 800 nm) also indicate large phase-gradients across the RHWP, photocathode or both.

3. The 4θ-term in Aq is given as $\frac{\epsilon}{T}(\Delta - \Delta^0)\cos(4\theta - 2\psi)$, Eq. 6.3.4. $(\Delta - \Delta^0)$ is the phase-offset arising from PC. Large 4θ-terms at zero PITA offset voltages indicate that the PC orientation and voltages were not optimized. Large Dx and Dy 4θ-terms indicate large phase-gradients across the PC, large analyzing power gradient across the photocathode or both.

4. The 2θ and 4θ-terms reverse sign between the IHWP states indicating that these terms are dominated by the polarization effects [1]. The offset-terms, however, does not flip sign with the IHWP state reversal, indicating that these terms are dominated by the non-polarization effects. As mentioned earlier, these non-polarization effects can be suppressed by judicious PC translations. Large offset-terms in Dx and Dy that do not reverse sign on IHWP state reversal indicate that the PC positions were not optimized to suppress these non-polarization effects in position. Aq offset-terms that reverse sign on IHWP reversal but with different magnitudes were most likely due to the IA cell [2] [Hu04]: the

---

[1] A change in IHWP state reverses only the polarization effects, leaving the non-polarization effects unchanged. So IHWP IN and OUT data sets were used to separate the polarization effects from the non-polarization effects, and characterize and correct for the non-polarization effects. In Figure 6.2, the top and the bottom set of plots correspond to data acquired at IHWP IN and OUT states respectively, with other conditions unchanged. Although the PITA offset voltages for the bottom two plots are not the same in Figure 6.2, (such data sets presented in the rest of this chapter have identical voltages), the non-polarization effects can still be separated from the polarization effects. Different PITA offset voltages made the characterization of the polarization effects a little tricky, but not impossible.

[2] IA cell was unplugged at the beginning of the laser table studies, and left unplugged for the entirety of the source studies, as well as during both HAPPEX-III and PREX, but it was operational during the acquisition of the data presented in Figure 6.2.

sign reversal could arise from the polarization effects resulting from the IA cell, and the differences in magnitude between the IHWP states could be due to misalignment of the IA cell.

5. The offset-terms and the 2θ-terms do not change much (for the most part) between different PITA offset voltages while the 4θ-terms changes substantially [1] confirming that the offset and 2θ-term effects arose dominantly from sources other than the PC. The 4θ change in Aq relates entirely to the analyzing power $\frac{\epsilon}{T}$ and the fractional change in the retardation of the PC (Δ). The change in 4θ of the position differences are only due to the position variations in the analyzing power $\frac{\partial}{\partial x}(\frac{\epsilon}{T})$ or $\frac{\partial}{\partial y}(\frac{\epsilon}{T})$.

The data presented in Figure 6.2 indicates that the laser table optics and associated parameters were not optimized to suppress the HC effects in the beam. The offset, 2θ and the 4θ-terms all need to be further suppressed. The offset-term is dominated by the vacuum-window effects, so it could only be optimized with electron beam source studies. The 2θ and 4θ-term, however, depend on the laser table optics, and laser table studies and optimization are sufficient to suppress the HC effects associated with these terms. The laser table study was centered around PC alignment and voltages optimization, which is discussed in the next section.

---

[1] The PITA voltage offset determines the extent of circular polarization (and the residual linear polarization) of the beam, with an offset of zero ideally leading to a perfectly circular polarized beam. The PITA offset voltages only affects the HC properties via the 4θ-term, Eq. 6.3.6. So data sets with different amount of PITA offsets are used to separate the 4θ-term effects. In essence, these effects are the Δ-phase effects arising from PC, and depends on the quality of the PC alignment and voltages. The left and right set of plots in Figure 6.2 were acquired at different PITA offset voltages with other conditions unchanged.

6.6   Pockels Cell Alignment

The PC alignment was initially performed with the laser light alone. The insertable mirror was inserted into the laser's path, and the laser read out into a QPD detector [1]. The PC alignment procedure is chronologically outlined below:

1. **Extinction ratio maximization:** The PC, IHWP and RHWP were *removed*, and the analyzer *inserted* into the laser's path, Figure 6.2.1. With the polarization axis of the clean-up linear polarizer (immediately downstream of the IA cell) set perpendicular (or parallel) to the horizontal, the analyzer's roll-angle was adjusted to maximize the extinction ratio (this set the analyzer's polarization axis perpendicular to the clean-up linear polarizer's polarizing axis). Then the PC was *inserted* between the two polarizers with its fast-axis at 45° to the polarization axis of the polarizers. The PC pitch and yaw were adjusted to maximize the extinction ratio, which was usually slightly less than the extinction ratio achieved with the two polarizers alone.

   Maximizing extinction ratio alone does not guarantee that the PC longitudinal axis is well aligned with the direction of laser light propagation. A maximum extinction ratio can also result when the PC axis is not well aligned to the laser propagation direction, though such instances occur rarely. Regardless, the PC's alignment with respect to the laser light propagation direction was confirmed by observing an "isogyre pattern" [BW64].

2. **Isogyre observation:** A viewer centered about the beam propagation axis [2] was *placed* immediately downstream of the analyzer, and a transparent tape

---

[1] A LAPD detector was used during the laser table studies as well. But the PC alignment was performed with the QPD, and the LAPD detector used only for laser light HC spot-size and shape differences characterization.

[2] The beam propagation axis on the viewer was marked before the PC was inserted into the laser's path because the PC could steer the beam.

placed on the face of the PC with the tape on the laser's path (in order to disperse the laser light for isogyre observation). An isogyre centered about the beam propagation axis was visible on the viewer with this setup. If the isogyre was not centered about the beam propagation axis marked on the viewer, the PC pitch and yaw were further adjusted until the isogyre was centered about the marker. A well centered isogyre indicates that the PC longitudinal axis is parallel to the direction of beam propagation. The viewer and the transparent tape were *removed* after aligning with respect to the isogyre pattern.

3. α-**phase minimization:** The analyzer was *replaced* with a spinning linear polarizer, and PC voltages adjusted to equalize the intensity of the laser light passing through the polarizer for both helicity states [1]. The voltage adjustments affects both the α and Δ-phases [2], but the α-phases cancel to first-order in the HC parameters, and cannot be corrected via HC parameter studies. So the α-phase effects had to be minimized with this technique (of equalizing the total intensity of laser light transmitted for each helicity state). The voltages that minimized the α-phases in each helicity state were the base voltages that were used during the RHWP scans and the PITA scans [3].

4. Dx and Dy (**non-polarization) offset-terms minimization:** Although the dominant source of Dx and Dy offset-terms was the vacuum-window, the static effects of the PC itself also led to non-zero contributions to these terms. To minimize these contributions, the spinning linear polarizer was *removed* from the laser's path, and the HC position differences Dx and Dy measured. Dx

---

[1]In instances when the voltages between the two states were very different, or the voltage adjustments did not equalize the intensity of transmitted laser light, the PC roll-angle (about the beam propagation axis) was adjusted.

[2]See Section 6.3.2 for details on α and Δ-phases.

[3]PITA scans were used to suppress the Δ-phases, Section 6.3.2.

and Dy were primarily due to the non-polarization effects because the analyzer was absent from the laser's path. If these terms were large, PC translation scans in x and y were performed. The dependencies of Dx and Dy on PC translation amount [1] extracted from these scans were used to translate the PC to appropriate x and y positions, and minimize Dx and Dy [2]. Without the analyzer on the laser's path, Dx and Dy could usually be constrained to 50 nm [3].

5. **4θ-term minimization:** The 4θ-term was dominated by the polarization effects. So the analyzer was *inserted* back into the laser's path and PITA scans taken. The PITA scan is described in Section 6.3.2. These scans were acquired with both the analyzer's roll-angle unchanged (so that the fast-axis of the analyzer was at 45° to PC fast-axis) and the analyzer's roll-angle rotated by 45° (so that the fast-axis of the analyzer was parallel to the PC fast-axis). The analyzer's first orientation is maximally(minimally) sensitive to S1(S2) [4] Δ-polarization and the second orientation is maximally(minimally) sensitive to S2(S1) Δ-polarization. Both the S1 and S2 Δ-polarization effects were studied during PC alignment and voltage adjustments because suppression of these effects along one direction increased it in the other, and the S2 effects could only be adjusted via PC alignment adjustments; S2 Δ-polarization effects were unaffected by the PC voltages, Eq. 6.3.6.

---

[1] The PC was mounted on Thorlabs translation stages that could be adjusted with pico-motors, and translated in x and y. The translation unit was mill, thousand of an inch.

[2] This procedure was insensitive to the presence of Δ-phases due to the absence of elements with significant analyzing power downstream of the PC along the laser's path. So the PC voltages did not need to be optimized for Δ-phases suppression before this procedure.

[3] These were measured both on the QPD and LAPD.

[4] S1 and S2 are the Stokes polarization parameters. S1 describes the preponderance of linear horizontal polarization (LHP) over linear vertical polarization (LVP), and S2 describes the preponderance of the linear light polarized at +45° to horizontal (L+45P) to the linear light polarized at −45° to the horizontal (L−45P). These descriptions are taken from Collett [Co05].

If the PITA scan Aq, Dx and Dy offsets were reasonably small ($Aq < 100$ ppm and $Dx(Dy) < 1$ μm) along both S1 and S2 then the PC was considered to be well aligned, and no further PC alignment adjustments were necessary. Voltages adjustment based on the PITA scan slopes were then made to suppress Aq, without increasing Dx and Dy much. However, as was often the case, the PITA scans Aq, Dx and Dy offsets were large along either one or both of S1 and S2, necessitating PC alignment adjustments.

The PC alignment adjustments started with the PC pitch and yaw scans. The PC was rotated in pitch and yaw, and the HC parameter responses to these adjustments measured along S1 and S2. These measurements were simultaneously used for judicious PC pitch and yaw adjustments. Ideally, both the S1 and S2 effects would be suppressed with these adjustments, but these adjustments usually split the HC effects between S1 and S2 such that the S2 effects were reasonably well suppressed while the S1 effects were left slightly larger than the S2 effects, but still small enough to be managed by PC voltage adjustments.

6. Dx **and** Dy **(polarization) offset-terms minimization:** With the analyzer still present on the laser's path, the HC offset-terms were further suppressed via PC translation scans in a process similar to the one outlined above for the offset-terms minimization.

7. **PITA scans:** PITA scans were routinely taken after each PC pitch/yaw and translation adjustments. These scans were used to establish appropriate PC voltages that minimized Aq, which, in this case, was equivalent to zeroing ($\Delta - \Delta^0$).

8. **IHWP IN/OUT scans:** All the representative PITA and the PC pitch/yaw and translation scans were performed with both the IHWP states to character-

ize and correct the non-polarization effects arising from the PC during these adjustments.

9. **RHWP scans:** The RHWP was inserted into the laser's path after PC adjustments, and a set of four RHWP scans like the one presented in Figure 6.2 taken to summarize the laser table setup. After a satisfactory PC alignment was achieved, the RHWP was left on the laser's path.

After the PC was aligned by employing the techniques employed above, the characteristic set of RHWP scan data was acquired on the QPD and LAPD on the laser table.

6.6.1 Helicity-Correlated Position Differences

The characteristic set of RHWP scans acquired after aligning the PC are presented in Figure 6.3. These plots were acquired on the QPD with the analyzer present in the laser's path. The quality of the laser light and the laser table setup are summarized by these scans as follows:

1. The offset-terms are due to the optical elements present between the RHWP and the analyzer as discussed in Section 6.3. In the laser-table studies setup used to acquire Figure 6.3, however, nothing was present between the RHWP and the analyzer, Figure 6.2.1. So the offset-terms are negligible for PITA offset of 0 V, as expected. However, they get larger at PITA offset of 60 V, suggesting a slight dependence of these terms on the polarization effects arising from the PC.

   The offset-terms also flip sign between the IHWP states, with comparable magnitude (for the most part) indicating that the non-polarization effects are mostly under control.

IHWP IN	IHWP OUT	
Aq = -7.25 + -32896.33 sin (2θ +43.77) + -2397.50 sin (4θ +81.55)	Aq = 20.57 + 33012.14 sin (2θ +43.51) + 2980.28 sin (4θ +43.86)	PITA = 0 V
Dx = -0.19 + -0.22 sin (2θ +66.12) + -7.66 sin (4θ +171.88)	Dx = 0.11 + 0.39 sin (2θ +42.08) + 5.77 sin (4θ +167.69)	
Dy = -0.15 + -0.01 sin (2θ +122.27) + -3.56 sin (4θ +119.40)	Dy = 0.28 + 0.13 sin (2θ +16.30) + 3.11 sin (4θ +58.69)	
Aq = 552.49 + -33659.56 sin (2θ +43.78) + -39984.85 sin (4θ +171.47)	Aq = -565.46 + 33717.01 sin (2θ +43.64) + 38322.70 sin (4θ +171.41)	PITA = 60 V
Dx = -0.30 + 0.38 sin (2θ +179.51) + -7.46 sin (4θ +173.15)	Dx = 0.03 + 0.25 sin (2θ +27.41) + 5.65 sin (4θ +167.73)	
Dy = -0.16 + -0.13 sin (2θ +16.84) + -3.52 sin (4θ +119.33)	Dy = 0.35 + 0.14 sin (2θ +84.52) + 3.09 sin (4θ +57.78)	

Table 6.3: RHWP scans acquired on a QPD detector with the analyzer present along the laser's path, after laser table PC alignment and voltages adjustments.

2. The Aq 2θ-term is large that suggests a significant phase-offset due to the RHWP [1]. The large Dx and Dy 2θ-terms indicate big phase-gradients across the RHWP.

   The 2θ-terms flip sign between the IHWP states with comparable magnitudes, indicating that these terms are dominated by the polarization effects. These terms also remain roughly constant at different PITA offset voltages indicating that these effects are independent of the Δ-phases arising from the PC, and that these terms can only be suppressed by using a more closely matched half-wave plate.

3. The Aq 4θ-term is reasonably small [2] indicating that the zeroth-moment HC effects of $(\Delta - \Delta^0)$ are well suppressed. The large Dx and Dy 4θ-terms indicate large $(\Delta - \Delta^0)$ phase-gradients.

   These 4θ-terms flip sign on IHWP state reversal with comparable magnitudes, indicating that these terms are dominated by the polarization effects. Aq 4θ-term scale in agreement with the measured PITA slopes at different PITA offsets. For instance, the Aq 4θ-term increased by ~ 37500 ppm when the PITA offset was changed by 60 V for the IHWP IN state. This suggested a PITA slope of ~ 626 ppm/V, in agreement with the measured PITA slope of 657 ppm/V to about 5%.

   The Dx and Dy 4θ-terms, however, do not vary much with PITA offset voltages, indicating that these terms are dominated by the Δ^0 phase-gradients which arise due to the residual birefringence of the PC and the analyzer (and were

---

[1] The 2θ HC charge asymmetry of $\sim 33.4e3$ ppm ($\frac{\epsilon}{T} \approx 1$ for 100% analyzer) was equivalent to 47 V PITA offset, for instance. PITA slope averaged between the two IHWP states was about 700 ppm/V during the laser table source studies. This was PITA slope along the S1 Δ-polarization direction without the RHWP present on the laser's path.

[2] The Aq 4θ-term of ~ 3000 ppm at PITA offset of 0 was ~ 4 PITA offset voltages off. Typical PITA slopes were ~ 700 ppm/V.

unaffected by the PITA offset voltages).

The RHWP scan plots of Figure 6.3 suggest that the PC was well aligned: the offset-terms are small and the Δ-phases arising from the PC are mostly suppressed. However, these plots only refer to the zeroth and the first-moment HC effects (Aq and Dx/Dy). But the second-moment HC effects (spot-size and shape differences that arose due to the gradients in Dx/Dy) could be significant as well. Therefore, the laser light was also characterized for any second-moment HC effects, which is discussed in the next section.

6.6.2 Helicity-Correlated Spot-Size and Shape Differences

The laser light spot-size and shape HC differences were characterized with the LAPD detector [1]. The laser table setup for this study was similar to the one used for PC alignment and laser light characterization above, but with the QPD replaced by the LAPD. A cylindrical lens expanded the laser light across the multiple photodiode pads of the LAPD. This lens was placed immediately upstream of the LAPD.

The LAPD detector measures the HC intensity asymmetry, HC position differences and HC spot-size and shape differences simultaneously. But these parameters can only be measured along *one* particular direction at a time; the direction along which the pads are arranged in the array. So a complete laser table setup characterization requires measurements along 4 different axes: 2 along S1 and 2 along S2. The characteristic RHWP scan plots along these axes are presented in Figures 6.4, 6.5, 6.6 and 6.7. These plots were acquired at the same PC alignment and voltage settings as those used in Figure 6.3. The RHWP rotated S1 and S2 across the analyzer, and the LAPD detector measures averages of the S1 and S2 effects along a particular

---

[1] Discussion of how the LAPD was used to measure these beam parameters are presented in Appendix C.2.

axis. The scans with the LAPD in vertical and horizontal orientations characterized the S1 components, while the scans with the LAPD at $\pm45°$ characterized the S2 components.

Like in Section 6.5, the HC intensity asymmetry and the position differences in these LAPD RHWP scans are fitted based on Eq. 6.3.4 with a parameterization of the form

$$Aq = A + B\sin(2\theta + \phi) + C\sin(4\theta + \zeta) \qquad (6.6.1)$$

where A, B, C, ϕ and ζ are the fit-parameters, and θ is the fit-variable. The HC spot-size and shape differences are parameterized in this form with the assumption that the HC spot-size and shape differences arise due to phase-gradients in the position differences (i.e. second-moment of phase-gradients in Aq).

In the RHWP scan plots of Figures 6.4, 6.5, 6.6 and 6.7, the HC position differences (Dx) [1], and spot-size and shape differences $(Drms)$ refer to the differences along the direction in which the LAPD acquired data. These plots characterize the laser table setup as follows:

1. As discussed in Section 6.6.1, the offset-terms were expected to be tiny because nothing was present between the RHWP and the analyzer. However, the offset-terms in these plots are larger than those in Figure 6.3. Specifically, comparison of Aq and Dx in Figure 6.4 to Aq and Dx in Figure 6.3 (HC parameters along the horizontal), and Aq and Dx in Figure 6.5 to Aq and Dy in Figure 6.3 (HC parameters along the vertical) reveal that all these HC parameters increased when the QPD was replaced with the LAPD [2]. But $Drms$ along both S1 and

---

[1] The sign of the HC position differences measured on the LAPD is opposite to that measured on the QPD. This is due to differences in the coordinate systems used to calibrate these detectors in PAN.

[2] As to why these offsets would be so big, and different when the laser beam was already 100% analyzed at the analyzer was a mystery. Perhaps, this was the result of a combination of beam
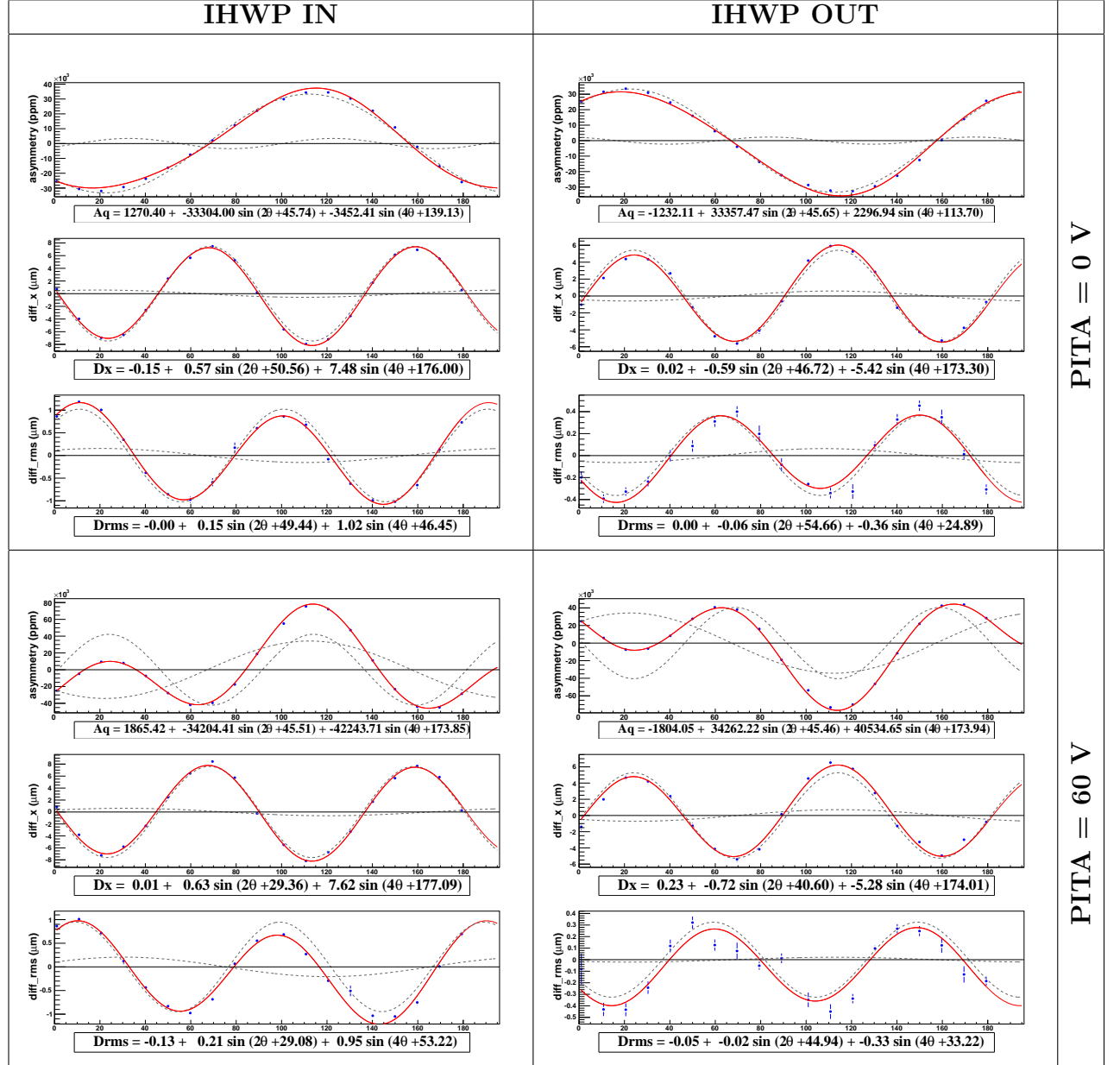
Table 6.4: RHWP scans acquired on LAPD detector in horizontal orientation after PC alignment and voltage adjustments.

IHWP IN	IHWP OUT	
Aq = 1156.20 + -33634.10 sin (2θ +45.16) + -3103.10 sin (4θ +131.84) Dx = 0.29 + -0.12 sin (2θ +167.44) + 3.62 sin (4θ +120.30) Drms = 0.04 + -0.35 sin (2θ +51.52) + -0.78 sin (4θ +164.95)	Aq = -1150.12 + 33408.59 sin (2θ +44.86) + 2251.03 sin (4θ +99.00) Dx = -0.60 + -0.08 sin (2θ +38.50) + -3.18 sin (4θ +66.83) Drms = -0.03 + 0.26 sin (2θ +51.81) + 0.92 sin (4θ +135.35)	PITA = 0 V
Aq = 1792.99 + -34380.22 sin (2θ +45.05) + -42535.03 sin (4θ +173.36) Dx = 0.28 + -0.13 sin (2θ +139.02) + 3.71 sin (4θ +119.00) Drms = -0.07 + -0.18 sin (2θ +80.06) + -0.90 sin (4θ +165.50)	Aq = -1786.26 + 34232.30 sin (2θ +44.91) + 40816.00 sin (4θ +173.19) Dx = -0.49 + 0.16 sin (2θ +130.95) + -3.16 sin (4θ +70.31) Drms = -0.10 + 0.31 sin (2θ +52.56) + 1.14 sin (4θ +145.30)	PITA = 60 V

Table 6.5: RHWP scans acquired on LAPD detector in vertical orientation after PC alignment and voltage adjustments.

IHWP IN	IHWP OUT	
Aq = 1269.01 + -33232.33 sin (2θ +44.60) + -3109.39 sin (4θ +136.47)	Aq = -1215.09 + 33242.12 sin (2θ +44.40) + 1955.80 sin (4θ +96.19)	PITA = 0 V
Dx = -0.17 + 0.39 sin (2θ +45.41) + -4.49 sin (4θ +22.00)	Dx = 0.37 + -0.50 sin (2θ +46.46) + 5.05 sin (4θ +16.41)	
Drms = -0.13 + 0.36 sin (2θ +41.21) + 0.62 sin (4θ +114.69)	Drms = -0.18 + -0.17 sin (2θ +33.41) + 0.45 sin (4θ +13.12)	
Aq = 1831.45 + -34090.75 sin (2θ +44.56) + -42271.66 sin (4θ +173.20)	Aq = -1764.34 + 34014.52 sin (2θ +44.40) + 40385.63 sin (4θ +173.15)	PITA = 60 V
Dx = -0.16 + 0.51 sin (2θ +62.46) + -4.46 sin (4θ +22.59)	Dx = 0.45 + -0.39 sin (2θ +35.16) + 5.17 sin (4θ +16.18)	
Drms = -0.25 + 0.38 sin (2θ +44.92) + 0.98 sin (4θ +142.17)	Drms = -0.16 + -0.26 sin (2θ +41.95) + -0.79 sin (4θ +179.50)	

Table 6.6: RHWP scans acquired on LAPD detector at +45° after PC alignment and voltage adjustments.

	IHWP IN	IHWP OUT	

Aq = 1192.94 + -33885.94 sin (2θ +44.66) + -2559.63 sin (4θ +130.03)

Dx = 0.20 + 0.38 sin (2θ +22.86) + 7.21 sin (4θ +158.97)

Drms = 0.14 + -0.08 sin (2θ +52.49) + 1.75 sin (4θ + 4.00)

Aq = -1235.51 + 33630.18 sin (2θ +44.41) + 1923.13 sin (4θ +98.38)

Dx = -0.39 + -0.54 sin (2θ +23.69) + -4.04 sin (4θ +143.13)

Drms = 0.20 + 0.21 sin (2θ +37.23) + 1.47 sin (4θ +165.33)

Aq = 1841.53 + -34570.21 sin (2θ +44.58) + -42331.95 sin (4θ +173.41)

Dx = 0.26 + 0.49 sin (2θ +24.69) + 7.19 sin (4θ +160.05)

Drms = 0.04 + -0.16 sin (2θ +48.87) + 1.95 sin (4θ + 3.16)

Aq = -1816.05 + 34471.98 sin (2θ +44.42) + 40747.08 sin (4θ +173.15)

Dx = -0.35 + -0.47 sin (2θ +28.21) + -4.09 sin (4θ +143.60)

Drms = 0.13 + 0.18 sin (2θ +46.58) + 1.61 sin (4θ +166.90)

PITA = 0 V

PITA = 60 V

Table 6.7: RHWP scans acquired on LAPD detector at $-45°$ after PC alignment and voltage adjustments.

S2 are small that indicates negligible amount of second-moment in the phase-gradients of the Aq offset-terms.

Like in Figure 6.3, the offset-terms in these plots flip sign on IHWP state reversal with comparable magnitudes, indicating that the non-polarization effects are mostly suppressed. The slight variations in these terms at PITA offset of 60 V indicates a slight dependence of these terms on the polarization effects arising from the PC, as observed in Figure 6.3.

2. The Aq and Dx 2θ-terms are consistent with those of Figure 6.3. However, the $Drms$ 2θ-terms are alarmingly big in these plots, indicating a large second-moment of the phase-offsets (a phase-gradient in the HC position difference) across the RHWP.

   Like the Aq and Dx 2θ-terms, $Drms$ 2θ-terms flip sign on IHWP reversal with comparable magnitudes, indicating that these terms are dominated by the polarization effects. These terms also do not vary much between PITA offset of 0 and 60 V. This indicates that the RHWP is the primary source of these polarization effects, and that these 2θ-terms are insensitive to the PC polarization effects.

3. The Aq and Dx 4θ-terms are also consistent those of Figure 6.3. Like the 2θ-terms, the $Drms$ 4θ-terms, however, are large that indicate a large second-moment of the $(\Delta - \Delta^0)$ phase-offsets.

   The $Drms$ 4θ-terms flip sign with the IHWP state reversal, but with a slightly varying magnitudes in some instances. The PITA offset voltages affects the $Drms$ 4θ-terms only in some instances. This indicates that the Δ^0 phase-

---

steering and efficiency variation across the linear array pads, as the LAPD was challenging to use accurately. It could also have resulted from some other change in the beam such as a small beam deflection from a bumped optical element.

gradients dominated along some directions, while the Δ phase-gradients dominated along others.

4. The offset, 2θ and 4θ-terms of Figures 6.4- 6.5 are comparable to those of Figures 6.6- 6.7, indicating that the phase-gradients averaged across S1 and S2 were similar. The similarities in the 2θ and 4θ-terms could also be the result of instrumental effects, where false Dx or $Drms$ was related to Aq. But, this was unlikely, and no conclusive evidence to support this claim was observed.

The RHWP scans of Figure 6.4, 6.5, 6.6, 6.7 are consistent with the QPD RHWP scans of Figure 6.3: the offset-terms are mostly small, the 2θ-terms (due to the RHWP) are large with substantial phase-gradients, the 4θ-terms arising from the PC misalignment (Δ-phases) are mostly suppressed. But the large $Drms$ 2θ and 4θ-terms, particularly the 4θ-term indicating large $(\Delta - \Delta^0)$ phase-gradients across the PC and the analyzer, are causes for concern (especially if the PC was the dominant source of these effects).

6.7   Final Optimization

After the PC voltages and alignment were optimized with the laser table studies, the insertable mirror was retracted, Figure 6.2.1, and further studies done with the electron beam alone. The goal of these electron beam source studies was to optimize the RHWP orientation, and to suppress the offset-terms (that primarily arose due to the vacuum-window).

Figure 6.8 are RHWP scan plots of data acquired with the electron beam. These data were acquired after the PC alignment and voltage optimizations with the laser light. These plots summarize the new laser table setup and electron beam properties.

A comparison of these plots to a similar set of plots acquired before the PC alignment and voltage adjustments, and displayed in Figure 6.2, are presented below:

1. The Aq, Dx and Dy offset-terms in both data sets are similar. This is expected considering that terms are primarily due to the vacuum-window, which remained untouched between the acquisition of these data sets. In both these plots, the offset-terms remain unaffected by the PITA offset voltages, Aq flips sign on IHWP state reversal, and Dx does not flip sign between different IHWP states, with only a slight variation in magnitudes. Dy flips sign between the IHWP states as well between the data sets. However, Dy decreases by about 0.9 μm in Figure 6.2 and only about 0.60 μm in Figure 6.8 between the IHWP states.

   The IA cell was operational when the plots of Figure 6.2 were acquired, but it was unplugged from its power source shortly thereafter, and was not operational when the plots of Figure 6.8 were acquired. Thus, some of the differences in the offset-terms between these data sets most likely came from the IA cell. The incidence point of the laser light on the vacuum-window, which most likely changed between the two sets of plots as well, also could be the cause of some of these differences.

   Despite these differences, however, the offset-terms remain large in both these data sets. So, these terms were suppressed via a combination of photocathode rotation and PC translation, which are topics of discussion later.

2. The 2θ-terms remain mostly unchanged between the data sets, because these terms are due to the RHWP (and the same RHWP was used for both data sets).

3. All the 4θ-terms at zero PITA offset voltage are much smaller in Figure 6.8

IHWP IN	IHWP OUT	

Aq = 571.00 + -1371.58 sin (2θ +41.50) + 105.87 sin (4θ +133.31)

Dx = -1.14 + -0.24 sin (2θ +43.88) + -0.28 sin (4θ +18.66)

Dy = 0.29 + -0.50 sin (2θ +39.56) + 0.16 sin (4θ +44.93)

Aq = -532.50 + 1359.91 sin (2θ +42.99) + -178.81 sin (4θ +156.41)

Dx = -1.32 + -0.13 sin (2θ +152.81) + -0.36 sin (4θ +171.12)

Dy = -0.19 + 0.59 sin (2θ +37.41) + -0.25 sin (4θ +73.54)

Aq = 589.27 + -1486.98 sin (2θ +17.77) + -3538.11 sin (4θ +174.74)

Dx = -1.02 + 0.22 sin (2θ +140.46) + 0.11 sin (4θ +41.50)

Dy = 0.44 + 0.53 sin (2θ +171.00) + -1.23 sin (4θ +172.56)

Aq = -557.97 + 1453.68 sin (2θ +18.31) + 3443.09 sin (4θ +173.54)

Dx = -1.39 + 0.19 sin (2θ +62.42) + 0.41 sin (4θ +155.07)

Dy = -0.24 + 0.63 sin (2θ +23.54) + 1.43 sin (4θ +174.90)

PITA = 0 V

PITA = 120 V

Table 6.8: RHWP scan after PC alignment and voltage adjustments taken with the electron beam.

compared to those of Figure 6.2, indicating that the Δ-phase effects are better suppressed in Figure 6.8. These terms also flip sign with comparable magnitudes between the IHWP states in Figure 6.8, indicating better suppression of any non-polarization effects in these terms. These improvements in the 4θ-terms are due to the PC alignment and voltage adjustments during the laser table studies.

The RHWP scan plots of Figure 6.8 indicate that the 4θ-terms are under control. While the offset and the 2θ-terms are still big, not much could be done about the 2θ-term, short of replacing the current RHWP with the one closely matched to the specific laser light wavelength [1]. The offset-terms were suppressed via both the photocathode rotation and PC translation, and are topics of discussion below.

6.7.1 Offset-Term

The offset-terms were suppressed via a combination of the photocathode rotation and the PC translation.

6.7.1.1 Photocathode Rotation

The photocathode used so far was replaced by a new photocathode before this study. So this study was performed with this new photocathode. However, the discussion presented below is applicable to any photocathode.

As mentioned previously, the photocathode was rotated to suppress the polarization effects appearing in the offset-terms. The photocathode orientation was adjusted[2], and a RHWP scan acquired at each of these orientations, until the offset-

---

[1]The birefringence deviation on the wave-plate was < 5 nm, and another plate had not been identified to improve this term. This is an obvious area for improvement in future work.

[2]The photocathode orientation was determined with reference to a crack on its surface observed on the quantum-efficiency (QE) scan pictures, Figure 6.7.1. The angle subtended by this crack to
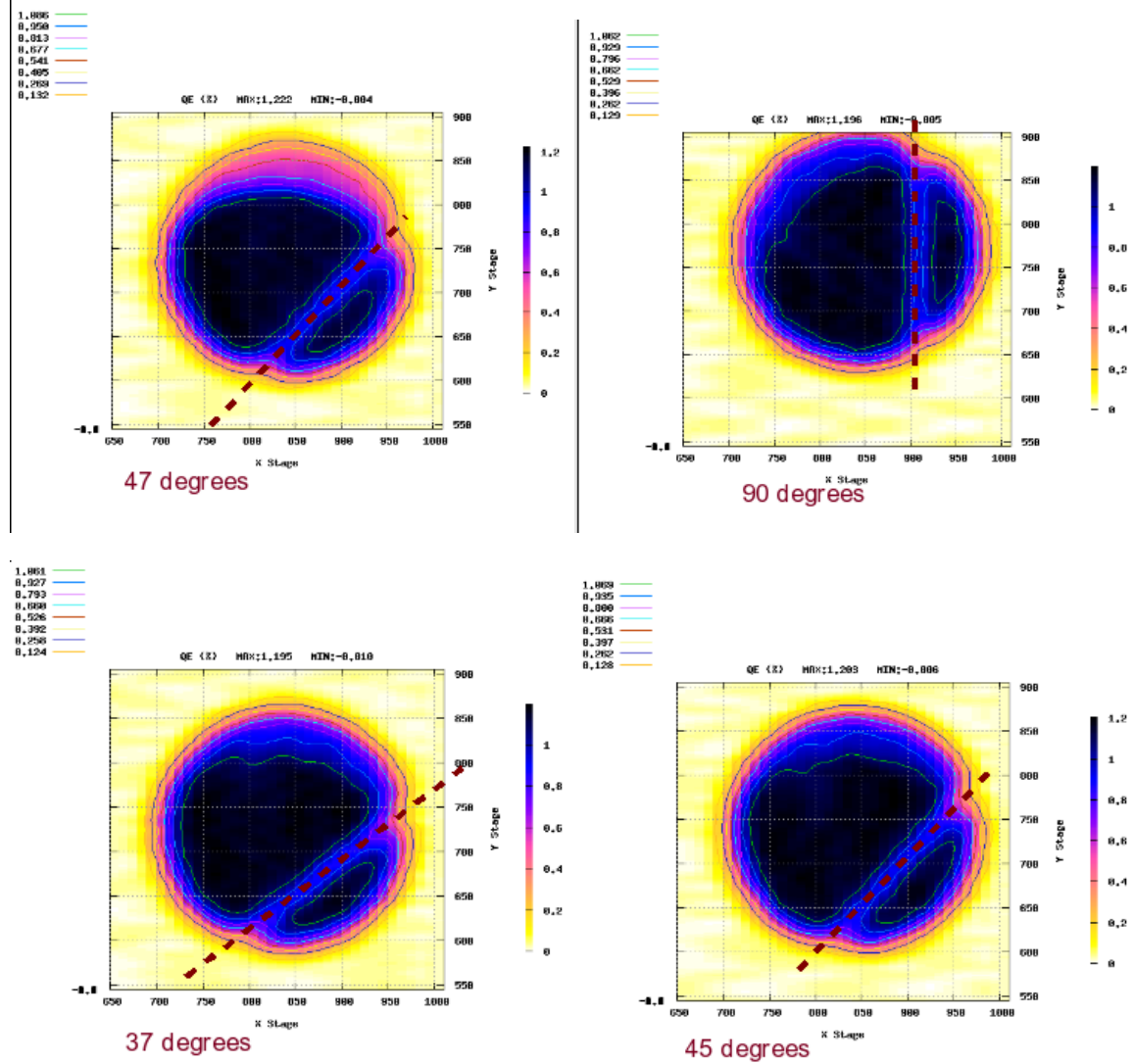
Figure 6.7.1: Quantum-Efficiency (QE) scan pictures of the new photocathode at different orientations. This photocathode had a crack on its surface that provided a reference point to determine its orientation.
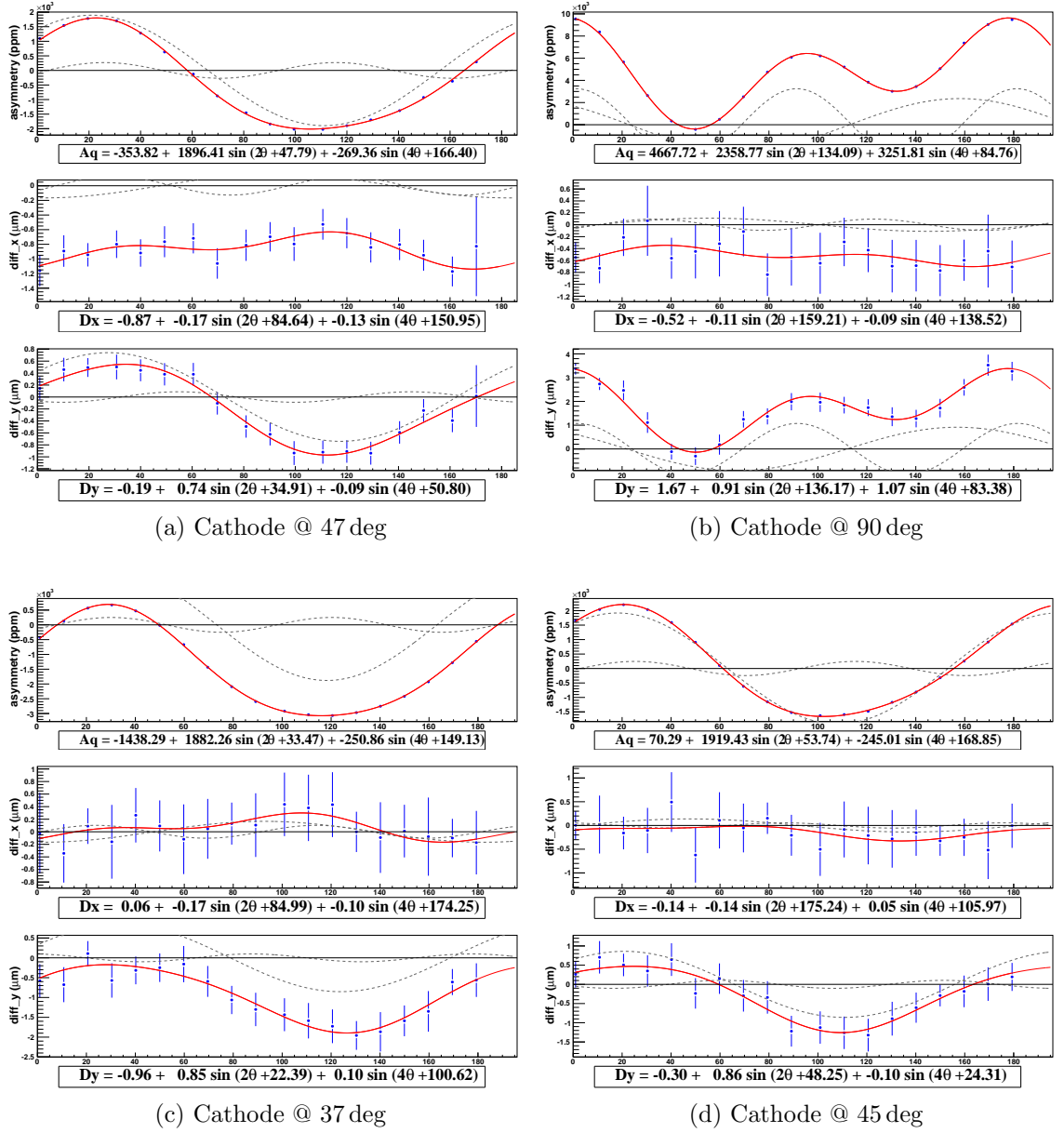
Figure 6.7.2: The new photocathode was rotated to suppress the polarization effects in the offset-terms of the RHWP scans. The offset-terms were suppressed best when the photocathode was at 45°, and least at 90°.

terms were satisfactorily suppressed. A representative set of photocathode orientations, and the corresponding RHWP scans are presented in Figures 6.7.1 and 6.7.2 respectively.

The offset-terms were suppressed best when the photocathode was at $45°$ and were largest when it was at $90°$. At $45°$, Aq offset-term is tiny. But the Dx and Dy offset-terms are still large, suggesting big phase-gradients in the vacuum-window or the analyzing power of the photocathode.

6.7.1.2   PC Translation

The new photocathode was replaced with the one previously used during these studies. However, the "old" photocathode was reactivated before being used again. This photocathode's orientation was adjusted in a processes similar to the one outlined above, and the offset-terms minimized.

The photocathode's orientation optimization suppressed the Aq offset-terms. But, the Dx and Dy offset-terms were still non-zero. Therefore, further PC translations were preformed to suppress these HC position differences. During the PC translations, the PC was remotely translated, and Dx and Dy responses to these translations measured. These measurements, along with the magnitude of Dx and Dy were then used to translate the PC to appropriate positions in x and y, and suppress Dx and Dy. PC translations only suppressed the offset-terms arising from non-polarization effects.

The characteristic RHWP scan plots of Figure 6.9 were taken after the offset-terms minimization with the photocathode's orientation adjustments and the PC translations. The 2θ and 4θ-terms in these plots are similar to the plots taken before these adjustments, Figure 6.8. But the offset-terms are much better suppressed in

the horizontal (in the picture) is approximated, and used as the photocathode orientation angle.

IHWP IN	**IHWP OUT**	

Aq = -125.15 + -1311.57 sin (2θ +55.10) + -118.14 sin (4θ +54.16)

Dx = 0.07 + -0.16 sin (2θ +53.81) + 0.05 sin (4θ +169.17)

Dy = 0.07 + -0.16 sin (2θ +62.46) + 0.06 sin (4θ +53.28)

Aq = 154.31 + 1305.10 sin (2θ +55.49) + 183.38 sin (4θ +34.78)

Dx = -0.03 + 0.19 sin (2θ +45.03) + -0.09 sin (4θ +152.06)

Dy = 0.00 + 0.24 sin (2θ +49.40) + -0.06 sin (4θ +91.29)

Aq = -93.16 + -1325.60 sin (2θ +29.04) + 3333.34 sin (4θ + 4.89)

Dx = 0.04 + -0.20 sin (2θ +29.32) + -0.36 sin (4θ +177.11)

Dy = 0.05 + -0.19 sin (2θ +16.20) + 0.53 sin (4θ + 2.65)

Aq = 130.55 + 1317.26 sin (2θ +29.91) + -3226.37 sin (4θ + 4.79)

Dx = -0.00 + 0.21 sin (2θ +25.61) + -0.39 sin (4θ + 7.11)

Dy = 0.06 + 0.24 sin (2θ +22.86) + -0.65 sin (4θ + 4.26)

PITA = 0 V

PITA = 120 V

Table 6.9: RHWP electron beam scan acquired after the photocathode orientation and the PC translation adjustments. These adjustments were performed after the PC alignment and voltage adjustments.

Figure 6.9 compared to Figure 6.8.

6.7.1.3   RHWP Angle Determination

The RHWP scans, besides being used to summarize the source setup, were also used to optimize the sensitivity of the analyzing elements to any residual linear polarization present in the laser light. Ideally an appropriate RHWP angle would be selected such that the HC position differences, along with the HC intensity asymmetry are zero, but the PITA slope is non-zero and big enough to allow charge feedback. In addition, at this ideal RHWP angle, the phase-gradients would be insensitive to PC voltage adjustments so that the HC position differences are unaffected by charge feedback.

The characteristic RHWP scans acquired after the final photocathode rotation and PC position adjustments were used to determine an appropriate RHWP angle. These plots from Figure 6.9 were replotted as presented in Figures 6.7.3(IHWP OUT) and 6.7.4(IHWP IN). In each of these plots, the first and the second columns are the RHWP scan plots at PITA offsets of zero and 120 V respectively, identical to those of Figure 6.9. In the third column are the PITA slope plots for each of the Aq, Dx and Dy plotted against the RHWP angle. These slopes are generated by using the scans at PITA offsets of zero and 120 V from the first and second columns. The Aq PITA slope, along with the Aq from RHWP scan at PITA offset of zero V are used to calculate the amount of voltage required to set Aq to zero, and plotted against the RHWP angle in the first plot of the fourth column. The other two plots of the fourth column plots the HC position differences Dx and Dy after these voltage corrections are made against the RHWP angle. The Dx and Dy PITA slopes, the Dx and Dy values from the zero PITA offset RHWP scan along with the voltage adjustments required to set Aq to zero are used to generate these plots. The asymptotes in these plots correspond to the RHWP orientation at which the HC effects are dominated

by the S2 polarization components of the beam; the S2 effects are insensitive to PC voltage adjustments.

With the plots of Figure 6.7.3 and 6.7.4, it is straightforward to determine the optimal RHWP angle. Since a non-zero Aq PITA slope is desirable, RHWP angles in the neighborhood of $\sim 40, 90, 135$ or $135°$ are ruled out. An RHWP angle where the Aq PITA slope is non-zero, and Dx and Dy PITA slopes are zero was highly desirable, but Dx and Dy PITA slopes closely tracked the behavior of the Aq PITA slope. So a non-zero Dx and Dy PITA slopes are unavoidable at a non-zero Aq PITA slope. More importantly, Dx and Dy also needed to be small at this RHWP angle. There are only a few RHWP angles where both the Dx and Dy are simultaneously zero or small (second two plots of the fourth column) after PC voltage adjustments are made to zero Aq. Of Figures 6.7.3 and 6.7.4, Figure 6.7.3 has more such RHWP angles, and smaller Dx and Dy compared to those of Figure 6.7.4. Since one optimal RHWP angle is desirable for both the IHWP states (IHWP OUT:Figure 6.7.3, IHWP IN:Figure 6.7.4), Figure 6.7.4 is used to extract the optimal RHWP angle: Dx and Dy are simultaneously minimum after the PC voltages adjustments, and the Aq PITA slope reasonably large to allow charge feedback at RHWP angles of ~ 50 and $150°$ in Figure 6.7.4. Although these angles are not optimal for Figure 6.7.3, the Dx and Dy are still reasonably small and the Aq PITA slope large as well. Thus, RHWP angles of ~ 50 and $150°$ are optimal for both the IHWP states. On testing each of these RHWP angles, $50°$ seemed slightly better. So the RHWP angle was set to $50°$.

6.7.2 Injector-Transmission

All the electron beam source studies presented so far were performed by using BPM1I02 alone, the BPM immediately downstream of the photocathode. But the beam passed through numerous other BPMs when it circulated around the accelerator and into
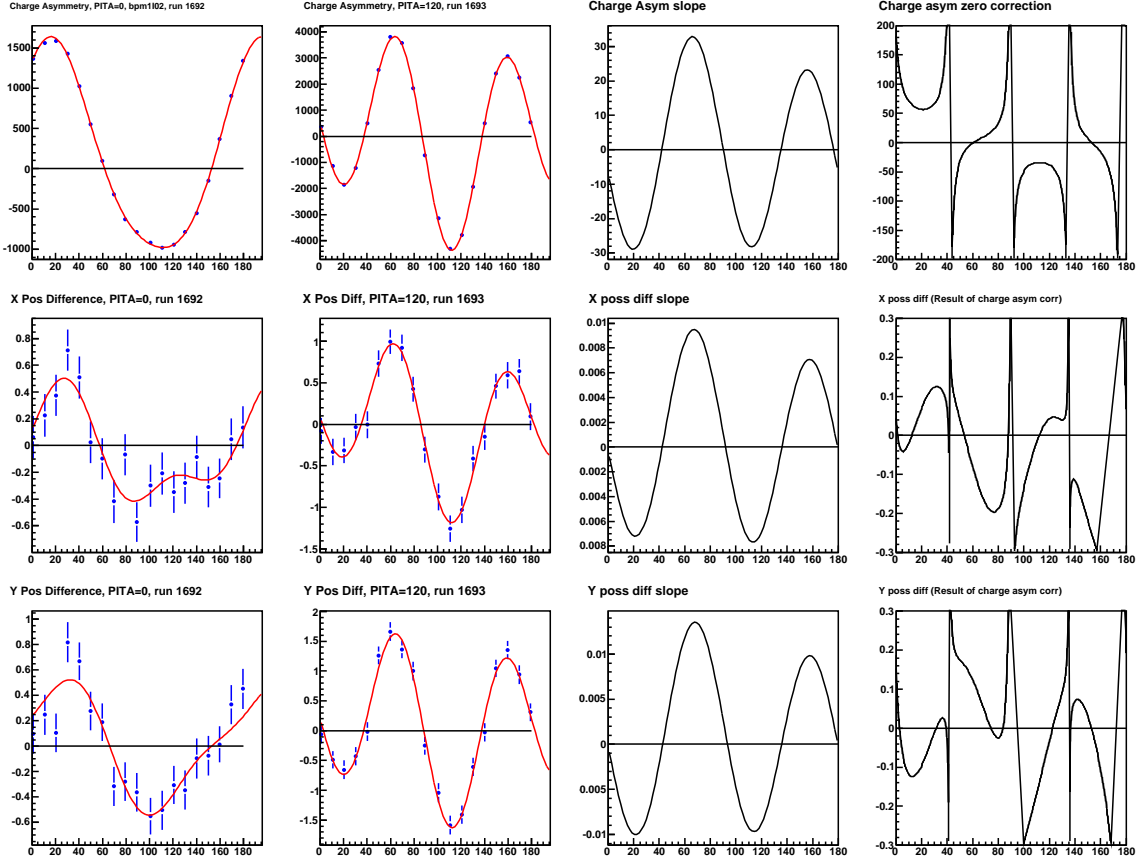
Figure 6.7.3: RHWP electron beam scans for IHWP OUT. The first and the second column were IHWP OUT RHWP scans from Figure 6.9 at PITA offsets of zero and 120 V respectively. The third column plots each of the Aq, Dx and Dy PITA slopes against the RHWP angle generated by using data from the first two columns. The topmost plot of the fourth column plots the amount of voltage required to set Aq to zero with RHWP angle, calculated by using the Aq PITA slope and the Aq from the first column. The other two plots of the fourth column plots the HC position differences Dx and Dy against the RHWP angle after these voltage corrections were made; these were calculated using the corresponding Dx and Dy PITA slopes, Dx and Dy values from the first column plot along with the voltage adjustments required to set Aq to zero. The asymptotes in these plots correspond to the RHWP orientation at which the HC effects were dominated by the S2 polarization components of the beam.
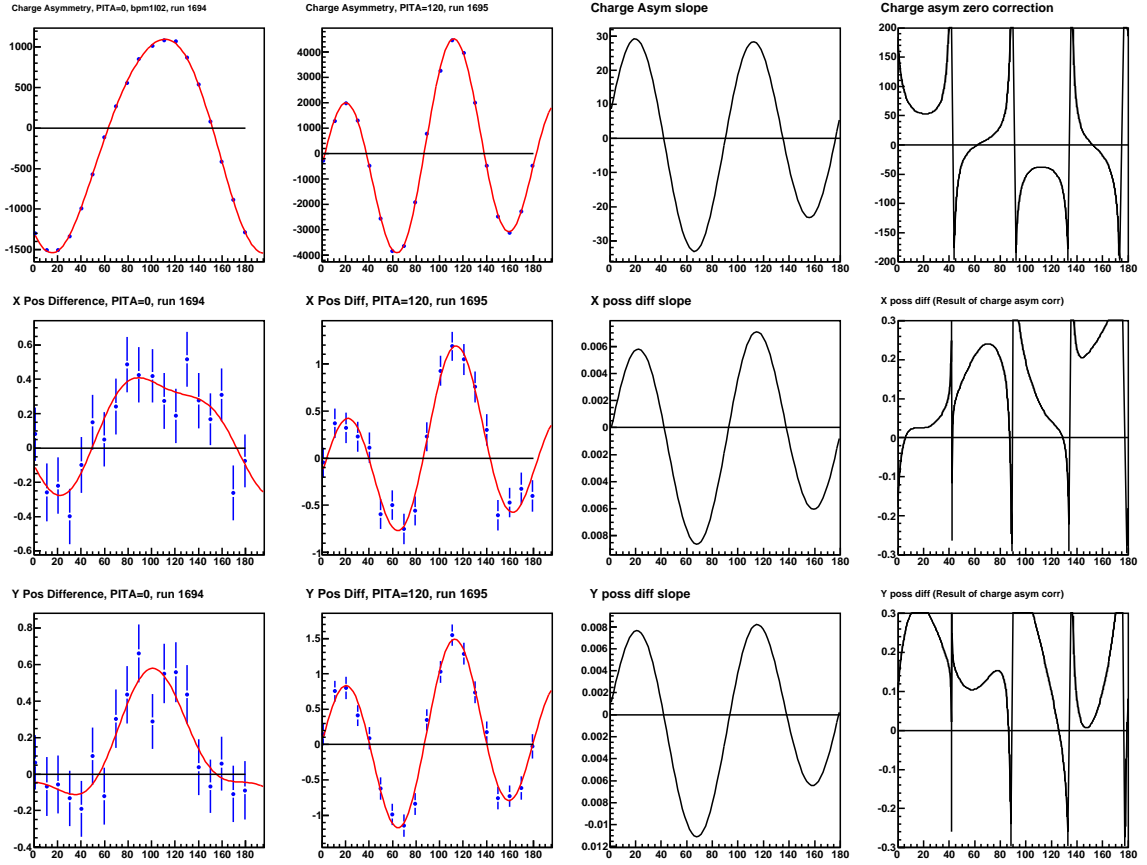
Figure 6.7.4: RHWP electron beam scans for IHWP IN presented in format identical to the one in Figure 6.7.3.
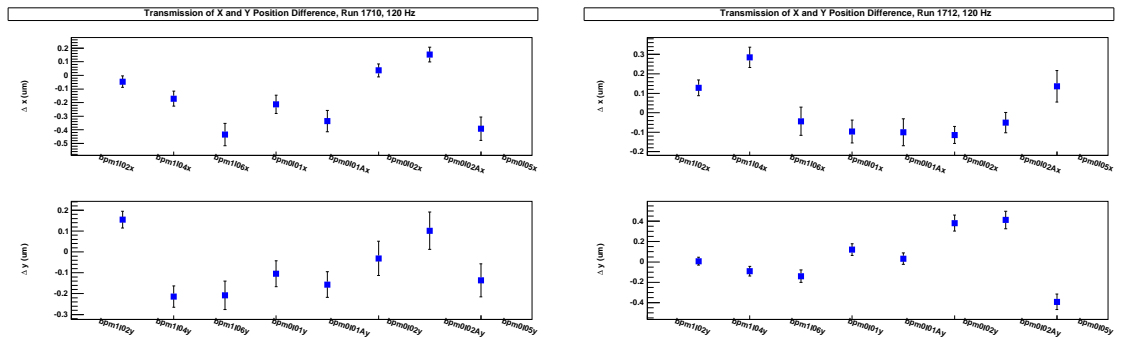
Figure 6.7.5: The HC position differences for optimized source setup. run#1710 is IHWP OUT, run#1712 is IHWP IN. On the y-axes the HC position differences in x and y are plotted. On the x-axis, the BPM that measured these parameters are plotted. The BPMs are arranged in the order in which the beam propagated through them, with the one closest to origin being the most upstream of the BPMs. The HC parameters averaged to zero, indicating a good injector setup.

the experimental hall. So, it was desirable to observe the beam HC parameters as it propagated along the accelerator. This was done by making *transmission plots*, like the ones displayed in Figure 6.7.5, in which the HC position differences measured by the BPMs are plotted against the BPMs. In Figure 6.7.5, the HC position differences in x and y are plotted on the y-axes and the BPMs on the x-axes. The BPMs are arranged in the order in which the beam propagated through them, with the one closest to origin being the most upstream of the BPMs.

In Figure 6.7.5, the HC position differences are not constant across the BPMs. This is because the BPMs measured only the position, and not the angle of the beam. As a result, minimizing only the HC position differences in one BPM could have left the HC differences in angle big, leading to big HC position differences across other BPMs. So an optimal HC parameters minimization with the BPMs required HC position differences minimization across multiple (at least two) BPMs simultaneously, so that the HC parameters spanning both the position and angle were minimized[1]. This optimization was achieved with only minor adjustments to the PC positions by performing PC translation scans, and utilizing the translation slopes to evenly distribute the HC position differences among the BPMs[2].

6.7.2.1   PC Turned Off

Figure 6.7.6 are transmission scans acquired with the PC turned off. This is a good check for any "ground-loop" contamination of the beam dynamics from the helicity control signals. The HC position differences averaged to zero indicating that the "ground-loop" contamination was virtually non-existent.

---

[1]These HC variations in position and angle may also have been affected by non-linearities in the beamline transport optics such as apertures or field imperfections.

[2]The HC position differences and their responses to PC translation varied between the BPMs. These results are presented in Appendix C.9.
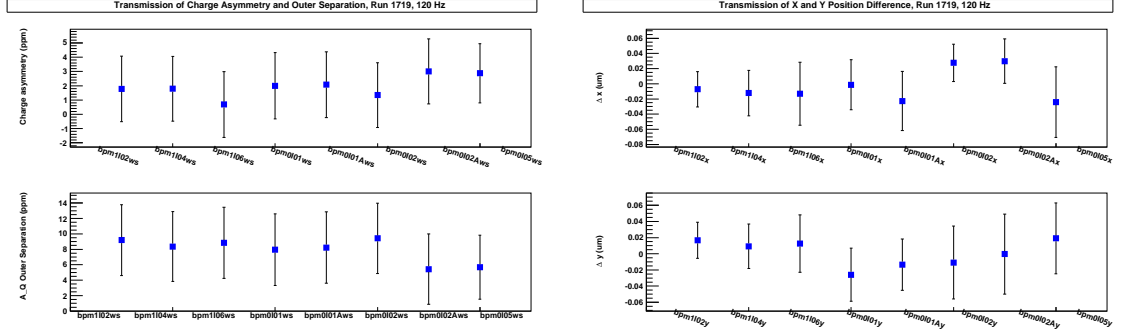
Figure 6.7.6: Transmission scan data acquired with the PC turned off, after source optimization. The HC charge asymmetry and the position differences averaged to zero, indicating no "ground-loop" contamination of the beam dynamics from the helicity control signals.

6.7.3 Wien Optimization

All the studies presented so far were performed without optimizing the Wien filter that was located between the photocathode and the first BPM (BPM1I02). Although this optimization was not expected to affect the results of the source studies, it was expected to improve other qualities of the beam. Thus, a Wien optimization was performed. This optimization, however, was preceded by PC translations that optimized the HC position and angle differences across the BPMs. The RHWP plots acquired after these adjustments, Figure 6.10, compared to those acquired before these adjustments, Figure 6.9 as follows:

- The offset-terms varies slightly, but are comfortably small in both the data sets. The variations in these terms are most likely the result of the PC position changes; the PC could have steered the beam to a different spot on the vacuum-window. As a result, the laser light could have experienced a different vacuum-window phase-gradient.

- The 2θ-term's coefficient changes from ~ 1314 ppm to ~ 1124 ppm, a decrease of $\sim 7\%$. Although this is a welcome change, the cause of this change was
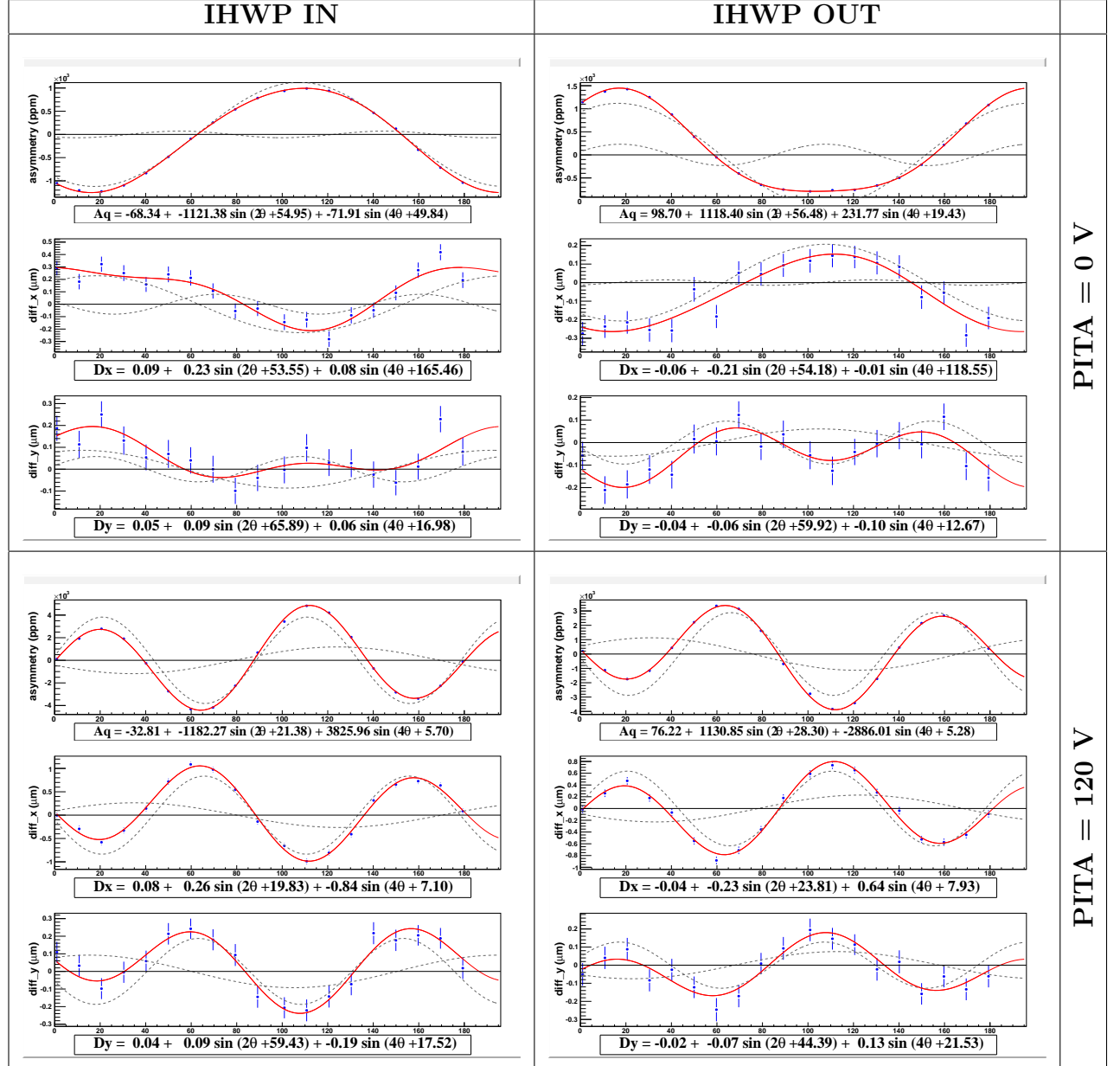
Table 6.10: RHWP scans acquired after the Wien optimization. The Wien optimization was preceded by further PC translations in order to optimize the HC position and angle difference across the BPMs.

a mystery: the sources of the 2θ-term were the RHWP's phase-shift and the photocathode's analyzing power, both of which haven't changed between these data sets.

- The 2θ-terms reverse sign between the data sets as well. The Wien adjustments, however, could only scale or mix the HC differences in position and angle, and not reverse the HC differences polarity outright. So, perhaps, the operational settings of the solenoid upstream of the Wien filter changed between the two data sets. The solenoid could reverse the polarity of the HC differences.

- The Aq 4θ-term remains relatively unchanged for zero PITA offset, but changes significantly for 120 V PITA offset. Figure 6.9 suggests Aq PITA slope of ~ 25 ppm for both IHWP states, while Figure 6.10 suggested Aq PITA slopes of ~ 31 and ~ 22 ppm for IHWP IN and OUT states respectively.

- All the Dx and Dy 4θ-terms reverse sign between the data sets as well, and there are substantial differences in Dx and Dy magnitudes in some cases.

Although the Wien optimization was not expected to affect the results of the source studies, the HC parameters of the electron beam at BPM1I02 are substantially altered by "something" that must have changed between the acquisition of plots of Figure 6.9 and the Wien optimized plots of Figure 6.10. Perhaps a dedicated Wien adjustment study was necessary in order to completely understand the sources of these HC parameters variations.

7

HAPPEX-III Analysis and Results

7.1 Overview

In HAPPEX-III, longitudinally polarized electrons, whose helicity was rapidly flipped, was scattered from unpolarized protons, and asymmetry in the scattering rate was measured between the complementary helicity-pairs. The experimental setup and the instrumentation of HAPPEX-III are described in Chapter 3. The asymmetry data were collected with the insertable half-wave plate (IHWP) state reversed about every 10^6 helicity-pairs. The IHWP reversal reversed the sign of the parity-violating (PV) asymmetry, A_{PV}, but left the sign of some of the false asymmetries unchanged. As a result, data from complementary IHWP states could be averaged to cancel these false asymmetries. The utility of IHWP reversal is described in Section 5.6.2. The data acquired over a period between two successive changes in the IHWP state were referred to as belonging to a "slug". HAPPEX-III collected a total of 28 acceptable slugs, that contained a total of 823 individual data runs. Typical data runs lasted about an hour, and a "good" one-hour run contained about 50 K pairs. However, many runs contained far fewer helicity-pairs. The final data set consisted of a total

of 29.9×10^6 helicity-pairs.

During HAPPEX-III, the helicity-pairs formed the helicity-correlated (HC) raw detector asymmetry, A_{raw}. A_{raw} included corrections for the HC beam intensity asymmetry, A_I, that arose from the HC beam intensity fluctuations. The evaluation of A_{raw} for HAPPEX-III is described in Section 7.2, and A_I is described in Sections 7.3.1 and 5.6.1. The corrected detector asymmetry, A_{corr}, was formed from A_{raw} as

$$A_{corr} = A_{raw} - A_F \qquad (7.1.1)$$

where A_F is the HC false beam asymmetry calculated as

$$A_F = A_{Fb} + A_{FT}. \qquad (7.1.2)$$

A_{Fb} is the HC false beam asymmetry arising from random fluctuations in the beam position, angle and energy, and A_{FT} is the HC false beam asymmetry arising from any transverse beam polarization. The PV asymmetry, A_{PV}, for HAPPEX-III was then evaluated as

$$A_{PV} = \frac{K}{P_b} \frac{A_{corr}}{1 - \sum_i f_i} - \frac{\sum_i A_i f_i}{1 - \sum_i f_i} \qquad (7.1.3)$$

where K is the kinematic (finite) acceptance correction, P_b is the beam polarization, f_i is the fractional background, and A_i the background asymmetry corresponding to the fraction f_i.

This chapter describes the extraction of the variables in the above equations, and the determination of the strange form-factors (FFs) from A_{PV}. The strange FFs, and how A_{PV} can be used to extract these FFs are described in Section 2.3.

7.2 Raw Asymmetry (A_{raw})

During HAPPEX-III, the raw asymmetry was formed as

$$A_{raw} = \left(\frac{D_R/I_R - D_L/I_L}{D_R/I_R + D_L/I_L} \right) \tag{7.2.1}$$

where $D_{R(L)}$ and $I_{R(L)}$ are the integrated detector and the beam current monitor (BCM) responses respectively of the right(left) helicity state in a helicity-pair [1]. The raw asymmetry was calculated for each high-resolution spectrometer (HRS) detector: left-HRS (LHRS) detector (det1) and right-HRS (RHRS) detector (det2).

A cumulative raw asymmetry of the two HRS detectors, A_{raw}^{all}, was also calculated as

$$A_{raw}^{all} = \frac{(S_R^1 w^1 + S_R^2 w^2) - (S_L^1 w^1 + S_L^2 w^2)}{(S_R^1 w^1 + S_R^2 w^2) + (S_L^1 w^1 + S_L^2 w^2)} \tag{7.2.2}$$

where $S_{R(L)}^i = D_{R(L)}^i / I_{R(L)}$ is the integrated response of the ith detector (det1, det2) normalized to the response of the BCM for the right(left) helicity state of a helicity-pair, and the weight w^i is the ith detector weight. The weights corrected for differences in the size of the detector responses that arose primarily because of differences in the electronics used to read out the detectors: det1 was read out into a 16-bit analog-to-digital converter (ADC) while det2 was read out into a 18-bit ADC. As a result, when the integrated responses of det1 was ~ 52 K ADC channels, the response of det2 was ~ 156 K ADC channels at similar electron flux [2]. Similar distribution widths of the asymmetry measured by each detector indicated similar electron flux [3]. Therefore,

---

[1]HAPPEX-III used helicity-quartet, but analyzed the asymmetry data as helicity-pairs. PREX, on the other hand, used helicity-quartet, and also analyzed the asymmetry data as helicity-quartet. The helicity pattern used during HAPPEX-III is described in Section 3.4 and Section 5.7.

[2]These were typical detector responses with 100 μA beam on the liquid-hydrogen (LH2) cryo-target at HAPPEX-III experimental kinematics.

[3]The electron flux at each detector was also counted using the Hall A standard detector package described in Section 3.9.2.

normalizing the size of the detector responses was necessary for proper statistical weighting, which was performed by the weights. During HAPPEX-III, det1 was used as the reference detector and assigned a weight of $w^1 = 1$. Then the det2 weight was calculated as $w^2 = 52/156 \sim 0.33$.

An average cumulative raw asymmetry of the two detectors was also evaluated as

$$A_{raw}^{ave} = \frac{A_{raw}^1 w^1 - A_{raw}^2 w^2}{w^1 + w^2} \tag{7.2.3}$$

where $A_{raw}^{1(2)}$ are det1(det2) raw asymmetries evaluated using Eq. 7.2.1.

A_{raw}, in addition to including the PV asymmetry, also contains any false asymmetries that arise due to HC beam effects, and periods of beam and instrumentation instabilities. Some of these false asymmetries were discarded with appropriate choice of cuts on the data (that selectively threw away unacceptable data), and others were measured and A_{raw} corrected explicitly.

7.2.1   Data Selection and Cuts

Numerous cuts were imposed on the data to reject unusable or compromised data. The cuts were strictly non-helicity correlated i.e. cuts were never made on any HC asymmetries or HC position differences. The cuts were used to check for instabilities in the helicity signals, beam intensity, position, angle and energy, and instrument malfunctions. There were three distinct types of cuts: helicity sequence cuts, beam instability cuts and equipment malfunction cuts.

- The helicity sequence cuts located data with incorrect helicity sequence and discarded them. The helicity sequence used during HAPPEX-III is described in Section 3.4. These cuts were implemented by comparing the helicity pattern recorded in the data with the expected helicity pattern. The HAPPEX-III

parity-analyzer software (PAN) [PAN] ran a copy of the pseudo-random helicity generator algorithm identical to the one used to generate the beam helicity pattern. PAN used this helicity information to check for any missing or corrupt events in the helicity information read into the data stream [1]. The helicity-pairs corresponding to the events that failed the helicity sequence cut were discarded. 25 events before and after each event that failed this cut were discarded as well.

- Beam instability cuts located data with periods of large beam instabilities that rendered the data unacceptable and discarded them. These instabilities caused electron rate fluctuations at the detectors and monitoring devices, and increased the sensitivity of these devices to instrument non-linearities. The instrument non-linearities introduce false asymmetry and systematic uncertainties in the measured asymmetry, as described in Section 5.5.

For HAPPEX-III data, unacceptable beam conditions included periods of beam trips, event-to-event variations in the response of the BCMs of more than $\sim 2\%$ at 100 μA beam current, fluctuations in the responses of the beam position monitor (BPM) 12x/y of more than 200 nm, energy drifts resulting in the responses of BPM12x of more than 200 nm [2], and beam position and energy drifts resulting in more than $\sim 3\%$ change in the cumulative responses of the 4-stripline wires of BPM12 (BPM12ws). The BPM instrumentation and how its responses determine beam positions are described in Section 3.5.2. 10(400) events were discarded before(after) every beam trip event and 10(40) events were discarded before(after) every unacceptable event resulting from beam instabilities other

---

[1]The helicity read into the data stream was delayed by eight windows behind the beam helicity to suppress electronics crosstalk. Therefore, PAN was adjusted to perform the helicity pattern check with an offset of eight helicity windows.

[2]BPM12x was located in the region of high dispersion where the beam was bent into Hall A. As a result, BPM12 was sensitive to fluctuations in beam energy. The location of BPM12 along the beamline is illustrated in Figure 3.5.1 of Section 3.5.

than the beam trips. The size of the discarded events were empirically determined to allow sufficient time for the detectors and monitors to fully recover from the instabilities, and avoid non-linearities.

- The equipment malfunction cuts located data corresponding to periods of equipment malfunctions and discarded them. Periods of equipment malfunctions included periods of BPMs (specifically BPM12) saturation, a non-functional HRS (one or both) and ADC internal errors.

  The data collected with periods of BPM12 saturation were discarded because BPM12 was the primary BPM used to correct for false asymmetries arising from random fluctuations in beam energy. Without reliable BPM12x data, such corrections for the effects of random fluctuations in energy could not be performed. These corrections as described in Section 5.8, and the corrections performed for HAPPEX-III data are described in Section 7.3.2.

  Failure of one or more of the HRS magnets resulted in a non-functional HRS. Usually, only one of the HRS was non-functional at a time, with the other HRS fully operational. During these instances, only the data collected in the functional HRS was retained. In instances when both HRSs were non-functional, no data were acquired, or any data acquired discarded.

  The internal ADC errors were intermittent and resulted in inconsequential amounts of data loss.

All the low current (< 60 μA) data were discarded to ensure that most of the data were collected at similar rates. The low current data made up a negligible fraction of the total data collected, and contributed marginally to the statistics.

The amount of data discarded by the cuts discussed above are summarized in Table 7.1. All but the HRS-nonfunctional cuts were applied by PAN during standard

	# Pairs(10^6)	Frac(%)
Beam Instability	–	–
Low beam	6.86	17.97
Beam inten. fluc	1.34	3.50
Beam pos. fluc	3.00	7.86
Equip. Malfunction	1.27	3.34
Mon. saturation	0.52	1.37
HRS non-func.	0.75	1.97
Helicity Sequence	0.0	0.0

Table 7.1: The amount of helicity-pairs discarded by various cuts used during HAPPEX-III data quality verification are presented above. These cuts, except for the HRS non-functionality cut, were enforced by PAN independent of one another, i.e. same "bad" pairs could be discarded by more than one cut. The numbers above only reflect the net pairs discarded by each cut, without considering the overlap between the pairs discarded by various cuts. A total of 38.2×10^6 helicity-pairs were collected during HAPPEX-III, of which only 29.9×10^6 passed the data quality cuts.

analysis. PAN applied these cuts independently of one another. As a result, the same helicity-pair could be discarded by more than one cut. The numbers in Table 7.1 only reflect the net amount of helicity-pairs discarded by each cut, and do not account for the overlap between the cuts. The periods of HRS non-functionality were kept track of manually, and the corresponding cuts enforced after the standard PAN analysis. A total of 38.2×10^6 helicity-pairs were collected during HAPPEX-III, of which only 29.9×10^6 passed the data quality cuts. The final data set consisted of 28.9×10^6 helicity-pairs collected with both HRS functional simultaneously, 0.5×10^6 helicity-pairs collected with only the LHRS functional (on det1) and 0.5×10^6 helicity-pairs collected with only the RHRS functional (on det2).

Figure 7.2.1: The raw detector helicity-pair asymmetry distributions of HAPPEX-III data are presented above. det1 distribution includes all the "good" helicity-pair asymmetry acquired with the LHRS detector and det2 distribution includes all the "good" helicity-pair asymmetry data with the RHRS. det_all and det1 − det2 distributions only include the "good" helicity-pair asymmetry data when both LHRS and RHRS were functional. det1, det2 and det_all distributions are Gaussian over six orders of magnitude, indicating that these distributions are dominated by counting statistics.
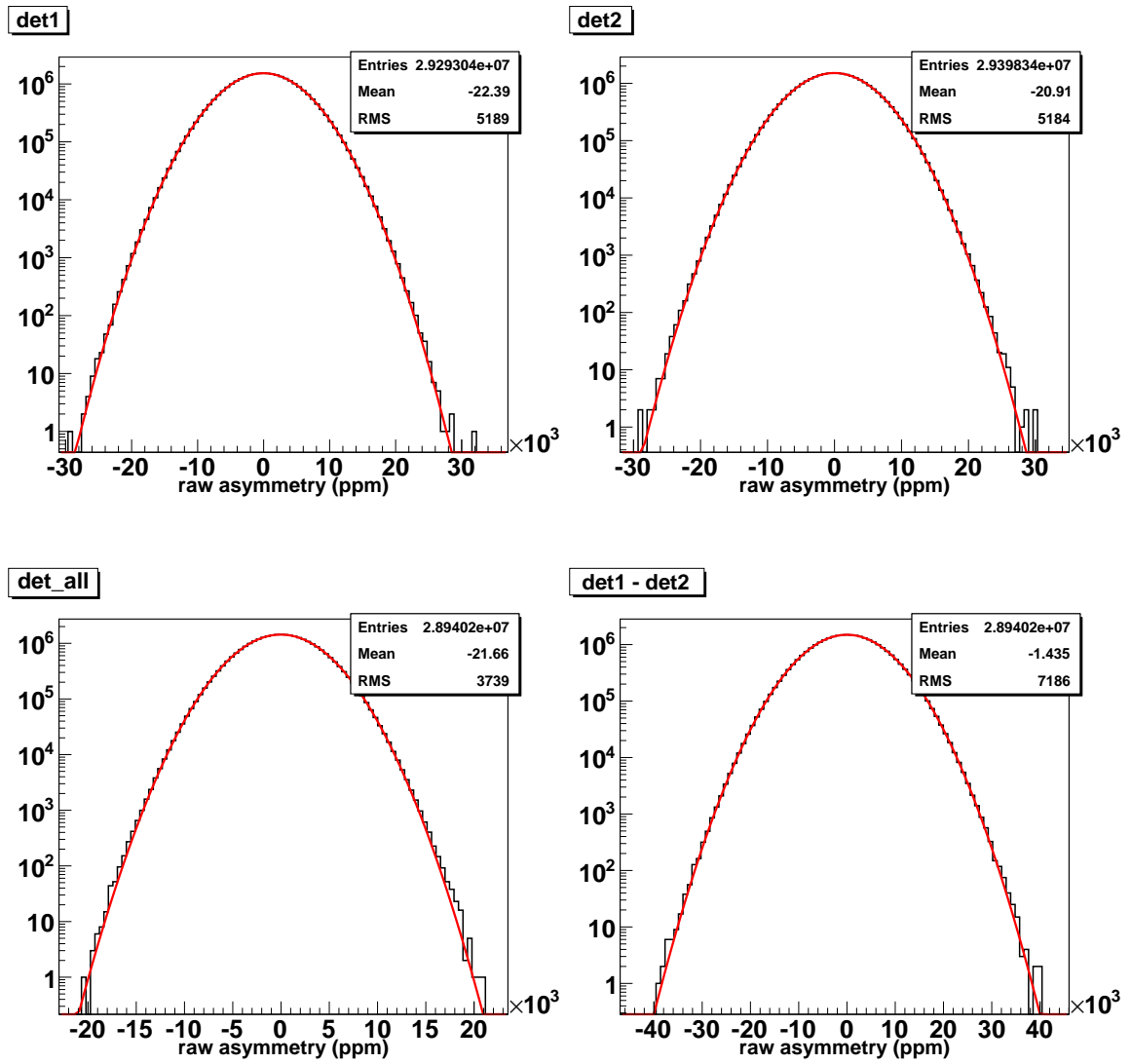
After imposing the data cuts discussed above, and verifying the data quality, the raw asymmetry, A_{raw}, measured during HAPPEX-III was [1]

$$\boxed{A_{raw} = -21.577 \pm 0.688(\text{stat}) \text{ ppm}}$$

where the uncertainty is statistical. The distribution of the helicity-pair raw asymmetries are shown in Figure 7.2.1.

7.3 False Beam Asymmetry

The A_{raw} measured by the detectors also included the false beam asymmetries that arose due to random fluctuations in the beam intensity, energy and trajectories at the target, as well as the false beam asymmetries that resulted from any transverse polarization present in the beam. Therefore, A_{raw} had to be corrected for these false beam asymmetries.

Left unchecked, electronic pickup also results in false asymmetries in A_{raw}. However, appropriate measures were taken that sufficiently suppressed the electronic pickups, and did not affect A_{raw}. These measures included delaying the helicity read into the data stream by 8 windows to break any correlation to the true beam helicity. The helicity generator (HG) electronics were also contained in an isolation cage and powered by batteries in order to completely isolate their ground. The HG is discussed in Section 3.4. The resulting false asymmetries due to electronic crosstalk were negligible compared to the false beam asymmetries.

---

[1]This is statistically weighted asymmetry evaluated following the process discussed in Section 7.5. There is also a systematic uncertainty in A_{raw}, which is not shown here.

7.3.1 Beam Intensity Asymmetry (A_I)

The HC beam intensity asymmetry, A_I, arose due to HC beam intensity fluctuations, and was evaluated as

$$A_I = \frac{I_R - I_L}{I_R + I_L} \tag{7.3.1}$$

where $I_{R(L)}$ is the integrated response of the beam cavity monitors (BCMs) for the right(left) helicity state of a helicity-pair. The PV raw asymmetry measured by the detectors, A_{raw}, would also include a false asymmetry due to A_I if left uncorrected. Therefore, A_{raw} was corrected for A_I by normalizing the integrated response of the detectors by the integrated response of the BCM for each helicity state on a pulse-by-pulse basis. This normalization is presented in Eq. 7.2.1.

All the beam monitors (BCMs and BPMs) were sensitive to A_I, but during HAPPEX-III, only the integrated response of BCM1, the BCM immediately upstream of the target, normalized the detectors' integrated response. This BCM measured an average [1] A_I of [2]

$$\boxed{A_I = -237 \pm 8 \text{ ppb}}$$

over the course of the run, with the uncertainty above determined as

$$\sigma_{A_I} = \text{BCM}_{\text{res}}/\sqrt{N} \tag{7.3.2}$$

---

[1]This is the statistically weighted average. See Section 7.4 for further details on statistical weighting.

[2]In the HAPPEX-III publication [Ah12], $A_I = -202$ ppb. The differences in A_I presented here and HAPPEX-III publication is because of differences in the weighting used to determine A_I. The A_I presented here is determined using the technique discussed in Section 7.4, while the A_I in the publication uses a similar technique, but with one important difference: for the runs during which part of the data were acquired on the single HRS detector (det1 *or* det2 only) and the rest on both HRS detectors (det1 *and* det2), only the data acquired with both HRS detectors weighted the A_I for periods of both the single and both HRS data in the publication. However, the A_I reported here is determined by weighting the A_I acquired during both HRS running with both HRS data and those acquired during single HRS running with single HRS data. Nevertheless, the A_{PV} in the publication is not affected, because A_I affects only the accounting for the estimated correction in A_{PV}. Therefore, A_I of -202 ppb is wrong, but the A_{PV} in the publication is correct.
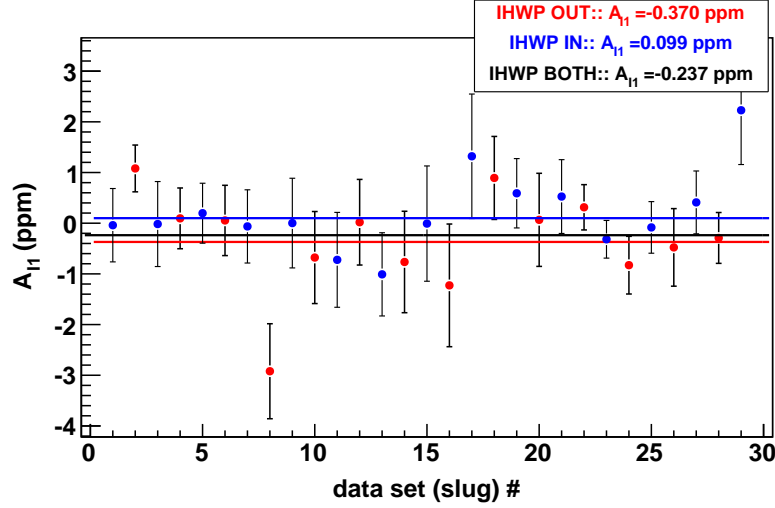
Figure 7.3.1: The helicity-correlated (HC) beam intensity asymmetry calculated from the response of the beam current monitor # 1 (BCM1), the one located immediately upstream of the target, A_{I1}, is presented by insertable half-wave plate (IHWP) states above. Each data point is a "slug" summary that consists of $\sim 10^6$ helicity-pairs.

where $N(= 29.9 \times 10^6)$ is the total number of helicity-pairs collected over the experiment, and $\text{BCM}_{\text{res}}(= 43 \text{ ppm})$ is the estimated resolution of the BCM. The BCM resolution was determined from the differences in the HC beam intensity asymmetries measured by BCM1 (A_{I1}) and BCM2 (A_{I2}) as

$$\text{DD}_{12} = A_{I1} - A_{I2}. \tag{7.3.3}$$

DD_{12} is referred to, within the context of this work, as the double-difference (DD) of BCM1 and BCM2. Assuming similar resolutions for each BCM, the BCM resolution is given as $\sigma_{\text{DD}_{12}}/\sqrt{2}$. The width of DD_{12} distribution gives the BCM resolution because the HC beam intensity asymmetries cancel in DD.

BCMs 1 and 2 were both located upstream of the target, and were separated by ~ 3 meters. The location of these BCMs relative to the target is illustrated in Figure 3.5.1 of Section 3.5. These BCMs provided independent HC beam intensity

IHWP state	A_I (ppb)
OUT	-370
IN	99
BOTH	-237

Table 7.2: The helicity-correlated (HC) beam intensity asymmetry measured over the course of HAPPEX-III in parts-per-billion (ppb).

measurements.

A_I distributions by slug for each IHWP state, along with cumulative averages of the IHWP states are presented in Figure 7.3.1. Table 7.2 lists the A_I averages by IHWP states for the whole run.

7.3.2   False Beam Asymmetry due to Beam Fluctuations (A_{Fb})

The sensitivity of the scattering cross-section to random fluctuations in the beam position, angle and energy led to HC rate variations at the detectors that gave rise to false beam asymmetry, A_{Fb}. These fluctuations were the largest source of noise beyond counting statistics in A_{raw}. Typical beam jitter between complementary states in the window-pairs was less than 5 ppm [1] in energy, and 14 μm in position. A_{raw} was corrected for A_{Fb} and the associated noise reduced via two independent techniques: beam modulation (BM) and regression.

HAPPEX-III used the results of both the BM and regression technique to correct A_{raw}: slugs 0-2 were regression corrected and slugs 3-28 were BM corrected. This was necessitated by the unavailability of BM data for slugs 0-2; the BM system was not functional until slug 3. The regression results of slugs 3-28 were used to cross-check BM corrected results. After A_{Fb} correction, the noise in the resulting detector

---

[1]The window-pairs jitter measured on BPM12x, averaged over the course of HAPPEX-III, was $\sim$ 19.08 μm. This translates to 19.08μm/4.0m $\sim$ 5 ppm. 4 m is the dispersion length.

asymmetry ($= A_{raw} - A_{Fb}$) was about 3733 ppm [1] per helicity-pair (compared to a similar asymmetry width of about 3733 ppm before correction, i.e. the asymmetry width broadening due to A_{Fb} was negligible) at the nominal HAPPEX-III beam current of 100 μA. This noise was dominated by counting statistics, corresponding to a rate of about 500 KHz at a beam current of 100 μA. The noise due to A_{Fb} was negligible.

7.3.2.1 Beam Modulation (BM) Correction

HAPPEX-III used the BM system to correct A_{raw} for the false beam asymmetry (A_{Fb}) arising from random fluctuations in beam position (x, y), angle (θ_x, θ_y) and energy (ΔE). The BM system performed controlled excursions of the beam in position, angle and energy, and measured the responses of the detector and BPMs to these excursions. These responses were encoded as [Hu03]

$$\mathbf{B}_{ij} = \frac{\partial M_i}{\partial C_j} \qquad \mathbf{D}_{kj} = \frac{\partial d_k}{\partial C_j} \qquad (7.3.4)$$

where i runs over five beam parameters $M(x, y, x', y', E)$ extracted from the responses of BPMs 4ax, 4ay, 4bx, 4by and 12x respectively. j runs over the eight modulation coils and k runs over the responses of the two detectors (det1,det2), normalized to the response of the BCM ($d_k = D_k/I_k$).

BPMs 4a and 4b were located immediately upstream of the target. BPM12x was located at the arc, where the beam was bent before being transported into the hall. Therefore, BPM12x was sensitive to fluctuations in beam energy, E. Together, this

---

[1]These numbers are the distribution widths of the detector combination asymmetry A_{raw}^{all} for slugs 3-28 data: the uncorrected A_{raw}^{all} distribution width was 3733 ppm, and the associated distribution widths of regression and BM corrected asymmetries were 3731 and 3733 ppm respectively. For slugs 0-28 data, the distribution widths of A_{raw}^{all} was 3745 ppm, and the associated regression corrected distribution width was 3743 ppm.

set of five BPMs monitored beam position, angle, and energy fluctuations. The BM system used during HAPPEX-III is described in Section 3.12.

The responses of the BPMs and the kth detector were then used to calculate A_{Fb} in the kth detector asymmetry as

$$(A_{Fb})_k = \frac{1}{2\bar{d}_k} \sum_{i=1}^{5} \beta_{ik} \Delta M_{LR,i} \qquad (7.3.5)$$

where $\beta_{ik} = \partial d_k / \partial M_i$, also referred to herein as the BM coefficient, is the average (normalized) response of the detector to the response of the ith BPM to fluctuations in the beam parameters M. $\Delta M_{LR,i}$ is the HC position difference $(\Delta x, \Delta y)$ determined from the response of the ith BPM to the fluctuations in beam parameters M. The fluctuations in E was measured by BPM12x as HC position difference (along x). $\bar{d}_k = \frac{1}{2}\langle d_{R,k} + d_{L,k}\rangle$ is the response of the kth detector averaged over the helicity states of a helicity-pair. The formalism of the BM system is described in [Hu03].

Typical BPM responses during a BM cycle are presented in Figure 7.3.2. A complete cycle comprised of the beam excursion horizontally four times (red traces), vertically three times (blue traces), and in energy once (magenta trace). The beamline optics were configured to establish an orthogonal set in the space of beam position, angle, and energy.

The responses of the target BPMs, 4a and 4b, like those presented in Figure 7.3.2 were used, along with the separation between the BPMs and the distance of the BPMs from the target, to extrapolate the beam position and angle responses at the target. These extrapolations are presented in Figure 7.3.3. Detector responses corresponding to the beam excursions in Figure 7.3.2 and 7.3.3, representative of typical detector responses during a BM cycle, are presented in Figure 7.3.4. The BM coefficients averaged over the course of HAPPEX-III are presented in Table 7.3.
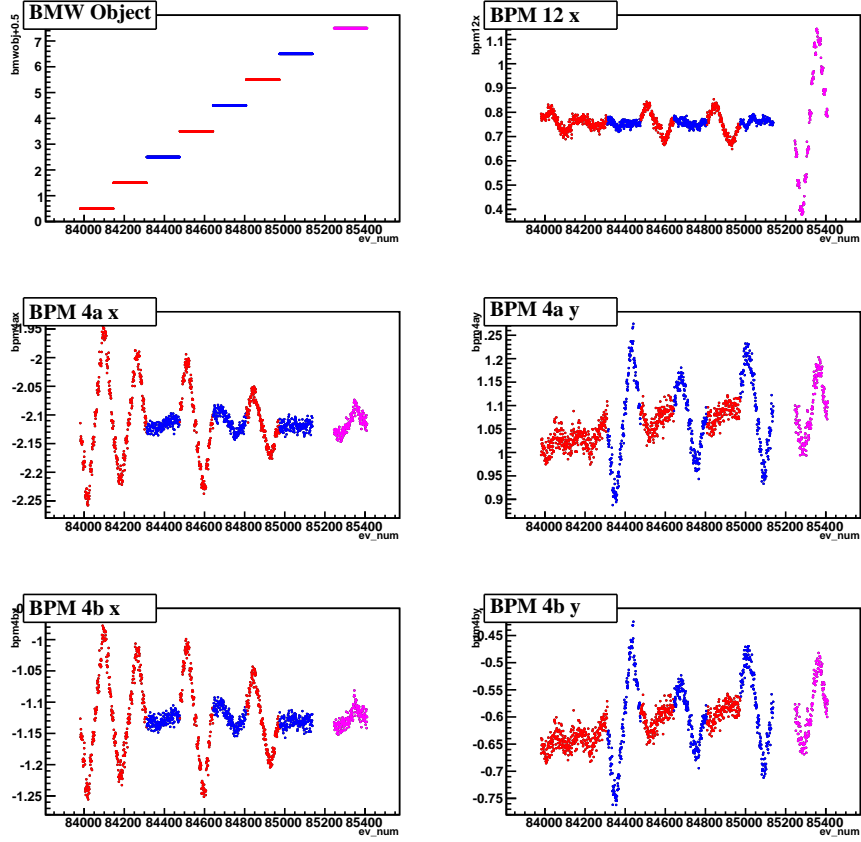
Figure 7.3.2: During HAPPEX-III, the BM system performed controlled excursions of beam in position and energy to measure the false beam asymmetries arising from random fluctuations in these parameters, A_{Fb}, and correct A_{raw}. The traces in the red are x-position modulation, blue are y-position modulation and magenta are energy modulation. BPMs 4a and 4b measured fluctuations in beam position, and BPM12x measured fluctuations in beam energy.

	det1(LHRS)	det2(RHRS)	det_all(Both HRS)
BPM4ax	5.06 ± 0.77	-3.00 ± 0.74	0.99 ± 0.69
BPM4ay	-2.68 ± 1.27	-1.32 ± 1.21	-1.92 ± 1.13
BPM4bx	-10.05 ± 0.84	5.11 ± 0.81	-2.35 ± 0.75
BPM4by	6.09 ± 1.48	2.97 ± 1.42	4.42 ± 1.32
BPM12x	-0.26 ± 0.07	0.071 ± 0.062	-0.085 ± 0.058

Table 7.3: The BM coefficients ($\beta_{ik} = \partial d_k / \partial M_i$ of Eq. 7.3.5) in units of ppm/μm averaged over the course of the run.
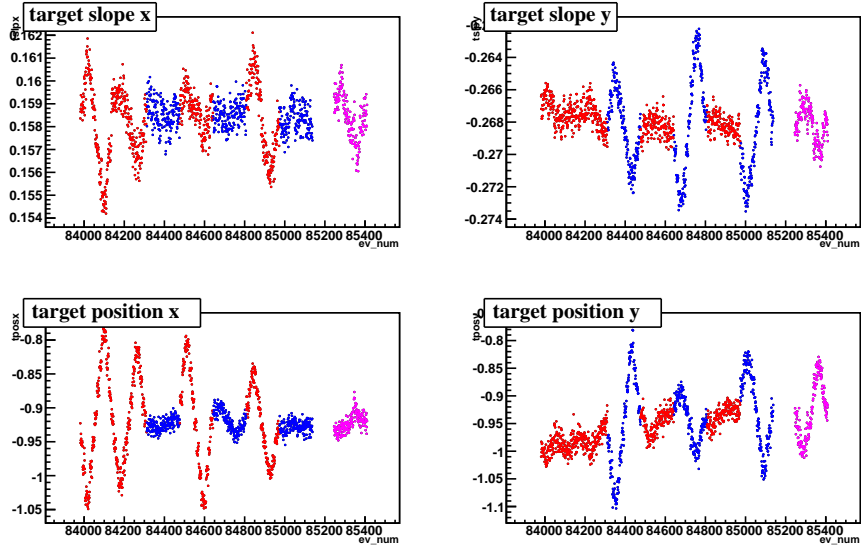
Figure 7.3.3: The BM responses at the target corresponding to the modulation cycle of Figure 7.3.2 are presented above. The responses at the BPMs 4a and 4b, along with the distance between them and their distances from the target are used to extrapolate the BM responses in position and angle at the target. The traces in the red are horizontal (x-position) modulation, blue are vertical (y-position) modulation and magenta are energy modulation.
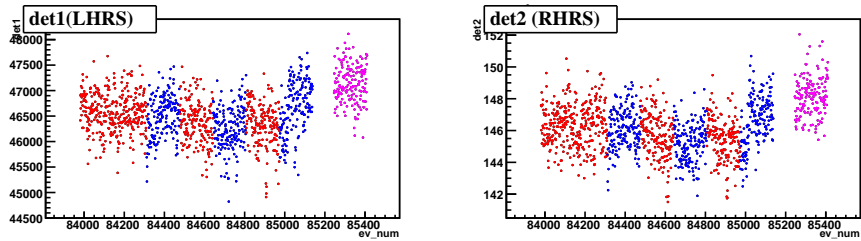
Figure 7.3.4: Typical detector responses during a BM cycle are presented above. The traces in the red are horizontal (x-position) modulation, blue are vertical (y-position) modulation and magenta are energy modulation. Due to weak detector responses to excursions in beam position, angle and energy, repeated measurements were needed to extract the detector responses to these fluctuations with the necessary precision. However, the weak responses of the detectors also allowed all the BM cycle data to be used as asymmetry data.

	Δ(nm)	A_{fluc}^{det1} (ppb)	A_{fluc}^{det2} (ppb)	$A_{fluc}^{det\_all}$ (ppb)
BPM4ax	-2.29	-11.6	6.9	-2.3
BPM4ay	-1.99	5.3	2.6	3.8
BPM4bx	0.13	-1.3	0.7	-0.3
BPM4by	-2.44	-14.9	-7.2	-10.8
BPM12x	12.40	-3.2	0.9	-1.1
Total	–	-25.6	3.8	-10.6

Table 7.4: The BM corrections, A_{fluc}^{i}, to the corresponding raw detector asymmetries, A_{raw}^{i}, averaged over the course of HAPPEX-III running. The HC beam position differences summarized in Table 7.6 are also listed on the first column. The fluctuations in the beam position and angle (BPMs 4a and 4b) dominated the corrections, with only a small correction resulting from fluctuations in beam energy (BPM12x).

The HC position differences along with the corresponding A_{Fb} averaged over the course of HAPPEX-III are presented in Table 7.4. The HC position differences are discussed in Section 7.4. The BM correction reduced the width of $\langle A_{raw} \rangle$ distribution by about 1 ppm, a negligible amount, indicating that both A_{raw} and $A_{raw} - A_{Fb}$ were dominated by the counting statistics. The correction arising from the fluctuations in energy (BPM12x) was small compared to those arising from fluctuations in beam position and angle (BPMs 4a and 4b) at the target. The total BM correction was only -10 ppb, which was a tiny correction to A_{raw} of -21.576 ppm. This small correction was the result of small rate variations at the detectors arising from the beam position, angle and energy fluctuations, and also due to small HC position differences.

The BM corrected asymmetries were Gaussian over six orders of magnitude as illustrated in Figure 7.3.5. This indicated that the asymmetry distributions were dominated by the counting statistics, and that the data had very little window-to-window instrumentation and residual noise.

Figure 7.3.5: The BM corrected detector asymmetry by helicity-pairs are presented above. This data set only includes slugs 3-28 data because the BM system was not functional during the acquisition of slugs 0-2 data, and, hence, slugs 0-2 could not be corrected via the BM technique. det1 distribution includes all the "good" helicity-pair asymmetry acquired with the LHRS detector and det2 distribution includes all the "good" helicity-pair asymmetry data with the RHRS. det_all and det1 − det2 distributions only include the "good" helicity-pair asymmetry data when both LHRS and RHRS were functional. det1, det2 and det_all asymmetry distributions are Gaussian over six orders of magnitude indicating that the distributions are dominated by counting statistics, and that the data had very little window-to-window instrumentation and residual noise.
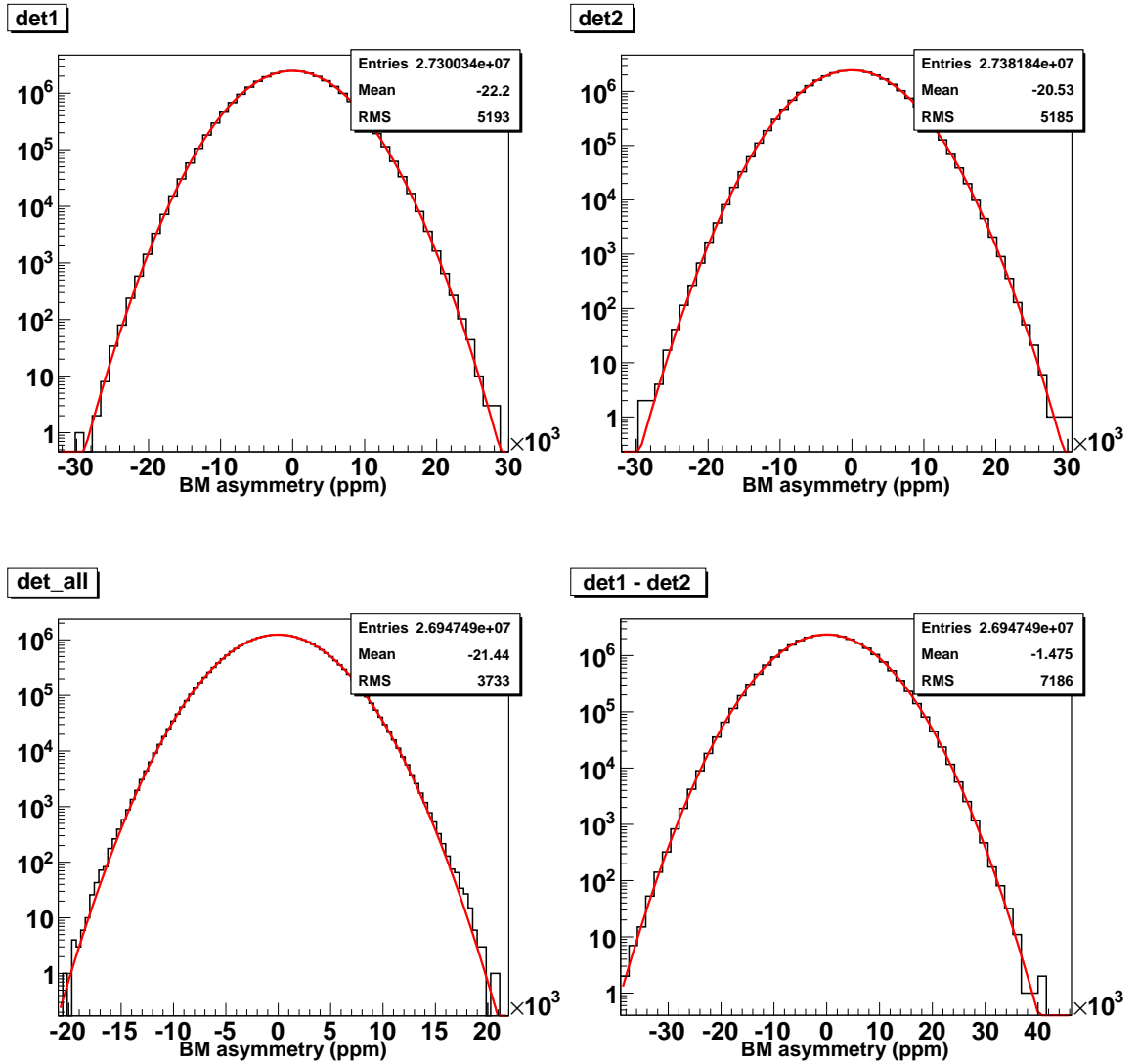
Figure 7.3.6: The regression corrected detector asymmetry distributions by helicity-pairs are presented above. det1 distribution includes all the "good" helicity-pair asymmetry acquired with the LHRS detector and det2 distribution includes all the "good" helicity-pair asymmetry data with the RHRS. det_all and det1 − det2 distributions only include the "good" helicity-pair asymmetry data when both LHRS and RHRS were functional. Note that these data includes those of slugs 0-2, not presented in Figure 7.3.5. det1, det2 and det_all asymmetry distributions are Gaussian over six orders of magnitude, very much like the BM corrected asymmetry distributions of Figure 7.3.5.
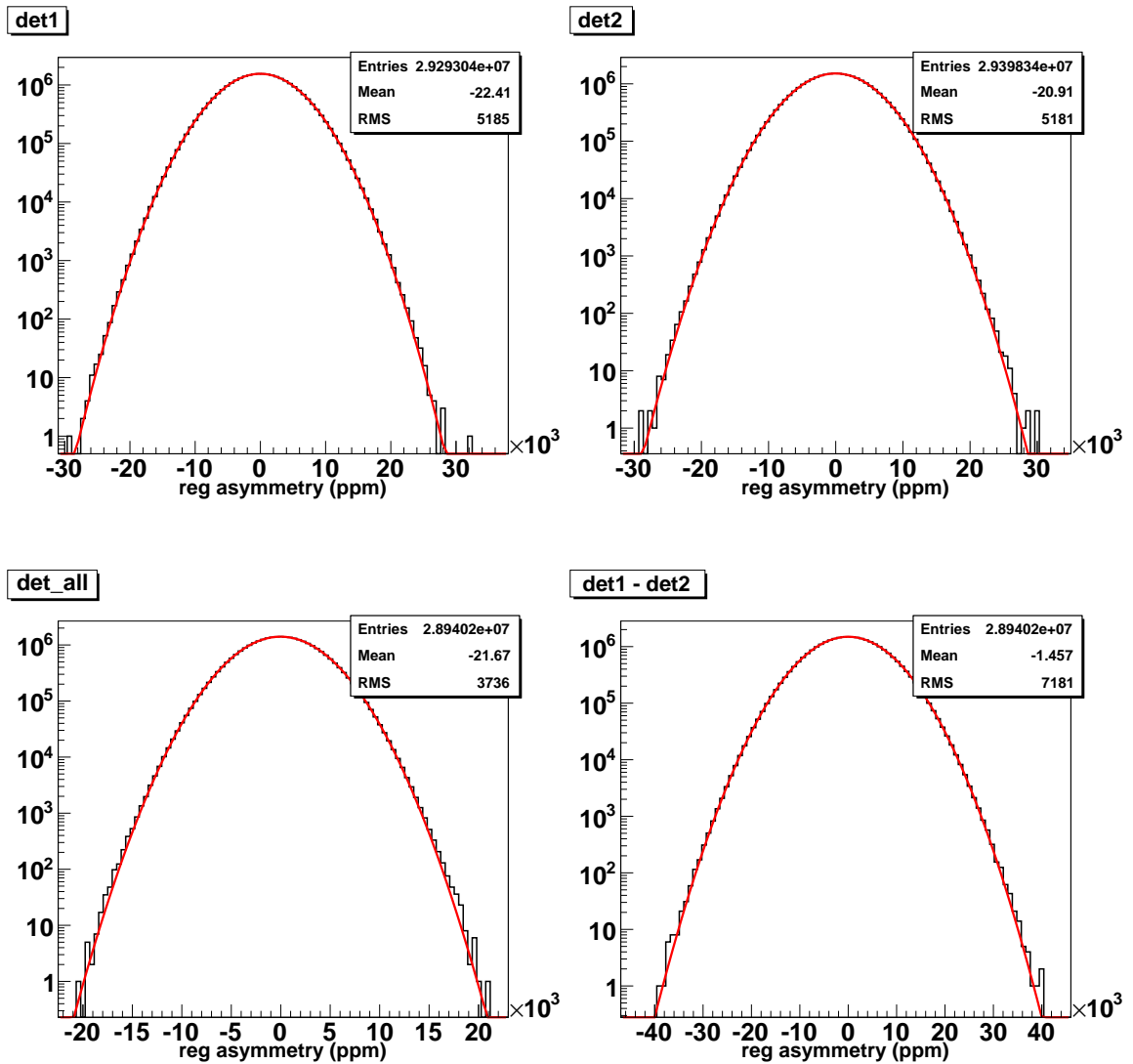
7.3.2.2   Linear Regression Correction

The raw asymmetry, A_{raw}, was also corrected for A_{Fb} via the linear regression technique during HAPPEX-III. The regression technique uses a linear regression algorithm to minimize the correlation of the detector responses to the "natural" beam motion inferred from the responses of the beam monitors, and correct A_{raw} for A_{Fb}. The formalism of the regression algorithm is described in [Mo07]. During HAPPEX-III, regression analysis was used to correct A_{raw} for slugs 0-2. For the rest of the slugs, the regression corrections were used to check the results of BM corrections.

The regression corrected asymmetries of HAPPEX-III are presented in Figure 7.3.6. The total amount of regression correction to A_{raw} was -15 ppb, consistent with the correction obtained via BM analysis. Like the BM corrected asymmetry distributions of Figure 7.3.5, the regressed asymmetries are Gaussian over six orders of magnitude as well.

7.3.2.3   False Beam Asymmetry due to Beam Fluctuations (A_{Fb})

As mentioned earlier, during HAPPEX-III, A_{raw} was corrected for A_{Fb} by using the results of regression correction for slugs 0-2, and BM correction for slugs 3-28. This resulted in a total A_{Fb} for the entire data set of

$$\boxed{A_{Fb} = -10 \pm 30 \text{ ppb.}}$$

The uncertainty above is based on the self-consistency of the BM and regression results, along with the resolution of the BPMs.

$A_T \cos \phi$	-10 ± 5 ppm
$(P_b)_H$	$0 \pm 10\%$
$(\mathrm{HRS}_{acc})_H$	$\sim 20\%$
$(\mathrm{HRS}_{sym})_H$	$\sim 10\%$
Potential syst.	20 ppb

Table 7.5: The estimated transverse asymmetry, $A_T \cos \phi$, horizontal beam polarization, $(P_b)_H$, HRS acceptance in horizontal, $(\mathrm{HRS}_{acc})_H$, and the imperfection in the HRS acceptance symmetry, $(\mathrm{HRS}_{sym})_H$, are presented above. The potential systematic uncertainty due to the transverse beam polarization in the raw asymmetry is evaluated as $A_T \cos \phi \times (P_b)_H \times (\mathrm{HRS}_{acc})_H \times (\mathrm{HRS}_{sym})_H = 20$ ppb.

7.3.3 False Asymmetry due to Transverse Beam Polarization

As discussed in Section 5.11, any transverse polarization present in the electrons results in a transverse asymmetry, $A_T \cos \phi$, where ϕ is the HRS angle. If the symmetry of the HRSs does not perfectly cancel the $A_T \cos \phi$ between the HRSs, the transverse polarization of the beam results in a false asymmetry A_{FT}. During HAPPEX-III, A_{FT} was estimated from the measurements of A_{FT} performed during HAPPEX-II [AnH06, Ac07] to be

$$\boxed{A_{FT} = 0 \pm 20 \text{ ppb.}} \tag{7.3.6}$$

The estimated transverse asymmetry, $A_T \cos \phi$, horizontal beam polarization, $(P_b)_H$, HRS acceptance in horizontal, $(\mathrm{HRS}_{acc})_H$, and the imperfection in the HRS acceptance symmetry, $(\mathrm{HRS}_{sym})_H$, are presented in Table 7.5. From these numbers, a correction of zero, and a systematic uncertainty of $(A_T \cos \phi \times (P_b)_H \times (\mathrm{HRS}_{acc})_H \times (\mathrm{HRS}_{sym})_H =)$ 20 ppb is extracted. A_F arising from any vertical (transverse) beam polarization, and associated uncertainties are negligible.

7.4   Helicity-Correlated (HC) Beam Position Differences

During HAPPEX-III, the helicity-correlated (HC) beam position difference of a helicity-pair was calculated as

$$\Delta x = x_R - x_L \qquad (7.4.1)$$

where $x_{R(L)}$ is the beam position of the right(left) helicity state.

A statistically weighted average HC position difference was evaluated for the data collected over the course of the run as

$$\langle \Delta x \rangle = \frac{\sum_i \epsilon_i \langle \Delta x \rangle_i wt_i}{\sum_i wt_i} \qquad (7.4.2)$$

where i runs over the acceptable data runs. The parameter $\epsilon_i = \pm 1$ accounts for the sign reversal in A_{raw} arising from IHWP state reversal; the HC position differences may or may not reverse sign with IHWP state reversal. The effects of IHWP reversal on HC beam parameters are described in Sections 5.6.2 and 6.3. The quantity $\langle \Delta x \rangle_i$ is the average HC position difference and wt_i is the statistical weight of the ith run in the measurement of A_{PV}. The quantity wt_i is calculated as

$$wt_i = \left(\sum_j wt_j \right)_i = \left(\sum_j 1/(\sigma_{raw})_j^2 \right)_i \qquad (7.4.3)$$

where j runs over data collected with *only* the LHRS functional, *only* the RHRS functional and *both* HRSs functional for the ith run, accommodating periods during which either one or both HRSs were non-functional. Although the majority of the data were collected with *both* HRSs functional, some data runs were acquired with only one functional HRS for part of or the entirety of the run. In cases where *both* HRSs

were functional for the entire run, $wt_i = (wt_{both})_i = (1/(\sigma_{raw})^2_{both})_i$. The quantity $(\sigma_{raw})_j$ is calculated as

$$(\sigma_{raw})_j = (RMS/\sqrt{N})_j \tag{7.4.4}$$

where RMS_j is the statistical width of raw detector asymmetry $(A_{raw})_j$, and N_j is the number of acceptable helicity-pairs corresponding to the jth state (LHRS *only*, RHRS *only*, or *both* HRS) of the ith run.

$\langle \Delta x \rangle_i$ for the ith run is calculated as

$$\langle \Delta x \rangle_i = \left(\frac{\sum_j \langle \Delta x \rangle_j wt_j}{\sum_j wt_j} \right)_i \tag{7.4.5}$$

where j runs over data collected by LHRS *only*, RHRS *only*, and *both* HRS as in Eq. 7.4.3.

The uncertainty in HC position differences is determined by the BPM resolution, BPM_{res}, as

$$\sigma_{\Delta\langle x\rangle} = \text{BPM}_{res}/\sqrt{N} \tag{7.4.6}$$

where $N(= 29.9 \times 10^6)$ is the total number of helicity-pairs collected over the experiment. Since $\text{BPM}_{res} \sim 2$ μm, $\sigma_{\Delta\langle x\rangle}$ is essentially negligible.

The HC position differences averaged over the course of HAPPEX-III are summarized in Table 7.6. These HC position differences are plotted against the slug number in Figure 7.4.1. These differences are weighted by the raw detector asymmetry, A_{raw}, statistics.

7.5 Corrected Asymmetry (A_{corr})

The corrected detector asymmetry, A_{corr}, for HAPPEX-III was evaluated using Eq. 7.1.1 as $A_{corr} = A_{raw} - A_F$. A_{corr} is generated by correcting A_{raw} for the false beam asym-
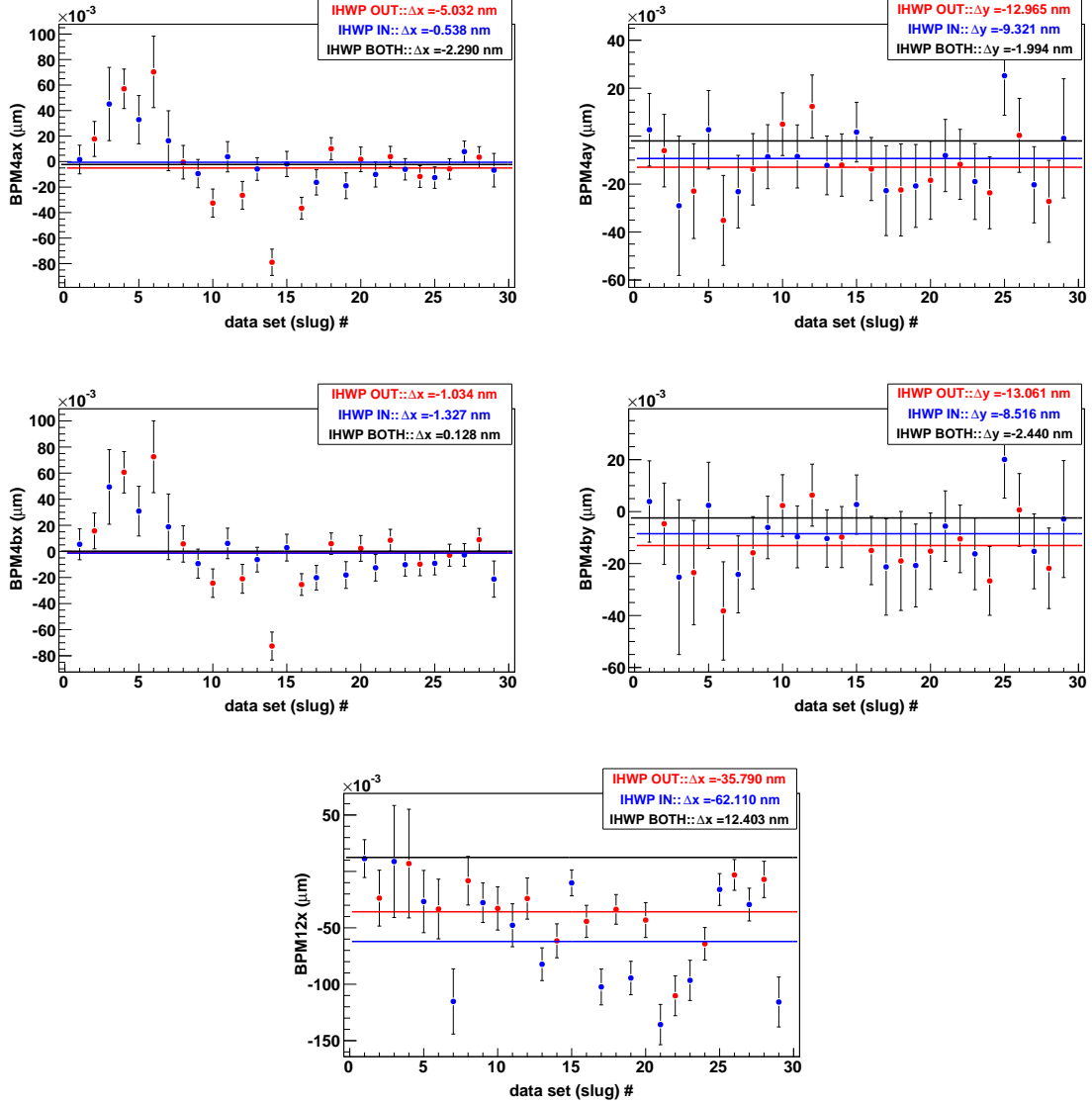
Figure 7.4.1: The helicity-correlated (HC) position differences acquired over the course of HAPPEX-III are presented by IHWP states above. The IHWP OUT and IN numbers correspond to data acquired with the IHWP retracted and inserted on the laser's path respectively. The schematic of laser table is illustrated in Figures 3.3.1, and 6.2.1. The IHWP BOTH numbers correspond to the average of data corresponding to IHWP IN and OUT states. The IHWP IN state position differences are multiplied by -1 (to account for the effects of IHWP insertion; see text for further details) during averaging. All these position differences are weighted by A_{raw} statistics as described above.

IHWP	OUT	IN	BOTH
BPM4ax(nm)	-5.03	-0.54	-2.29
BPM4ay(nm)	-12.97	-9.32	-1.99
BPM4bx(nm)	-1.03	-1.33	0.13
BPM4by(nm)	-13.06	-8.52	-2.44
BPM12x(nm)	-35.79	-62.11	12.40

Table 7.6: The helicity-correlated (HC) position differences averaged over the course of HAPPEX-III summarized by IHWP states. These are weighted by A_{raw} statistics as described above.

metries A_{Fb} and A_{FT}, as described in Section 7.3. A_{raw} already includes correction for A_I as described in Section 7.2. Given that A_{FT} is zero, as discussed in Section 7.3.3, and results in no correction to A_{raw}, $A_F = A_{Fb} + A_{FT} = A_{Fb}$. As result, either BM or regression correction essentially yields A_{corr} ($A_{corr} = A_{raw} - A_F = A_{raw} - A_{Fb}$). Therefore, A_{corr} evaluated via BM and regression corrections are the "final" corrected asymmetries. These asymmetries, along with A_{raw}, are considered in this section.

This section describes appropriate statistical weighting of the detector asymmetries by data runs. Summaries of A_{raw}, A_{corr} evaluated via both regression and BM corrections, and a cumulative A_{corr} which includes regression corrected data from slugs 0-2 and BM corrected data from slugs 3-28 are also presented in this section.

7.5.1 Statistical Weighting

The detector asymmetries were summarized by statistically weighting the asymmetries from each data run. This technique is similar to the one used to summarize the HC position differences in Section 7.4. All the detector asymmetries A_{raw}, and A_{corr} evaluated via both regression and BM methods were summarized by statistically weighting them. Only the generation of A_{raw} summary is described below.

The raw detector asymmetry, A_{raw}, data acquired over the course of HAPPEX-III

were averaged with appropriate statistical weighting as

$$\langle A_{raw} \rangle = \frac{\sum_i \epsilon_i \langle A_{raw} \rangle_i wt_i}{\sum_i wt_i} \tag{7.5.1}$$

where i runs over the data runs, and $\epsilon_i = \pm 1$ accounts for the reversal in sign of $\langle A_{raw} \rangle_i$ due to IHWP state reversals. wt_i is the statistical weight of the ith run expressed by Eq. 7.4.3. $\langle A_{raw} \rangle_i$ is the average detector asymmetry of ith run calculated as

$$\langle A_{raw} \rangle_i = \left(\frac{\sum_j \langle A_{raw} \rangle_j wt_j}{\sum_j wt_j} \right)_i \tag{7.5.2}$$

where j runs over data collected with LHRS *only*, RHRS *only*, and *both* HRS of the ith run. $\langle A_{raw} \rangle_j$ is the average detector asymmetry corresponding to the jth state of the ith run and $wt_j = (1/(\sigma_{raw})^2)_j$ with $(\sigma_{raw})_j = (RMS/\sqrt{N})_j$, as expressed in Eq. 7.4.4.

The uncertainty in the statistically weighted average detector asymmetry is

$$\sigma_{\langle A_{raw} \rangle} = \frac{1}{\sqrt{\sum_i wt_i}} \tag{7.5.3}$$

with wt_i given by Eq. 7.4.3.

The raw, regression corrected, BM corrected and cumulative corrected (slugs 0-2 regression corrected and slugs 3-28 BM corrected) detector asymmetries are presented in Figures 7.5.1 and 7.5.2. These asymmetries are summarized by detectors in Table 7.7. The data acquired during *both* HRS operation only are summarized in Table 7.8, and data acquired during *one* HRS operation alone are summarized in Table 7.9. The differences between the raw and cumulative corrected asymmetries corresponding to the data in these tables are presented in Table 7.10.

Table 7.7: The asymmetries summarized by the detectors that acquired the asymmetry data: LHRS detector (det1) and RHRS detector (det2). IHWP IN and OUT refer to the data acquired with IHWP inserted and retracted from the laser's path respectively. The schematic of laser table is illustrated in Figures 3.3.1, and 6.2.1. IHWP BOTH corresponds to the average of IHWP IN and OUT data. The asymmetries corresponding to the IHWP IN state are multiplied by -1 (to account for its sign reversal due to IHWP insertion) during averaging. All the asymmetries are weighted by their corresponding statistics as described above. Raw refers to A_{raw}, Reg to regression corrected A_{raw}, BM to BM corrected A_{raw}, and Corr to the data set that consists of slugs 0-2 regression corrected A_{raw} and slugs 3-28 BM corrected A_{raw}. All the asymmetries are in parts-per-million (ppm) and the uncertainties are statistical.

	Raw(0-28)	Reg(0-28)	BM(3-28)	Corr(0-28)
		IHWP BOTH		
det1	-22.318 ± 0.956	-22.342 ± 0.955	-22.114 ± 0.989	-22.351 ± 0.956
det2	-20.858 ± 0.955	-20.857 ± 0.955	-20.708 ± 0.988	-20.853 ± 0.955
		IHWP IN		
det1	23.022 ± 1.370	23.049 ± 1.369	22.523 ± 1.412	23.037 ± 1.370
det2	21.207 ± 1.355	21.156 ± 1.354	21.097 ± 1.396	21.179 ± 1.355
		IHWP OUT		
det1	-21.651 ± 1.333	-21.674 ± 1.332	-21.721 ± 1.385	-21.702 ± 1.333
det2	-20.513 ± 1.346	-20.563 ± 1.346	-20.317 ± 1.400	-20.531 ± 1.346

The average of the cumulative corrected detector asymmetry for HAPPEX-III was

$$\boxed{A_{corr} = -21.591 \pm 0.688(\text{stat}) \text{ ppm.}} \quad (7.5.4)$$

There is a systematic uncertainty associated with A_{corr} as well, which is not displayed above. The systematic uncertainty is discussed in Sections 7.6, 7.7 and 7.8.

7.5.2 Asymmetry Pull Plots

Pull plots are useful to check the statistical behavior of data. The pull of each run was calculated as

$$P_i = \frac{\langle A_{raw} \rangle_i - \langle A_{raw} \rangle}{(\sigma_{raw})_i} \quad (7.5.5)$$

Table 7.8: Only data acquired with *both* HRSs functional (so that data was acquired on both det1 *and* det2 simultaneously) are summarized below. Any data acquired during periods of only one functional HRS (when only det1 *or* det2 acquired data) are not included in this summary. All the asymmetries are in parts-per-million (ppm) and the uncertainties are statistical.

	Raw(0-28)	Reg(0-28)	BM(3-28)	Cor(0-28)
	IHWP BOTH			
det1	-22.338 ± 0.964	-22.357 ± 0.963	-22.122 ± 0.998	-22.362 ± 0.964
det2	-20.903 ± 0.962	-20.904 ± 0.961	-20.772 ± 0.995	-20.900 ± 0.962
det_all	-21.610 ± 0.694	-21.620 ± 0.694	-21.434 ± 0.719	-21.620 ± 0.694
	IHWP IN			
det1	23.049 ± 1.374	23.074 ± 1.373	22.546 ± 1.416	23.061 ± 1.374
det2	21.284 ± 1.372	21.239 ± 1.371	21.210 ± 1.413	21.257 ± 1.372
det_all	22.177 ± 0.989	22.167 ± 0.989	21.886 ± 1.019	22.170 ± 0.989
	IHWP OUT			
det1	-21.650 ± 1.352	-21.664 ± 1.351	-21.704 ± 1.406	-21.686 ± 1.352
det2	-20.535 ± 1.349	-20.581 ± 1.349	-20.341 ± 1.403	-20.554 ± 1.349
det_all	-21.060 ± 0.975	-21.089 ± 0.974	-20.987 ± 1.013	-21.086 ± 0.975

Table 7.9: Only data acquired with *one* functional HRS (when only det1 *or* det2 acquired data) are summarized below. Any data acquired during periods when both HRSs were functional (i.e. both det1 *and* det2 acquired data) are not included in this summary. All the asymmetries are in parts-per-million (ppm) and the uncertainties are statistical.

	Raw(0-28)	Reg(0-28)	BM(3-28)	Cor(0-28)
	IHWP BOTH			
det1	-21.134 ± 7.410	-21.459 ± 7.401	-21.697 ± 7.406	-21.697 ± 7.406
det2	-17.652 ± 8.000	-17.583 ± 7.995	-16.337 ± 8.236	-17.621 ± 8.000
	IHWP IN			
det1	18.121 ± 18.549	18.490 ± 18.536	18.570 ± 18.547	18.570 ± 18.547
det2	18.080 ± 8.676	17.817 ± 8.671	16.553 ± 8.980	18.048 ± 8.676
	IHWP OUT			
det1	-21.706 ± 8.083	-22.022 ± 8.073	-22.290 ± 8.078	-22.290 ± 8.078
det2	-15.226 ± 20.668	-16.252 ± 20.657	-15.197 ± 20.668	-15.197 ± 20.668

Table 7.10: The differences in the raw asymmetry (Raw) and the corrected asymmetry (Corr) are presented below. The Corr asymmetry includes regression corrected A_{raw} data from slugs 0-2 and BM corrected data from slugs 3-28. The first two columns are differences in data that were acquired when *both* HRSs were functional (BOTH ONLY), and correspond to data presented in Table 7.8. The third and fourth columns are differences in data that were acquired with only *one* functional HRS (SINGLE ONLY), and correspond to data summarized in Table 7.9. The last two columns refer to all the data acquired by each of the HRS detectors alone, and correspond to data summarized in Table 7.7. All the asymmetry differences are in parts-per-billion (ppb).

	BOTH ONLY		SINGLE ONLY		SINGLE + BOTH HRS	
	Raw-Reg	Raw-Corr	Raw-Reg	Raw-Corr	Raw-Reg	Raw-Corr
IHWP BOTH (0-28)						
det1	19.2	24.1	325.0	562.9	24.2	33.0
det2	0.9	-3.8	-69.6	-31.9	-0.1	-4.2
det_all	10.5	10.0	–	–	–	–
IHWP IN (0-28)						
det1	-24.4	-12.0	-369.6	-449.2	-26.3	-14.4
det2	45.3	27.3	262.8	32.4	50.6	27.4
det_all	9.3	6.8	–	–	–	–
IHWP OUT (0-28)						
det1	14.1	35.8	315.9	583.9	22.3	50.7
det2	45.7	18.9	1026.1	-29.1	49.8	18.7
det_all	29.8	26.3	–	–	–	–
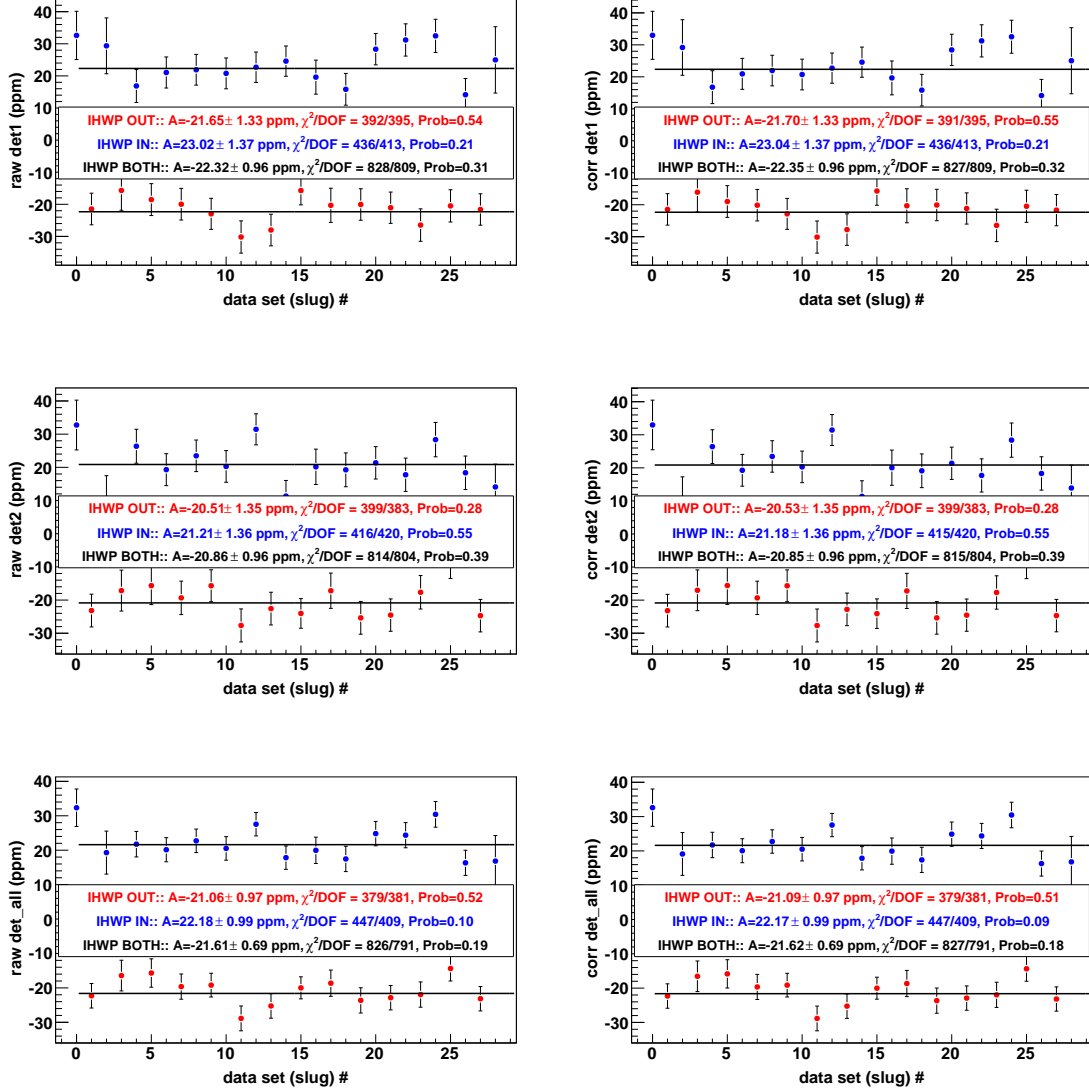
Figure 7.5.1: The raw asymmetries (raw) and the cumulative corrected asymmetries (corr) are presented above. The corr asymmetries include regression corrected asymmetries from slugs 0-2 and BM corrected asymmetries from slugs 3-28. In each column, the top plot corresponds to *all* the data acquired in the LHRS detector (det1), the second plot corresponds to *all* the data acquired in the RHRS detector (det2), and the bottom plot corresponds to the cumulative of the LHRS and RHRS detectors (det_all). det_all is formed from det1 *and* det2 data. Therefore, only data acquired with *both* HRS operational are used to form det_all; data from periods of only *one* functional HRS are excluded from det_all. A_{raw}^{all} is evaluated using Eq. 7.2.2, and is described in Section 7.2.
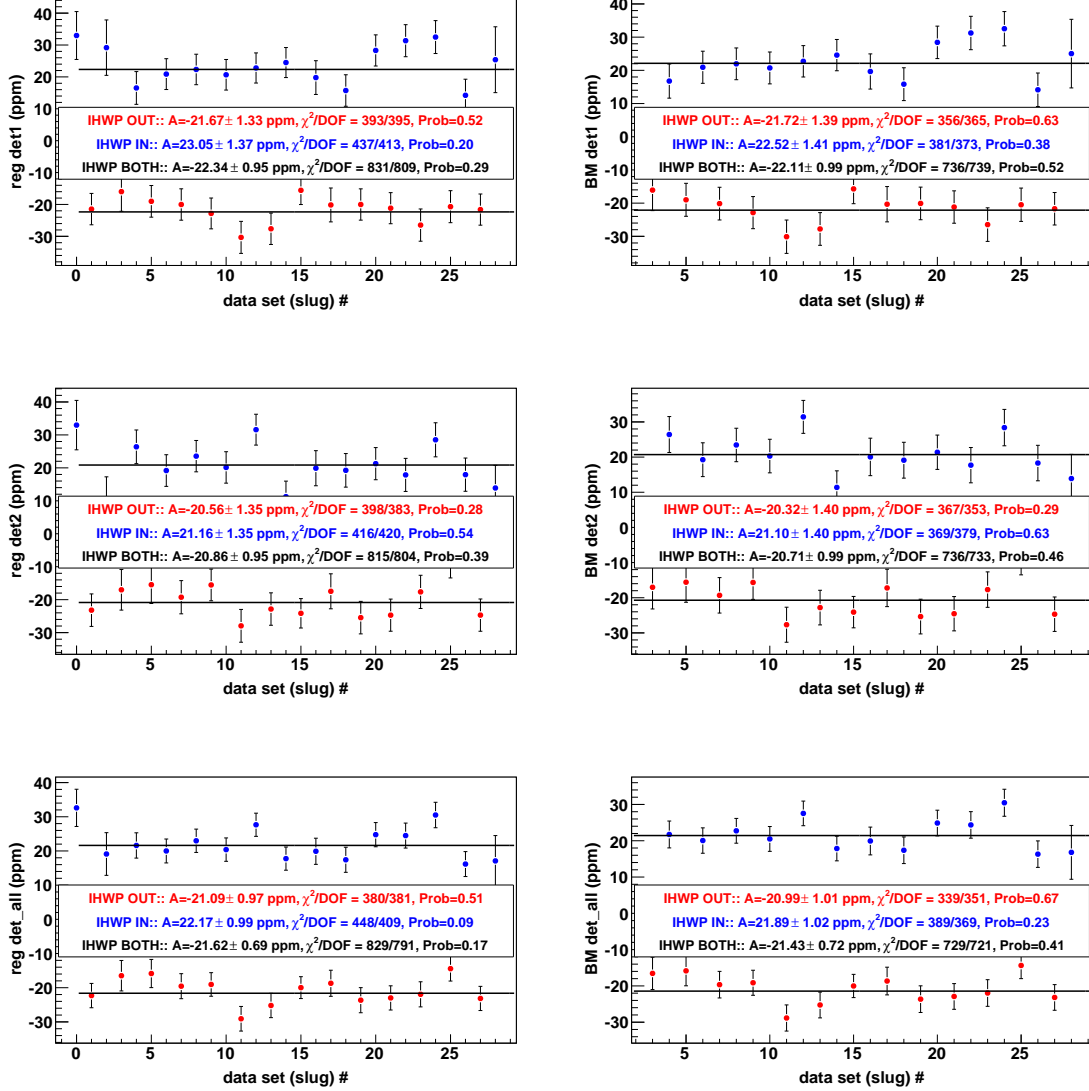
Figure 7.5.2: The regression and BM corrected detector asymmetries are presented above. Only data from slugs 3-28 are included in the BM data set because slugs 0-2 data could not be BM corrected (the BM system was not functional during slugs 0-2 data acquisition). Similar to Figure 7.5.1, in each column, the top plot corresponds to *all* the data acquired in the LHRS detector (det1), the second plot corresponds to *all* the data acquired in the RHRS detector (det2), and the bottom plot corresponds to the cumulative asymmetry (det_all) formed from the data acquired with *both* HRS functional. The det_all asymmetry, A_{raw}^{all}, is evaluated using Eq. 7.2.2, and is described in Section 7.2.
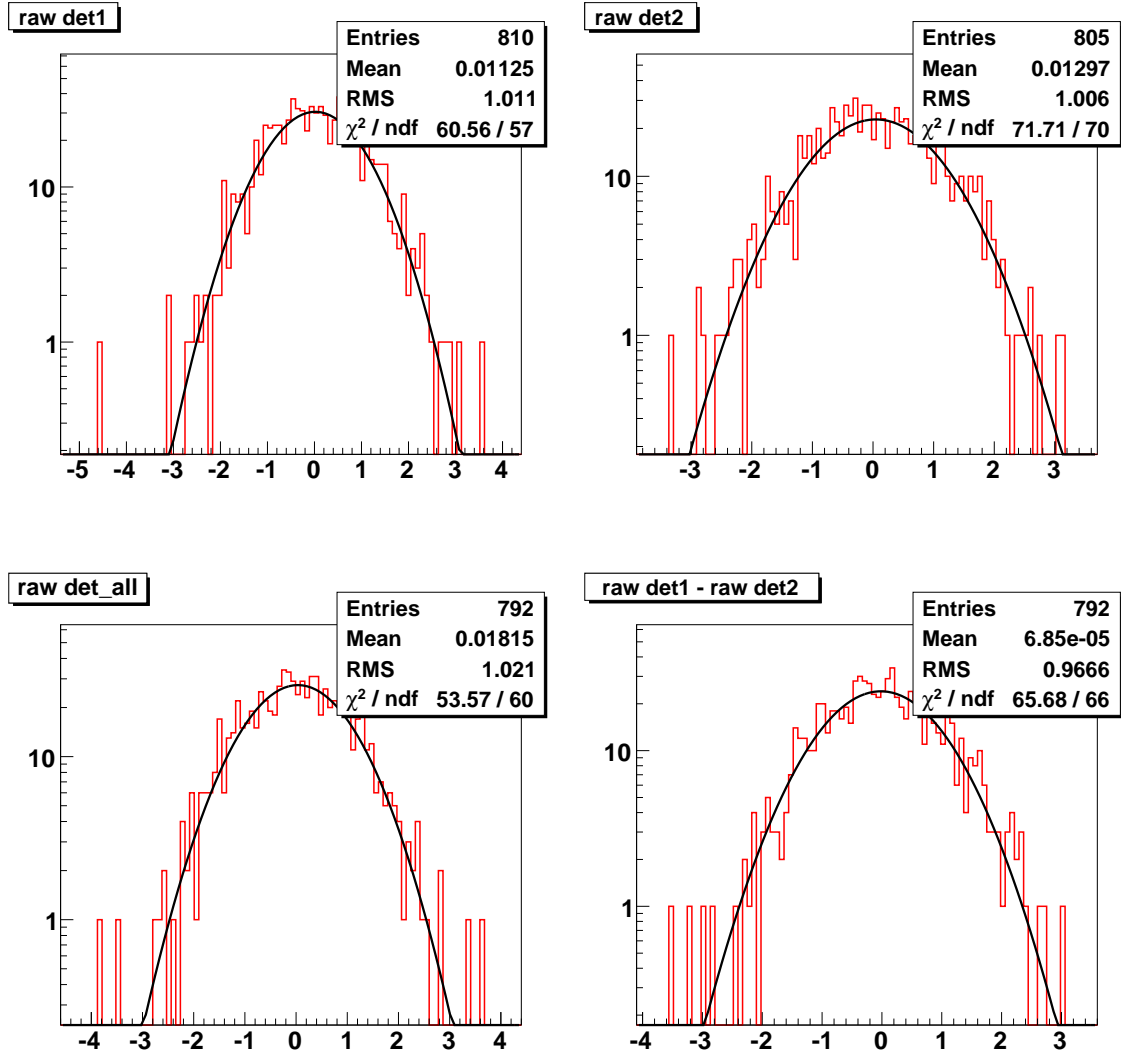
Figure 7.5.3: The histograms of the raw detector asymmetry pull are presented above. The pulls are evaluated by data run as given in Eq. 7.5.5, and its evaluation is described in the text. The plots of det1 and det2 include all the "good" data runs acquired on the LHRS and RHRS detector respectively. The plots of det_all and (det1-det2) include only the "good" data runs acquired when both HRSs were functional. The mean of the pulls are ≈ 0, and the widths are ≈ 1, which indicate that the data set is statistically well behaved.
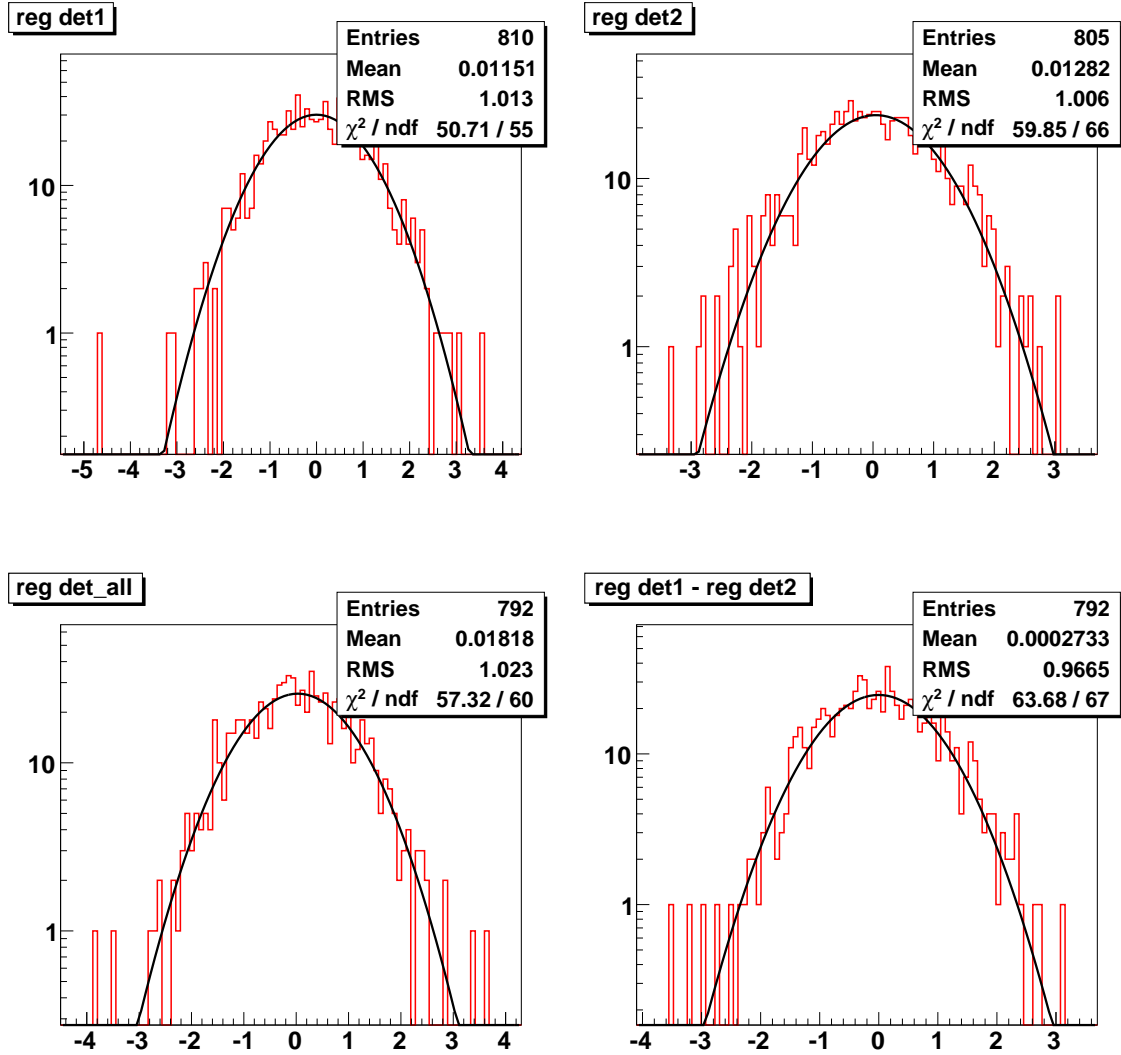
Figure 7.5.4: The histograms of the pull of the regression corrected detector asymmetries are presented above. The pulls are evaluated by data runs as given in Eq. 7.5.5. The mean of these pulls are about zero, and their widths about 1, indicating that these data sets are statistically well behaved. The plots of det1 and det2 include all the "good" data runs acquired on the LHRS and RHRS detector respectively, while the plots of det_all and (det1-det2) include only the "good" data runs acquired when both HRSs were functional.
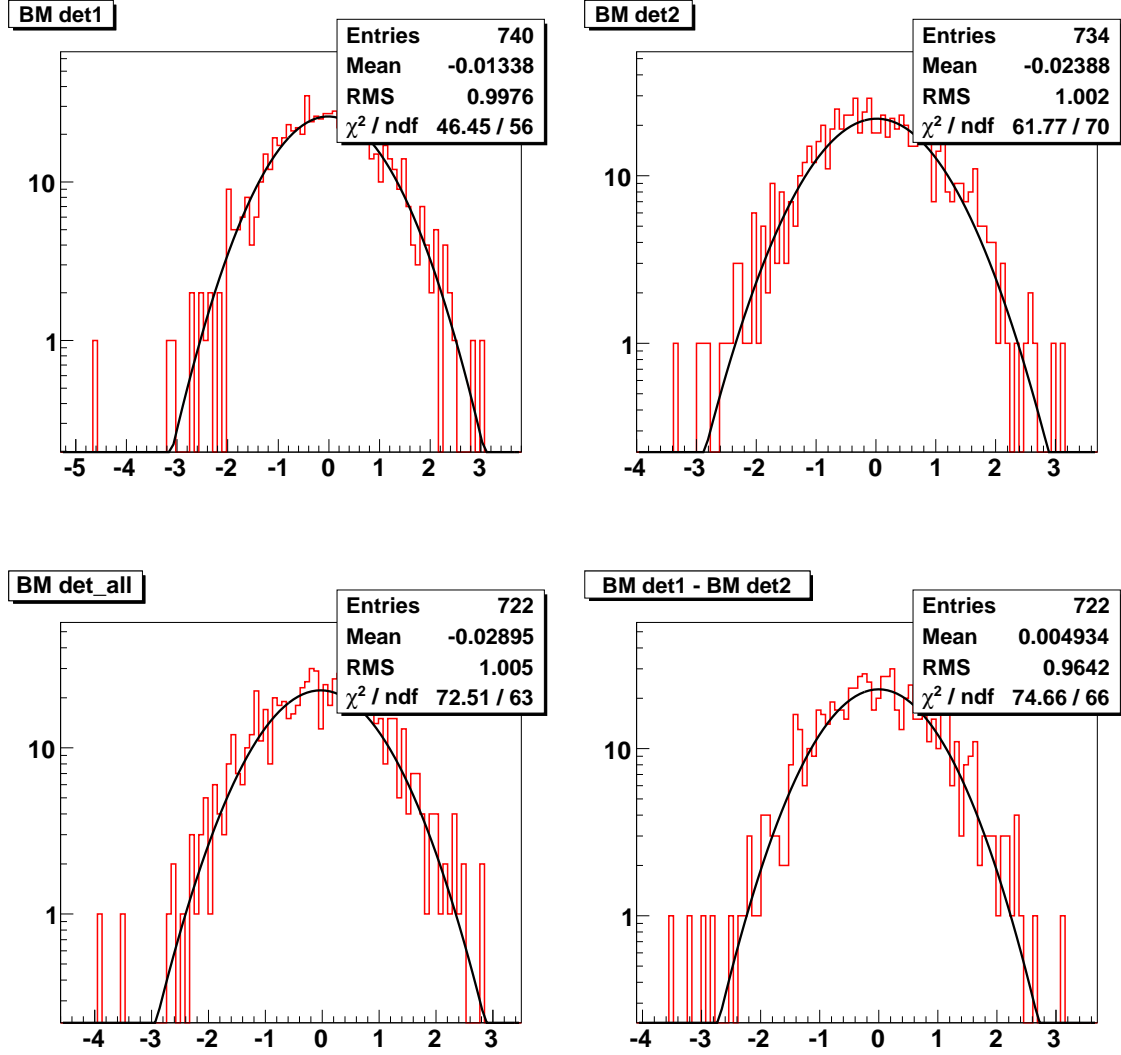
Figure 7.5.5: The histograms of the pull of the BM corrected detector asymmetries are presented above. Like the histograms of the raw and regression corrected detector asymmetries, the pulls are calculated as given in Eq. 7.5.5. The mean of the pulls are close to zero, and the pulls have a width of about 1, indicating that these data sets are statistically well behaved. The plots of det1 and det2 include all the "good" data runs acquired on the LHRS and RHRS detector respectively, while the plots of det_all and (det1-det2) include only the "good" data runs acquired when both HRSs were functional.
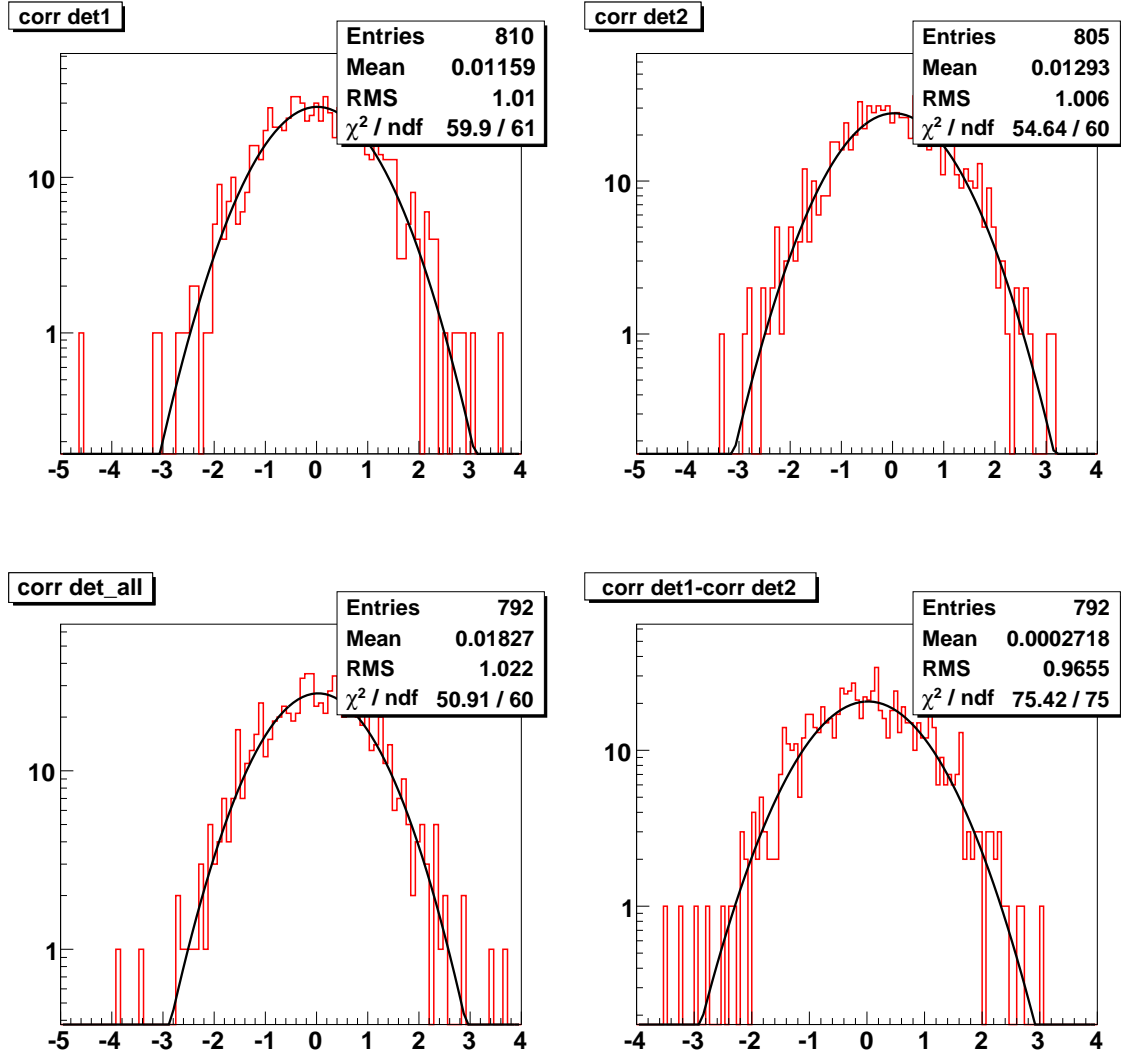
Figure 7.5.6: The histograms of the pull of the corrected detector asymmetries presented above. The plots of det1 and det2 include all the "good" data runs acquired on the LHRS and RHRS detector respectively, while the plots of det_all and (det1-det2) include only the "good" data runs acquired when both HRSs were functional. The corrected data set includes regression corrected detector asymmetries from slugs 0-2 and beam modulation (BM) corrected detector asymmetries from slugs 3-28. The pulls are evaluated as given in Eq. 7.5.5. The mean of these pull plots are about zero, and their widths close to 1, indicating that these data sets are statistically well behaved.

where $\langle A_{raw} \rangle$ was the statistically weighted average detector asymmetry of all the data and is given in Eq. 7.5.1, $\langle A_{raw} \rangle_i$ was the average detector asymmetry of the ith run as given in Eq. 7.5.2, and $(\sigma_{raw})_i$ was the average error in $\langle A_{raw} \rangle_i$ calculated using expression similar to the one given in Eq. 7.4.4.

A statistically well behaved data set has a Gaussian pull plot with a unit variance. This was what was observed in the pull plots in Figures 7.5.3- 7.5.6.

7.6   Normalizations and Corrections to Parity-Violating Asymmetry

The parity-violating (PV) asymmetry, A_{PV}, given in Eq. 7.1.3, was calculated during HAPPEX-III as

$$A_{PV} = \frac{K}{P_b} \frac{A_{corr}}{1 - \sum_i f_i} - \frac{\sum_i A_i f_i}{1 - \sum_i f_i} \tag{7.6.1}$$

where $A_{corr} = -21.591 \pm 0.689 (\text{stat})$ ppm from Section 7.5. The determination of the rest of the terms in the expression of A_{PV}, along with the extraction of A_{PV}, is discussed in this section.

In order to facilitate the discussion of the systematic uncertainties arising from the terms in the expression of A_{PV} in Eq. 7.6.1, it is recast in a slightly different format as

$$A_{PV} = \alpha A_{corr} - \frac{\sum_i A_i f_i}{1 - \sum_i f_i} \tag{7.6.2}$$

where

$$\alpha = \frac{K}{P_b} \frac{1}{1 - \sum_i f_i}. \tag{7.6.3}$$
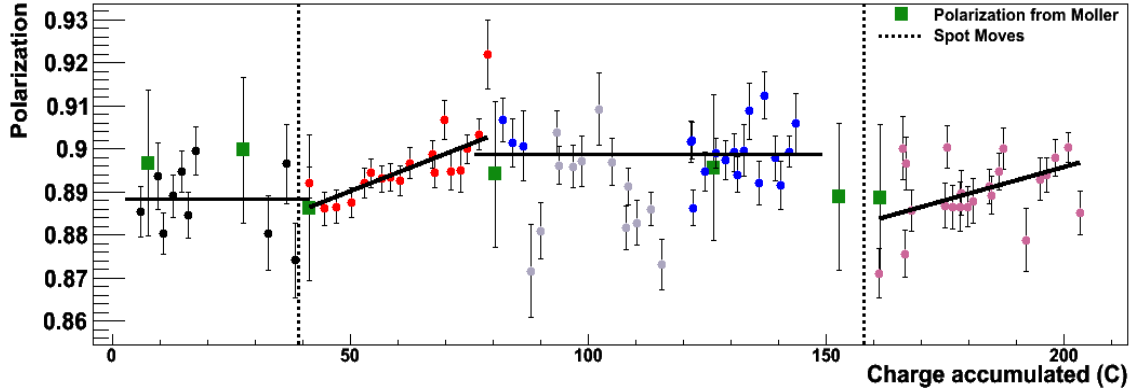
Figure 7.6.1: The Compton beam polarization measurements over the course of HAPPEX-III. The green points were the Møller beam polarization measurements. These polarimeters provided independent beam polarization measurements, and their measurements were consistent with each other within the uncertainties. Reproduced from [Fr12].

7.6.1   Polarization

During HAPPEX-III, the beam polarization was measured via two independent polarimeters: Compton and Møller polarimeters. Both of these polarimeters were part of the experimental Hall A apparatus, and are described in Section 3.14.

The Compton polarimeter provided a continuous, non-invasive beam polarization measurement concurrently with data acquisition. The electron detector of the Compton polarimetry wasn't functional during HAPPEX-III. Therefore, the beam polarization was determined with the photon detector alone. The Compton polarimeter measured an average beam polarization of $89.41\pm0.19(\text{stat})\pm0.84(\text{syst}) = (89.41\pm0.86)\%$ during HAPPEX-III. The beam polarization measurements of the Compton polarimeter are presented in Figure 7.6.1. The beam polarization determination with the Compton polarimeter is described in [Fr12].

The Møller polarimeter provided beam polarization measurements independent of the measurements provided by the Compton polarimeter. The beam polarization determination by the Møller polarimeter was invasive, and each measurement typ-

	Polarization %
Compton	89.41 ± 0.861
Møller	89.22 ± 1.517
Average	89.36 ± 0.747

Table 7.11: The average beam polarizations measured by the Compton and Møller polarimeters. These polarimeters provided independent beam polarization measurements, and their measurements were consistent with each other within the uncertainties. Their results were averaged to extract a cumulative average beam polarization.

ically took ~ 4 hrs, including the time required to change to Møller measurement configuration, and back to the experimental configuration after Møller polarimeter measurements. The Møller polarimeter provided the beam polarization measurement with a statistical precision of $\sim 0.2\%$ with an hour of data. However, uncertainty in the determination of target foil polarization, typically of $\sim 1.5\%$, resulted in systematic uncertainty of $\sim 1.7\%$ (relative) in the beam polarization measurement provided by the Møller polarimeter. During HAPPEX-III, the Møller polarimeter measured a beam polarization of $(89.22 \pm 1.52)\%$ polarization. The uncertainty here is absolute $(1.7 \times 89.36 = 1.52)$.

The Compton and Møller polarimeters provided independent beam polarization measurements. The beam polarization measurements of these polarimeters were consistent with each other within the uncertainties. During HAPPEX-III, their results were averaged to extract a cumulative beam polarization of $P_b = (89.36 \pm 0.75)\%$. The beam polarization measurements performed by the Compton and Møller polarimeters averaged over the course of HAPPEX-III, and the cumulative average are summarized in Table 7.11.

7.6.1.1   Correction and Systematic Uncertainty in A_{PV}

During HAPPEX-III, the correction, A_{P_b}, and systematic uncertainty, $\sigma_{A_{P_b}}$, in A_{PV} due to imperfect ($< 100\%$) beam polarization was calculated as

$$A_{P_b} = A_{PV} \times (1 - P_b), \tag{7.6.4a}$$

$$\sigma_{A_{P_b}} = A_{PV} \times \left(\frac{\sigma_{P_b}}{P_b} \right). \tag{7.6.4b}$$

These equations yield a correction of -2532 ppb and a systematic uncertainty of 199 ppb in the A_{PV} arising from imperfect beam polarization.

7.6.2   Backgrounds

The backgrounds arise due to electrons other than the ones that elastically scatter from the primary target material, and arrive at the detector without any further scattering. During HAPPEX-III, the sources of backgrounds included electrons that scattered from the aluminum (Al) windows of the liquid-hydrogen (LH2) target, electrons that scattered inelastically from the target and rescattered inside the high-resolution spectrometers (HRSs), and electrons that rescattered with the ferromagnetic material of the HRSs. The LH2 target is described in Section 3.6, and the HRSs are described in Section 3.8. This section describes the measurement of backgrounds for HAPPEX-III, and the associated corrections and systematic uncertainties in A_{PV}.

7.6.2.1   Aluminum (Al)

During HAPPEX-III, the electrons that scattered from the aluminum (Al) windows of the liquid-hydrogen (LH2) target were the largest background. These electrons were dominated by the electrons that scattered quasi-elastically (QE) from Al. The

	Frac(%)
LHRS	1.0
RHRS	1.3
Average	1.15

Table 7.12: The fractional aluminum (Al) data contamination for each HRSs are presented above. A large uncertainty of 30% was assigned to these measurements due to uncertainties in target wall thickness determination.

electrons that elastically scattered from Al did not contribute significantly because of high Q^2.

The fractional data contamination from these QE electrons was determined by using the evacuated target cell to directly measure the Al-scattering rate. These rates were also checked using the Al-"dummy" target that matched the full LH2 target radiation length. The targets used during HAPPEX-III are described in Section 3.6.

The average fractional data contamination was determined to be $f_{Al} = (1.15 \pm 0.35)\%$. The fractions were slightly different between the two HRSs due to differences in the spectrometer tunes: the LHRS data contamination fraction was 1.0% and the RHRS data contamination was 1.3%. These fractions are summarized in Table 7.12. A large uncertainty of 30% was assigned to the average of these fractions because of uncertainties in the determination of the Al window thicknesses of the LH2 target, and the thickness of the Al-dummy target.

The asymmetry of the QE electrons was calculated to be $A_{Al} = -34.5$ ppm, with an uncertainty of 30% to account for potential contributions from inelastic states.

7.6.2.2   Inelastic Electrons

Electrons that scattered inelastically from the target (both Al and proton) and rescattered inside the HRSs also contributed substantially to background. The fractional

data contamination from these inelastic electrons was estimated as [An04]

$$f_{rs} = \int_{E_{thr}}^{E_{max}} dE \ P_{rs}(E) \ R(E) \qquad (7.6.5)$$

where P_{rs} is given as

$$P_{rs}(E) = \text{rescatter probability} \times \left(\frac{E_{dep}}{E_0} \right). \qquad (7.6.6)$$

The "rescatter probability" is the probability for the inelastic electrons to rescatter inside the HRS. E_{dep} is the energy deposited by the rescattered electrons on the detector, and E_0 is the energy of the elastically scattered electrons. $R(E)$ is the ratio of the inelastic to elastic cross-section given as

$$R(E) = \left(\frac{d\sigma}{d\Omega dE} \right)_{inelastic} / \left(\frac{d\sigma}{d\Omega} \right)_{elastic} \qquad (7.6.7)$$

The integral in energy in Eq. 7.6.5 extends from the inelastic threshold, E_{thr}, to the maximum amount of energy loss in the inelastically scattered electrons to reach the dipole exit aperture of the HRS, E_{max}. The schematic of the HRSs is described in Section 3.8. E_{max} runs to $\sim 20\%$ below the beam energy [An04].

During HAPPEX-III, f_{rs} was determined from the data collected during HAPPEX-I for its f_{rs} determination, because the HAPPEX-III kinematics were similar to HAPPEX-I kinematics [An04]. During HAPPEX-I the rescattering function, P_{rs}, was determined by scanning the magnetic field in the HRS to force the elastic trajectories to follow the path of the inelastic trajectories. This procedure is described in the HAPPEX-I publication [An04]. P_{rs} that was determined during HAPPEX-I was used without any modification during HAPPEX-III. $R(E)$ was determined by parameterization of the SLAC data [Wh92] at the HAPPEX-III Q^2. This parameterization

was similar to the one performed for HAPPEX-I $R(E)$ extraction.

The fractional data contamination in the HAPPEX-III asymmetry data from these inelastic electrons, f_{rs}, was estimated to be $(0.29\pm0.08)\%$. The dominant mechanism was Δ production, for which the theoretical calculated asymmetry of $A_{rs} = -63$ ppm was used with an uncertainty of 20%.

7.6.2.3 Magnetized Iron

During HAPPEX-III, the electrons that rescattered with the magnetized iron of the HRSs also contributed to background. The polarization dependent asymmetry arising from the Møller scattering of the electrons, that scattered elastically from the target, with the polarized electrons of the magnetized iron is a potential source of systematic uncertainty.

During HAPPEX-III, the fractional data contamination due to the magnetized iron of the HRSs was taken to be $f_{iron} \ll 10^{-4}$. This fraction was determined during HAPPEX-I by measuring the "excess" energy in the low energy-tail of the spectra (which contains backgrounds) of electrons whose trajectories were close to the magnetized iron of the HRS [An04]. The excess was measured relative to the energy inferred from the spectra of the electrons whose trajectories were towards the middle of the HRSs [An04]. This procedure is described in [An04].

The asymmetry in the Møller scattering of the elastically scattered electrons from the electrons of the magnetized iron of the HRS was determined as

$$A_{iron} = P_e \ e_{pre} \ A = 1320 \text{ ppm} \qquad (7.6.8)$$

where $P_e \sim 0.08$ is the polarization of the electrons in saturated iron of the HRS. $e_{pre} \sim 0.15$ is the electron precession and $A \sim 0.11$ is the analyzing power. A is

the "well-known" Møller analyzing power, and is bound to ≤ 0.11. This estimate is consistent with that used for HAPPEX-I [An04].

7.6.2.4 Corrections and Systematic Uncertainties

The correction, A_i^{bk}, and systematic uncertainty, $\sigma_{A_i^{bk}}$, in A_{PV} due to the electrons that scattered from Al windows of the target or the inelastic electrons was given as

$$A_i^{bk} = (A_{pre} - f_i A_i)(1 + f_i) - A_{pre} \tag{7.6.9a}$$

$$\sigma_{A_i^{bk}} = \sqrt{\left(\frac{A_{PV} - A_i}{1 - \sum_j f_j}\sigma_{f_i}\right)^2 + \left(\frac{f_i}{1 - \sum_j f_j}\sigma_{A_i}\right)^2} \tag{7.6.9b}$$

where

$$A_{pre} = \frac{K}{P_b} \times A_{corr}. \tag{7.6.9c}$$

f_i is the fractional data contamination due to the ith background contaminant. σ_{f_i} is the uncertainty in f_i. A_i and σ_{A_i} are the asymmetry of the ith background contaminant, and associated uncertainty in A_i.

The correction to A_{PV} due to background arising from the magnetized iron in the HRS was calculated as [An04]

$$dA = f_{iron}P_b P_e A \tag{7.6.10}$$

where $P_b \sim 0.89$ is the polarization of the elastically scattered electrons (determined by the Compton and Møller polarimeters). The beam polarization measurements are discussed in Section 7.6.1. $P_e \sim 0.08$ is the polarization of the electrons in iron of the HRS, and $A \leq 0.11$ is the analyzing power. Both P_e and A were determined during

Source	Frac.(%)	Correction (ppb)	Syst. Uncer. (ppb)
Al(QE)	1.15 ± 0.34	114	126
Inelastics	0.29 ± 0.07	125	55
Mag. Iron	0 ± 10^{-4}	0	136
Total	$-$	237	193

Table 7.13: The sources of backgrounds during HAPPEX-III, and the associated correction and systematic uncertainties in the parity-violating asymmetry, A_{PV}.

HAPPEX-I [An04]. The systematic uncertainty in A_{PV} arising from magnetized iron was calculated using Eq. 7.6.9 from above.

These corrections and systematic uncertainties, as well as the associated fractional data contamination are summarized in Table 7.13.

7.6.3   Finite Acceptance

During HAPPEX-III, the HRSs accepted elastically scattered electrons in a solid angle of about 5 msr. Due to this finite acceptance, and due to a finite range of initial-state energy of the elastically scattered electrons, A_{raw} measured during HAPPEX-III was essentially an asymmetry averaged over a range of Q^2. These finite-acceptance effects are discussed further in Section 5.13. The asymmetry was corrected to relate to the quoted Q^2 by the finite (kinematic) acceptance factor K in Eq. 7.6.1. The quantity K was calculated as

$$K = \frac{A(\langle Q^2_{\text{det}} \rangle)}{\langle A(Q^2_{\text{ver}}) \rangle} \tag{7.6.11}$$

where $A(\langle Q^2_{\text{det}} \rangle)$ is the asymmetry evaluated at the average Q^2 at the location of the detectors. $\langle A(Q^2_{\text{ver}}) \rangle$ is the average of the asymmetries evaluated at the scattering vertex inside the target. The difference between the two asymmetries is that $A(\langle Q^2_{\text{det}} \rangle)$ contains the effects of energy losses in the electrons after scattering. These losses are incurred when the electrons are transported to the detectors through the HRSs.

$\langle A(Q^2{}_{\mathrm{ver}})\rangle$, on the other hand, does not contain any of these energy losses. $A(\langle Q^2{}_{\mathrm{det}}\rangle)$ and $\langle A(Q^2{}_{\mathrm{ver}})\rangle$ were evaluated by simulating the electron-proton (ep) scattering at HAPPEX-III kinematics with Hall A Monte-Carlo software (HAMC) [HAMC].

HAMC simulated the ep scattering at the center of Hall A, and the transport of the elastically scattered electrons through the HRSs into the focal plane, where the detectors were located. The schematic of Hall A and the HRSs are described in Sections 3.1 and 3.8. The simulation was performed at the kinematics of HAPPEX-III. The central scattering angles and target offsets determined by the pointing analysis [SN10], along with the detector attenuation coefficients measured during the experiment were used as well. The detector attenuation coefficients are described in Appendix B.6.

The results of simulation indicated a mismatch between the HRS acceptances used in HAMC and the true HRS acceptances observed in data at HAPPEX-III kinematics. Minor adjustments were made to the HAMC kinematic parameters to match the HAMC HRS acceptances to what was observed. However, this effort was not successful. Instead, the sensitivity of K to the HRS acceptance variations was studied, and the affects of the acceptance mismatches on K bounded. This was done by varying the HRS collimator sizes in HAMC and extracting the associated K.

Figure 7.6.2 displays the plots and values of $\langle A(Q^2{}_{\mathrm{ver}})\rangle$ and $A(\langle Q^2{}_{\mathrm{det}}\rangle)$ for the RHRS at HAPPEX-III kinematics, with HAMC set to different HRS collimator sizes. $p10$ and $m10$ refer to HAMC results with the HRS collimators changed by $+10$ mm and -10 mm respectively, while the third set of values refer to the HAMC results without any change to the HRS collimator size. The HRS collimator was $\sim 63 \times 122$ mm. 10 mm was $\sim 16\%$ change in HRS acceptance along the horizontal and $\sim 8\%$ HRS acceptance change along the vertical. The K parameters of Figure 7.6.2, along with an analogous set of K for the LHRS, are summarized in Table 7.14.

The numbers in Table 7.14 suggest that K is fairly insensitive to the HRS accep-
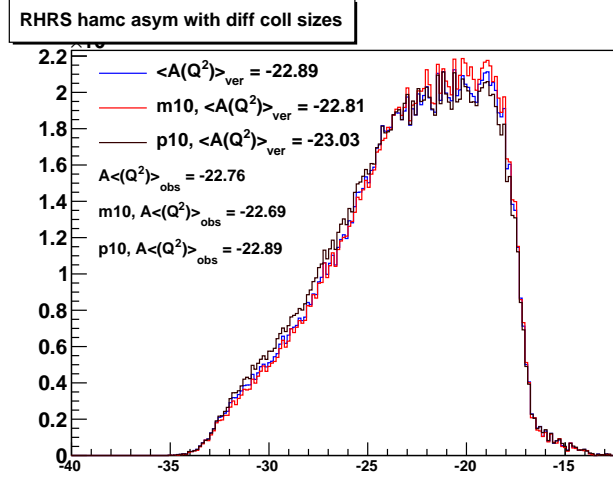
Figure 7.6.2: $A(Q^2)$ plots of HAMC simulation at the nominal collimator size, collimator size increased by 10 mm(p10) and collimator size decreased by 10 mm (m10) for the RHRS. $\langle A(Q^2)_{ver}\rangle$'s are the means of the histograms. $A(\langle Q^2_{det}\rangle)$'s are evaluated at the average Q^2 at the detector.

	LHRS			RHRS		
	coll_nom	coll_m10	coll_p10	coll_nom	coll_m10	coll_p10
$< A(Q^2_{ver}) >$	-24.63	-24.49	-24.84	-22.89	-22.81	-23.03
$A(< Q^2_{det} >)$	-24.51	-24.38	-24.71	-22.76	-22.69	-22.89
K	0.995	0.996	0.995	0.994	0.995	0.994

Table 7.14: $< A(Q^2_{ver}) >$ and $A(< Q^2_{det} >)$ at the nominal collimator size, and the collimator sizes changed by ± 10 mm. K is calculated using Eq. 7.6.11

tances. Therefore, K determined from HAMC simulation was used during HAPPEX-III, despite the HRS acceptance mismatches between HAMC and data. The K averaged over both HRSs was 0.995 ± 0.002. An uncertainty $\sigma_K = 0.002$ was assigned to K due to variations in K at $\sim 0.2\%$ level between the different HRS collimator sizes.

7.6.3.1   Correction and Systematic Uncertainty in A_{PV}

The correction, A_K, and uncertainty, σ_{A_K}, in A_{PV} due to K was calculated as

$$A_K = A_{PV} \times \left(1 - \frac{1}{K}\right) \tag{7.6.12a}$$

$$\sigma_{A_K} = A_{PV} \times \left(\frac{\sigma_K}{K}\right). \tag{7.6.12b}$$

These equations yielded a correction of 120 ppb, and systematic uncertainty of 48 ppb in A_{PV} due to K.

7.6.4   Non-Linearity

As discussed in Section 5.5, instrument non-linearities can result in false asymmetries and systematic uncertainties in the measured asymmetry. Specifically, A_{corr} is affected by the non-linearities in the responses of the detectors, as well as the non-linearities in the responses of the beam monitors (BCMs and BPMs). This is because, the responses of the BCMs and BPMs determine A_I and A_F, which are corrections in A_{raw}, which, in turn, is determined from the responses of the detectors. A_{corr} is given in Eq. 7.1.1 as $A_{corr} = A_{raw} - A_F$, which in turn is used in A_{PV} determination as given in Eq. 7.6.2. Therefore, the non-linearities in the measurements of A_I, A_F, and A_{raw} increases the systematic uncertainty in A_{PV} as

$$(\sigma_{A_{PV}})_{alin} = \left(\sqrt{\sigma_{A_{raw}}^2 + \sigma_{A_I}^2 + \sigma_{A_F}^2}\right)_{alin} \tag{7.6.13}$$

with

$$(\sigma_{A_j})_{alin} = A_j \times (\text{instr})_{alin} \times \alpha \tag{7.6.14}$$

where $A_j = \{A_{raw}, A_I, A_F\}$, $(instr)_{alin}$ is the amount of non-linearity in the apparatus that measured A_j, and α is given by Eq. 7.6.3.

A_{raw} was measured by the detectors, A_I by the BCMs and A_{Fb} via a combination of the detectors and the BPMs. A_{Fb} was tiny compared to A_{raw} and A_I, and the associated false asymmetries arising from non-linearities in its determination were negligible. Therefore, no non-linearity correction was made for A_{Fb}. The non-linearities in the measurement of A_{raw} and A_I, and the associated correction and systematic uncertainties in A_{PV} are discussed below.

7.6.4.1   Detector Non-Linearity

The non-linearity in the detector photo-multiplier tubes (PMTs) was measured *in-situ* tests during the experiment, and in bench tests after the experiment. The results of the non-linearity studies for HAPPEX-III detectors are presented in Figure 7.6.3. In both plots of Figure 7.6.3, the responses of the detector PMTs to changes in the size of the detector responses by a fixed amount is plotted on the vertical axis. The detector response was modified by $\sim 10\%$ for the LHRS (Jack) detector PMT, and by $\sim 4\%$ for the RHRS (Joe) detector PMT. A light-emitting diode (LED) was toggled, at a fixed frequency and amplitude, to modify the size of the PMT responses. The test method and bench test setup are described in Section 3.9.1.1. The PMT responses were varied to mimic running conditions with 0-100 μA electron beam, and these responses, normalized to the size of average detector PMT response at 100 μA electron beam, are plotted on the horizontal axis in Figure 7.6.3.

The non-linearities in the detector PMTs were constrained from the plots of Figure 7.6.3 by observing the average deviation of the PMT responses, plotted on the vertical axis, from the mean of these responses. For instance, in the plot corresponding to the LHRS (Jack) detector PMT, the average variation in the PMT response is
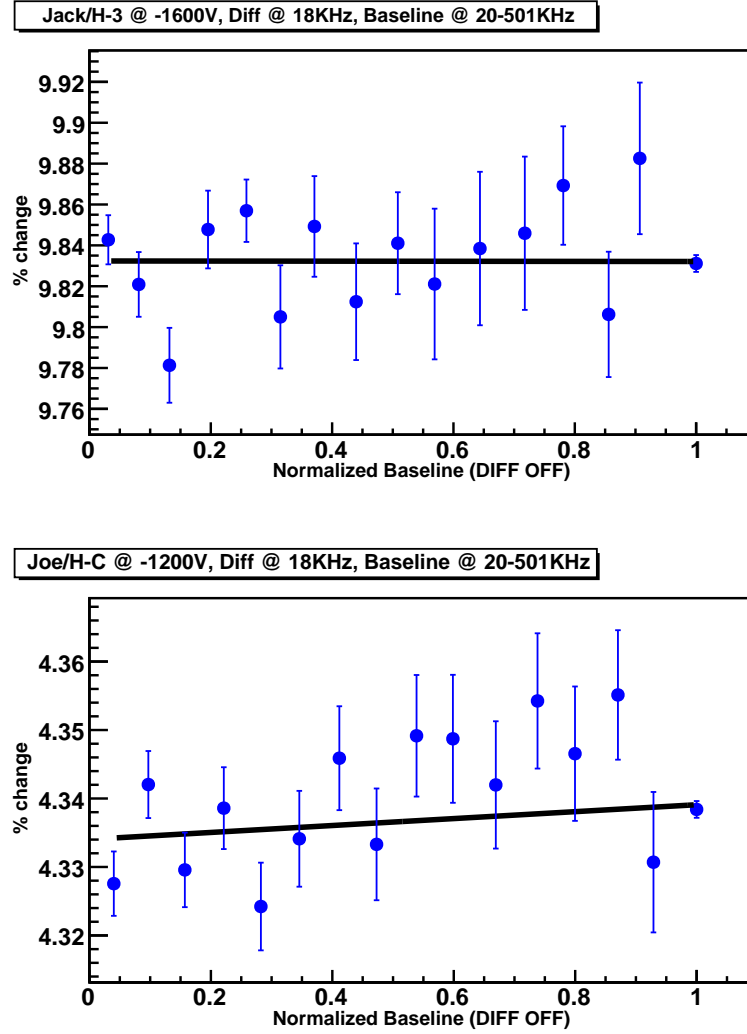
Figure 7.6.3: The responses of the detector photo-multiplier tubes (PMTs) to variation in the size of the PMT responses by a fixed amount ($\sim 10\%$ for the LHRS (Jack) detector PMT, and $\sim 4\%$ for the RHRS (Joe) detector PMT) is plotted on the vertical axis. The PMT responses were varied to mimic running conditions with 0-100 μA electron beam, and normalized to the size of average detector PMT response at 100 μA electron beam, and plotted on the horizontal axis. The plot corresponding to the LHRS (Jack) detector PMT suggests 0.05% non-linearity in the LHRS detector PMT, and the plot corresponding to the RHRS (Joe) detector PMT suggests 0.03% non-linearity in the RHRS detector PMT. These non-linearity are inferred by observing the average deviation of the PMT responses, plotted on the vertical axis, from the mean of these responses, roughly given by the mean of straight line fit. However, due to slight variations in the amount of PMT non-linearities between repeated measurements, LHRS detector PMT non-linearity is bound to $\sim< 0.2\%$, and RHRS detector PMT non-linearity is bound to $\sim< 0.1\%$.

$\sim 9.83\%$ with a deviation of $\sim \pm 0.05\%$. Thus, this plot suggests 0.05% non-linearity in the LHRS detector PMT. Similarly, the RHRS plots suggests 0.03% non-linearity in the RHRS detector PMT. However, repeated measurements yielded slight variations in the detector PMT non-linearities. Nevertheless, these variations were small, and could be comfortably accounted for with an upper bound of 0.2% non-linearity on LHRS detector PMT, and 0.1% non-linearity on the RHRS detector PMT.

Despite repeated measurements, however, only limited number of non-linearity measurements (about 10) were reliable. Therefore, a conservative 0.5% was assigned as the average detector non-linearity.

7.6.4.2   BCM Non-Linearity

The BCM non-linearity was extracted by plotting DD_{12} against the HC beam intensity asymmetry determined from the responses of either the detectors or the BPMs. DD_{12} is the double-difference (DD) of the HC beam intensity asymmetry measured by BCMs 1 and 2, and is described in Section 7.3.1. The detector or the BPM asymmetry is used to avoid correlations with the BCM measurements.

The DD_{12} plotted against det1 raw asymmetry (A^1_{raw}), typical of the ones used for DD_{12} determination, is presented in Figure 7.6.4. In this plot, the slope of the straight line fit is -0.00012, indicating a relative non-linearity of -0.012% in the BCM. However, a much larger BCM non-linearity of $\sim 2.0\%$ was used for HAPPEX-III for two reasons: a) the A_I was small and resulted in tiny uncertainty in A_{PV}, and b) a detailed study was not performed to check for variations in the BCM non-linearity across runs.
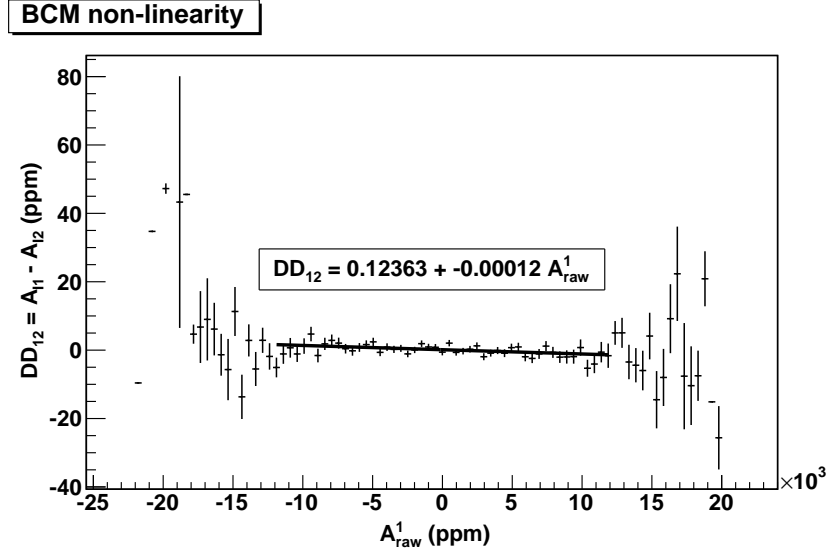
Figure 7.6.4: The BCM non-linearity was extracted by plotting the double-difference (DD) of the HC beam asymmetries measured by BCMs 1 and 2 ($DD_{12} = A_{I1} - A_{I2}$) against the asymmetry measured by the detector, det1 (A_{raw}^1) in this case. The slope of the straight line fit of this plot indicates a relative non-linearity of -0.012%.

7.6.4.3 Corrections to A_{PV} from Non-linearity

The non-linearities of the detector PMTs and the BCMs, along with the associated corrections and the systematic uncertainties in A_{PV} are summarized in Table 7.15. No corrections were made in A_{PV} for either of these non-linearities. The non-linearity systematic uncertainty in A_{PV} was dominated by the BCM non-linearity. The systematic uncertainties were evaluated by using Eq. 7.6.13.

Non-lin. Source	Non-linearity (%)	Correction (ppb)	Syst. Uncer. (ppb)
Detector PMTs	0.5	0.0	122.0
BCMs	2.0	0.0	5.0
Total	-	0.0	122.1

Table 7.15: During HAPPEX-III, the non-linearity in the responses of the detector PMTs was limited to 0.5%, and in the beam current monitors (BCMs) was limited to 2.0%. The associated corrections and systematic uncertainties in the parity-violating asymmetry, A_{PV}, are listed above.

7.7 Four-Momentum Transfer Squared (Q^2)

During HAPPEX-III, the four-momentum transfer squared, Q^2, was measured in dedicated low current runs ($\sim 2 - 5\mu A$) that were taken once every two weeks or so. The focal plane detectors, the S0-scintillators and the VDCs, described in Section 3.9, were used for Q^2 determination. The Hall A counting data acquisition system (DAQ) acquired the Q^2 data, and the standard Hall A analyzer software package analyzed them. The counting DAQ is descried in Section 3.11.2.

The Q^2 was calculated as

$$Q^2 = 2E_{beam}E'(1 - \cos\Theta) \tag{7.7.1}$$

where E_{beam} is the electron beam energy, E' is the energy of the scattered electron and Θ is the scattering angle. The determination of these variables are discussed below.

During HAPPEX-III, an average beam energy of 3.483 GeV was measured, but E_{beam} of 3.481 GeV was used during Q^2 evaluation. This reduction of 2 MeV in energy accounted for the average ionization energy losses that occurred inside the liquid-hydrogen (LH2) target before the electrons scattered with the protons. The total ionization energy loss due to multiple scattering (dE/dx) for an electron propagating through a 25 cm LH2 target is ~ 4 MeV. This was calculated using Bethe-Block equation. If the electrons scattered at the center of the target on average, then the average ionization energy loss in the electrons would be 2 MeV, and these electrons would only have an average of ~ 3.481 GeV energy when they elastically scattered off the protons.

(a) Hall coordinate sys (top view)   (b) Transport coordinate sys (side view)
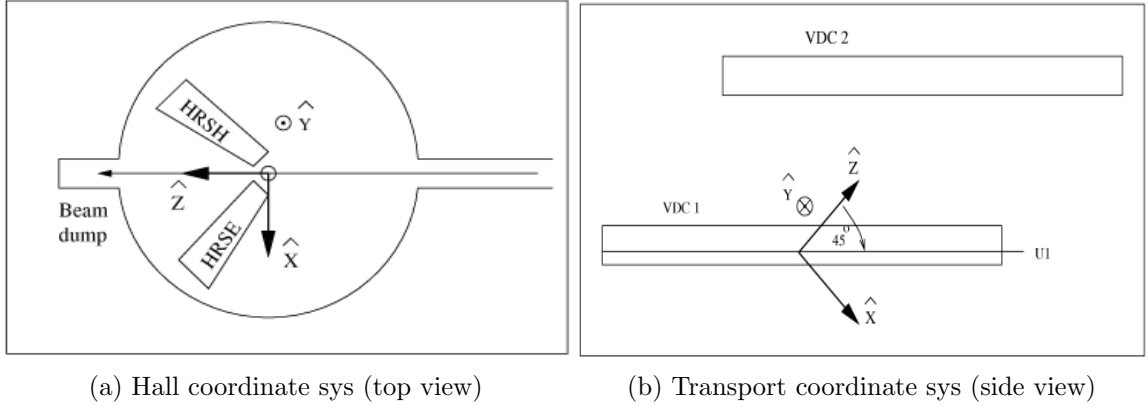
Figure 7.7.1: The HRS "hall" and "transport" coordinate systems. Reproduced from [Ni02].

E' was determined as

$$E' = \frac{E_{beam}}{1 + \frac{E_{beam}}{m_H}(1 - \cos \Theta)} \tag{7.7.2}$$

where $m_H = 0.93827$ GeV^2 is the proton mass. The scattering angle Θ is given as

$$\Theta = \cos^{-1}\left(\frac{\cos \Theta_0 - \phi \sin \Theta_0}{\sqrt{1 + \theta^2 + \phi^2}}\right) \tag{7.7.3}$$

where Θ_0 is the central scattering angle in the xz-plane of the "hall" coordinate system. The hall coordinate system is shown in Figure 7.7.1a. Θ_0 is determined via pointing studies [SN10]. θ and ϕ [1] are the angles subtended by the reconstructed trajectories of the electrons to the z-axis along the xz- and yz-planes of the "transport" coordinate system. The transport coordinate system is illustrated in Figure 7.7.1b. z is along the direction of beam propagation in both these coordinate systems. θ and ϕ were determined by the standard Hall A tracking analysis software, podd, with the tracking information collected by the VDCs [Ni02].

---

[1]During HAPPEX-III, θ and ϕ were corrected for the extended structure of the target. This correction was performed by "podd", the standard Hall A HRS tracking data analysis software.

7.7.1   Energy Weighted Q^2

Data acquired via integration was implicitly weighted by the amount of the electrons' energy deposited in the detector scintillators, while data acquired via counting was not. Electrons with similar energies but incident at different distances from the PMT generated signals of different sizes due to attenuation along the detector. Electrons with different energies incident at the same point on the detector generated signals of different sizes at the PMT as well. So the counting data needed to be weighted to remove these biases arising from variations in the energy deposited by the electrons as seen by the detector. This was performed for the Q^2 data as [1]

$$Q^2{}_{\text{wt}} = \frac{\Sigma_i \text{wt}_i Q^2{}_i}{\Sigma_i \text{wt}_i} \tag{7.7.4}$$

where wt_i was the relative energy deposition for the event, and was simply the pedestal subtracted detector ADC value as

$$\text{wt}_i = \det_i - \det_{\text{ped}} \tag{7.7.5}$$

where $\det_i$ and $\det_{\text{ped}}$ referred to the detector signal size of the ith event and the average detector pedestal. Q^2 histograms before and after energy weighting are presented in Figure 7.7.2. Energy weighting decreased the Q^2 slightly.

There were two major issues with the plots of Figure 7.7.2:

1. The Q^2 histogram profiles were different between the HRSs, which was not what one would expect considering that the HRS were symmetrical in design, and kinematics.

---

[1]The Q^2 could also be weighted by filling histogram with Q^2 weighted by wt_i event-by-event and taking the histogram mean.
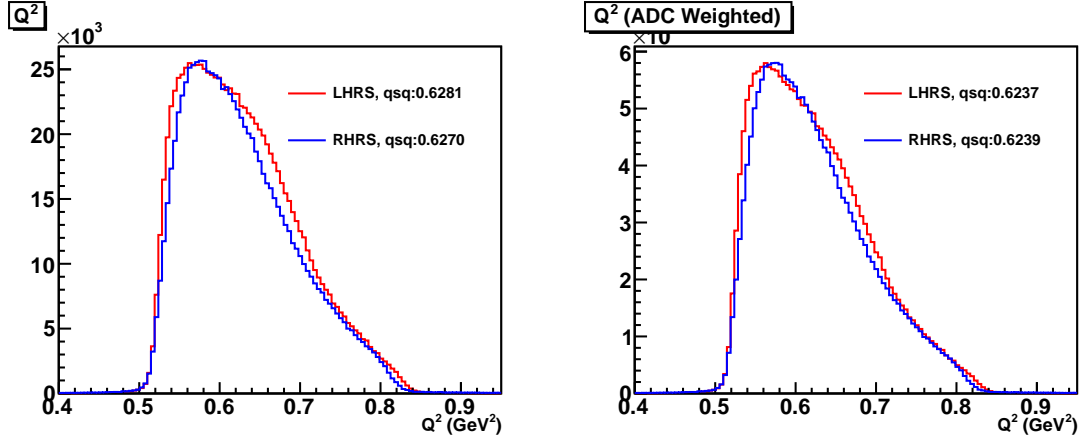
Figure 7.7.2: Q^2 plots before (left) and after (right) energy weighting. These runs were taken with the beam at $-0.8mm$ in BPM4bx.

2. The differences in Q^2 between the HRSs did not scale with the differences in the HRS central scattering angles. The LHRS central scattering angle (=0.2463 rad) was greater than the RHRS central scattering angle (=-0.2424 rad) by $\sim 1.59\%$, but the Q^2 between the HRSs only differed by $\sim 0.18\%$ instead of the expected $\sim 1.59 \times 2 = 3.18\%$.

7.7.1.1 HRS Acceptances

Differences in the HRS acceptances could explain the differences in Q^2 histogram profiles. Figure 7.7.3 are plots of Carbon-Multifoil target for each of the HRS, with foils at $\pm 12.5, \pm 6.25$ and 0 cm from the center of the target, with $+(-)$ indicating downstream(upstream) of target center. The acceptances at the center of the target looked similar between the HRSs. But the acceptances at either end of the target (± 12.5 cm) were very different. There were acceptance losses towards the back end ($+12.5$ cm) of the target in LHRS i.e. some fraction of the electrons scattered at higher angles didn't make it to the detector, pushing the average scattering angle towards a lower value in the LHRS. A lower central scattering angle would mean
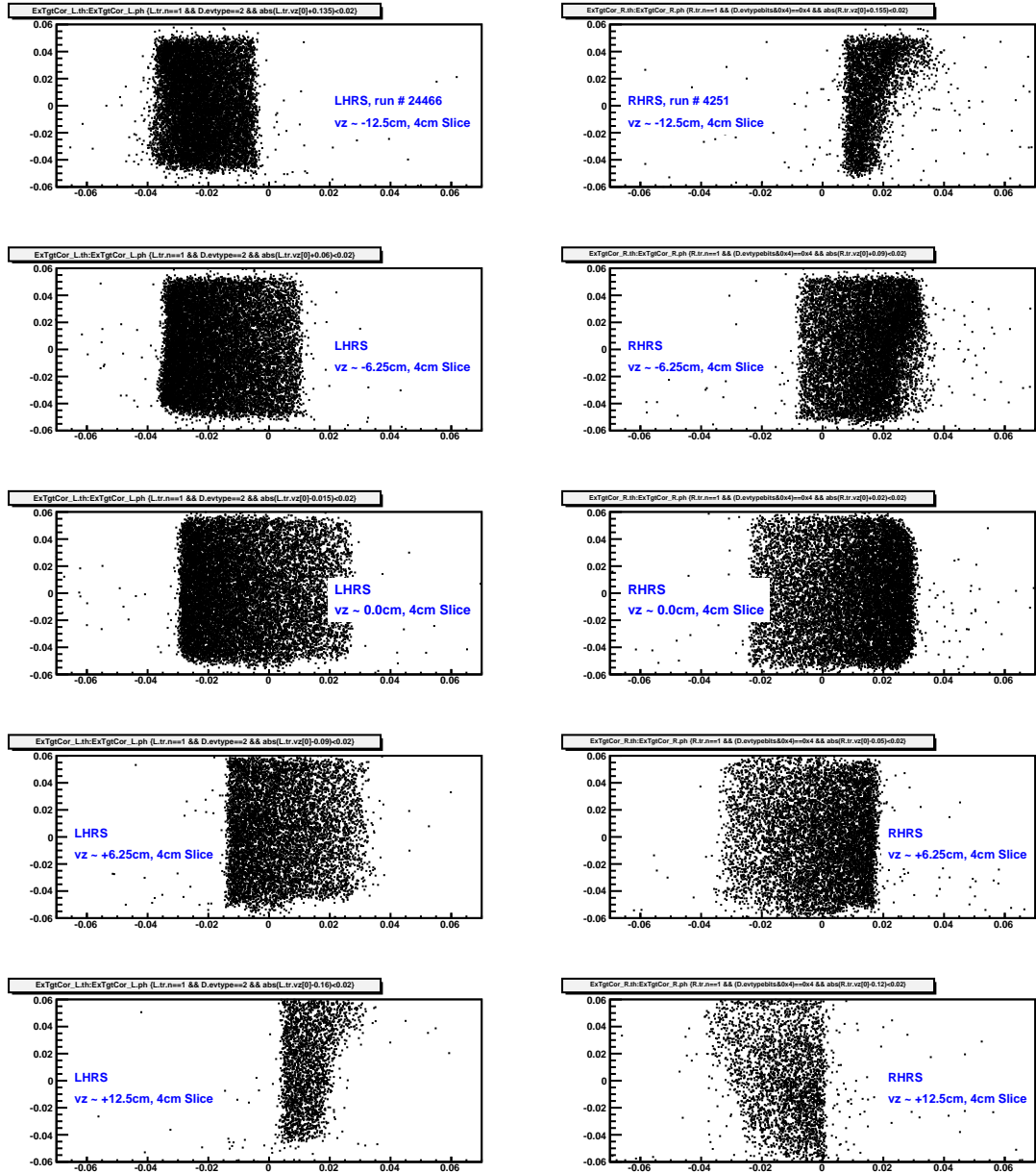
Figure 7.7.3: Acceptances of the Carbon Multifoil target. The edges of acceptance for LHRS and RHRS were different due to slight differences in the HRS offsets from the target. For instance, for foil 1, RHRS's edge fell off $\sim 8 - 9$ mrad, while LHRS's edge fell off at 5 mrad. The HRS offsets can be seen in all the foils, with the downstream foils being affected in the opposite direction.
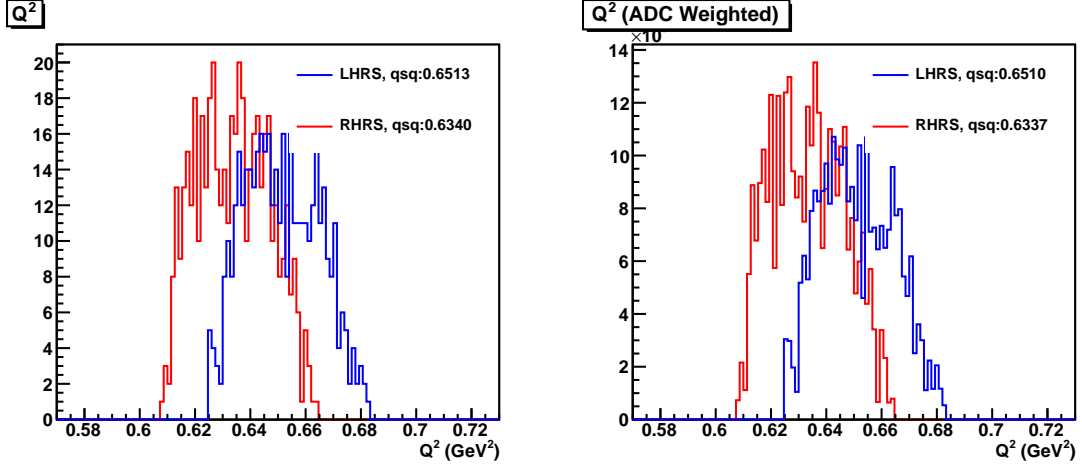
Figure 7.7.4: Q^2 plots for both HRS with x/y sieve cut of 5 mm, and target z cut of 2 cm. The beam position at BPM4bx was -2.2 mm. Q^2 variation between the HRSs was $\sim 2.69\%$.

lower Q^2 (in the LHRS). On the RHRS, there were acceptance losses at both ends of the target, with relatively larger losses at the front end (-12.5 cm). So the Q^2 increased slightly in RHRS. The net effect of the acceptance losses is that it decreased the Q^2 in the LHRS and increased it in the RHRS, pushing the Q^2 between the HRSs towards each other, possibly providing an explanation for the Q^2 discrepancies observed in Figure 7.7.2.

To confirm that these discrepancies in Q^2 between the HRSs were due to the differences in HRS acceptances, the Q^2 at the center of the target (where the HRS acceptances were similar, with minimal acceptance losses, Figure 7.7.3) were evaluated. Figure 7.7.4 are Q^2 histograms of scattering events corresponding to 2 cm segment of the target center along z [1]. Cuts of 5 mm along x and y about the center of HRS acceptance [2] were also enforced to suppress the effects of beam position

---

[1] The target z variables ($L.tr.vz/R.tr.vz$) were calculated incorrectly in podd, so it was manually calculated. See Appendix B.7 for further details.

[2] These cuts were enforced at the location of the "sieve" by evaluating the beam position in x_{sieve} and y_{sieve} at the location of the sieve. This evaluation is described in Appendix B.8. Further details on the sieve is available at [Ni01, Ni02, SN10].
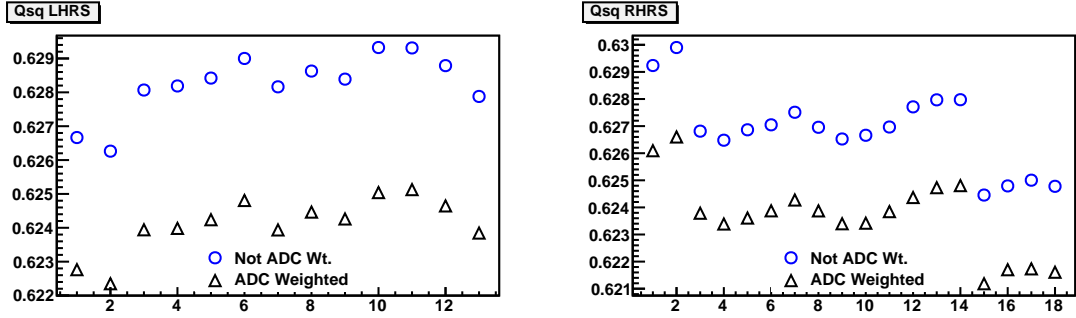
Figure 7.7.5: Detector ADC weighted and unweighted Q^2 plots. The ADC weighted points are in black and unweighted are in blue.

fluctuations on Q^2. These cuts were enforced close to the entrance of the first HRS dipole. In Figure 7.7.4, the Q^2 difference between the HRS was 2.69%, which was much closer to the expected Q^2 difference of $\sim 3.2\%$ for the HRS central scattering angles of (0.2463,-0.2424) rad which differed by $\sim 1.6\%$.

7.7.2   Average Q^2

All the HAPPEX-III Q^2 data are plotted in Figure 7.7.5 in the order in which they were acquired. The points labeled with circles were energy unweighted and the ones labeled with triangles were energy weighted Q^2. As observed earlier, the energy weighted Q^2 were slightly smaller than the energy unweighted counterpart.

The striking feature about Figure 7.7.5 was that the Q^2 fluctuated over the course of the run, even though the experimental kinematics remained unchanged. At a fixed experimental kinematics, one would expect the Q^2 to remain unchanged. So why did the Q^2 change over the course of the run?

The answer lay in the beam position fluctuations at the target. The Q^2 was sensitive to the beam position variations at the target because any beam position variation at the target in the scattering plane (xz-plane in Figure 7.7.1a) changed the effective scattering angle at the detector plane. Turns out that the beam position

at the target indeed varied over the course of the experiment, and the Q^2 variations tightly correlated to these variations. The Q^2 could cleanly be grouped into data sets corresponding to the unique beam positions (along horizontal) at the target. Figure 7.7.6 are plots of the average Q^2 of such data sets, along with the corresponding beam positions measured at the target BPMs (along horizontal). (There are more
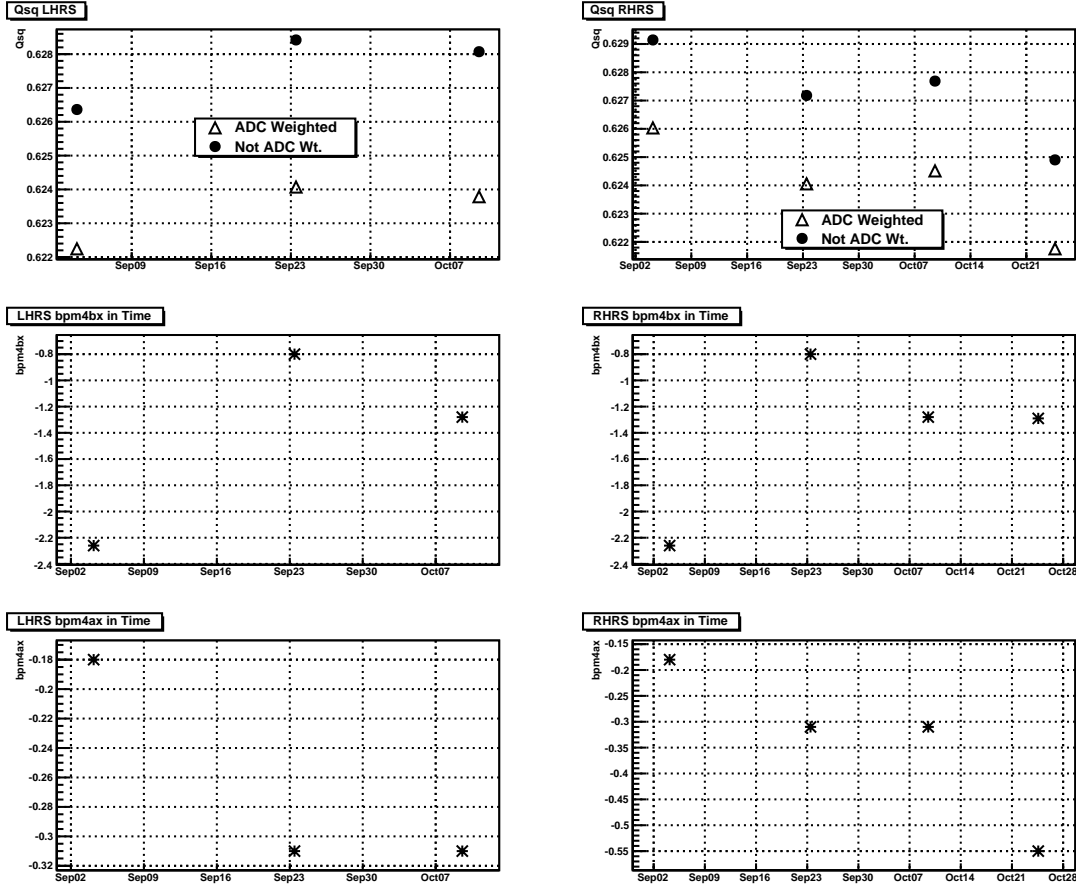
Figure 7.7.6: HAPPEX-III Q^2 correlated tightly with beam position variations at the target along the horizontal. This was because any beam position variations at the target in the scattering plane (xz) changed the effective scattering angle at the detector plane, leading to variation in scattered rates. The first three sets of Q^2 runs were taken simultaneously with both the HRSs. The last set of Q^2 runs (Oct 25) were taken with only the RHRS, because the LHRS was not functional. This set of data was also acquired with a 20 cm LH2 target instead of the 25 cm used for the rest of the Q^2 data.

data points for the RHRS than for the LHRS in Figure 7.7.6 because only the RHRS was functional during the last set of Q^2 data acquisition.)

To confirm that these Q^2 variations were due to beam position variations at the target, and not due to other effects, Q^2 runs from the first two Q^2 data sets (grouped by beam positions) were examined. The first data set was taken with the beam at -2.2 mm on BPM4bx, and the second data set taken with the beam at -0.8 mm on the same BPM. Assuming that the change in the beam positions observed at BPM4bx reflected the beam position changes at the target by a similar amount [1], the beam would have moved by +1.4 mm [2] between the two data sets. A +1.4 mm (towards the RHRS) beam position shift in x was $\sim +1.4/1.1759 = +1.19$ mrad change (increase) in the central scattering angle of the LHRS, and $\sim -1.4/1.1825 = -1.18$ mrad change (decrease) in the central scattering angle of the RHRS [3]. Considering that the HRS central scattering angles were (0.2463(LHRS),-0.2424(RHRS)) [4] rad for the first data set, the HRS central scattering angles for the second data set was $(0.2463 + 0.00119, -0.2424 + 0.00118) = (0.2475, -0.2412)$ rad. These were variations of $\sim 1.6\%$ and $\sim 2.6\%$ in the central scattering angles between the HRS in the first and second data set respectively. Therefore, one would expect Q^2 variations of $\sim 3.2\%$ and $\sim 5.2\%$ between the HRSs in these data sets.

The Q^2 plots presented in Figure 7.7.4 of Section 7.7.1.1 corresponds to the first data set. The Q^2 differences between the HRS was $\sim 2.69\%$ (This plot included only the data corresponding to the electrons scattered in the 2 cm thick segment at the

---

[1] The target was only 1.286 m downstream of BPM4bx, so one can reasonably assume that the beam position fluctuations were similar in magnitude at the target and BPM4ax.

[2] The direction of beam motion towards and away from each of the HRS was established in dedicated calibration runs. Any +ve change in beam position was a motion towards the RHRS and away from the LHRS.

[3] The distance to the center of the collimator from the center of the target was 1.1759 m for LHRS and 1.1825 m for RHRS [SN10].

[4] These were the results of pointing studies. The pointing studies were performed with the beam at -2.2 mm on BPM4bx [SN10].
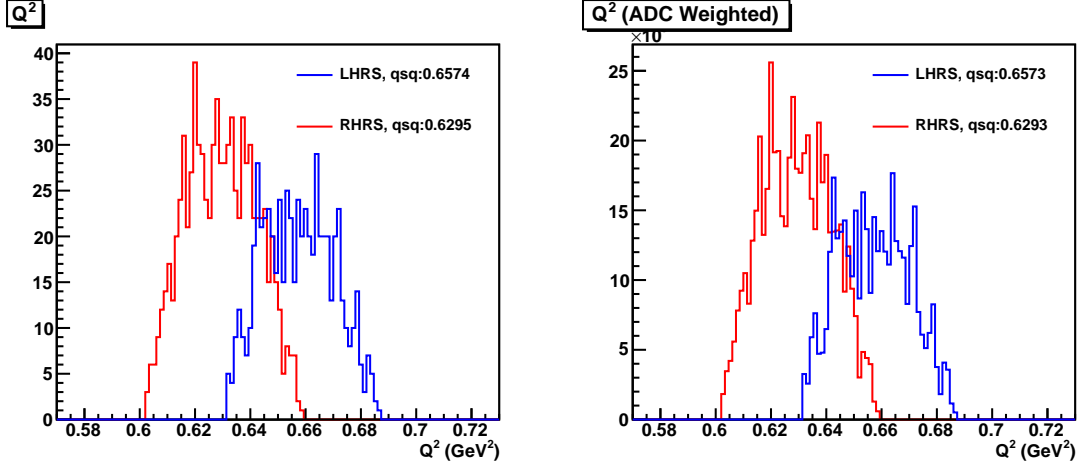
Figure 7.7.7: Q^2 plots for both HRS with x/y sieve cut of 5 mm, and target z cut of 2 cm. The beam position at BPM4bx is -0.8 mm. Q^2 variation between the HRS is $\sim 4.35\%$.

target center in order to suppress the HRS acceptance effects). Q^2 plots similar to the ones presented in Figure 7.7.4 (and with similar cuts) corresponding to the second data set are presented in Figure 7.7.7. The Q^2 differences between the HRS was $\sim 4.35\%$. The Q^2 differences between the HRS for both the data sets were fairly close to the expected differences. Thus, the variation in the average Q^2 in Figure 7.7.6 was well explained in terms of beam position variations over the course of the run.

The production data were taken at each of these beam positions, so no correction to the Q^2 was necessary at any of these beam positions. The average Q^2 by data set, grouped in these sets (determined by the beam positions at the target), are summarized in Table 7.16. The average Q^2 for each of the HRS, weighted by the amount of charge collected in each of the HRS are presented in Table 7.17.

7.7.3 Systematic Uncertainties in Q^2

The systematic errors in Q^2 increased the systematic error in A_{PV}, so it was important to minimize them. Some sources of systematic uncertainties, and their net

			LHRS		
Date	BPM4ax	BPM4bx	Q^2	Q$^2_{wt}$	Charge (mC)
Sep01-Sep04	-0.13	-2.23	0.6264	0.6222	2744.48
Sep04-Sep24	-0.30	-0.80	0.6284	0.6241	37649.30
Sep24-Oct20	-0.31	-1.30	0.6281	0.6238	56048.92
Oct24-Oct25	-0.54	-1.32			
			RHRS		
Date	BPM4ax	BPM4bx	Q^2	Q$^2_{wt}$	Charge (mC)
Sep01-Sep04	-0.13	-2.23	0.6291	0.6260	2899.67
Sep04-Sep24	-0.30	-0.80	0.6272	0.6241	35558.76
Sep24-Oct20	-0.31	-1.30	0.6277	0.6245	55438.164
Oct24-Oct25	-0.54	-1.32	0.6249	0.6218	2281.79

Table 7.16: The Q^2 averages of data sets corresponding to unique beam positions, along with the charge collected at each of these beam positions. The beam position did not change much between Sep24 and Oct25, but the accelerator went down on Oct20, and resulted in failure of 25 cm LH2 target fan. So 20 cm LH2 target is used instead from Oct20 onwards. The LHRS magnets never fully recovered as well, so all the runs after Oct20 are RHRS only runs.

	Q^2	Q$^2_{wt}$
LHRS	0.6282	0.6239
RHRS	0.6275	0.6243
Average	0.6278	0.6241

Table 7.17: Charge weighted Q^2.

contribution to the Q^2 uncertainty is described in this section.

7.7.3.1 HRS Central Scattering Angle (Θ_0)

Historically, the uncertainty in the HRS central angle determination has been the largest source of uncertainty in Q^2 determination. So, dedicated HRS central angle measurements were performed to keep the uncertainty in central angle to a minimum. The HRS central angles were measured via two independent techniques: pointing and survey.
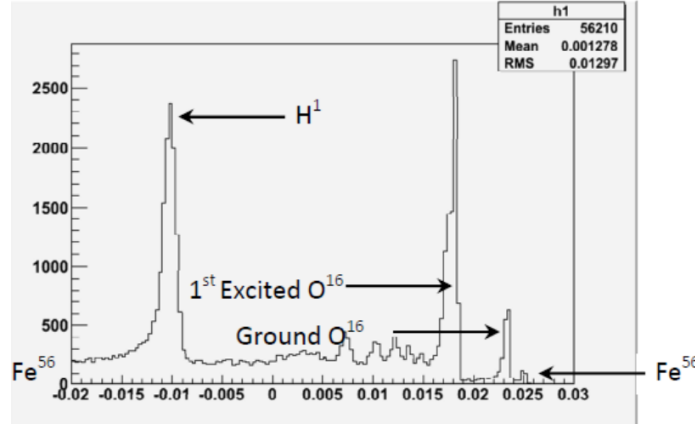
Figure 7.7.8: The spectra of the H_2O-cell target. The energy differences between the hydrogen nucleus peak and the rest of the nuclei peaks (ground state oxygen, first excited state oxygen, and iron) were used to determine the HRS central scattering angle. The x-axis is in units of GeV. Reproduced from [SN10].

7.7.3.1.1 Pointing Measurements: The pointing measurements [1] utilize the excellent momentum resolution of the hall A HRS (5×10^{-4} [Al04]) to determine the HRS central scattering angles. In this method, electrons were scattered off a water-cell and the energy differences between the elastic peaks of different nuclei measured to extract the HRS central scattering angle, see Figure 7.7.8. The first step in this measurement involved the calibration of the HRS transport matrices at the pointing kinematics. This calibration was performed by scattering electrons off a carbon foil target at the pointing kinematics, and adjusting the HRS transport matrices to reproduce the well known separation of ~ 4.38 MeV between the carbon ground state and first excited state. With the HRS transport matrices appropriately calibrated, the energy differences between the elastic peaks of different nuclei from the water-cell target data were determined. The HRS central angle was then extracted by using the following expression for the measured energy, E', of the scattered electron

$$E' = \frac{E_0 - \epsilon_0 - \frac{1}{2m}(m *^2 - m^2)}{1 - (1 - \cos\Theta_0)(E_0 - \epsilon_0)/m} - \epsilon' \qquad (7.7.6)$$

---

[1]All the pointing studies data were taken with the beam at -2.2 mm on BPM4bx.

where E_0 was the incident beam energy, Θ_0 was the scattering angle, m was the initial nucleon mass, $m*$ was the recoiling nucleon mass, and ϵ_0 and ϵ' were the energy losses of the incident and the detected electrons respectively. All the terms in Eq. 7.7.6 except Θ_0 were known, so Θ_0 could be trivially extracted. The HRS central scattering angles for HAPPEX-III were determined to be (0.2463(LHRS),-0.2424(RHRS)) rad.

The $33 - 42$ MeV separation between the nuclei peaks of the water-cell target could be resolved to better than 150 KeV resulting in Θ_0 determination to $\sim 0.4\%$, which translated to ~ 0.4 mrad uncertainty in the HRS central angle determination. However, the finite resolution of the HRS transport matrix elements' reconstruction also resulted in some uncertainty in Θ_0, which increased the uncertainty in the HRS central angle determination to an average of 0.55 mrad (0.59(LHRS), 0.51(RHRS) mrad).

This method of the central angle determination by utilizing the energy separation of the nuclei peaks was insensitive to the absolute energy. So, despite the pointing analysis being performed at a different beam energy than the HAPPEX-III nominal beam energy, the central angles are very well determined. This method also had the advantage of being relatively insensitive to any variations in energy and energy loss corrections.

7.7.3.1.2 Survey: The survey was performed by the target survey group. The survey group performed physical measurements of the target and HRS locations to determine the HRS central scattering angle. The results of survey are listed in Table 7.18.

The discrepancy between the pointing and survey results in Table 7.18 was due to the differences in the nominal beam positions at the target between these measurements. The survey measurements are taken from the nominal target center. However,

	LHRS	RHRS
Pointing(rad)	0.2463 ± 0.0004	0.2424 ± 0.0004
Survey(rad)	0.2443	0.2448

Table 7.18: HRS central scattering angle results of pointing measurements and survey. The discrepancy between the results of pointing and survey results were due to inconsistencies between the reference points (at the target) used by the measurements. The survey was performed from the nominal center of the target whereas the pointing measurements were performed with the beam offset ~ -2.0 mm from this nominal center.

the pointing measurements were taken with the beam at $\sim +1.9$ mm (towards the RHRS) off the nominal target center in the scattering plane, which is a shift of $\sim +1.9/1.1 \sim +2$ mrad [1] in the scattering angle at the LHRS (and $\sim -1.9/1.1 \sim -2$ mrad at the RHRS). When the central angles in Table 7.18 are accounted for these beam position shifts, the results of pointing analysis and survey agree well within the uncertainties.

HAPPEX-III used the results of the pointing measurements for Q^2 determination because of its increased precision compared to the survey results. The results of survey were nonetheless a good cross-check on the pointing results. The HRS central angle uncertainties of (0.24(LHRS),0.21(RHRS))% resulted in uncertainties of (0.48(LHRS),0.42(RHRS))% in Q^2. These uncertainties were averaged for an average Q^2 uncertainty of 0.45%.

7.7.3.2 Energy Weighting

The energy weighting changed the Q^2 by $-0.7\% \pm 0.08\%$ on the LHRS, and $-0.5 \pm 0.07\%$ on the RHRS. The $\pm 0.08\%$ and $\pm 0.07\%$ were the average fluctuations in the energy weighted Q^2 run-by-run for each HRS. Since there were only 3 distinct Q^2 data sets on the LHRS, and 4 distinct data sets on the RHRS, a generous 0.1% fluctuation

---

[1] The distance between the target and the collimator of the HRS is ~ 1.1 m.
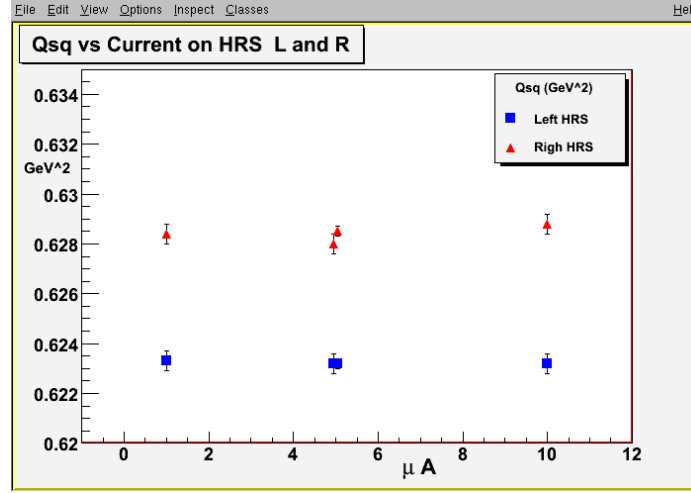
Figure 7.7.9: Q^2 at varying beam currents. There is very little difference, if any, in the Q^2 as the scattering rate increases.

was assigned as the uncertainty in Q^2 due to energy weighting.

7.7.3.3   Rate Dependence and Drifts in Time

A generous 0.2% uncertainty in Q^2 was assigned due to rate dependence of Q^2 and variations in Q^2 over the course of the experiment.

Uncertainty determination due to Q^2 variations over time was limited by a finite amount of data. There were only 3 distinct Q^2 measurements on the LHRS, and 4 on the RHRS. The Q^2 variations over time in each of these data sets was $\sim 0.1\%$.

Figure 7.7.9 presents the results of rate dependency study on the Q^2. The Q^2 at all these rates were identical to within 0.05%. Despite the relative insensitivity of the Q^2 on rates, all theHAPPEX-III Q^2 data were acquired at $2 - 5~\mu$A in order to minimize the DAQ deadtime.

The uncertainty in Q^2 due to rate dependence was negligible. But this effect was nonetheless taken into account with the generous assignment of 0.2% uncertainty in Q^2 as the cumulative uncertainty due to drifts in Q^2 over the course of the experiment and Q^2 dependence on rates.

Table 7.19: A breakdown of the Q^2 systematic uncertainties. The largest source of Q^2 uncertainty was the uncertainty in HRS central angle determination. The HRS central angle uncertainty was slightly different between the HRS, so an average of these uncertainties was presented in the table.

Error Source	Error	Error in Q^2
HRS Central Angle	0.4 mrad	0.45%
HRS Momentum (5×10^{-4}) [Al04]	1.5 MeV	0.05%
Beam Energy (1×10^{-3}) [Al04]	3.0 MeV	0.1%
Beam Position Fluctuations	1 um	1.4×10^{-3}%
Drifts in Time		0.2%
Energy Weighting		0.1%
Total Systematic Error		0.52%

7.7.3.4 Beam Position Fluctuations

The beam position fluctuations were extracted to be of the order of nm from the asymmetry data, as is summarized in Table 7.6. Nevertheless, a very conservative amount of 1 μm is taken as the average beam position fluctuations for the Q^2 data. The contribution to the total systematic uncertainty in Q^2 from 1 μm beam position fluctuation is negligible as given in Table 7.19.

7.7.3.5 Summary of Systematic Uncertainties in Q^2

The total uncertainty in the Q^2, along with a breakdown of the contribution from various sources are presented in Table 7.19.

7.7.4 Average Q^2

The average of all the Q^2 measurements performed over the course of HAPPEX-III is

$$Q^2 = 0.6241 \pm 0.0032 \ \text{GeV}^2.$$ (7.7.7)

7.7.5 Correction and Systematic Uncertainty in A_{PV}

The uncertainty in A_{PV}, quoted at the Q^2 measured during HAPPEX-III, due to uncertainty in Q^2 was calculated as

$$\sigma_{A_{Q^2}} = \frac{dA_{NS}}{dQ^2}\sigma_{Q^2} \tag{7.7.8}$$

where

$$\frac{dA_{NS}}{dQ^2} = \frac{A_{NS}(Q^2 + \Delta Q^2) - A_{NS}(Q^2 - \Delta Q^2)}{2\Delta Q^2} \tag{7.7.9}$$

with $A_{NS}(= A_A + A_V)$ being the non-strange parity-violating asymmetry (See Eq. 2.3.3). ΔQ^2 was taken to be 0.005 GeV^2.

The systematic uncertainty in A_{PV} due to uncertainties in Q^2 determination was 182 ppb for HAPPEX-III.

7.8 Parity-Violating Asymmetry (A_{PV})

The physics asymmetry, A_{PV}, is calculated using Eq. 7.6.1 to be

$$A_{PV} = -23.803 \pm 0.778(\text{stat}) \pm 0.359(\text{syst}) \text{ ppm} \tag{7.8.1a}$$

$$= -23.803 \text{ ppm} \pm 3.267\%(\text{stat}) \pm 1.509\%(\text{syst})$$

The corrections to A_{PV} and the associated uncertainties are summarized in Table 7.20.

Description	Correction (ppb)	Uncertainty (ppb)
Detector Linearity	0	122
False Asymmetry	251	41
A_I	268	5
A_F	-16	41
Kinematic Acceptance	120	48
Polarization	-2532	199
Background	237	194
Al (QE)	125	126
Inelastics	114	55
Mag. Iron	0	136
Q^2	–	182
Total	**-1924**	**359**

Table 7.20: HAPPEX-III corrections to the physics asymmetry, A_{PV}, and associated systematic uncertainties. The correction arising from A_I is applied to A_{raw} on a pulse-to-pulse basis by normalizing the response of the detector by the response of the beam current monitor (BCM) on a pulse-by-pulse basis.

7.9   Strange Form Factors

As described in Section 2.3, the parity-violating asymmetry, A_{PV}, of the electron-proton scattering of HAPPEX-III can be expressed as

$$
\begin{aligned}
A_{PV} =& A_{PV}^0 \times \{(1 - 4\sin^2\theta_W)(1 + R_V^p) \\
& - \frac{(\epsilon G_E^p G_E^n + \tau G_M^p G_M^n)(1 + R_V^n)}{\epsilon(G_E^p)^2 + \tau(G_M^p)^2} \\
& - \frac{\epsilon G_E^p (G_E^s + \eta G_M^s)(1 + R_V^{(0)})}{\epsilon(G_E^p)^2 + \tau(G_M^p)^2} \\
& - \frac{\epsilon'(1 - 4\sin^2\theta_W)G_M^p \tilde{G}_A^{Z,p}}{\epsilon(G_E^p)^2 + \tau(G_M^p)^2}\} \\
=& A_V + A_S + A_A
\end{aligned}
\tag{7.9.1}
$$

with

$$A_V = A_{PV}^0 \left[(1 - 4\sin^2\theta_W)(1 + R_V^p) - \frac{(\epsilon G_E^p G_E^n + \tau G_M^p G_M^n)(1 + R_V^n)}{\epsilon(G_E^p)^2 + \tau(G_M^p)^2} \right] \quad (7.9.2a)$$

$$A_S = -A_{PV}^0 \left[\frac{\epsilon G_E^p (G_E^s + \eta G_M^s)(1 + R_V^{(0)})}{\epsilon(G_E^p)^2 + \tau(G_M^p)^2} \right] \quad (7.9.2b)$$

$$A_A = -A_{PV}^0 \left[\frac{\epsilon'(1 - 4\sin^2\theta_W)G_M^p \tilde{G}_A^{Z,p}}{\epsilon(G_E^p)^2 + \tau(G_M^p)^2} \right] \quad (7.9.2c)$$

where the contributions to A_{PV} from the vector, axial-vector and the strange content (A_V, A_A and A_S) have be separated following the notational convention of [Ma05]. A_{PV}^0 is defined in Eq. 2.1.9 as [Ze59]

$$A_{PV}^0 \equiv -\frac{G_F |Q^2|}{4\pi\alpha\sqrt{2}} \quad (7.9.3)$$

where G_F is the weak interaction Fermi constant and α is the fine-structure constant. G_E^p and G_M^p are the electric and magnetic form-factor (FF) of the proton. G_E^n and G_M^n are electric and magnetic FF of the neutron. $\tau = Q^2/4M_p$, where M_p is the proton mass. $\epsilon = [1 + 2(1 + \tau)\tan^2(\Theta/2)]^{-1}$ where Θ is the central scattering angle in the lab frame. θ_W is the weak mixing angle defined as $\sin^2\theta_W \equiv 1 - M_W^2/M_Z^2$ in the on-shell renormalization scheme, where M_Z and M_W are the masses of the Z^0 and W bosons respectively. The R-coefficients contain the radiative corrections described in Section 2.4, and are summarized in Table 7.21.

The A_{PV} of Eq. 7.9.1 ($= A_V + A_S + A_A$) is determined from the measurements performed during HAPPEX-III, and is used to extract the strange FFs, G_E^s and G_M^s. For this extraction, the parity-violating asymmetry expected if $G_E^s = G_M^s = 0$ is evaluated as

$$A_{NS} = A_V + A_A. \quad (7.9.4)$$

	Tree-Level	One-Quark	Anapole
R_V^p	0	-0.0438087	–
R_V^n	0	-0.012192	–
$R_V^{(0)}$	0	-0.012192	–
$R_A^{T=1}$	0	-0.171419	0.086 ± 0.34
$R_A^{T=0}$	0	-0.2362	0.014 ± 0.20
$R_A^{(0)}$	0	-0.525718	N/A

Table 7.21: The R-factors corresponding to tree-level, one-quark and anapole corrections in the $\overline{\text{MS}}$-scheme of the Standard Model. The one-quark corrections are determined by using the values published in [Na11], and the anapole corrections are adopted from [Zh00].

A_{NS}, along with the A_{PV} of Eq. 7.9.1 is used to calculate the linear combination of the strange FFs, $G_E^s + \eta G_M^s$, as

$$G_E^s + \eta G_M^s = \frac{1}{A_{PV}^0} \frac{\epsilon (G_E^p)^2 + \tau (G_M^p)^2}{\epsilon G_E^p (1 + R_V^{(0)})} (A_{PV} - A_{NS}) \qquad (7.9.5)$$

where $\eta = \frac{\tau G_M^p}{\epsilon G_E^p}$.

The extraction of strange FFs during HAPPEX-III uses the parameterization of electromagnetic FFs (G_E^p, G_M^p, G_E^n, G_M^n) described by Arrington and Sick [AS07]. This method incorporates the two-photon-exchange corrections to published FF data, and performs a global fit to parameterize the electromagnetic FFs.

The axial-vector FFs, $\tilde{G}_A^{Z,p}$, is given by Eq. 2.2.11 as

$$\tilde{G}_A^{Z,p} = -(1 + R_A^{(T=1)}) G_A^{(3)} + \sqrt{3} R_A^{(T=0)} G_A^{(8)} + (1 + R_A^{(0)}) G_A^s \qquad (7.9.6)$$

where $G_A^{(3)}$, $G_A^{(8)}$, and G_A^s are the isovector, isoscaler, and the strange axial-vector FFs [Mu94]. The R-coefficients contain the radiative corrections associated with these axial-vector FFs, and are given in Table 7.21. For later discussions, the isovector

component of the $\tilde{G}_A^{Z,p}$ is defined as

$$G_A^{e(T=1)} = -(1 + R_A^{(T=1)})G_A^{(3)}. \tag{7.9.7}$$

The axial-vector FFs of Eq. 7.9.6 are parametrized with a dipole or Galster form [AS07] as discussed in Section 2.2.2 of Chapter 2 as

$$G_A^j(Q^2) = G_A^j(0)G_A^D(Q^2) \tag{7.9.8a}$$

$$\text{with} \quad G_A^D(Q^2) = \frac{1}{(1 + Q^2/\Lambda_A^2)^2} \tag{7.9.8b}$$

where $\Lambda_A = 1.001 \pm 0.02\,\text{GeV}$ [Bu03] is the axial-vector dipole mass parameter.

7.9.0.1 Strange Form Factors Extraction

At the kinematics of HAPPEX-III ($\langle Q^2 \rangle = 0.624\,\text{GeV}^2$), the non-strange parity-violating asymmetry is

$$\boxed{A_{NS} = A_V + A_A = -24.062 \pm 0.734(\text{FF})\text{ ppm.}} \tag{7.9.9}$$

The uncertainty above (FF) results from the uncertainty in the electromagnetic FFs and radiative corrections to the axial-vector FFs. Using the parity-violating asymmetry, A_{PV}, of Eq. 7.8.1a, along with Eq. 7.9.5, the linear combination of the strange FFs are extracted to be

$$\boxed{G_E^s + 0.517\,G_M^s = 0.003 \pm 0.010 \pm 0.004 \pm 0.009} \tag{7.9.10}$$

where the uncertainties are statistical, systematic, and FF respectively.

8

PREX Analysis and Results

This chapter presents a brief summary of the analysis and results of PREX. While I was heavily involved with the studies relating to the polarized electron source in preparation for PREX, along with various aspects of the experimental instrumentation and data analysis during the experiment, I was only partially involved in the "offline" asymmetry data analysis for PREX. After the asymmetry data had been filtered by imposing various cuts, I performed further statistical analysis, and generated various summaries using these data. My results only served as an independent cross-check on the results of the main analysis. Therefore, I make no attempt to provide an exhaustive summary of the PREX analysis and results.

8.1 Overview

The techniques used to collect the asymmetry data during PREX were similar to the ones used during HAPPEX-III. During PREX, the asymmetry data were collected with the IHWP state reversed once every 12 hours or so for slow helicity reversal. In addition to the IHWP, a Wien filter also performed slow helicity reversal once every

few days. Roughly equal statistics were collected in each of the "slow helicity states".

Like during HAPPEX-III, the data acquired over a period between two successive IHWP or Wien reversals were referred to as belonging to a "slug". A total of 21 acceptable slugs were collected during PREX. A typical data run lasted about an hour, and entire data set consisted of 316 individual data runs. Each one-hour run contained about 50 K quadruplets. The final data set consisted of a total of 2×10^7 helicity-quadruplets.

The parity-violating asymmetry for PREX is evaluated as

$$A_{PV} = \frac{1}{P_b} \frac{A_{corr} - P_b \sum_i A_i f_i}{1 - \sum_i f_i} \tag{8.1.1}$$

where the corrected detector asymmetry, A_{corr}, is given as

$$A_{corr} = A_{raw} - A_F. \tag{8.1.2}$$

A_{raw} is the helicity-correlated (HC) raw detector asymmetry, and its determination is discussed in Section 8.2.1. A_{raw} is normalized for beam intensity on a pulse-by-pulse basis. Therefore, any HC beam intensity asymmetry, A_I, that arises due to HC beam intensity fluctuations are already corrected in A_{raw}. A_I is described in Section 5.6.1. A_F is the HC (false) beam asymmetry expressed as

$$A_F = A_{Fb} + A_{FT} \tag{8.1.3}$$

where A_{Fb} is the HC beam asymmetry arising from differences in beam position, angle and energy. A_{FT} is the false asymmetry arising from imperfect cancellation of the asymmetry due to transverse beam polarization. P_b is the longitudinal beam polarization and f_i is the fractional background with asymmetry A_i. The extraction

of these variables, and A_{PV} determination is discussed in this chapter.

8.2   Asymmetry Analysis

The asymmetry data analysis procedure used during PREX was similar to the one used during HAPPEX-III. The asymmetry data were first cleaned by imposing various non-HC cuts, and A_{raw} and A_F extracted. A_{raw} was corrected for A_{Fb} by either via beam modulation (BM). During PREX, A_{FT} was determined from dedicated A_{FT} runs. Although a dedicated A_{FT} detector was used during PREX, this detector was only used to monitor A_{FT} in real time to guard against drifts in transverse beam polarization. The corrected asymmetry was evaluated using Eq. 8.1.2.

8.2.1   Raw Asymmetry (A_{raw})

The raw asymmetry, A_{raw}, for PREX data was formed from helicity-quartets (RLLR or LRRL) unlike for HAPPEX-III data for which A_{raw} was formed from helicity-pairs. The helicity-patters are described in Section 3.4. To calculate A_{raw} from helicity-quartets, detector responses corresponding to the same helicity state in each quartet were averaged to form "averaged" helicity-pairs. These averaged helicity-pairs were then used to calculate A_{raw} using Eq. 7.2.1, much like in HAPPEX-III. As discussed in Section 5.7, this "averaging" canceled the power-line 60 Hz noise from A_{raw}.

During PREX, the asymmetry data were collected by four focal plane detectors: det_1, det_2, det_3 and det_4. det_1 and det_2 were located on the right high-resolution spectrometer (RHRS), and det_3 and det_4 on the left high-resolution spectrometer (LHRS). det_1 and det_3 were the bottom detectors, and det_2 and det_4 were the top detectors in each of the HRSs. The raw asymmetries were calculated for each of these individual detectors using equations similar to Eq. 7.2.1. The detector combinations

of the raw asymmetries were also evaluated for the detectors in LHRS alone (det_l), RHRS alone (det_r), upper two detectors (det_hi), lower two detectors (det_lo) and all the detectors (det_all) using equations similar to Eq. 7.2.2 as

$$A_{raw}^X = \frac{\sum_i S_R^i w^i - \sum_i S_L^i w^i}{\sum_i S_R^i w^i + \sum_i S_L^i w^i} \tag{8.2.1}$$

where $X = \{$l,r,hi,lo,all$\}$, $S_{R(L)}^i$ is the normalized i^{th} detector response integrated over the right(left) helicity window. i runs over detectors $\{1,2\}$ for det_r, $\{3,4\}$ for det_l, $\{1,3\}$ for det_lo, $\{2,4\}$ for det_hi and $\{1,2,3,4\}$ for det_all. All the weights $w^i = 1$.

The PREX data were acquired in runs that typically lasted an hour, very much like in HAPPEX-III. Therefore, the detector asymmetry mean from each run was weighted by the width of the asymmetry distribution. This weighting is discussed in Section 7.5. The A_{raw}^{all} measured during PREX was [We12]

$$\boxed{A_{raw}^{all} = -555 \pm 63 \text{ ppb.}}$$

8.2.2 Beam Intensity Asymmetry (A_I)

During PREX, the HC beam intensity asymmetry, A_I, was measured to be

$$\boxed{A_I = -84.0 \pm 1.3 \text{ ppb.}}$$

The raw asymmetry, A_{raw}, already accounts for A_I because of pulse-to-pulse normalization, as given in Eq. 7.2.1.

8.2.3   False Asymmetry due to HC Beam Fluctuations (A_{Fb})

The false asymmetry arising from HC differences in the beam parameters such as the beam trajectory and energy at the target, A_{Fb}, was extracted using the techniques of beam modulation (BM) and regression discussed in Section 7.3.2. The random fluctuations in the beam parameters were the largest source of noise beyond counting statistics in A_{raw}. Typical beam jitter between complementary states in the window-quadruplets was less than 2 ppm in energy, and 20 μm in position.

After A_{Fb} correction, the noise in the resulting asymmetry $A_{raw} - A_{Fb}$ was about 210 (180) ppm per quadruplet, when the beam current was of 50 (70) μA. This remaining noise was dominated by counting statistics, corresponding to a rate of about 1 GHz at a beam current of 70 μA. During PREX, A_{Fb} was measured to be

$$\boxed{A_{Fb} = -39.0 \pm 5.9 \text{ ppb.}}$$

8.2.4   False Asymmetry due to Transverse Beam Polarization (A_{FT})

During PREX, the transverse beam polarization was measured to be

$$\boxed{A_T^{Pb} = +280 \pm 210(\text{stat}) \pm 140(\text{syst}) \text{ ppb.}}$$

This asymmetry is essentially zero within the uncertainties, and the false asymmetry arising from imperfect cancellation of A_T^{Pb} between the two HRS detectors, A_{FT}, was negligible.

A_T^{Pb} was measured with fully transverse (vertical) beam polarization on the primary detectors that also collected the asymmetry data. PREX used lead-diamond

sandwich target as the primary target, so the net transverse asymmetry, A_T, included the effects from ^{12}C as well as the ^{208}Pb in the target. Therefore, A_T^C, arising due to the presence of ^{12}C, was measured with dedicated data runs. A_T^{Pb} was determined by subtracting A_T^C from A_T. The A_T^C was measured to be [Ac12]

$$A_T^C = -6.49 \pm 0.36(\text{stat}) \pm 0.10(\text{syst}) \text{ ppm.}$$

The transverse asymmetry measurements performed during PREX is described in [Ac12].

8.2.5 Corrected Asymmetry (A_{corr})

The corrected asymmetry, A_{corr}, was evaluated, using Eq. 8.1.2, to be

$$\boxed{A_{corr} = 594 \pm 50 \text{ (stat) ppb.}}$$

A_{corr} is the asymmetry that has been corrected for A_I, A_{Fb} and A_{FT}.

The helicity-pair distribution of the asymmetries for the complete data sample had negligible non-Gaussian tails over more than four orders of magnitude, indicating that the asymmetry distribution width was dominated by the counting statistics.

The statistical behavior of the asymmetries summarized by runs were also checked to test that the data behaved statistically and the errors were being accurately calculated. Typical runs lasted about one-hour, and consisted of 50 K quadruplets each. There were a total of 316 runs. The asymmetries from the "run summaries", normalized by the corresponding statistical error, populated a Gaussian distribution of unit variance, indicating a statistically well behaved distribution.

BPM4ax(nm)	3.78
BPM4ay(nm)	−0.17
BPM4bx(nm)	2.34
BPM4by(nm)	−0.20
BPM12x(nm)	0.42

Table 8.1: The helicity-correlated (HC) position differences averaged over the course of PREX. These numbers are weighted by the statistics of BM corrected A_{raw}. The HC position differences weighting is described in Section 7.4.

8.3   HC Beam Asymmetry and Position Differences

During PREX, the HC beam asymmetry and position differences were evaluated following the procedure similar to the one used during HAPPEX-III, which is described in Section 7.4. The HC position differences averaged over the course of PREX is summarized in Table 8.1. The cumulative average is small due to cancellations as a consequence of the slow helicity reversals, the IHWP reversal and the Wien filter adjustments. The slow helicity reversals reverse the sign of the physics asymmetry while leaving certain beam asymmetries unchanged, as is described in Section 5.6.2. The differences in the beam position and energy, averaged over the course of PREX, were under 4 nm and 0.6 ppb respectively.

8.4   Normalizations and Corrections to A_{PV}

8.4.1   Beam Polarization (P_b)

During PREX, the beam polarization was measured with two independent polarimeters, the Compton and the Møller polarimeters.

The Compton polarimeter continuously monitored the beam polarization concurrently with asymmetry data acquisition. During PREX, the average beam polariza-

tion measured by the Compton polarimeter was

$$P_b = 88.20 \pm 0.12(\text{stat}) \pm 1.04(\text{syst})\%.$$

The beam polarization was stable within systematic errors.

The Møller polarimeter made nine measurements of the beam polarization at different times during PREX. These measurements were invasive, and could not be performed concurrently with asymmetry data taking. The average of the beam polarization measurements performed by Møller polarimeter was

$$P_b = 90.32 \pm 0.07(\text{stat}) \pm 1.12(\text{syst})\%.$$

The Compton and Møller beam polarization measurements were averaged to obtain an average beam polarization of

$$\boxed{P_b = 89.2 \pm 1.0\%}$$

over the experiment.

8.4.2 Backgrounds

During PREX, the dominant backgrounds in the asymmetry data were the electrons that elastically scattered from the diamond (^{12}C) cooling foils. The backgrounds arising from other sources such as the electrons that scattered inelastically from ^{12}C and ^{208}Pb, and the elastically scattered electrons that re-scattered inside the HRSs were negligible.

The electrons that elastically scattered from the diamond cooling foils made up about $6.3\pm0.6\%$ of the measured signal at the detectors. This resulted in a correction

Source	Frac.(%)	Correction (ppb)	Syst. Uncer. (ppb)
Carbon Backing	6.3 ± 0.6	-8.8	2.6
Inelastics	< 0.1	0.0	0.0
Rescattering	< 0.1	0.0	0.0
TOTAL	$-$	-8.8	2.6

Table 8.2: The sources of backgrounds during PREX, and the associated correction and systematic uncertainties in the parity-violating asymmetry, A_{PV}. The dominant source of background was the elastically scattered electrons from the carbon backing (diamond cooling foils).

of -8.8 ppb in A_{PV}, and increased the systematic uncertainty in A_{PV} by 2.6 ppb.

The electrons that scattered inelastically at the target made up a negligible fraction, $< 0.1\%$, because the acceptance of the first-excited states of both ^{12}C and ^{208}Pb was negligible. The fractional contamination of data due to the electrons that rescattered inside the HRS was negligible, $< 0.1\%$, as well. Therefore, these sources of data contamination resulted in no correction or significant systematic uncertainties in A_{PV}.

The amount of data contamination from each of these sources of backgrounds, and the associated corrections and systematic uncertainties in A_{PV} are summarized in Table 8.2.

8.4.3 Non-linearity

The non-linearity in the responses of the detector photo-multiplier tubes (PMT) that acquired the asymmetry data during PREX was limited to 1.0%. The non-linearity studies were performed *in-situ* during the experiment, and in bench-tests, before and after the experiment, that mimicked running conditions. These studies, and their results are described in [Me12].

The non-linearity in the response of the beam current monitors (BCMs) was determined to be less than 1.5%. The BCM non-linearity was determined by studying

Non-lin. Source	Non-linearity (%)	Correction (ppb)	Syst. Uncer. (ppb)
Detector PMTs	1.0	0.0	7.6
BCMs	1.5	0.0	1.5
Total	-	0.0	7.7

Table 8.3: During PREX, the non-linearity in the responses of the detector PMTs was limited to 1.1%, and in the beam current monitors (BCMs) was limited to 1.5%. The associated corrections and systematic uncertainties in the parity-violating asymmetry, A_{PV}, are listed above.

the correlation of measured beam intensity to detector PMT responses.

No correction was made due to non-linearity in the responses of the detector PMTs and the BCMs. However, the non-linearity in the responses of the detector PMTs resulted in 7.6 ppb systematic uncertainty in A_{PV}, and the non-linearity in the responses of the BCMs resulted in 1.5 ppb systematic uncertainty in A_{PV}. The non-linearity, and the associated corrections and systematic uncertainties in A_{PV} resulting from it are summarized in Table 8.3.

8.4.4 Summary of A_{PV} Corrections and Systematics

The corrections and systematic uncertainties in the parity-violating asymmetry, A_{PV}, arising from various sources are summarized in Table 8.4. The total systematic uncertainty was only 2.09% of the A_{PV}, indicating that the systematic uncertainties were well suppressed during PREX.

8.5 Finite Acceptance

During PREX, the A_{PV} measurement was performed by integrating over a finite range of the HRS acceptance. Therefore, the theoretical asymmetry needs to be integrated over the HRS acceptance as well for comparison with A_{PV} as measured during PREX. The acceptance of the HRS during PREX was characterized in order to facilitate this.

	Corr.(ppb)	Corr.(%)	Syst. Uncer.(ppb)	Syst. Uncer.(%)
Linearity	0.0	0.00	7.6	1.16
Beam Effects	-45.0	-6.88	7.4	1.13
A_I	-84.0	-12.81	1.5	0.23
A_{Fb}	39.0	5.93	7.2	1.09
A_{FT}	0.0	0.00	1.2	0.18
Polarization	70.9	10.81	8.3	1.26
Backgrounds	-8.8	-1.34	2.6	0.40
Carbon Backing	-8.8	-1.34	2.6	0.40
Inelastics	0.0	0.00	0.0	0.00
Rescattering	0.0	0.00	0.0	0.00
Total	**17.1**	**2.60**	**13.7**	**2.09**

Table 8.4: The corrections and systematic uncertainties in A_{PV} arising from various sources are summarized above.

This characterization was performed via an acceptance function, $\epsilon(\theta)$ [Ab12].

The HRS acceptance function, $\epsilon(\theta)$, gives the probability for an electron to reach the detector, located at the HRS focal plane, after elastically scattering from ^{208}Pb as a function of scattering angle θ. This function was extracted from data, and tested on Hall A Monte Carlo (HAMC) [HAMC] software. Further information on the HRS acceptance function is available at [Ab12].

The errors in $\epsilon(\theta)$ were evaluated from the changes observed when varying the parameters of the HAMC simulation within their respective errors, and are expressed as an equivalent error in the Q^2 of 0.8%. The results of Q^2 measurement for PREX is described in the next section.

8.6 Four-Momentum Transfer Squared(Q^2)

During PREX, the four-momentum transfer, Q^2, was measured to be

$$Q^2 = 0.00880 \pm 0.00011 \, \text{GeV}^2.$$

The Q^2 was measured in dedicated low-current runs at regular intervals during the experiment. Like during the HAPPEX-III Q^2 evaluation, the Q^2 data were appropriately weighted to correct biases arising from variations in the energy deposited by the electrons on the detectors. The largest source uncertainty in Q^2 was the uncertainty in the HRS central angle determination, which was suppressed to 1% by using a nuclear recoil technique [SN10] described in Section 7.7.3.1.1. The total uncertainty in Q^2 determination was 1.3%, with the uncertainties in the acceptance function $\epsilon(\theta)$ included.

The Q^2 uncertainty is not included in the A_{PV} systematic uncertainty. However, 1.3% uncertainty in Q^2 would increase the A_{PV} systematic uncertainty by 3 ppb (0.5% of A_{PV}). This number is based on $dA_{PV}/dQ^2 \approx 30$ ppm/ GeV^2, calculated in [Ho98]. This is comfortably below our quoted statistical uncertainty.

8.7 Parity-Violating Asymmetry (A_{PV})

The parity-violating asymmetry measured during PREX was

$$A_{PV} = 656 \pm 60(\text{stat}) \pm 14(\text{syst}) \text{ ppb} \tag{8.7.1}$$

at

$$\langle Q^2 \rangle = 0.00880 \pm 0.00011 \, \text{GeV}^2. \tag{8.7.2}$$

8.8 Neutron Radius of ^{208}Pb (R_n)

The extraction of the point neutron radius, R_n, was performed by first extracting the weak charge radius, R_W [Ho12]. The quantity R_W was extracted by using the A_{PV}
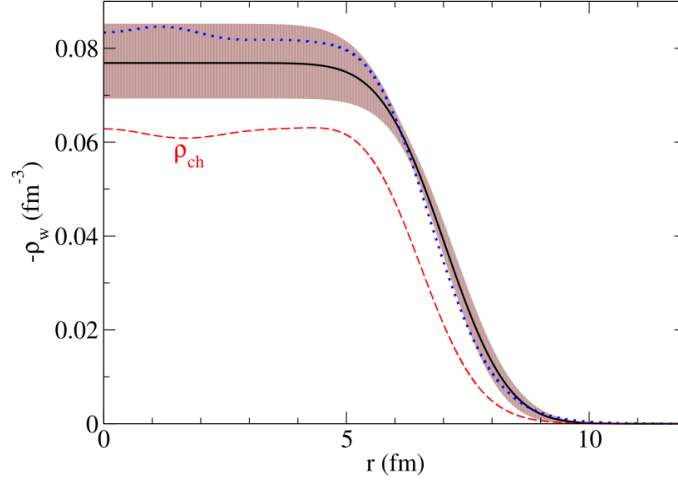
Figure 8.8.1: The weak charge density extracted from the measurements of PREX (solid black line) along with the well known electromagnetic charge density (ρ_{ch}), and a sample mean-field result based on FSUGold interaction is presented above [Ho12]. The brown error band represents uncertainties due to experimental and model errors. The PREX result is the first direct evidence that the weak charge density, of a heavy nucleus, is more extended than the electromagnetic charge density. Reproduced from [Ho12].

determined from the measurements of PREX to be

$$R_W = 5.826 \pm 0.181(\text{exp}) \pm 0.027(\text{mod}) \text{ fm.} \tag{8.8.1}$$

The uncertainties above refer to PREX statistical and systematic experimental uncertainty (exp), and uncertainty arising from the model dependence of R_n extraction (mod). Comparing this to the previously known charge radius of $R_{ch} = 5.503$ fm [Ho12], the thickness of the "weak charge skin" is determined to be [Ho12]

$$R_W - R_{ch} = 0.323 \pm 0.181(\text{exp}) \pm 0.027(\text{mod}) \text{ fm.} \tag{8.8.2}$$

Eq. 8.8.2 represents an experimental milestone: this is the first direct evidence that the weak charge density, of a heavy nucleus, is more extended than the electromagnetic
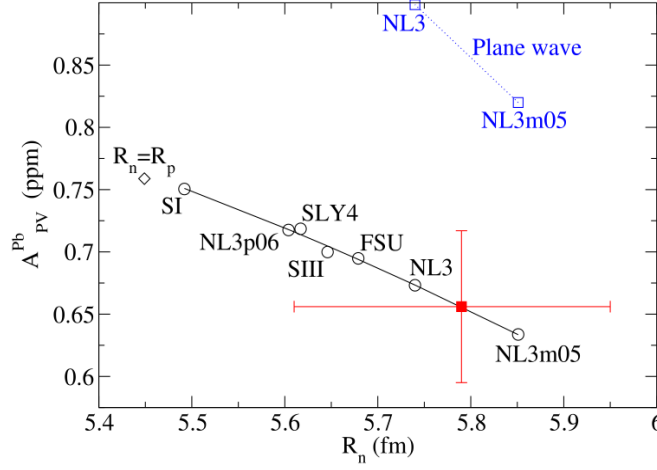
Figure 8.8.2: The left plot presents ^{208}Pb parity-violating asymmetry, A_{PV}, as a function of the neutron radius, R_n, for various theoretical models (indicated by circles). The diamond point is the expected A_{PV} for $R_n = R_p$, where R_p is the proton radius. The blue squares represent plane-wave calculations, *without* any Coulomb distortion corrections, and merely emphasize the importance of the Coulomb distortions. The results of PREX is the red square, with the vertical error bar indicating experimental uncertainty, and the horizontal error bar indicating uncertainties arising from model dependence. Reproduced from [Ab12].

charge density [Ho12]. Figure 8.8.1 presents the weak charge density distribution extracted from the measurements of PREX, along with the electromagnetic charge density (ρ_{ch}) and a sample mean-field result based on FSUGold interaction [Ho12].

The point neutron radius, R_n, was extracted by using the weak charge radius, R_W to be [Ho12]

$$R_n = 5.751 \pm 0.175(\text{exp}) \pm 0.026(\text{mod}) \pm 0.005(\text{str}) \text{ fm} \tag{8.8.3}$$

As before, the exp uncertainty is the total statistical and systematic experimental uncertainty and the mod uncertainty arises from the model dependence of R_n extraction. The str uncertainty is due to possible strange quark contributions [Ho12]. Figure 8.8.2 presents the A_{PV} plotted against R_n for various theoretical models, along

with the results of PREX [Ab12].

Using the proton point radius, R_p, of 5.449 fm, the neutron skin thickness is evaluated to be [Ho12]

$$R_n - R_p = 0.302 \pm 0.175(\text{exp}) \pm 0.026(\text{mod}) \pm 0.005(\text{str}) \text{ fm.}$$

This result implies that the neutron distribution is 1.8σ larger than that of the protons. The extraction of R_n from A_{PV} measured during PREX is described in [Ho12].

9

Conclusion

This chapter presents a brief summary of the existing measurements of form-factors (FFs), and presents the results of HAPPEX-III in the context of these other experiments. A brief summary is also given of the determination of neutron radius by PREX, and the outlook for future high precision parity-violating experiments is presented.

9.1 Existing Measurements of A_{PV}

The parity-violating asymmetry, A_{PV}, in the scattering of electrons from hydrogen (^{1}H), deuterium (^{2}H) and helium are sensitive to the strange form-factors (FFs), G_E^s and G_M^s: forward-angle electron-hydrogen (e-^{1}H) scattering measurements are sensitive to a linear combination of G_E^s and G_M^s, backward-angle e-^{1}H scattering measurements are sensitive to G_M^s, forward-angle electron-helium (e-^{4}He) scattering measurements are sensitive to G_E^s, and backward-angle electron-deuterium (e-^{2}H) scattering is sensitive to a linear combination of G_M^s and $G_A^{e(T=1)}$. $G_A^{e(T=1)}$ is the isovector component of the axial-vector FF and is described in Section 7.9. Several

experiments have been performed over the past 15 years or so to determine these FFs by measuring A_{PV}. This section provides a brief summary of these experiments, and the associated A_{PV}. The measurements of HAPPEX-III are not discussed in this section.

9.1.1   HAPPEX-I

HAPPEX-I [An04] was performed in experimental Hall A of JLab in 1998/1999. The experimental setup of HAPPEX-I was similar to that of HAPPEX-III that is illustrated in Figure 3.1.1 in Section 3.1. In HAPPEX-I, 3.356 GeV longitudinally polarized electrons were scattered from a 15 cm cryogenic liquid hydrogen (^{1}H) target that was located at the center of Hall A. The electrons scattered elastically at an average Q^2 of 0.477 GeV^2 were focused by the twin high-resolution spectrometers (HRSs) onto detectors comprised of lead-lucite sandwiches. The HRSs were set at $\langle \theta_{lab} \rangle = \pm 12.3°$. The same lead-lucite sandwich detectors were used during HAPPEX-III as well. These detectors are described in Section 3.9.1. The helicity of the beam was set every 33.3 ms, and locked to the 60 Hz power-line frequency. The responses of the beam monitors and detectors were integrated for 32.0 ms, about 1 ms into each helicity-window. These responses were digitized by custom 16-bit analog-to-digital converters (ADCs) [An04]. During the 1998 run, an electron beam with an average current of $I = 100$ μA and polarization of $P_b = 38\%$ was used. During the 1999 run, an electron beam with an average current of $I = 35$ μA and polarization of $P_b = 70\%$ was used, effectively providing greater effective rate of data taking, which is proportional to $P_b^2 I$.

The measurements of HAPPEX-I (at $Q^2 = 0.477$ GeV^2) yielded an A_{PV} of [An04]

$$A_{PV} = -15.05 \pm 0.98(\text{stat}) \pm 0.56(\text{syst}) \text{ ppm.} \tag{9.1.1}$$

The uncertainties above are statistical (stat) and systematic (syst). The systematic uncertainty includes uncertainties arising from beam polarization, background, helicity-correlated (HC) beam systematics and Q^2. The corrections in the measured asymmetry were dominated by the backgrounds, and the uncertainties dominated by the uncertainties in beam polarization measurement. The backgrounds were dominated by the electrons that scattered from the Aluminum (Al) windows of the target, followed by the inelastic electrons [An04].

9.1.2 HAPPEX-II

HAPPEX-II [AnH06, AnHe06, Ac07] was also performed in experimental Hall A of JLab, and used a setup similar to that of HAPPEX-I and HAPPEX-III. HAPPEX-II ran in 2004/2005. During HAPPEX-II, the electrons were elastically scattered from 20 cm cryogenic hydrogen (^{1}H) target [AnH06, Ac07], and from 20 cm cryogenic high-pressure helium (^{4}He) gas target [AnHe06, Ac07]. The electrons were detected by total absorption calorimeters made of layers of brass and quartz [AnH06, AnHe06, Ac07]. These detectors were located at the HRS focal plane, much like during other HAPPEXexperiments. The beam helicity was set every 33.3 ms, and the responses of the beam monitors and detectors were integrated during each helicity window.

The 2004 runs used 3.03 GeV electron beam at an average current of 35 μA and polarization of $75 - 85\%$. The HRSs selected elastically scattered electrons at $\langle \theta_{lab} \rangle = \pm 5.7°$ during the 2004 ^{4}He run, corresponding to $Q^2 = 0.091$ GeV^2, and $\langle \theta_{lab} \rangle = \pm 6.0°$ during the 2004 ^{1}H run, corresponding to $Q^2 = 0.099$ GeV^2.

During the 2005 runs, the HRSs selected elastically scattered electrons at an average angle of $\langle \theta_{lab} \rangle \sim \pm 6.0°$. Beam currents in the range of $\sim 35 - 55$ μA were used during these runs. The 2005 ^{1}H run used a 3.18 GeV electron beam with an average polarization of $87.1 \pm 0.9\%$. The Q^2 of this run was 0.109 GeV^2. The 2005

	Q^2 (GeV^2)	A_{PV} (ppm)
2004 ^{4}He	0.091	$+6.72 \pm 0.84 \pm 0.21$
2005 ^{4}He	0.077	$+6.40 \pm 0.23 \pm 0.12$
2004 ^{1}H	0.099	$-1.14 \pm 0.24 \pm 0.06$
2005 ^{1}H	0.109	$-1.58 \pm 0.12 \pm 0.04$

Table 9.1: The A_{PV} extracted from the asymmetries measured in the elastic scattering of electrons from liquid hydrogen (^{1}H) and helium (^{4}He) targets by the HAPPEX-II collaboration during 2004-2005 are presented above. The uncertainties in A_{PV} are experimental statistical, and systematic respectively. The 2004 HAPPEX-II ^{1}H results are taken from [AnH06], 2004 ^{4}He from [AnHe06], and 2005 ^{1}H and ^{4}He from [Ac07].

^{4}He run used a 2.75 GeV electron beam with an average polarization of 84.4 ± 0.8. The Q^2 of this run was 0.077 GeV^2.

For the ^{1}H and ^{4}He runs of both 2004 and 2005, the dominant corrections resulted from helicity-correlated (HC) beam parameters, followed by quasi-elastic electrons scattered from the Al target windows. The dominant uncertainty in the measured asymmetries resulted from HC parameters and non-linearity in the detector and beam monitors. The uncertainty in the measured asymmetry from Al background was also big for ^{1}H runs.

9.1.3 SAMPLE

The SAMPLE experiment was performed at MIT-Bates [Be05, Sp04, It04] in 1998, 1999 and 2000/2001. During SAMPLE, longitudinally polarized electrons were scattered from 40 cm liquid hydrogen (^{1}H) and deuterium (^{2}H) targets, and the elastically scattered electrons were detected at backward-angles. Air Čerenkov detectors, with a large acceptance of ~ 1.5 steradians, detected electrons scattered in the range of 138° to 160° [Be05]. The schematic of the SAMPLE detector setup is shown in Figure 9.1.1. An array of ten large ellipsoidal mirrors focused the Čerenkov cones onto
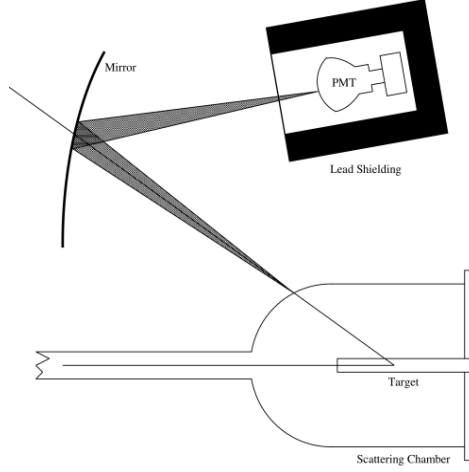
Figure 9.1.1: SAMPLE collected the Čherenkov photons from back-scattered electrons into the photomultiplier tubes (PMTs) by using large ellipsoidal mirrors that focused the Čherenkov cones onto the PMTs. Electrons scattered in the range of 138° to 160° were collected by the PMTs. Ten such mirror-PMTs were used to collect back-scattered electrons for azimuthal coverage about the central beamline [Be05]. Reproduced from [Li06].

ten photomultiplier tubes (PMTs), each encased in a Lead (Pb) cylinder. The electron beam was pulsed at 600 Hz, and the responses of detector PMTs and beam monitors were integrated and digitized every 25 μs [Sp04]. The backward-angle ^{1}H measurements are sensitive to the strange magnetic FF G_M^s. The backward-angle ^{2}H measurements are sensitive to the isovector component of the axial-vector FF $G_A^{e(T=1)}$, which is defined by Eq. 7.9.7.

The first SAMPLE measurement (SAMPLE-I) [Sp04, Be05] was performed with a ^{1}H target at a beam energy of 200 MeV and Q^2 of ~ 0.1 GeV^2. The second SAMPLE measurement (SAMPLE-II) [Be05] was performed with a ^{2}H target at a beam energy of 200 MeV and Q^2 of 0.091 GeV^2. The third SAMPLE measurement (SAMPLE-III) [It04, Be05] was performed at a beam energy of 125 MeV and Q^2 of 0.038 GeV^2. The A_{PV} extracted from these measurements are summarized in Table 9.2.

	$Q^2(\,\mathrm{GeV}^2)$	A_{PV} (ppm)
^{1}H	0.1	$-5.61 \pm 0.67 \pm 0.88$
D(^{2}H)	0.091	$-7.77 \pm 0.73 \pm 0.72$
D(^{2}H)	0.038	$-3.51 \pm 0.57 \pm 0.58$

Table 9.2: The A_{PV} extracted from the results of the measurements made by SAMPLE with hydrogen (^{1}H) and deuterium (^{2}H) targets at Q^2 of $\sim$ 0.1 GeV^2 and 0.038 GeV^2 [Be05] are presented above. In A_{PV}, the first uncertainty is experimental statistical and the second is systematic.

9.1.4 PVA4

The PVA4 experiment performed forward-angle and backward-angle measurements of the parity-violating asymmetry, A_{PV}, in electron-proton (e-^{1}H) scattering at the Mainzer Mikrotron accelerator facility (MAMI) [Ma04, Ma05, Ba09].

The first PVA4 experiment (PVA4-I) [Ma04] scattered a 20 μA electron beam with an average longitudinal polarization of 80% and energy of 854.3 MeV from a 10 cm liquid hydrogen (^{1}H) target. The elastically scattered electrons in the range of $30° \leq \theta_e \leq 40°$, corresponding to an average $Q^2 = 0.23$ GeV^2, were detected by a total absorption calorimeter composed of 1022 layers of lead fluoride (PbF$_2$) crystals, of which only 511 channels were operational during the experiment. No magnetic spectrometer was used, unlike in other experiments. The detector is shown in Figure 9.1.2. The signals from each PbF$_2$ crystal were integrated and digitized by an 8-bit analog-to-digital converter (ADC) every 20 ns. A typical histogram of the PbF$_2$ response is presented in Figure 9.1.3. The elastic events were selected by imposing the cuts around the elastic peak as show in Figure 9.1.3. The total number of elastically scattered electrons for each helicity state was determined by summing over the inner 345 detector channels. Individual helicity states were held constant for 20.08 ms, during which data was acquired for 20.00 ms. Eight auxiliary water-Čherenkov detectors, that were placed symmetrically around the beamline and
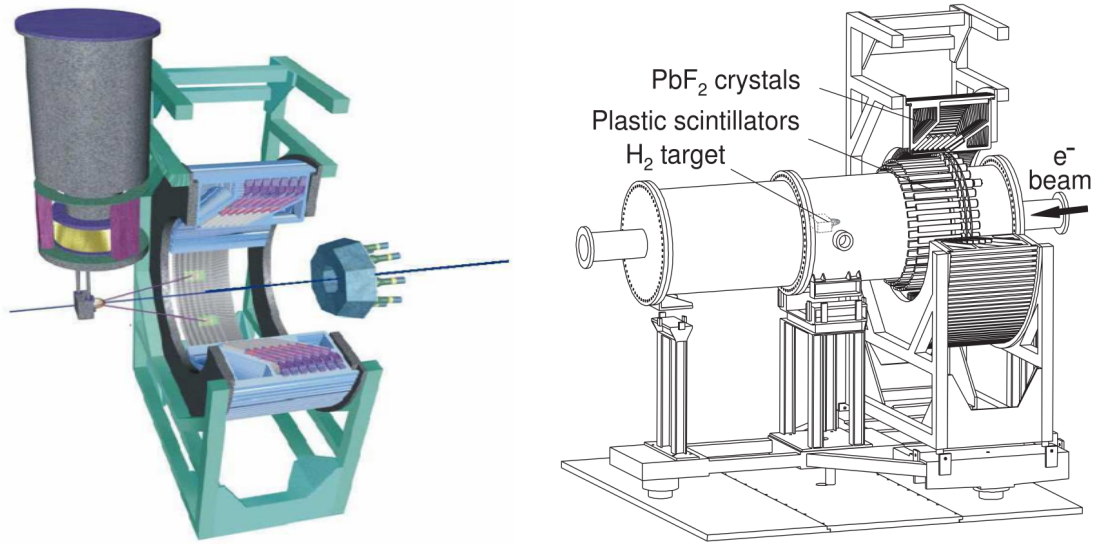
Figure 9.1.2: The PVA4 detectors consisted of an array of 1022 PbF_2 crystals, that provided complete azimuthal acceptance, and accepted electrons scattered at $30° \leq \theta_{lab} \leq 40°$ or $140° \leq \theta_{lab} \leq 150°$. These are shown on both the pictures, as mounted on the metal bars. Eight auxiliary water-Čherenkov detectors placed symmetrically around the beamline downstream of the PbF_2 calorimeters monitored the beam luminosity at scattering angles in the range of $4° \leq \theta_e \leq 10°$. This is shown on the left picture as the octagonal feature towards the right. For the backward-angle measurements an array of 72 plastic scintillators in front of the PbF_2 calorimeters were added, as shown on the right above. In the left picture, beam propagation direction towards the right, and in the right picture, beam propagation direction is towards the left. Left picture reproduced from [Li06]. Right picture reproduced from [Ba09].

downstream of the PbF_2 calorimeters, monitored the beam luminosity at scattering angles in the range of $4° \leq \theta_e \leq 10°$.

The second PVA4 experiment (PVA4-II) [Ma05] performed a similar forward-angle measurement of A_{PV} in elastic e-^{1}H scattering, but with an electron beam of 570.4 MeV, corresponding to an average $Q^2 = 0.108$ GeV^2. During A4-II, all of the 1022 PbF_2 channels were operational.

The third PVA4 experiment (PVA4-III) [Ba09] measured the elastic e-^{1}H backward-angle measurements. PVA4-III used a beam energy of 315.1 MeV and accepted elec-
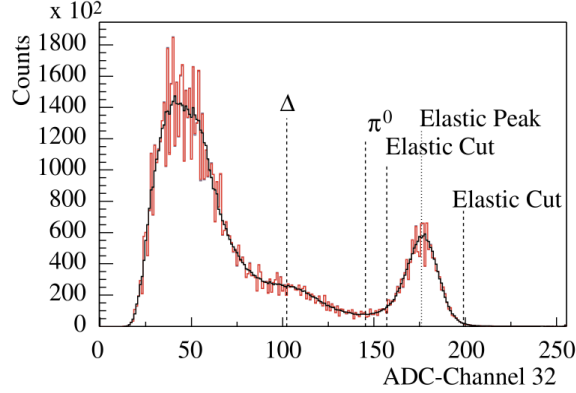
Figure 9.1.3: A typical spectrum of the response of a PbF$_2$ crystal, digitized and integrated by an 8-bit analog-to-digital (ADC) every 20 ns is presented above. The red histogram is the raw energy spectrum and the black histogram is the same spectrum corrected for measured variations in the ADC channel width. The elastic peak, and associated cuts, as well as the peak corresponding to the energy losses in the inelastic electrons due to Δ excitation, and the threshold for π^0 production are marked. Reproduced from [Ma04].

trons scattered in the range of $130° \leq \theta_e \leq 140°$, corresponding to $Q^2 = 0.230$ GeV^2.

The average beam polarization was 70%, and the electrons were scattered from a 23.4 cm ^{1}H target. In addition to the array of 1022 PbF$_2$ calorimeters, an array of 72 plastic scintillators in front of the PbF$_2$ calorimeters were added. These scintillators were used in coincidence with the PbF$_2$ calorimeter responses to separate charged particles from neutral particles.

Q^2 (GeV^2)	A_{PV} (ppm)
0.230	$-5.44 \pm 0.54 \pm 0.26$
0.108	$-1.36 \pm 0.29 \pm 0.13$
0.230	$-17.23 \pm 0.82 \pm 0.89$

Table 9.3: The A_{PV} extracted from the results of forward- [Ma04, Ma05] and backward-angle [Ba09] measurements of elastic electrons in electron-proton (e-^{1}H) scattering by the PVA4 collaboration. The uncertainties above are experimental statistical and systematic.

The A_{PV} extracted from all PVA4 measurements are summarized in Table 9.3.
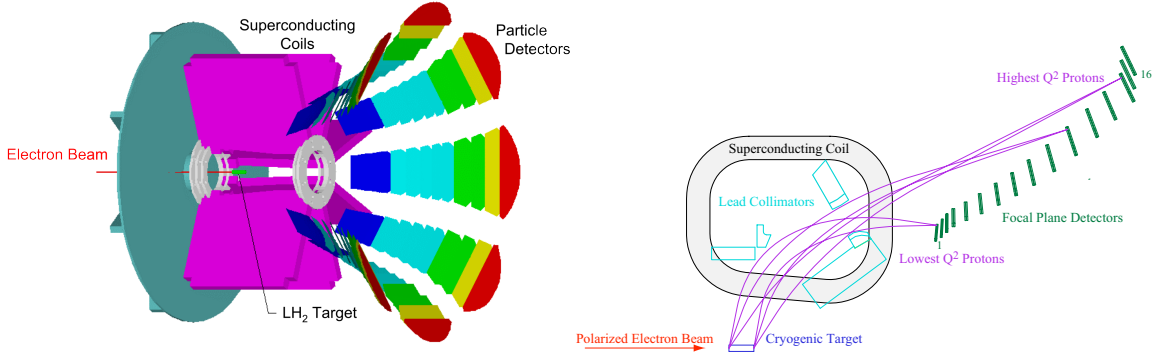
Figure 9.1.4: G0 detectors. Right plot reproduced from [Pa11].

9.1.5 G0 Forward

The G0 forward-angle experiment [Ar05] measured forward-angle electron-proton (e-^{1}H) scattering. These measurements were performed in the experimental Hall C of JLab in 2003 and 2004. G0 scattered longitudinally polarized electrons from unpolarized protons in a 20 cm long liquid hydrogen (^{1}H) target, and detected the protons using eight azimuthally symmetric arrays of plastic scintillator detectors, with 16 different focal plane detectors (FPD) in each array. The acceptance was about 0.9 steradians centered about the recoil angle of 70°, corresponding to a Q^2 in the range of $0.12 \leq Q^2 \leq 1.0$ GeV^2 at the G0 beam energy of 3 GeV. An average beam current of 40 μA with an average polarization of 74% was used.

The G0 experiment recorded the responses of the FPD using a counting method. Therefore, A_{meas} was formed by using time-of-flight (TOF) spectra for each of the FPD. The TOF was recorded using custom "time-encoding" electronics [Ar05], which were used to distinguish the elastic protons from inelastically scattered protons and fast pions (π^+) that were also incident on the FPDs. A typical TOF distribution is shown is Figure 9.1.5. Each detector was sensitive to a different range of Q^2, with the exception of FPD 16 which was outside the kinematic limit, and was used for monitoring backgrounds. The FPD 15 was sensitive to Q^2 in the range of $0.44 \leq$
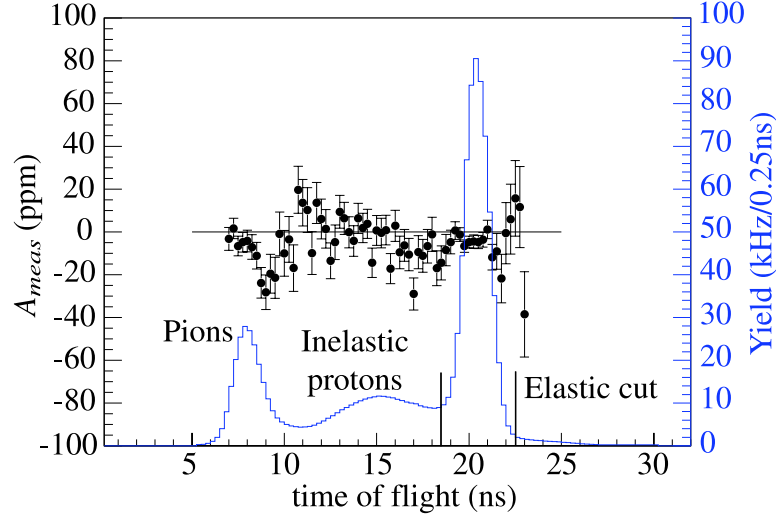
Figure 9.1.5: The time-of-flight (TOF) distribution (histogram) of the response of focal plane detector (FFD) 8, typical of the FPD spectra obtained during G0 forward-angle experiment is presented above. The associated raw asymmetries (circular dots) as a function of TOF is also presented. The error bars in the asymmetries are statistical. Reproduced from [Ar05].

$Q^2 \leq 0.88$ GeV^2. Therefore, it was divided into three TOF bins with average Q^2 of 0.51, 0.63, 0.79 GeV^2. Similarly, the FPD 14 was divided into two TOF bins with average Q^2 of 0.41 and 1.0 GeV^2.

$$A_{meas} = (1 - f_b)A_{raw} + f_b A_b \tag{9.1.2}$$

The measured asymmetry, A_{meas}, had two components as given in Eq. 9.1.2, where A_{raw} is the elastic asymmetry, and f_b and A_b are background fraction and its associated asymmetry. The dominant background in A_{meas} was due to protons that scattered inelastically from the protons and aluminum (Al) target windows, and protons that scattered quasi-elastically from the Al target windows [Ar05]. The FPD responses due to these protons are seen on both sides of the elastic proton peak at TOF$\sim$ 20 ns in Figure 9.1.5. The corrections arising from backgrounds were as much as 20-110% of A_{raw} for higher number FPDs because of additional backgrounds from a
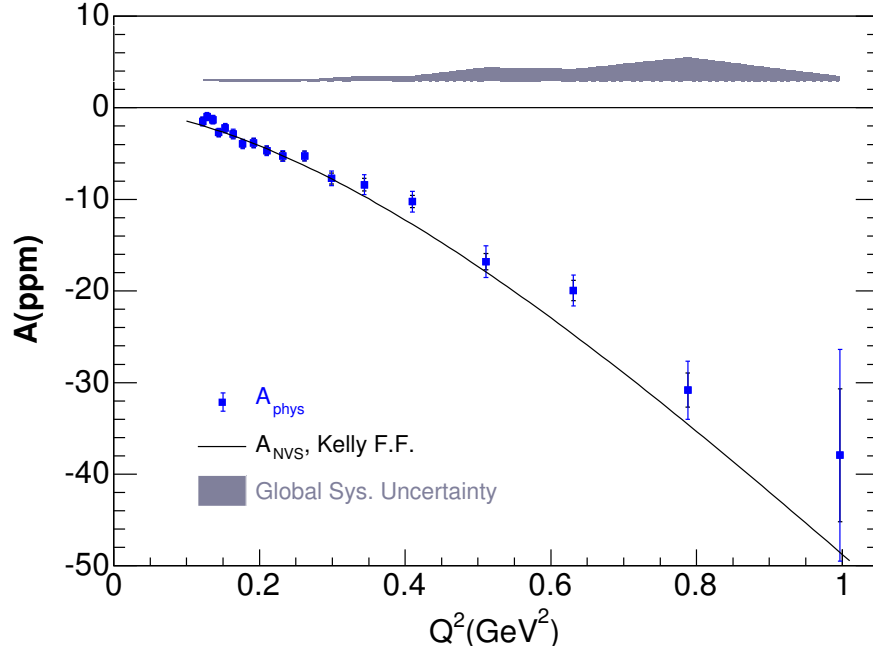
Figure 9.1.6: The A_{PV} (A_{phys}) extracted from G0 forward-angle measurements in the elastic electron-proton scattering [Ar05] is presented as a function of Q^2 above. Data points are shown with statistical and point-to-point systematic error bars combined, while the shaded band represents the magnitude of systematic errors which are highly correlated between the data points. The curve A_{NS} is calculated by using Kelly FFs parameterization for the electromagnetic FFs [Ke04], and represents the expected value of A_{PV} in the absence of strange contributions to the vector form factors. Reproduced from [Li06].

small fraction of protons arising from the weak decay of Λ and Σ that scattered inside the spectrometer magnets. The net corrections, along with the measured and corrected asymmetries are summarized in Table 9.4 [Li06]. The corrected asymmetries are plotted as a function of Q^2 in Figure 9.1.6.

9.1.6   G0 Backward

The G0 backward-angle experiment [An10] measured backward-angle electron-proton (e-^{1}H) and electron-deuteron (e-^{2}H) scattering. These measurements were performed in experimental Hall C of JLab in 2006 and 2007, utilizing most of the same equipment

Q^2	A_{PV}	σ_{stat}	σ_{sys}^{pt-pt}	σ_{sys}^{glob}
(GeV^2)	ppm	ppm	ppm	ppm
0.122	-1.51	0.44	0.22	0.18
0.128	-0.97	0.41	0.20	0.17
0.136	-1.30	0.42	0.17	0.17
0.144	-2.71	0.43	0.18	0.18
0.153	-2.22	0.43	0.28	0.21
0.164	-2.88	0.43	0.32	0.23
0.177	-3.95	0.43	0.25	0.20
0.192	-3.85	0.48	0.22	0.19
0.210	-4.68	0.47	0.26	0.21
0.232	-5.27	0.51	0.30	0.23
0.262	-5.26	0.52	0.11	0.17
0.299	-7.72	0.60	0.53	0.35
0.344	-8.40	0.68	0.85	0.52
0.410	-10.25	0.67	0.89	0.55
0.511	-16.81	0.89	1.48	1.50
0.631	-19.96	1.11	1.28	1.31
0.788	-30.83	1.86	2.56	2.59
0.997	-37.93	7.24	9.00	0.52

Table 9.4: G0 forward-angle asymmetries by the Q^2 bins [Li06]. The columns in the table are: the average four-momentum transfer squared Q^2, the parity-violating asymmetry A_{PV} and its statistical, point-to-point, and global systematic uncertainties σ_{stat}, σ_{sys}^{pt-pt}, and σ_{sys}^{glob}. The quantity σ_{sys}^{pt-pt} is associated with individual Q^2-bin data, without any correlation to rest of the data. The quantity σ_{sys}^{glob} is "common" to all the Q^2-bin data.

used during G0 forward-angle measurements. Electrons scattered at an average angle of about 110° from 20 cm liquid hydrogen (^{1}H) and deuterium (^{2}H) targets were detected by the detectors. The G0 toroidal spectrometer was turned 180° around with respect to the beam direction of G0 forward-angle setup for these measurements, and an additional array of scintillators, labeled as CED in Figure 9.1.7, near the exit of the magnet augmented each of the eight FPDs array. Coincidences between these
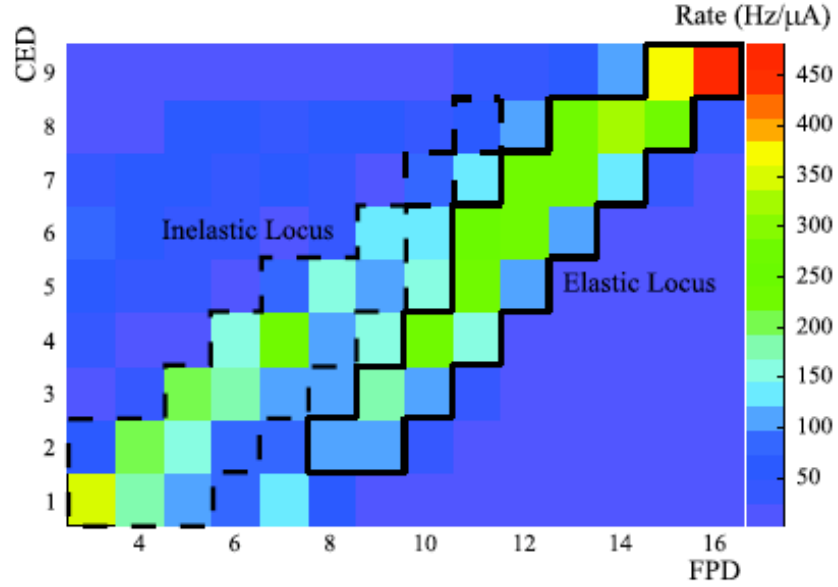
Figure 9.1.7: The distribution of measured yields from the backward-angle measurements of G0, as a function of FPD and CED, for hydrogen data taken at a beam energy of 687 MeV are presented above (FPDs 1 and 2 are not used). Electrons from elastic (inelastic) scattering are in the upper right (lower left). Reproduced from [An10].

two scintillator arrays allowed electrons from elastic and inelastic scattering to be distinguished, as shown in Figure 9.1.7. An aerogel Čherenkov detector with pion threshold of 570 MeV was used in coincidence with the scintillators in each octant to distinguish the pions from the electrons. An average beam current of 60 μA, with beam polarization of $85.8 \pm 2.1(1.4)\%$ and energy of 359(684) MeV was used.

The G0 backward-angle measured asymmetries can be expressed as indicated in Eq. 9.1.2, and are summarized in Table 9.5. The dominant source of backgrounds was the aluminum target window. However, corrections to A_{raw} arising from backgrounds were small because the background asymmetries had values close to those of the elastic asymmetry [An10]. Significant sources of corrections included those arising from deadtime, beam polarization, and electromagnetic radiative corrections. Other corrections such as those due to helicity-correlated beam parameters, transverse

Table 9.5: The A_{PV}s extracted from the measurements of the G0 backward-angle experiment are presented below. The uncertainties are statistical, point-to-point systematic and global systematic, respectively. The point-to-point systematic uncertainty is associated with the particular Q^2-bin data. The global systematic uncertainty is "common" to all Q^2-bin data. Reproduced from [An10].

Target	$Q^2(\,\mathrm{GeV}^2)$	$A_{PV}(\mathrm{ppm})$
^{1}H	0.221	$-11.25 \pm 0.86 \pm 0.27 \pm 0.43$
D(^{2}H)	0.221	$-16.93 \pm 0.81 \pm 0.41 \pm 0.21$
^{1}H	0.628	$-45.9 \pm 2.4 \pm 0.8 \pm 1.0$
D(^{2}H)	0.628	$-55.5 \pm 3.3 \pm 2.0 \pm 0.7$

component of beam polarization, and two-boson exchange were not as significant.

9.1.7 Summary of Existing Measurements of A_{PV}

The A_{PV} extracted from all the existing forward- [An04, AnH06, AnHe06, Ac07, Ma04, Ma05, Ar05] and backward-angle [Sp04, It04, Be05, Ba09, An10] measurements, excluding that of HAPPEX-III, are summarized in Table 9.6, and Table 9.7 respectively.

9.2 Form-Factors prior to HAPPEX-III

The results of strange FFs extraction from the A_{PV} presented in the previous section is presented in this section. The results of the HAPPEX-III are not presented in this section.

9.2.1 Strange FFs at $Q^2 \sim 0.1\,\mathrm{GeV}^2$

A global analysis of the A_{PV} determined at $Q^2 \sim 0.1$ GeV^2 is performed to extract the values of the strange FFs, G_E^s and G_M^s at this Q^2 [Li07]. The measurements of HAPPEX-II(2004/2005) ^{1}H, HAPPEX-II(2004/2005) ^{4}He, PVA4-II(2005),

Table 9.6: The summary of all existing forward-angle measurements of parity-violating asymmetries, A_{PV}, are presented below. The values of θ_{lab} for $Q^2 \leq$ 0.410 GeV^2 are adopted from [Li07]. The uncertainties are total experimental for HAPPEX and PVA4 numbers. For the G0 asymmetries, the uncertainties are correlated (quadrature sum of statistical and point-to-point) and uncorrelated (global) respectively. The measurements of HAPPEX-III are not included below.

Experiment	Target	Q^2 (GeV^2)	θ_{lab} (deg)	A_{PV} (ppm)	Ref.
HAPPEX-I(1999)	^{1}H	0.477	12.3	-15.05 ± 1.13	[An04]
HAPPEX-II(2004)	^{1}H	0.099	6.0	-1.14 ± 0.25	[AnH06]
HAPPEX-II(2005)	^{1}H	0.109	6.0	-1.58 ± 0.13	[Ac07]
HAPPEX-II(2004)	^{4}He	0.091	5.7	$+6.72 \pm 0.87$	[AnHe06]
HAPPEX-II(2005)	^{4}He	0.077	5.8	$+6.40 \pm 0.26$	[Ac07]
PVA4-I(2004)	^{1}H	0.23	35.45	-5.44 ± 0.60	[Ma04]
PVA4-II(2005)	^{1}H	0.108	35.52	-1.36 ± 0.32	[Ma05]
G0(2005)	^{1}H	0.122	6.68	$-1.51 \pm 0.49 \pm 0.18$	[Ar05]
G0(2005)	^{1}H	0.128	6.84	$-0.97 \pm 0.46 \pm 0.17$	[Ar05]
G0(2005)	^{1}H	0.136	7.06	$-1.30 \pm 0.45 \pm 0.17$	[Ar05]
G0(2005)	^{1}H	0.144	7.27	$-2.71 \pm 0.47 \pm 0.18$	[Ar05]
G0(2005)	^{1}H	0.153	7.50	$-2.22 \pm 0.51 \pm 0.21$	[Ar05]
G0(2005)	^{1}H	0.164	7.77	$-2.88 \pm 0.54 \pm 0.23$	[Ar05]
G0(2005)	^{1}H	0.177	8.09	$-3.95 \pm 0.50 \pm 0.20$	[Ar05]
G0(2005)	^{1}H	0.192	8.43	$-3.85 \pm 0.53 \pm 0.19$	[Ar05]
G0(2005)	^{1}H	0.210	8.84	$-4.68 \pm 0.54 \pm 0.21$	[Ar05]
G0(2005)	^{1}H	0.232	9.26	$-5.27 \pm 0.59 \pm 0.23$	[Ar05]
G0(2005)	^{1}H	0.262	9.92	$-5.26 \pm 0.53 \pm 0.17$	[Ar05]
G0(2005)	^{1}H	0.299	10.63	$-7.72 \pm 0.80 \pm 0.35$	[Ar05]
G0(2005)	^{1}H	0.344	11.46	$-8.40 \pm 1.09 \pm 0.52$	[Ar05]
G0(2005)	^{1}H	0.410	12.59	$-10.25 \pm 1.11 \pm 0.55$	[Ar05]
G0(2005)	^{1}H	0.511		$-16.81 \pm 1.73 \pm 1.50$	[Ar05]
G0(2005)	^{1}H	0.631		$-19.96 \pm 1.60 \pm 1.31$	[Ar05]
G0(2005)	^{1}H	0.788		$-30.83 \pm 3.16 \pm 2.59$	[Ar05]
G0(2005)	^{1}H	0.997		$-37.93 \pm 11.55 \pm 0.52$	[Ar05]

Table 9.7: The summary of all existing backward-angle measurements of A_{PV} are presented below. The quantity θ_{lab} for SAMPLE are reproduced from [Li07]. The uncertainties in SAMPLE and PVA4 asymmetries are experimental statistical and systematic. The uncertainties in G0 asymmetries are experimental statistical, point-to-point systematic, and global systematic.

Experiment	Target	Q^2 (GeV^2)	θ_{lab} (deg)	A_{PV} (ppm)	Ref.
SAMPLE-I(1998)	^{1}H	0.1	144.4	$-5.61 \pm 0.67 \pm 0.88$	[Be05, Sp04]
SAMPLE-II(1999)	^{2}H	0.091	140.8	$-7.77 \pm 0.73 \pm 0.72$	[Be05]
SAMPLE-III(2001)	^{2}H	0.038	–	$-3.51 \pm 0.57 \pm 0.58$	[It04, Be05]
PVA4-III(2009)	^{1}H	0.230	–	$-17.23 \pm 0.82 \pm 0.89$	[Ba09]
G0(2010)	^{1}H	0.221	–	$-11.25 \pm 0.86 \pm 0.27 \pm 0.43$	[An10]
G0(2010)	^{2}H	0.221	–	$-16.93 \pm 0.81 \pm 0.41 \pm 0.21$	[An10]
G0(2010)	^{1}H	0.628	–	$-45.9 \pm 2.4 \pm 0.8 \pm 1.0$	[An10]
G0(2010)	^{2}H	0.628	–	$-55.5 \pm 3.3 \pm 2.0 \pm 0.7$	[An10]

SAMPLE-I(1998), SAMPLE-II(1999) and three G0(2005) A_{PV} corresponding to $Q^2 \leq$ 0.136 GeV^2 are used during this analysis. These measurements are summarized in Tables 9.6 and 9.7. The analysis determines the FFs by minimizing χ^2 in the space of G_E^s vs G_M^s. This analysis yielded G_E^s and G_M^s of [Li07]

$$G_E^s = -0.006 \pm 0.016 \quad \& \quad G_M^s = +0.33 \pm 0.21, \tag{9.2.1}$$

with a correlation coefficient of -0.83. The correlation plot of this analysis is presented in Figure 9.2.1. In this figure, the G_E^s and G_M^s corresponding for the G0 data are shown as an average of the three G0 A_{PV}s. Each band represents a 1σ spread about the central value of the G_E^s and G_M^s combination., where the 1σ represents the overall uncertainty which is calculated by combining the total experimental and theoretical uncertainty in quadrature. The theoretical uncertainty is dominated by the uncertainties in electromagnetic FFs, and the radiative corrections to the isovector axial-vector FF $G_A^{e(T=1)}$ [Li07].
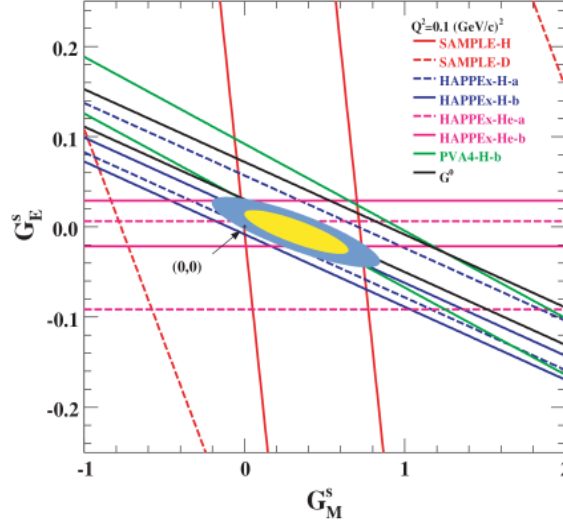
Figure 9.2.1: The strange form-factors (FFs) at $Q^2 \sim 0.1$ GeV^2 are extracted via a global analysis by using the APV measurements of HAPPEX-II(2004/2005) ^{1}H, HAPPEX-II(2004/2005) ^{4}He, PVA4-II(2005), SAMPLE-I(1998), SAMPLE-II(1999) and three G0(2005) A_{PV} corresponding to $Q^2 \leq 0.136$ GeV^2 [Li07]. Only the G_E^s and G_M^s corresponding to the average of the three G0 A_{PV} are plotted above. These measurements are listed in Tables 9.6 and 9.7. Each band represents a 1σ spread about the central value of the G_E^s and G_M^s combination. The 1σ represents the overall uncertainty which is calculated by combining the total experimental and theoretical uncertainty in quadrature. The theoretical uncertainty is dominated by the uncertainties in electromagnetic FFs, and the radiative corrections to the isovector axial-vector FF $G_A^{e(T=1)}$ [Li07]. The small (large) ellipse represents a 68% (95%) confidence level (C.L.) contour around the point of maximum likelihood at $G_E^s = -0.006, G_M^s = +0.33$. Reproduced from [Li07].

A similar analysis but with the range of Q^2 expanded to $Q^2 \leq 0.164$ GeV to include three more G0 A_{PV} yielded

$$G_E^s = -0.008 \pm 0.016 \quad \& \quad G_M^s = +0.29 \pm 0.21, \tag{9.2.2}$$

with a correlation coefficient of -0.85 [Li07]. The results of both these analysis suggest strange FFs of close to zero within the uncertainties.
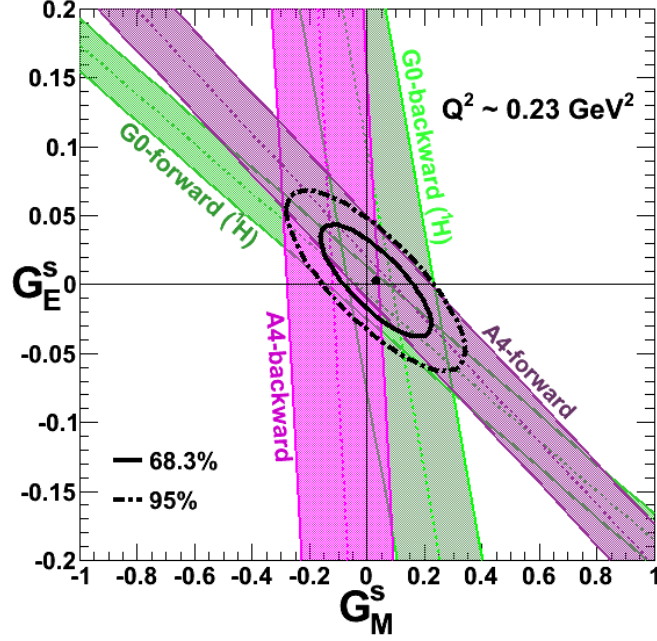
9.2.2 Strange FFs at $Q^2 \sim 0.23\,\mathrm{GeV}^2$

Figure 9.2.2: The strange FFs at $Q^2 \sim 0.2$ GeV^2 are extracted by χ^2 minimization in the space of G_E^s and G_M^s. The experimental constraints at 1σ are represented by the shaded bands indicating the combined statistical and experimental systematic error bars. The contours, representing the 68% and 95% uncertainty boundaries as indicated, also accounts for the (FFs) uncertainties in A_{NS}.

A similar χ^2 minimization analysis is performed with the data available at $Q^2 \sim 0.22$ GeV^2. This data set includes PVA4-I(2004), PVA4-III(2009), G0(2005) ^{1}H at $Q^2 = 0.232$ GeV^2 and G0(2010) ^{1}H at $Q^2 = 0.230$ GeV^2, which are listed in Tables 9.6 and 9.7. The corresponding plot spanned by G_E^s and G_M^s, is presented in Figure 9.2.2. The experimental constraints at 1σ are represented by the shaded bands indicating the combined statistical and experimental systematic error bars. The contours, representing the 68% and 95% uncertainty boundaries as indicated, also accounts for the (FFs) uncertainties in A_{NS}. The values of G_E^s and G_M^s extracted for the fit are

$$G_E^s = +0.003 \pm 0.027 \quad \& \quad G_M^s = +0.030 \pm 0.128 \qquad (9.2.3)$$

with a correlation coefficient of -0.78, suggesting strange FFs of zero within the uncertainties at $Q^2 \sim= 0.2 \; \mathrm{GeV}^2$.

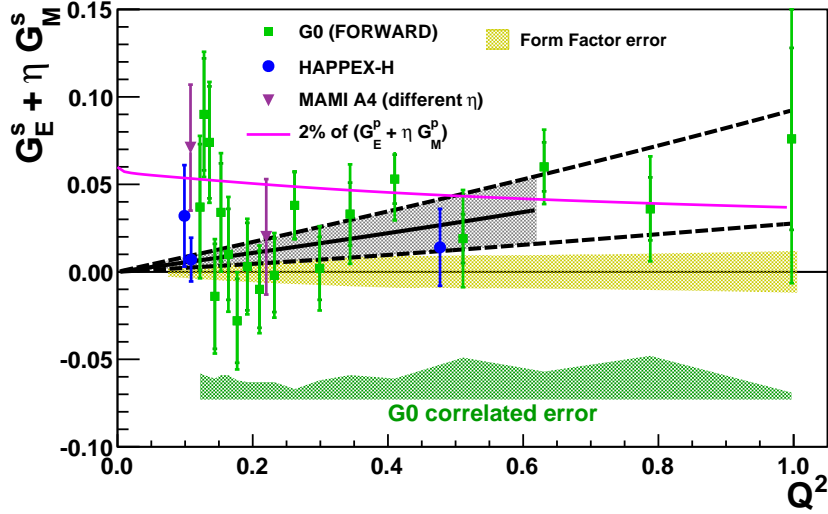### 9.2.3 Q^2 evolution of $G_E^s + \eta G_M^s$ prior to HAPPEX-III

Figure 9.2.3: The strange form-factors (FFs), G_E^s and G_M^s, extracted from the results of A_{PV} measurements from forward-angle electron-proton (e-^{1}H) scattering by HAPPEX-I/II [An04, AnH06, Ac07], G0 [Ar05], and PVA4-I/II [Ma04, Ma05] collaborations, backward-angle electron-proton (e-^{1}H) scattering by SAMPLE-I [Sp04, Be05], G0 [An10], and PVA4-III [Ba09] and the forward-angle electron-helium (e-[4]He) scattering by HAPPEX-II [AnHe06, Ac07] collaborations are presented above. The forward-angle e-^{1}H scattering is sensitive to $G_E^s + \eta G_M^s$, where $\eta = \tau G_E^p / \epsilon G_M^p$, and η is approximately equal to Q^2 / GeV^2 over this plot. The backward-angle e-^{1}H is sensitive to G_M^s alone, and the forward-angle e-[4]He is sensitive to G_E^s alone. On each data point, the error bars indicate both the statistical error and the quadrature sum of statistical and uncorrelated systematic error. For the G0 data, some systematic uncertainties are correlated between points with a magnitude indicated by the shaded region at the bottom of the plot.

The net strangeness contribution, $G_E^s + \eta G_M^s$, extracted from the measurements of all forward-angle electron-proton (e-^{1}H) experiments, excluding that of HAPPEX-III, are presented in Figure 9.2.3 as a function of Q^2. These measurements include those of HAPPEX-I [An04], HAPPEX-II [AnH06, Ac07] [1]H, PVA4-I [Ma04], PVA4-

II [Ma05] and G0 [Ar05]. The backward-angle electron-proton (e-^{1}H) measurements of SAMPLE-I [Sp04, Be05], G0 [An10], and PVA4-III [Ba09] and the forward-angle electron-helium (e-^{4}He) measurements of HAPPEX-II [AnHe06, Ac07] are also included in the figure. These measurements are summarized in Tables 9.6 and 9.7. The backward-angle e-^{1}H is sensitive to G_M^s alone, and the forward-angle e-^{4}He is sensitive to G_E^s alone. The quantity $\eta = \tau G_E^p / \epsilon G_M^p$, and is approximately equal to Q^2 / GeV^2 over this plot. On each data point, the error bars indicate both the statistical error and the quadrature sum of statistical and uncorrelated systematic error. For the G0 data, some systematic uncertainties are correlated between points with a magnitude indicated by the shaded region at the bottom of the plot. A shaded region around the zero-net-strangeness line represents the uncertainties in A_{NS} at 1σ; this uncertainty is not included in the individual data points. The uncertainties in A_{NS} is dominated by the uncertainties in the electromagnetic FFs and the radiative corrections in the isovector axial-vector $G_A^{e(T=1)}$.

The strange FFs are fit with the assumption of $G_E^s \propto Q^2$, and constant G_M^s [Yo06, Li07]. The cross-hatched region displays 1σ region allowed by a leading-order of this fit. The FFs for $Q^2 < 0.5$ GeV^2 are mostly zero within the uncertainties. The highest precision measurements [An04, AnH06, Ac07] constrain these FFs to be very near zero. However, the data set at higher Q^2, $Q^2 > 0.5$ GeV^2, suggests a small but positive strange FFs combination, but does not establish a clear and statistically significant signal.

9.2.4 Q^2 evolution of G_E^s, G_M^s & $G_A^{e(T=1)}$ prior to HAPPEX-III

The strange and axial form-factors (FFs) extracted from the results of G0 forward- and backward-angle measurements at Q^2 of 0.221 GeV^2 and 0.628 GeV^2, along with those extracted from other relevant experiments are summarized in Figure 9.2.4. The
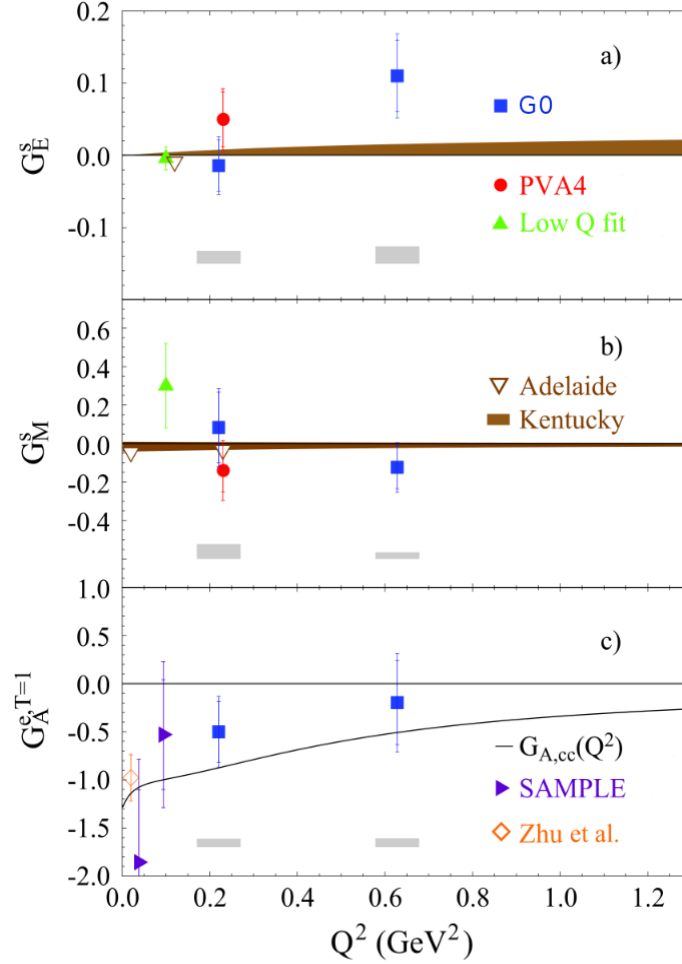
Figure 9.2.4: The G_E^s and G_M^s presented above correspond to the results of electron-proton (e-^{1}H) forward- and backward-angle measurements performed by PVA4 [Ma04, Ba09] at $Q^2 = 0.23$ GeV^2, G0 [Ar05, An10] at Q^2 of 0.221 GeV^2 and 0.628 GeV^2. Kelly's parametrization [Ke04] were used to parametrize the electromagnetic FFs. The PVA4 data point uses the theoretically determined value of $G_A^{e(T=1)}$ [Zh00], while the rest of the data points uses $G_A^{e(T=1)}$ determined by combining the ^{1}H and ^{2}H data. The results of global analysis performed by using all the available data (e-^{1}H,e-^{2}H,e-^{4}He) at $Q^2 = 0.1$ GeV^2 by [Li06] (Low Q fit), along with the calculation of the Adelaide [Le05] and Kentucky [Do09] groups are also included above. The quoted uncertainty of the Adelaide point is smaller than the marker in the plot. The $G_A^{e(T=1)}$ presented above corresponds to the results of electron-proton (e-^{1}H) and electron-deuterium (e-^{2}H) measurements performed by SAMPLE at Q^2 of 0.038 GeV^2 and 0.1 GeV^2 [It04, Be05] and G0 [Ar05, An10] at Q^2 of 0.221 GeV^2 and 0.628 GeV^2. The theoretical predictions of [Zh00] (Zhu et al.) is also presented. The inside error bars show statistical, and outside show statistical plus point-to-point systematic uncertainties (added in quadrature). The shaded bars below the G0 data points show global systematic uncertainties. Reproduced from [An10].

G_E^s and G_M^s results correspond to the results of electron-proton (e-^{1}H) forward- and backward-angle measurements performed by PVA4 [Ma04, Ba09] at Q$^2 = 0.23$ GeV^2, G0 [Ar05, An10] at Q^2 of 0.221 GeV^2 and 0.628 GeV^2. Kelly's parametrization [Ke04] were used to parametrize the electromagnetic FFs. The PVA4 data point uses the theoretically determined value of $G_A^{e(T=1)}$ [Zh00], while the rest of the data points use $G_A^{e(T=1)}$ determined by combining the ^{1}H and ^{2}H data. The results of global analysis performed by using all the available data (e-^{1}H,e-^{2}H,e-^{4}He) at Q$^2 = 0.1$ GeV^2 by [Li06], along with the calculation of the Adelaide [Le05] and Kentucky [Do09] groups are also included. The quoted uncertainty of the Adelaide point is smaller than the marker in the plot. The $G_A^{e(T=1)}$ results correspond to the results of electron-proton (e-^{1}H) and electron-deuterium (e-^{2}H) measurements performed by SAMPLE at Q^2 of 0.038 GeV^2 and 0.1 GeV^2 [It04, Be05] and G0 [Ar05, An10] at Q^2 of 0.221 GeV^2 and 0.628 GeV^2. The theoretical predictions of [Zh00] are also presented. The inside error bars show statistical, and outside show statistical plus point-to-point systematic uncertainties (added in quadrature). The shaded bars below the G0 data points show global systematic uncertainties. These plots of Figure 9.2.4 suggest small G_E^s, G_M^s and $G_A^{e(T=1)}$.

9.3 Form Factors with HAPPEX-III

9.3.1 Q^2 evolution of $G_E^s + \eta G_M^s$ with HAPPEX-III

The net strangeness contribution, $G_E^s + \eta G_M^s$, plot similar to the plot of Figure 9.2.3, but with the results of HAPPEX-III measurement included, is presented in Figure 9.3.1. In contrast Figure 9.2.3, the HAPPEX-III point constrains the cross-hatched fit into significant overlap with the band corresponding to the uncertainty in A_{NS}, and just over 1σ from zero. Thus, large contributions from strange vector
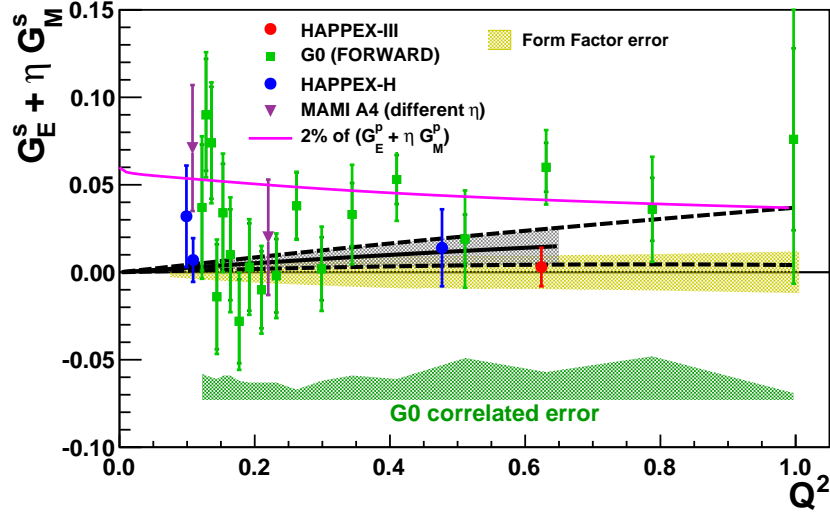
Figure 9.3.1: The strange FFs extracted from the data set plotted in Figure 9.2.3, and the measurements of HAPPEX-III are presented above. The solid curve represents a 2% contribution to the comparable linear combination of proton form factors.

FFs that fits the parameterization of the fit are ruled out. Recent lattice QCD results [Do09], however, suggest non-zero strange FFs, but the suggested values are smaller than the current FFs uncertainties.

9.3.2 Summary of All Data at $Q^2 \sim 0.62 \, \text{GeV}^2$

The constraints on the 2-D space spanned by the strange magnetic and electric FFs (G_E^s and G_M^s) at $Q^2 \sim 0.62 \, \text{GeV}^2$, without and with the HAPPEX-III measurements, are presented in Figure 9.3.2. The plot on the left in Figure 9.3.2 includes measurements from G0 forward-angle [Ar05] and G0 backward-angle [An10] only. The plot on the right includes the HAPPEX-III measurements in addition to the two G0 measurements presented in the left plot. The experimental constraints at 1σ are represented by the shaded bands indicating the combined statistical and experimental systematic error bars. The contours, representing the 68% and 95% uncertainty boundaries as indicated, also accounts for the (FFs) uncertainties in A_{NS}. The independently sepa-
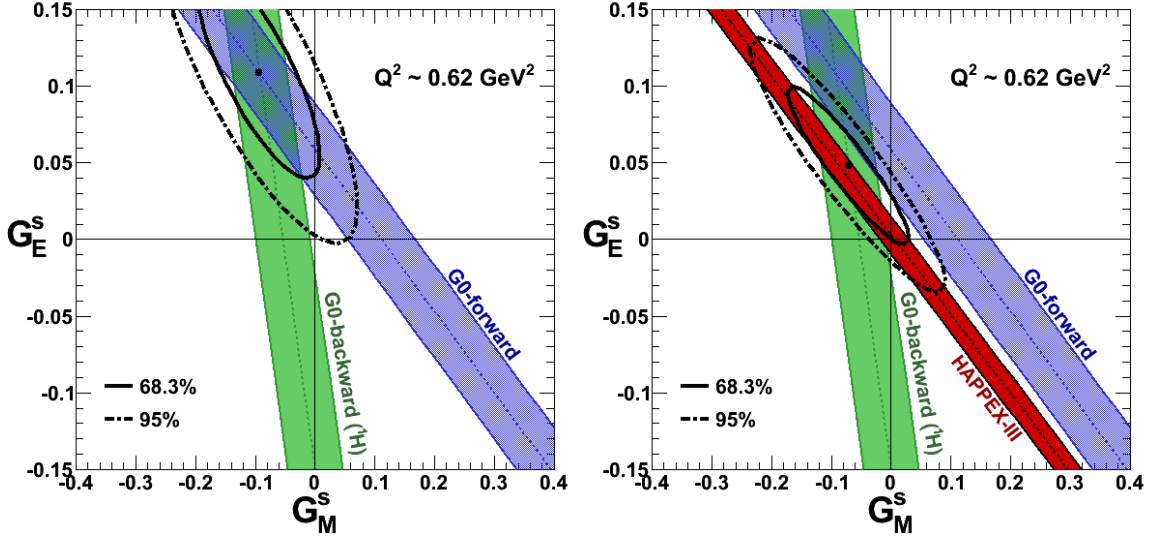
Figure 9.3.2: Constraints on G_E^s and G_M^s at $Q^2 \sim 0.62\,\text{GeV}^2$, without (left) and with (right) the HAPPEX-III measurements. Only G0 forward- [Ar05] and backward-angle [An10] measurements at $Q^2 = 0.6$ GeV^2 are presented in the left plot. The experimental constraints at 1σ are represented by the shaded bands which includes the combined experimental statistical and systematic uncertainties, as well as the uncertainties arising from the FFs.

rated values resulting from the fit of the data presented in these plots are summarized in Table 9.8. The combined constraint with the HAPPEX-III data point is consistent with $G_E^s = G_M^s = 0$.

9.3.3   All HAPPEX Programs

All the HAPPEX measurements are summarized in Figure 9.3.3. The error bars only include the experimental uncertainties, with the uncertainty in A_{NS} taken to be zero. These results of the forward-angle scattering measurements performed by the HAPPEX experiments give the most accurate determinations of the strange vector matrix elements at each Q^2. All these measurements show no indication of a signal for strange-quark contributions to the FFs, within uncertainties.

	Without HAPPEX-III	With HAPPEX-III
G_E^s	$+0.109 \pm 0.046$	$+0.048 \pm 0.034$
G_M^s	-0.095 ± 0.068	-0.071 ± 0.067
Corr. Coef.	-0.79	-0.92

Table 9.8: The strange form-factors, G_E^s and G_M^s, extracted from χ^2 minimization in the space of G_E^s and G_M^s [Li07], without the inclusion of HAPPEX-III measurement (second column) and with the inclusion of HAPPEX-III measurement (last column). These FFs are extracted using the measurements at $Q^2 \sim 0.6$ GeV^2 of G0 [Ar05, An10].
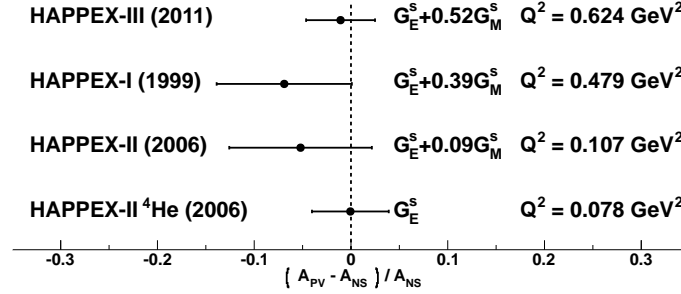

Figure 9.3.3: The measurements of A_{PV} performed by all the HAPPEX experiments are summarized above [An04, AnH06, AnHe06, Ac07, Ah12]. A_{PV} is the parity-violating asymmetry and A_{NS} is the expected parity-violating asymmetry when the strangeness contribution is zero. The error bars only include the experimental uncertainties, with the uncertainty in A_{NS} taken to be zero above. For each measurement, results are consistent with zero strangeness contribution.

9.3.4 Conclusions

The A_{PV} measurements of HAPPEX-III posses the highest precision and lowest systematic uncertainty at Q^2 of 0.6 GeV^2, and suggests no contributions within the uncertainties from the strange vector FFs to the nucleon electromagnetic FFs at this Q^2. Together with the rest of the world data, HAPPEX-III results constrain the contributions of strange FFs to the nucleon vector FFs at the level of a few percent. In the strange FFs determined from HAPPEX-III measurements, the uncertainties arising from the nucleon FFs are about the size of the experimental systematic uncertainty. Therefore, the precision measurements of HAPPEX-III are about the best one

can do for the time being. Any increase in the precision of such A_{PV} measurements must be accompanied by a further suppression of the uncertainties arising from the nucleon FFs.

9.4   Strangeness Content of Nucleon

The results of HAPPEX-III, together with other HAPPEX [An04, AnH06, AnHe06, Ac07] measurements, and the rest of the world data [Ma04, Ma05, An10, Sp04, It04, Be05, Ba09, Ar05], constrain the contributions from the strange vector FFs to the nucleon FFs at the level of a few percent in the region of Q^2 of up to ~ 1.0 GeV^2. The precision of some of these measurements have improved to a point where the non-experimental uncertainties are larger than the experimental systematic uncertainty, as is the case for HAPPEX-III. As the precision of the experimental measurements of A_{PV} have gotten better, the extraction of the strange FFs from these measurements have become increasingly limited by two major sources of uncertainties: 1) the uncertainties in the nucleon electromagnetic FFs, G_E^n and G_M^n, contribute an uncertainty of about half of the statistical error bar of the most precise A_{LR} measurement to date, and 2) the size of the uncertainties arising from the anapole corrections are also about half of the statistical error bar of the most precise A_{LR} measurement to date. In addition to these limitations, the assumption of charge symmetry in the nucleon, which is broken at the level of $\sim 1\%$ or less [Mi98], might also increase the uncertainty in the strange FFs determination at a level comparable to the statistical error of the most precise current measurements. Thus, without improvement in some of the limitations, measurements of G_E^s and G_M^s are about as accurate as can be presently justified.

9.5   Neutron Radius of ^{208}Pb (R_n)

PREX made the first measurement of the parity-violating asymmetry, A_{PV}, in the elastic scattering of polarized electrons from ^{208}Pb. This measurement yielded a difference between the neutron and proton distribution radii in the ^{208}Pb nucleus of $R_n - R_p = 0.33 \, ^{+0.16}_{-0.18}$ fm, providing the first electroweak evidence supporting the existence of a neutron skin in a neutron-rich nucleus. However, the first run of PREX did not achieve its statistical precision goal of $\sim 3\%$ due to equipment failure as a result of high radiation. A second run is planned for the near future, which will reduce the statistical precision by a factor of 3, and build on the considerable success of the first experiment.

9.6   Polarized Source and Future Outlook

Both HAPPEX-III and PREX benefited from the control and suppression of the helicity-correlated (HC) asymmetries in the beam, A_{LR}^{beam}. The systematic uncertainty due to A_{LR}^{beam} was bound to < 50 ppb during HAPPEX-III, and < 10 ppb during PREX. These numbers are well within the A_{LR}^{beam} systematic uncertainty goals of these experiments. The next generation of PV experiments such as MØLLER [Be08] and PVDIS [Ar07, Bo09], however, require even stricter control of A_{LR}^{beam}. The techniques used to suppress A_{LR}^{beam} have been continually improved through each generation of experiments, and study to achieve the A_{LR}^{beam} of next generation of PV experiments is well underway.

Appendix A

Total Charge

The total charge accumulated over the course of HAPPEX-III is summarized in Table A.1. The beam positions along the horizontal (x) varied over the course of the run, and thus, the charges are summarized by beam positions in x. Due to the dependence of the Q^2 on the beam positions along x, the charges collected at each of these beam positions weighted the corresponding Q^2.

Date	run #	BPM4ax	BPM4bx	LHRS (mC)	RHRS (mC)
Sep01-Sep04	11854-11199	-0.13	-2.23	2744.48	2899.67
Sep04-Sep24	12000-12639	-0.30	-0.80	37649.30	35558.76
Sep24-Oct20	12640-13445	-0.31	-1.30	56048.92	55438.16
Oct24-Oct25	13446-13596	-0.54	-1.32	0.00	2281.79
Total				96442.69	96178.38

Table A.1: The total charge accumulated over the course of HAPPEX-III by beam positions along the horizontal (x) are presented above. The beam positions were determined from the responses of the target beam position monitors (BPMs) BPM4ax and BPM4bx. The beam positions did not vary much between Sep24 and Oct25, but a site-wide power outage at Jefferson Lab on Oct20 resulted in the failure of the 25 cm LH2 target fan. Therefore, a 20 cm LH2 target was used from Oct20 onwards. The LHRS magnets never fully recovered from the power outage, and the data was acquired in only the RHRS detector after Oct20. The total cumulative charge of both runs is 192621.07 mC.

The beam position variations were monitored on the target beam position moni-
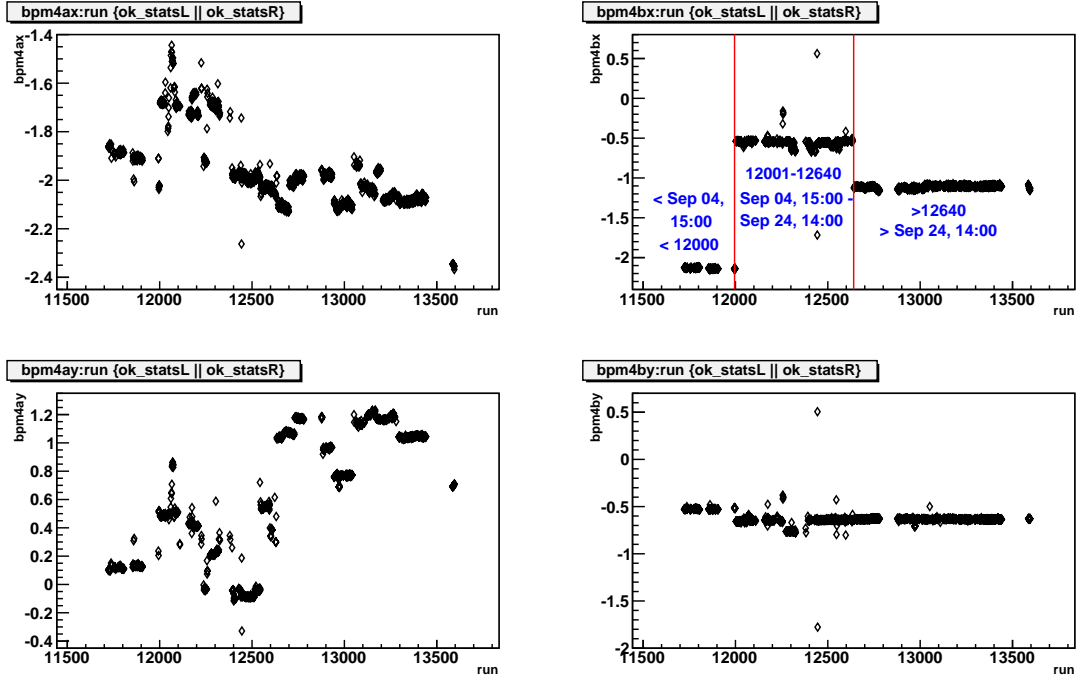
Figure A.0.1: The beam position variations over the course of HAPPEX-III are presented above. In each of the plots, the y-axis is the beam position in mm, and the x-axis is the run number.

tors (BPMs), 4a and 4b. The beam positions measured from the responses of these BPMs are summarized in Figure A.0.1.

A.1   Beam Monitor Pedestals

The pedestal is the response of the monitoring devices without any beam on them. The determination of the pedestals of the beam current monitors (BCMs) and beam position monitors (BPMs) during HAPPEX-III are discussed below.

A.1.1   Beam Current Monitor (BCM) Pedestals

The BCM pedestals were determined using the Unser [Un81]. The Unser was a parametric current transformer whose nominal response to beam current was determined
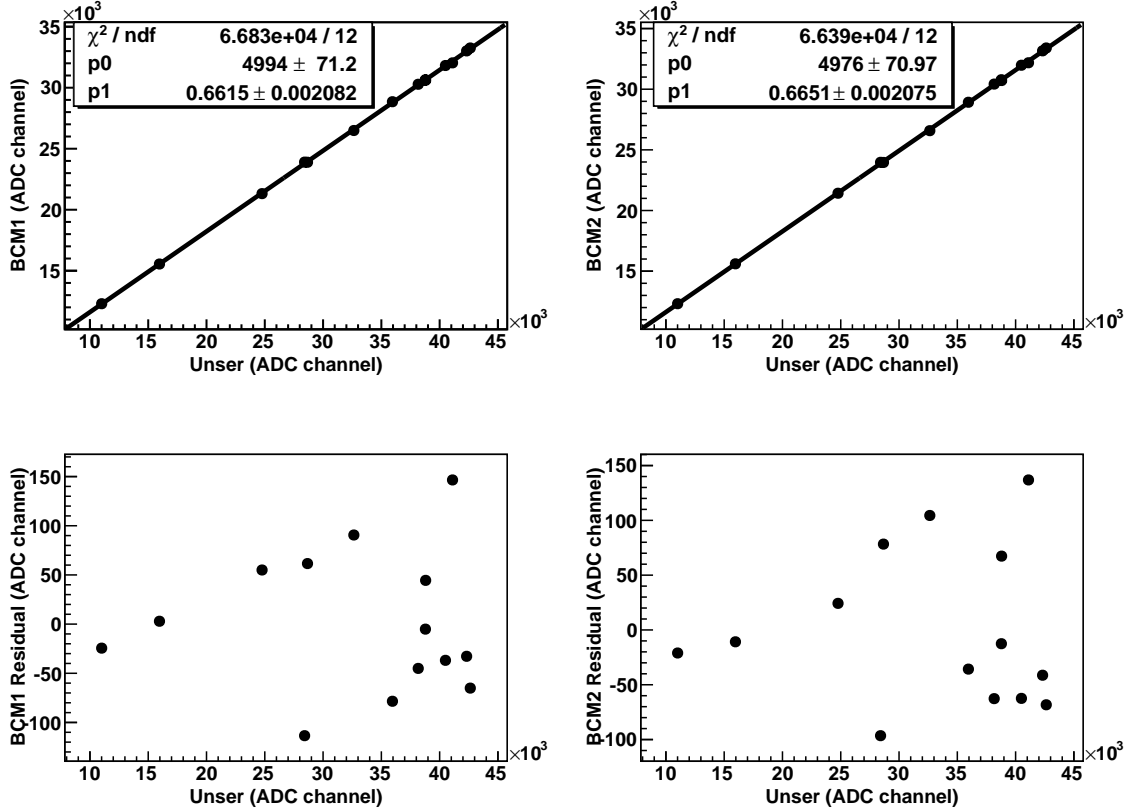
Figure A.1.1: The pedestal of the beam current monitors (BCMs) 1 and 2 were determined by plotting the responses of these BCMs against the response of the Unser for the pedestal calibration run. These are the top two plots above. The technique used to acquire the calibration data is discussed in the text. The intercepts of these plots are the BCM pedestals. The residuals corresponding to each of these calibration plots are shown in the bottom plots.

by its transformer. The Unser provided a linear response at short time scales, but its output drifted significantly on a time scale of several minutes [Al04]. Therefore its responses over short time scales were used to determine the BCM's pedestals.

The BCM's pedestals were determined in dedicated data runs acquired in the following manner: the beam current was stepped randomly between about 40 μA and 100 μA, with each current held constant for about 30 secs or so, a timescale short enough for the response of the Unser to be linear. The upper limit of 100 μA

run #	BCM1	BCM2
11695	4994.1	4976.38
12992	5055.11	-832.61
14175	5023.28	-148.50

Table A.2: The beam current monitor (BCM) pedestals determined from various calibration runs are summarized above. BCM1 was read out into a 16-bit analog-to-digital converter (ADC). BCM2 was read out into a 16-bit ADC for run # 11695 and into 18-bit ADC for the other runs. During HAPPEX-III data analysis, an average of these BCM1 pedestals was used as the BCM1 pedestal. The BCM2 pedestal of run # 11695 was used for runs < 11982, and an average of runs # 12992 and 14175 was used as the BCM2 pedestal for runs > 11982.

was the HAPPEX-III "production" current. Between successive steps, the beam current was set to 0 μA and held at this value for about the same duration (30 secs). The response of the Unser at 0 μA was used for the Unser's pedestal determination.

The integrated responses of the BCMs were plotted against the integrated responses of the Unser at each beam current. The Unser's responses were corrected for pedestals, with the Unser's pedestal at each beam current determined by averaging its responses at 0 μA immediately before and after the particular beam current. A straight line fit of this plot was performed, and the intercept was used as the beam monitor pedestal. The calibration plots of BCM1 and BCM2, typical of the calibrations, are shown in Figure A.1.1. These were the BCMs immediately upstream of the target. The BCM pedestals determined from various calibration runs performed over the course of HAPPEX-III are summarized in Table A.2.

A.1.2   Beam Position Monitor (BPM) Pedestals

The BPM pedestals could be determined by using a technique similar to the one used for BCM pedestal determination. In fact, the BCM calibration runs could have been used to extract the BPM pedestals as well, had the BPMs been set to the appropriate gain settings before the acquisition of these BCM calibration runs.
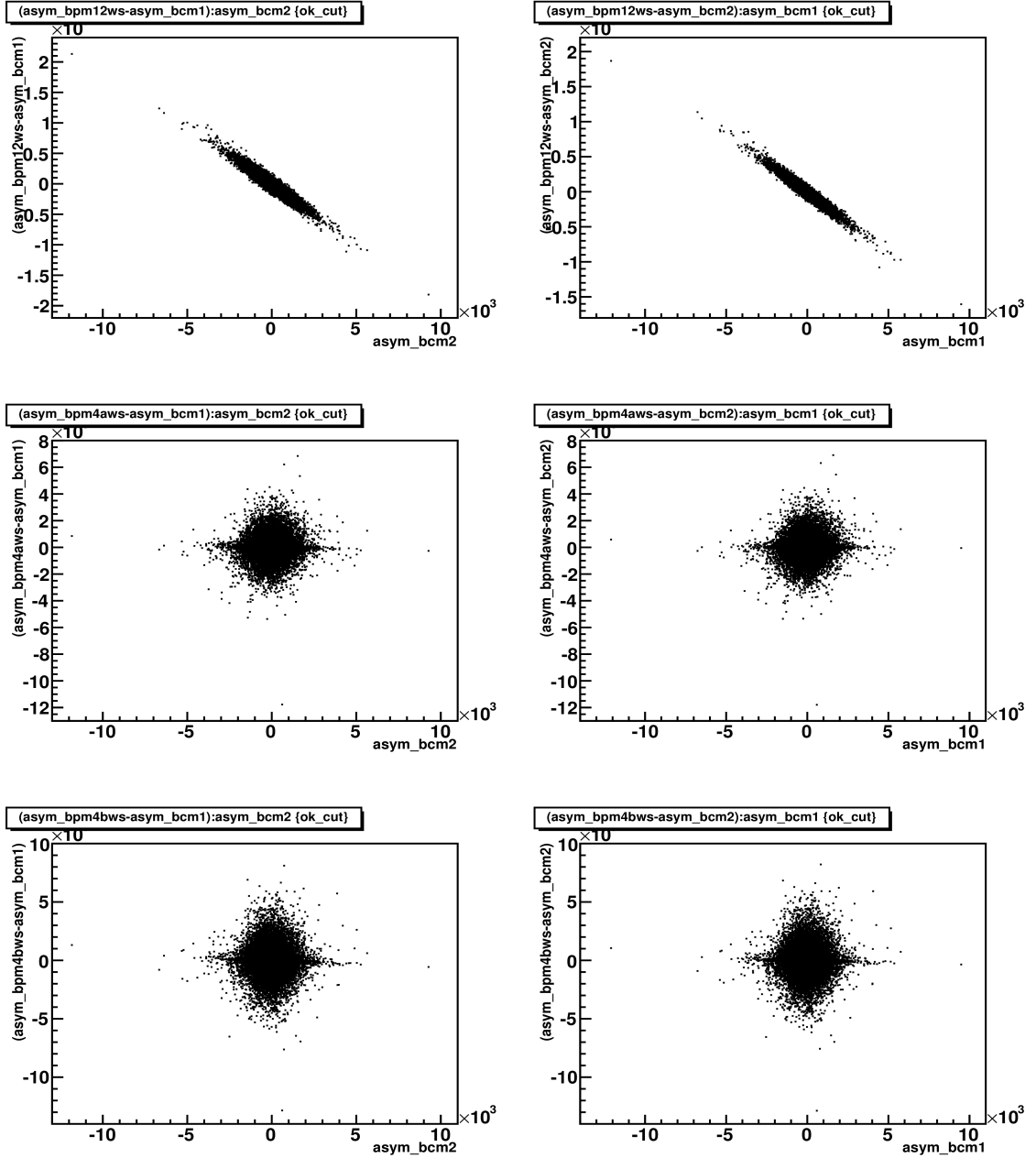
Figure A.1.2: The double-difference (DD) of the asymmetries determined from the responses of the BPMs and the BCMs plotted against the asymmetry determined from the responses of the BCM are presented above. The DD of BPMs 12, 4a and 4b are presented in the first, second and third row. The left column presents DD of the BPMs with BCM1 plotted against BCM2, and the right column presents DD fo the BPMs with BCM2 plotted against BCM1. A correct BPM pedestal would result in correct asymmetry determination from the responses of the BPMs, and these plots would show little or no correlation, as is observed for the BPMs 4a and 4b plots.

During the asymmetry data acquisition the BPMs are operated in "auto-gain" mode. In this mode, the BPM electronics adjust the BPM gains to generate a stable BPM output signal. As a result, during periods of beam trips, the BPM gains are high, while during the nominal beam current of 100 μA, the BPM gains are low. Therefore, the BPM gains need to be turned off for a proper BPM pedestal determination [1]. During the BCM calibration runs, the BPMs were operated in "auto-gain" mode, and hence, these data could not be used to determine BPM pedestals.

As an alternative, the BPM pedestals were approximated by observing the responses of the BPMs without any beam on them. The correctness of the BPM pedestals were then checked by plotting the double-difference (DD) of the asymmetry measured between the BCMs and the BPMs, against the asymmetry measured by the BCMs, as is presented in Figure A.1.2. A correct BPM pedestal would result in correct asymmetry determination from the responses of the BPMs, and the plot of DD vs BPM asymmetry would show little or no correlation. In Figure A.1.2, the plots of DD of BPMs 4a and 4b (target BPMs) against BCM2 and BCM1, the second and third row plots, show no correlation, indicating that the pedestals for these BPMs were correct. The BPM12 DD plots, the top row plots, however, are correlated with the BCMs.

A.2   Detectors Pedestal Calibration

The detector pedestals were simply taken to be the integrated responses of the detector without any electron beam on them. For each detector, the pedestals from a couple of characteristic runs were averaged, and this average value used as the

---

[1]During the BPM pedestal calibration run, the BPM gain settings need to be identical to the ones used during the nominal production beam current of 100 μA. Therefore, the BPM gains are turned off *after* establishing 100 μA beam current on the BPMs, and allowing a short time for its gains to fully stabilize.
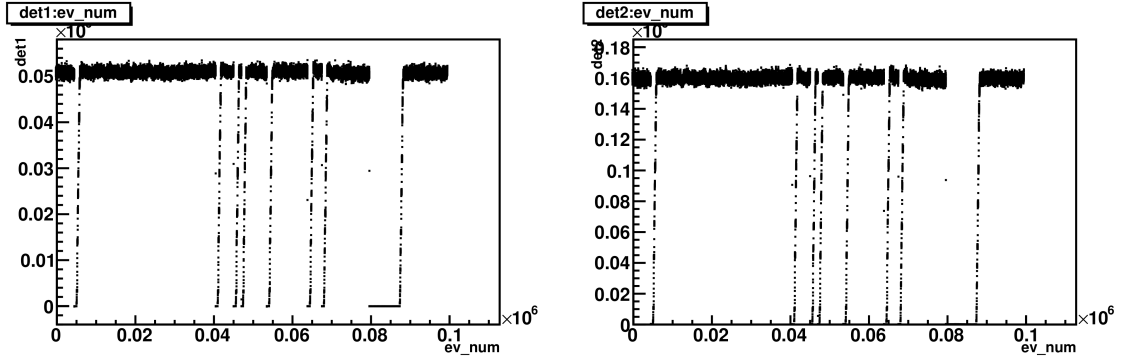
Figure A.2.1: Typical pedestal calibrated responses of the primary detectors of HAPPEX-III are presented above. The detector responses are plotted on the y-axis and the event number on the x-axis. Each event is 33.0 ms long. The LHRS detector (det1) is plotted on the left, and the RHRS detector (det2) is plotted on the right. Each of the detector's responses are close to zero during beam trips (when there is no beam current), indicating that the detector pedestals are well determined.

pedestal for all HAPPEX-III data. Typical pedestal corrected detector responses are presented in Figure A.2.1. For both det1 and det2, the integrated response is close to zero during beam trips (when there is no beam current), indicating that the pedestals are well determined.

Appendix B

Q^2 Data Checks and Calibrations

B.1 Detector Acceptances

The detector acceptances are checked to ensure that the detectors are well aligned and do not impose any geometric cuts on the acceptance of the elastically scattered electrons. The detector acceptances are checked by plotting the distribution of the detector responses to the scattered electrons that are incident on the detector as shown in Figure B.1.1. These are plots in the xy-plane. In each plot, the outline of the detector is shown overlapping the distribution of the electrons. The axes of the plots are scaled to reflect the true detector dimensions. The detector PMT is located at about 1.25 m in x. The highest energy electrons are incident at more positive x, and the lower energy electrons are incident towards more negative x.

In Figure B.1.1, the data presented in the top set of plots are acquired with the S0 triggers and those presented in the bottom set of plots are acquired with the detector triggers for each of the HRSs. The S0 scintillator paddles are larger than the detectors, and its acceptance in xy-plane contains the acceptance of the detectors as well. Therefore, all the electrons incident on the detectors necessarily pass through
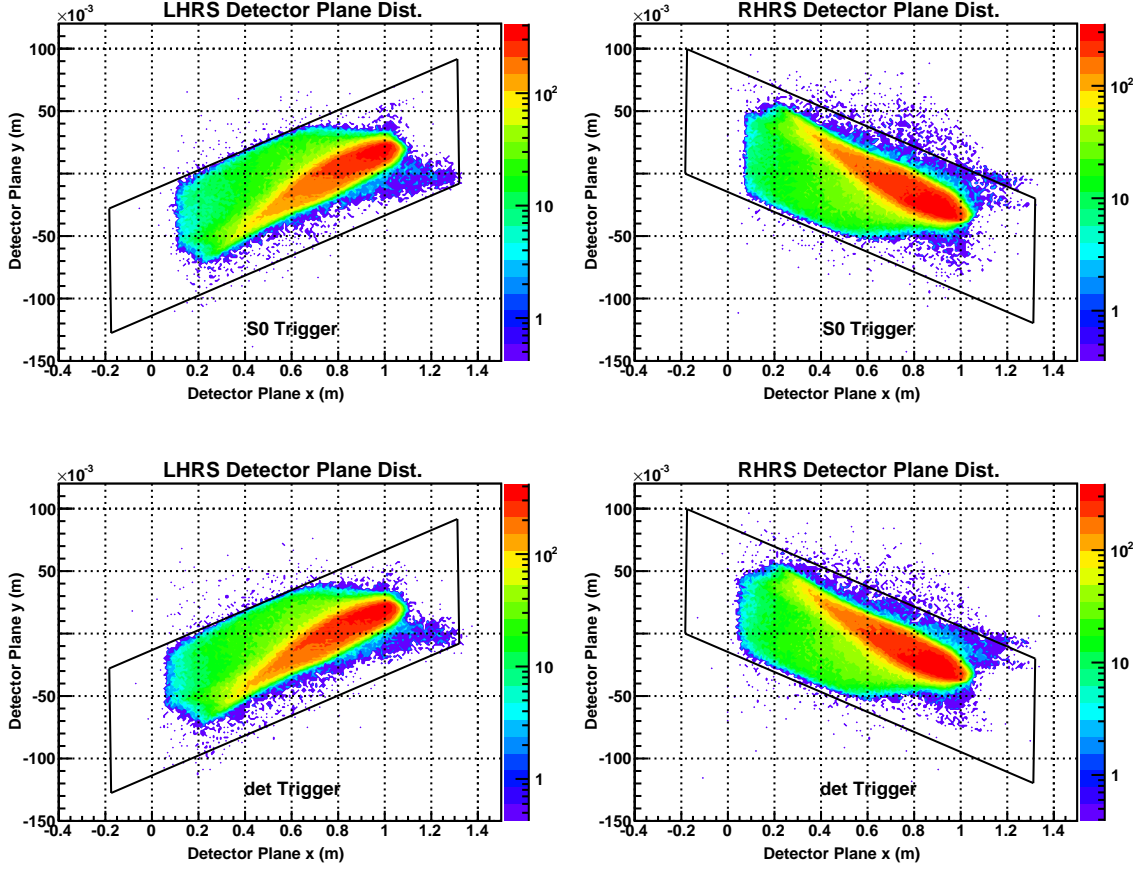
Figure B.1.1: The distribution of the detector responses to the incident electrons in the xy-plane are presented above. In each plot, the bounding box is the outline of the detector with the length of the detector along x. The axes above are scaled to reflect the true detector dimensions. The detector PMT is located at about 1.25 m in x. The electrons with higher energy are incident at more positive x. The elliptical stripe extending from about 0.3-0.4 to 1.0-1.1 in x arises due to the elastically scattered electrons, and the rest of the feature resulting from electrons that scattered in processes other than elastic scattering. The top set of plots are acquired with S0 trigger, and the bottom set of plots are acquired with the detector trigger on the Counting data-acquisition system (DAQ). The S0 scintillator paddles are larger than the detectors, and its acceptance in xy-plane contains the acceptance of the detectors as well. As a result, all the electrons incident on the detectors necessarily pass through the S0 paddles, while the reverse is not true. The S0 and detector triggered plots are not much different, indicating that the detector did not impose any geometric cuts on the acceptance of the scattered electrons.

the S0 paddles, while the reverse is not true. The S0 and detector triggered plots are

in Figure B.1.1 are not much different, indicating that the detector did not impose

any geometric cuts on the acceptance of the scattered electrons.

B.2 $E' - p$

$E' - p$ histograms are studied to check the correctness of the HRS transfer matrix elements that are used to determine Q^2. E' is the expected energy of the elastically scattered electron given in Eq. 7.7.2 as

$$E' = \frac{E_{beam}}{1 + \frac{E_{beam}}{m_H}(1 - \cos \Theta)},$$
(B.2.1)

where $m_H = 0.93827$ GeV^2 is the proton mass and E_{beam} is the energy of the incoming electron [1]. The scattering angle Θ is given in Eq. 7.7.3 as

$$\Theta = \cos^{-1}\left(\frac{\cos \Theta_0 - \phi \sin \Theta_0}{\sqrt{1 + \theta^2 + \phi^2}}\right)$$
(B.2.2)

where Θ_0 is the central scattering angle in the xz-plane of the "hall" coordinate system. Θ_0 is determined via pointing studies [SN10], and depends on the correctness of HRS transport matrices as discussed in Section 7.7.3.1.1. θ and ϕ [2] are the angles subtended by the reconstructed trajectories of the electrons to the z-axis along the xz- and yz-planes of the "transport" coordinate system. The hall and transport coordinate systems are illustrated in Figures 7.7.1a and 7.7.1b in Section 7.7. z is along the direction of beam propagation in both these coordinate systems. θ and ϕ were determined by the standard Hall A tracking analysis software, podd, with the tracking information collected by the VDCs [Ni02]. As a result, θ and ϕ also depend on the HRS transport matrices.

---

[1]See Section 7.7 for a discussion of E_{beam} used in the Q^2 determination.

[2]During HAPPEX-III, θ and ϕ were corrected for the extended structure of the target. This correction was performed by "podd", the standard Hall A HRS tracking data analysis software.

Spectrometer	Γ_0	Γ_1	Γ_2	Γ_3
LHRS	0.0	270.2 ± 0.15	0.0	$-1.6e^{-3} \pm 0.7e^{-3}$
RHRS	0.0	269.8 ± 0.15	0.0	$-1.6e^{-3} \pm 0.7e^{-3}$

Table B.1: Γ coefficients for the HRS

p is the four-momentum of the scattered electron calculated as

$$p = (dp + 1)p0 + E_{loss} \tag{B.2.3}$$

where $p0$ is the momentum of the HRS magnets, dp is the momentum transfer at the detectors, and has been corrected to reflect the extended structure of the liquid-hydrogen (LH2) target. $E_{loss} = 0.002$ GeV is the ionization energy loss due to multiple scattering (dE/dx) at the midpoint of the (25 cm) LH2 target (see Section 7.7 for further discussion of E_{loss}).

During HAPPEX-III, the podd only had the ability to calculate $p0$ by using terms to first order. However, at the HAPPEX-III energy of 3.484 GeV, higher order terms also affected the value of $p0$ [Ni01]. Therefore, $p0$ was manually calculated as

$$p0 = \Sigma\Gamma_i B_0^i = \Gamma_0 + \Gamma_1 B_0 + \Gamma_2 B_0^2 + \Gamma_3 B_0^3 \tag{B.2.4}$$

where B_0^i is the magnetic field strength of each of the four magnets of the HRS in Kilo Gauss (KG), and the Γ_i coefficients are listed in Table B.1. Using these Γ-coefficients and B_0^i, Eq. B.2.4 yields $p0$ for LHRS(RHRS) of 3.1431(3.1450) GeV.

p is independent the variables that are reconstructed by using the HRS transfer matrices, while E' is not. Therefore, studying $E' - p$ provides a check of the correctness of the HRS transfer matrices. A set of typical $E' - p$ spectrum for Q^2 data of HAPPEX-III are shown in Figure B.2.1. Both these plots are peaked about zero indicating that the HRS transfer matrices are correct. The finite width of the
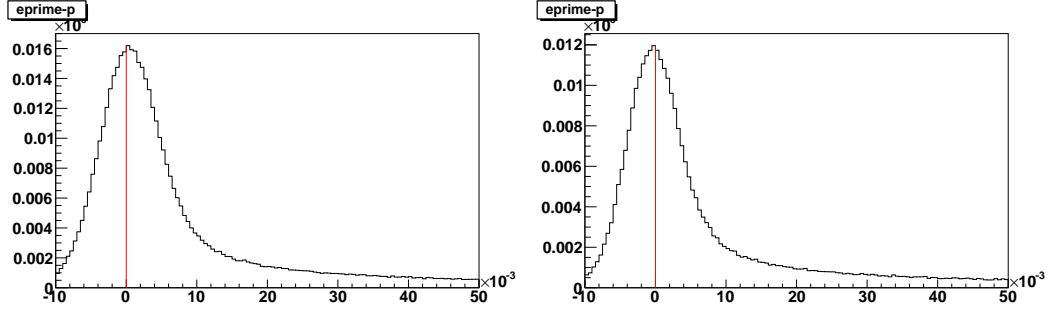
Figure B.2.1: Typical $E' - p$ spectra for the Q^2 data acquired in each HRS is presented above. The plot on the left(right) corresponds to the LHRS(RHRS). All the histograms are peaked about zero indicating that the HRS transport matrix elements are correct. These transfer matrices are used in Q^2 determination.

histogram is due to the disparity in energy loss corrections between E' and p: the internal and external Bremsstrahlung energy losses along with the ionization energy losses are implicitly accounted for in E' evaluation while p only takes the ionization energy losses inside the target into account.

B.3   Missing Mass Square

The missing mass square term is studied to check the correctness of Q^2 evaluation, similar to the $E'-p$ studies. The missing mass square is the difference in Q^2 calculated using two different techniques as

$$\text{mm}^2 = Q^2{}_1 - Q^2{}_2 \tag{B.3.1}$$

with

$$Q^2{}_1 = 2\text{m}_\text{H}(\text{E}_{beam} - \text{p}) \tag{B.3.2}$$

where $m_H = 0.938\,\text{GeV}^2$ is the proton mass, E_{beam} is the electron beam energy, p the effective momentum of the scattered electron given in Eq. B.2.3. $Q^2{}_2$ is the square of
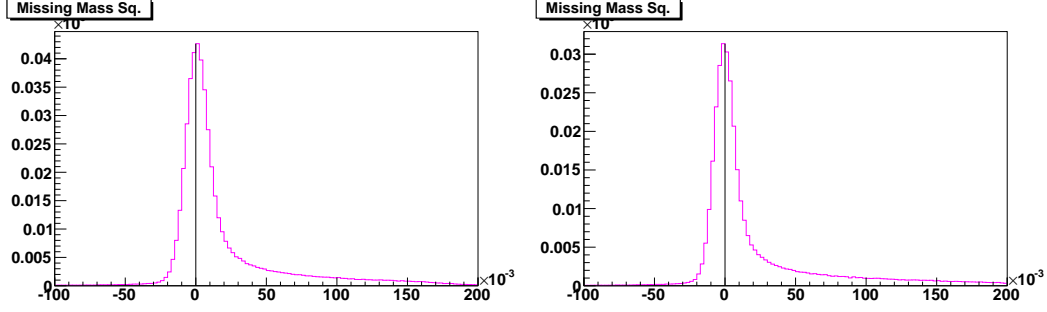
Figure B.3.1: Typical missing mass square histograms for the LHRS(left) and RHRS(right). These plots are centered about zero indicating that the HRS transport matrix elements and the central angles are well determined. The finite width of the plots are due to radiative correction discrepancies between Q^2_1 and Q^2_2 in Eq. B.3.1. See text for further details.

the four momentum transfer given in Eq. 7.7.1 as

$$Q^2_2 = Q^2 = 2E_{beam}E'(1 - \cos\Theta) \tag{B.3.3}$$

with E' as the energy of the scattered electron and Θ the scattering angle.

Q^2_1 does not depend on any of the variables reconstructed by using the HRS transport matrix elements and the HRS central scattering angle explicitly while Q^2_2 does, Eq. B.2.2. Thus, the mm^2 provides a check for the correctness of the HRS transport matrix elements, HRS central scattering angle and Q^2 evaluation itself. The mm^2 histograms in Figures B.3.1 are centered about zero, indicating that both Q^2_1 and Q^2_2 have similar averages. The long tail in these histograms reflect radiative losses than have been accounted for in Q^2_2 evaluation, but not in Q^2_1 evaluation. These mm^2 plots centered about zero indicate that the Q^2 is evaluated correctly, and that the associated HRS transport matrix elements and the HRS central scattering angles are correct.
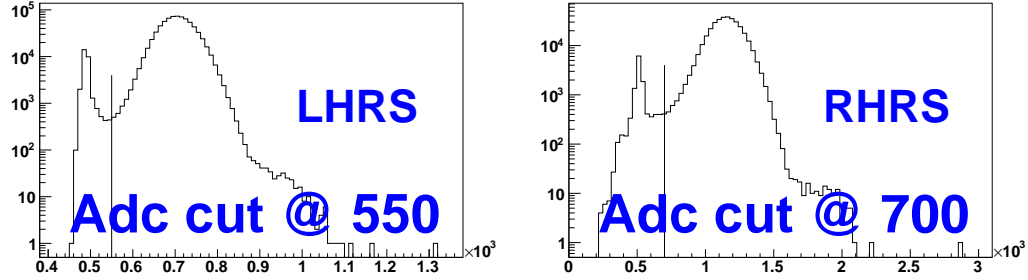
B.4   Detector Pedestals

Figure B.4.1: Typical LHRS(left) and RHRS(right) Q^2 detector histograms, with the cutoff threshold marked for pedestal determination. The LHRS(RHRS) detector pedestal cutoff occurs at 550(700), which is a typical cutoff value for the rest of the Q^2 runs as well.

The raw detector ADC values have to be properly pedestal subtracted to extract a correct Q^2 value. The first step in the pedestal extraction involves plotting the raw detector ADC histograms for each of the Q^2 runs and setting appropriate cutoff thresholds. These cutoffs are typically the minima of the histograms that occur between the pedestal peaks and the signal peaks. Typical Q^2 detector histograms for each of the HRS with the cutoff thresholds marked are presented in Figure B.4.1. With the cutoff threshold determined, a histogram of only the detector values that are smaller than the cutoff value is replotted, and its mean taken as the detector pedestal for the run. The histograms in Figure B.4.2 are LHRS(RHRS) detector pedestals corresponding to the plots in Figure B.4.1.

The detector pedestals are determined for each of the Q^2 runs individually, and averaged for each of the HRS separately. The pedestal shifts between the Q^2 runs are negligible because each of the HRS detector is operated at the same voltage. A pedestal cutoff value of 550(700) is used for all of LHRS(RHRS) Q^2 runs. The average LHRS(RHRS) detector pedestal is 491.91(513.39).
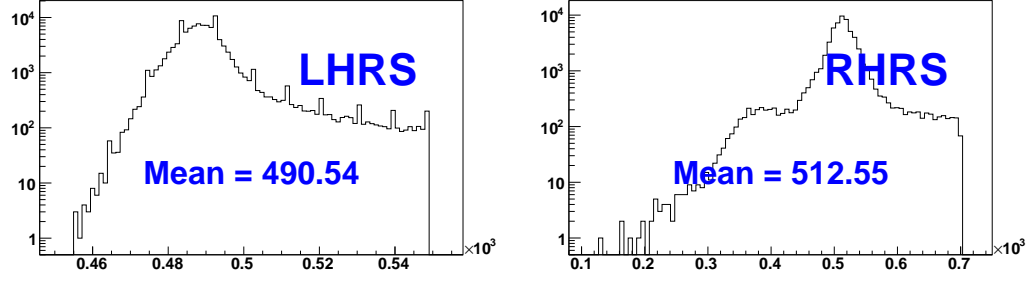
Figure B.4.2: Typical LHRS(left) and RHRS(right) detector pedestals plots. These plots correspond to the detector spectra of Figure B.4.1. Such plots are made for all the Q^2 runs, and the pedestals averaged. The average detector pedestal for LHRS(RHRS) is 491.91(513.39).

B.5 Detector Energy Resolution

The detector energy resolution needs to be considered during the detector design because the detector energy resolution can severely limit the precision of measurements. The detector energy resolution is calculated as

$$R_E = \sigma_{\mathrm{det}}/\mathrm{mean}_{\mathrm{det}} \tag{B.5.1}$$

where σ_{det} is the RMS width and $\mathrm{mean}_{\mathrm{det}}$ is the mean value of the measurement. The detector energy resolution affects the precision of the detector measurement as

$$\sigma_M = \sigma_{stat}\sqrt{1 + R_E^2} \tag{B.5.2}$$

where σ_M is the total uncertainty in the detector measurement, σ_{stat} is the statistical uncertainty and R_E is the detector energy resolution given by Eq. B.5.1.

The detector energy resolution is extracted from the raw detector ADC spectra like the ones presented in Figure B.4.1. Average σ_{det} and $\mathrm{mean}_{\mathrm{det}}$, along with the corresponding detector energy resolution factor, R_E, and its effect on the detector

Table B.2: Typical detector resolution of the HAPPEX-III detectors, and the associated increase in the asymmetry widths due to detector resolution.

	LHRS	RHRS
σ_{det}	56.7	159.4
mean_{det}	697.2	1130
$R_E(\%)$	8.13	14.2
$\sqrt{1 + R_E^2}$	1.003	1.01

measurement for each of the HRS detectors are presented in Table B.2. The detector energy resolution increases the uncertainty in measurement by $\sim 0.3(1.0)\%$ in the LHRS(RHRS) detectors.

B.6   Detector Attenuation Coefficient

There is some amount of signal attenuation along the length of the detector, so this attenuation needs to be quantified. The detector attenuation coefficient is extracted by plotting the pedestal subtracted raw detector ADC signal against the detector length, x_{det} [1], and fitting it to a straight line. Typical detector attenuation plots corresponding to the HAPPEX-III Q^2 data are presented in Figure B.6.1 for each of the HRSs. Only the data in the range of $0.15 - 1.0$ m in x_{det} is fitted, with those at either end of the detector unused. This is because, at $x_{det} > 1.0$ m, the electrons are too close to the PMT and could be incident directly on the PMT. At $x_{det} < 0.15$ m,

---

[1] The detector length is calculated as

$$\text{x}_{\text{det}} = \sqrt{2} \times (\text{x}_{\text{tr}} + \text{det\_dist} \times \cos(\phi_{\text{tr}}) \times \cos(\theta_{\text{tr}} + 45/180 \times 3.14159)) \qquad \text{(B.6.1)}$$

where det_dist is the distance from the first VDC plane (lower VDC in Figure 3.9.4) to the detector, and is 0.787(0.762) m for the LHRS(RHRS) detector. x_{tr} is the distance along x-axis in the transport coordinate system. θ_{tr} and ϕ_{tr} are the angle subtended by the electron trajectory to the z-axis along the xz- and yz-planes of the transport coordinate system. The transport coordinate system is illustrated in Figure 7.7.1b in Section 7.7. In podd x_{tr}, θ_{tr} and ϕ_{tr} are $L.tr.x$, $L.tr.th$ and $L.tr.ph$ respectively for the LHRS. 45° above is the amount by which the transport coordinate system is rotated about y-axis.
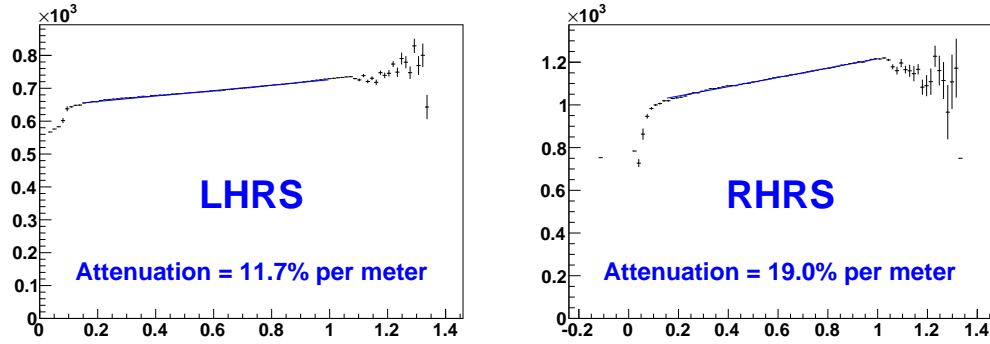
Figure B.6.1: Typical LHRS(left) and RHRS(right) detector attenuation plots corresponding to HAPPEX-III Q^2 data are presented above. The raw ADC values are plotted on the y-axis and the length of the detector, x_{det}, is plotted on the x-axis. Only the data in the range of $0.15 - 1.0$ m in x_{det} is fitted because data at either edges of the detector are unreliable.

the signal strength is too weak. The detector attenuation coefficient is extracted by using the slope of this straight line fit as $slope/mean_{det} \times 100\%/m$.
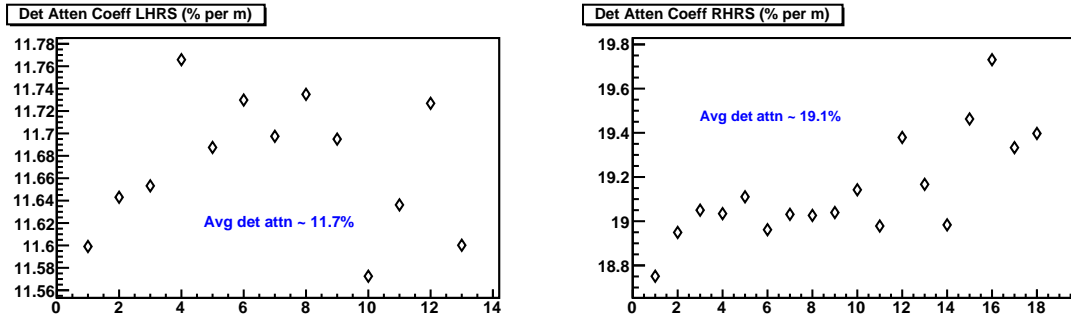

Figure B.6.2: The detector attenuation coefficients of *all* the HAPPEX-III Q^2 runs are summarized for each of the HRSs above. The detector attenuation coefficients are plotted on the y-axis and each point along the x-axis is a Q^2 data run. The average attenuation coefficients for the LHRS and RHRS detectors are $11.7\%/m$ and $(19.1)\%/m$ respectively.

The detector coefficients of *all* the Q^2 data collected during HAPPEX-III are summarized for each of the HRSs in Figure B.6.2. The average attenuation coefficient of the LHRS detector is $11.7\%/m$ and of the RHRS detector is $19.1\%/m$.
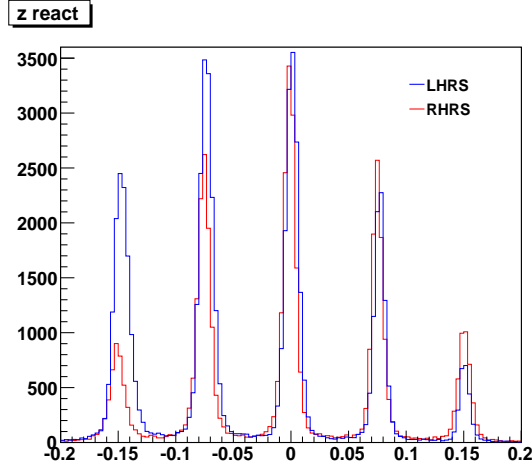
Figure B.7.1: The z_{react} evaluated using Eq. B.7.1 is checked for correctness by plotting the data acquired with the ^{12}C multi-foil target along z. The ^{12}C multi-foil target had foils at 0.0, ± 7.5 and 15.0 cm from the nominal target center, which is also what is observed in the spectra above to within 2.0 mm. The differences in the peak sizes between the HRS are due to differences in the acceptances between the HRSs.

B.7 Target z

The z location of the scattered electrons at the target is calculated as [Ni02]

$$z_{react} = -(y_{tg} + D)\frac{\cos \phi_{tg}}{\sin(\Theta_0 + \phi_{tg})} + x_{beam} \cot(\Theta_0 + \phi_{tg}) \qquad (B.7.1)$$

where y_{tg} is the distance along y-axis, and ϕ_{tg} is the angle in the yz-plane with respect to the z-axis in the "target" coordinate system [Ni02]. In podd y_{tg} and ϕ_{tg} are $L.tr.tg\_y$ and $L.tr.tg\_ph$ respectively for the LHRS. During HAPPEX-III, ϕ_{tg} was corrected for the extended structure of the LH2 target. $D(\text{LHRS,RHRS}) = (0.001, 0.003)$ m is the spectrometer "mispointing" [Ni02] and Θ_0 is the HRS central scattering angle. The parameter x_{beam} is the beam position along x at the target. The x_{beam} evaluated by podd was unreliable because the BPMs had not been properly calibrated before or after HAPPEX-III. Therefore, the average x_{beam} extracted from EPICS readout of the beam positions were used.
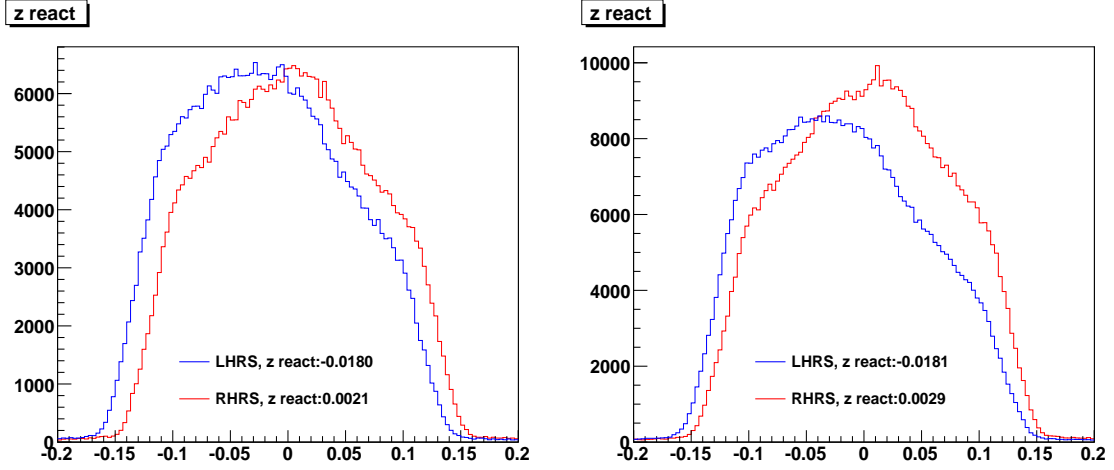
Figure B.7.2: Target z of Q^2 runs taken at x beam position of -2.2 and -0.8 mm. As expected, the mean z values are similar (to within 1.0 mm). The differences in histogram profiles between the HRS are reflect the mismatch in the acceptances between the HRS.

The correctness of z_{react} evaluated using Eq. B.7.1 was checked by plotting the data acquired with the ^{12}C multi-foil target along z, as is presented in Figure B.7.1. The ^{12}C multi-foil target is discussed in Section 3.6. This target consists of thin ^{12}C foils at 0.0, ± 7.5 and ± 15.0 cm from the nominal target center along z. If z_{react} were calculated correctly, the location of the peaks in the spectra would be at 0.0, ± 7.5 and ± 15.0 cm along$z$, as is observed in Figure B.7.1 to within 2.0 mm. (The beam also needs to be centered along x, i.e. $x_{beam} = 0.0$, for this observation because of dependence of HRS acceptances on x.)

The target z spectra are also plotted for Q^2 runs that were acquired with beam positions along x, x_{beam}, of $-2.2mm$ and $-0.8mm$, as shown in Figure B.7.2. These x_{beam} have been accounted for in these plots, and, as a result, the target z are centered about zero to within 1.0 mm. In both these plots, the differences between the LHRS and RHRS histograms are due to acceptances mismatches between the HRSs.

B.8   Sieve x/y

The x/y_{sieve} are calculated as [Ni02]

$$x_{sieve} = x_{tg} + L \times \tan \theta_{tg} \tag{B.8.1}$$

and

$$y_{sieve} = y_{tg} + L \times tan\phi_{tg} \tag{B.8.2}$$

where x_{tg} and y_{tg} are the beam positions at the target. The variables θ_{tg} and ϕ_{tg} are the angles in the xz- and yz-planes with respect to the z-axis in the "target" coordinate system [Ni02]. L is the distance to the collimator center from the center of the target [Ni02]. The quantities y_{tg}, θ_{tg} and ϕ_{tg} were the podd variables $L.tr.tg\_y$, $L.tr.tg\_th$ and $L.tr.tg\_ph$ respectively for the LHRS. The average of the EPICS read-out beam position along x was used as x_{tg}. The variables θ_{tg} and ϕ_{tg} were corrected to reflect the extended structure of the target.

B.9 Q^2 by Run

The Q^2 data runs acquired over the course of HAPPEX-III, along with relevant parameters, are summarized in Tables B.3, B.4 and B.5.

Table B.3: The Q^2 runs acquired over the course of HAPPEX-III, along with parameters relevant to Q^2 evaluation are summarized below.

			LHRS			RHRS		
Date, Time	BPM4ax	BPM4bx	run #	Q^2	Q^2_{wt}	run #	Q^2	Q^2_{wt}
	(mm)	(mm)		(GeV^2)	(GeV^2)		(GeV^2)	(GeV^2)
Sep04, 14:57	-0.15	-2.24	24650	0.6264	0.6223	4459	0.6291	0.6260
Sep04, 15:01	-0.19	-2.26	24651	0.6263	0.6222	4460	0.6292	0.6261
Sep23, 21:15	-0.27	-0.79	24830	0.6281	0.6237	4613	0.6270	0.6239
Sep23, 21:24	-0.34	-0.81	24833	0.6281	0.6237	4616	0.6270	0.6238
Sep23, 21:26	-0.32	-0.80				4617	0.6270	0.6239
Sep23, 21:29	-0.32	-0.81	24834	0.6281	0.6238	4618	0.6271	0.6240
Sep23, 21:47	-0.30	-0.80	24835	0.6284	0.6241	4619	0.6271	0.6240
Sep23, 21:59	-0.29	-0.80	24836	0.6285	0.6242	4620	0.6272	0.6241
Sep23, 22:08	-0.29	-0.76	24837	0.6284	0.6241	4621	0.6271	0.6240
Sep23, 22:19	-0.30	-0.80	24838	0.6283	0.6239	4622	0.6272	0.6240
Sep23, 22:39	-0.33	-0.80	24839	0.6288	0.6244	4623	0.6271	0.6240
Sep23, 22:45	-0.32	-0.79	24840	0.6290	0.6246	4624	0.6273	0.6241
Sep23, 22:47	-0.34	-0.81	24841	0.6289	0.6245	4625	0.6278	0.6246
Oct09, 23:53	-0.31	-1.28	25012	0.6281	0.6238	4682	0.6277	0.6245
Oct25, 00:58	-0.55	-1.28				4719	0.6248	0.6217
Oct25, 01:05	-0.52	-1.28				4720	0.6248	0.6217
Oct25, 01:07	-0.57	-1.32				4721	0.6251	0.6219
Oct25, 01:12	-0.56	-1.29				4722	0.6250	0.6218

Table B.4: The Q^2 runs acquired during HAPPEX-III on the LHRS detector is presented below. The prescales ps1 and ps2 correspond to the detector and S0 scintillator respectively. The detector PMT was set to -2100 V during these Q^2 runs.

Date, Time	run #	Events	Energy	Current	BPM4ax	BPM4bx	Prescales
			GeV	(μA)	(mm)	(mm)	(ps1,ps2)
Sep04, 14:58	24650	397893	3.483	0.5	-0.15	-2.24	1E6, 1
Sep04, 15:01	24651	396236	3.483	0.5	-0.19	-2.26	1E6, 1
Sep23, 21:14	24830	224625	3.483	1.1	-0.27	-0.79	1E6, 4
Sep23, 21:24	24833	397812	3.483	5.0	-0.34	-0.81	1E6, 4
Sep23, 21:29	24834	987363	3.483	5.0	-0.32	-0.81	1E6, 15
Sep23, 21:47	24835	985233	3.483	5.0	-0.30	-0.8	1E6, 15
Sep23, 21:59	24836	862913	3.483	5.0	-0.29	-0.8	1E6, 15
Sep23, 22:08	24837	953329	3.483	5.0	-0.29	-0.76	1E6, 15
Sep23, 22:19	24838	420857	3.483	5.0	-0.30	-0.8	1E6, 15
Sep23, 22:39	24839	300323	3.483	5.0	-0.33	-0.8	1E6, 15
Sep23, 22:45	24840	85517	3.484	10.00	-0.34	-0.79	1E6, 15
Sep23, 22:47	24841	741355	3.484	10.00	-0.34	-0.81	1E6, 15
Oct09, 23:53	25012	365306	3.483	1.1	-0.31	-1.28	1E6, 7

Table B.5: The Q^2 runs acquired during HAPPEX-III on the RHRS detector is presented below. The prescales ps1 and ps2 correspond to the detector and the S0 scintillator respectively. The detector PMT was set to -1600 V during these runs.

Date, Time	run #	Events	Energy	Current	BPM4ax	BPM4bx	Prescales
			GeV	(μA)	(mm)	(mm)	(ps1,ps2)
Sep04, 14:57	4459	392222	3.483	0.5	-0.15	-2.24	1E6, 1
Sep04, 15:01	4460	386317	3.483	0.5	-0.19	-2.26	1E6, 1
Sep23, 21:15	4613	270370	3.483	1.1	-0.27	-0.79	1E6, 4
Sep23, 21:24	4616	395883	3.483	5.0	-0.34	-0.81	1E6, 4
Sep23, 21:26	4617	382599	3.483	5.0	-0.32	-0.80	1E6, 4
Sep23, 21:29	4618	1236725	3.483	5.0	-0.32	-0.81	1E6, 15
Sep23, 21:47	4619	1181074	3.483	5.0	-0.30	-0.80	1E6, 15
Sep23, 21:59	4620	988539	3.483	5.0	-0.29	-0.80	1E6, 15
Sep23, 22:08	4621	1101019	3.483	5.0	-0.29	-0.76	1E6, 15
Sep23, 22:19	4622	482466	3.483	5.0	-0.30	-0.80	1E6, 15
Sep23, 22:39	4623	342667	3.483	5.0	-0.33	-0.80	1E6, 15
Sep23, 22:45	4624	128141	3.484	10.0	-0.34	-0.79	1E6, 15
Sep23, 22:47	4625	665616	3.484	10.0	-0.34	-0.81	1E6, 30
Oct09, 23:53	4682	392843	3.483	1.1	-0.31	-1.28	1E6, 7
Oct25, 00:58	4719	383419	3.483	1.1	-0.55	-1.28	1E6, 5
Oct25, 01:05	4720	13829	3.484	1.1	-0.52	-1.28	1E6, 5
Oct25, 01:07	4721	156790	3.483	1.1	-0.57	-1.32	1E6, 25
Oct25, 01:12	4722	204192	3.483	1.1	-0.56	-1.29	1E6, 50

Appendix C

Source

C.1 Quad-Photodiode (QPD)

The schematic of a typical QPD is shown in Fig-
ure C.1.1. The QPD measures the total beam in-
tensity, and the beam positions along two directions
simultaneously. The total beam intensity is the sum
of responses generated by the incident light on all four
pads. The beam positions are determined along the
horizontal (x) and vertical (y) (when the qpd symme-
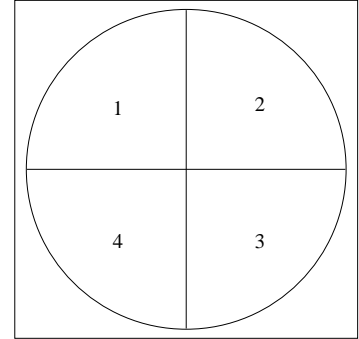try axes are aligned with x and y) as

Figure C.1.1: QPD Layout

$$x = \frac{(I_2 + I_3) - (I_1 + I_4)}{I_1 + I_2 + I_3 + I_4}; \qquad y = \frac{(I_1 + I_2) - (I_3 + I_4)}{I_1 + I_2 + I_3 + I_4}, \qquad (C.1.1)$$

where I_1, I_2, I_3 and I_4 are responses of the pads 1,2,3 and 4 respectively to the incident
light.

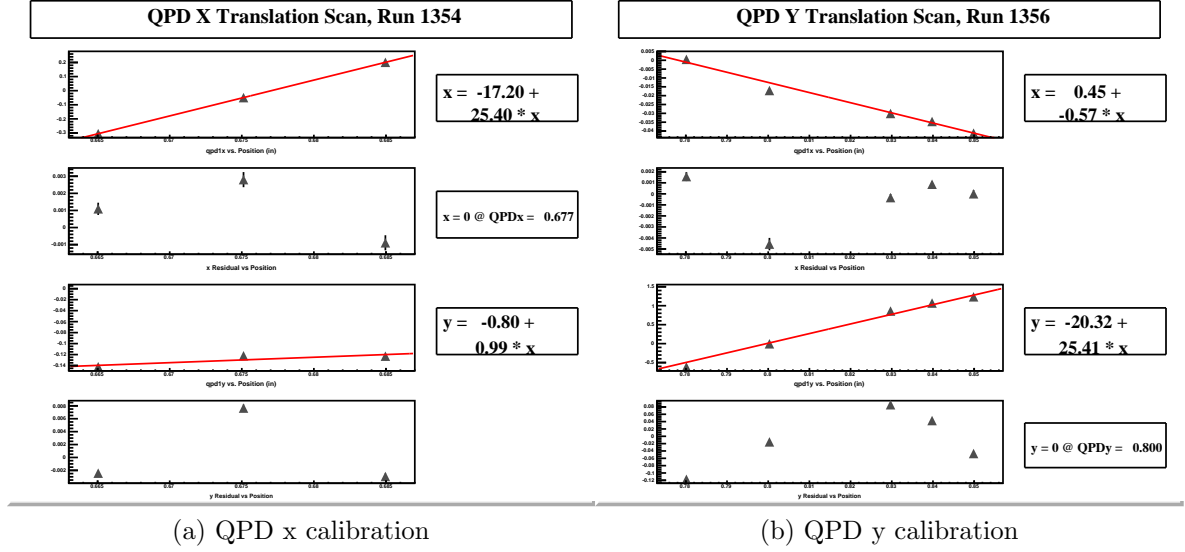(a) QPD x calibration   (b) QPD y calibration

Figure C.1.2: QPD calibration plots along x and y. In all these plots, the x-axes are the vernier readouts of the QPD positions. The first and second subplots plot the beam x-position and residuals of beam x-position on the y-axis. The third and fourth subplots plot the beam y-position and residuals of beam y-position on the y-axis. Only the first two subplots are relevant for QPD x-calibration, and only the last two subplots are relevant for the QPD y-calibration.

C.1.1   QPD Calibration Procedure

The QPD is calibrated in order to interpret the beam intensity variations across its pads as appropriate beam positions. The calibration also facilitates centering of the beam on the QPD pads, and provides an estimate the beam spot-size. During the laser table studies, the QPD was calibrated both along x and y. The calibrations along both these directions use a similar technique. Therefore, the calibration along only x is discussed below:

- The QPD calibration started with the beam roughly centered on the QPD. Then the QPD was translated to several locations in x [1], and the responses of the QPD, along with the associated vernier x-positions were recorded at each

---

[1]The QPD was mounted on a set of Thorlabs translation stages that allowed motion along x and y. These stages were equipped with verniers with a precision of 10 mills.

of these locations. During the QPD translation, care was taken to ensure that *all* four pads received some fraction of the beam, and that the beam did not fall off the outside edges of the pad. Eq. C.1.1 fails unless all the QPD pads receive some fraction of the beam. Any beam that falls off the pads reduces the accuracy of the QPD measurements.

- The beam x-positions measured by the QPD were plotted against the vernier x-position values. A straight line was then fitted to this plot as show in Figure C.1.2.

- If the slope of the beam x-position vs. vernier x-position was not 25.4, the beam x-position was rescaled to force this slope to be 25.4. The factor 25.4 was the conversion from inches to millimeters. Forcing the slope to be 25.4 forced a one-to-one correlation of the beam x-position measured by the QPD to the amount of QPD motion read off on the verniers. A slope of 25.4 in a plot with y-axis in units of mm and x-axis in units of inches corresponds to a slope of 1 when the both the axes are rescaled to the same unit.

  The slope rescaling was achieved by changing the QPD x-offset value defined in the appropriate .db file that the parity-analyzer software (PAN) [PAN] uses to calculate the beam x-position.

The QPD x- and y- offsets that were adjusted in the .db file to force the slopes of the appropriate plots of Figure C.1.2 to be 25.4 also gave an estimate of the beam spot-size along the calibration direction. During the source studies, HAPPEX-III and PREX, the average x- and y- offsets were

$$x - \text{offset} = 1.5 \text{ mm} \quad \& \quad y - \text{offset} = 1.4 \text{ mm}.$$
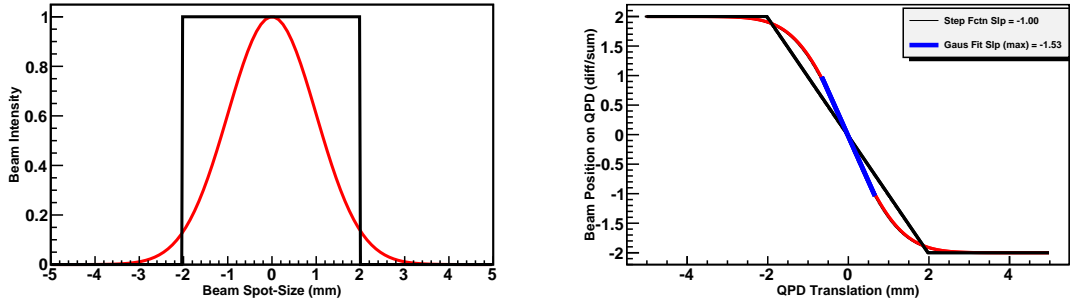
Figure C.1.3: The uncertainty in the QPD measurements due to limitation of the QPD calibration procedure was quantified with a simulation. A Gaussian and a step function beam intensity profile centered on the QPD is shown on the left plot. The beam position measured by the QPD against the QPD position for each of these beam intensity profiles are presented on the right plot. The slope of the Gaussian beam varies with the QPD position, whereas it is a constant for the step function, so long as the entire beam is profiled by all four QPD pads. In the plots above, the Gaussian beam width is set to $2\sigma = 2$ mm, and the step function width is set to $4\sigma = 4$ mm. The translational slope of the step function is 1 while the translational slopes for the Gaussian beam profile varied from 1.15 to 1.53. This indicated an inaccuracy of $15 - 53\%$ on the QPD calibration technique due to deviation of the beam profile from step-function to Gaussian.

C.1.2   Limitations of QPD Calibration Technique

The QPD was calibrated by fitting a straight line to a plot of the beam position measured by the QPD vs. the QPD position. The beam position measurements, however, is not linearly related to the QPD position as a result of the Gaussian profile of the beam intensity, as is illustrated in the right plot of Figure C.1.3. This is a plot of the beam position measured by the QPD vs the QPD position. The red trace corresponds to a Gaussian intensity profile which is shown as the red trace in the left plot of Figure C.1.3. The black trace, which is a straight line, corresponds to a step-function. This function is shown in the left plot of Figure C.1.3 in black. For a beam intensity with a Gaussian profile, the slope of the plot of beam position measured by the QPD vs. the QPD position depends on the extent of QPD translation relative to the beam spot-size.
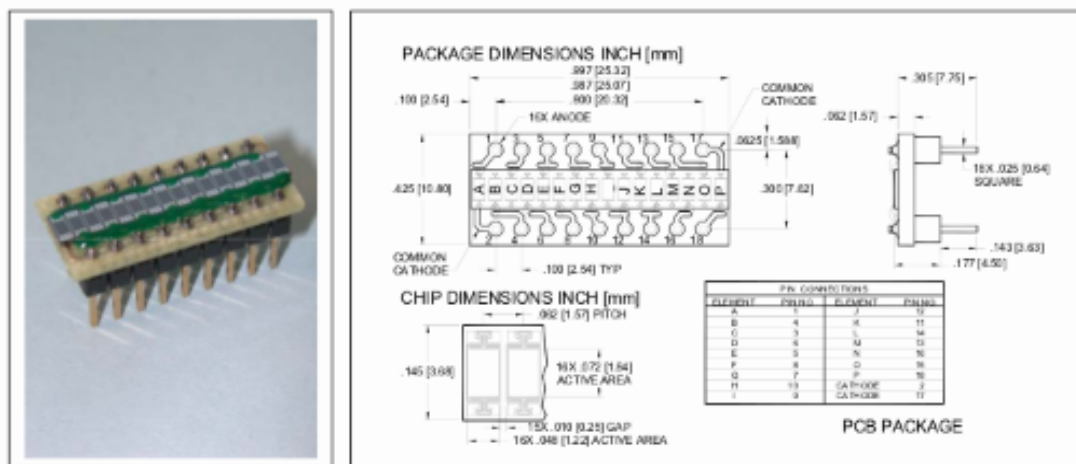
Figure C.2.1: A picture of the linear array photodiode detector (LAPD) is presented on the left. The dimensions of each photodiode pad in the array, the spaces between the pads, and the pin outputs are shown on the right.

In Figure C.1.3, the Gaussian beam intensity profile was assigned a width (diameter) of $2\sigma = 2$ mm, and the step function width was set to $4\sigma = 4$ mm. At these widths, when the translational slope of the step function was 1 (i.e. the beam position measured by the QPD was 1 mm for a change in QPD position of 1 mm), the translational slopes for the Gaussian beam profile varied from 1.15 to 1.53. This indicated an inaccuracy of $15 - 53\%$ on the QPD calibration technique for this particular case due to deviation of the beam intensity profile from a step-function to a Gaussian profile.

C.2   Linear Array Detector (LAPD)

The linear-array photodiode (LAPD) detector used during the source studies was an Advanced Photonic Inc's (API) Blue Enhanced Linear Array Silicon Photodiode (PDB-C216). This was an array of 16 photodiodes, each diode with an active area of 1.22×1.84 mm placed 0.25 mm apart in a straight line along the shorter dimension, Figure C.2.1.

The LAPD detector measured the beam intensity, position and spot-size simultaneously. These parameters could only be measured along *one* particular direction at a time; the direction along which the pads were arranged in the array. Therefore, a complete laser beam characterization usually involved repeated measurements with LAPD along different directions.

During the source studies, the LAPD was mounted on Thorlabs translation stages with verniers precise to 10 mills, and could be translated independently along the horizontal (x) and vertical (y).

C.2.1 Beam Position and Spot-size

The beam position and spot-size measured by the LAPD detector was calculated using two different techniques: arithmetic and Gaussian.

C.2.1.1 Arithmetic

In the arithmetic method, the beam position and spot-size was evaluated as

$$\bar{x} = \frac{\sum_i I(x_i) x_i}{\sum_i I(x_i)} \tag{C.2.1}$$

$$\sigma = \sqrt{\frac{\sum_i I(x_i)(x_i - \bar{x})^2}{\sum_i I(x_i)}} \tag{C.2.2}$$

where x_i and $I(x_i)$ are the beam position and intensity on the ith element of the array. $\bar{x}$ is the mean beam position, and σ is the beam spot-size. This method of measurement was used primarily to study the effect of the beam-fringes because this method of spot-size evaluation emphasizes the effect of the beam-fringes by weighing the intensity at the fringes by the square of the distance from the center.

C.2.1.2 Gaussian

In the Gaussian method, the beam intensity across all seven pads were plotted and a Gaussian fit performed to extract the beam position and spot-size. Unlike the arithmetic method, the Gaussian fit de-emphasizes the tail effects.

C.2.2 LAPD Calibration

The LAPD detector calibration was much simpler than the QPD detector calibration. Like the QPD parameters, LAPD detector parameters were defined in the appropriate .db file (that is read by PAN) that allowed adjustments of parameters such as the active number of pads, pad weights, and the distance between the pad centroids. The source studies only used the first 7 photodiodes, and thus, the pad number was set to 7. The weight of each pad was set to 1, and the distances between the pad centroids were set to 1.57 mm. The active pads were numbered $1 - 7$, with 1 being the pad closest to edge of the array. The beam position was evaluated relative to this edge. For instance, if the beam was centered on element 2, then the beam position readout on the LAPD would be $1.5 * 1.22 + 1 * 0.25 = 2.08$ mm.

C.2.3 Limitations of LAPD Detector

The beam intensity measured by the individual LAPD pads determined the total beam intensity, position and spot-size. Therefore, the accuracy of these measurements depended on the extent to which the entire beam intensity was profiled between the pads. The spaces between the pads inevitably resulted in loss of coverage across the beam spot, and resulted in loss of accuracy in the LAPD measurements. Expanding the beam along the length of the array mitigated the affects of these losses. Therefore, the laser beam was expanded along the length of the array during LAPD
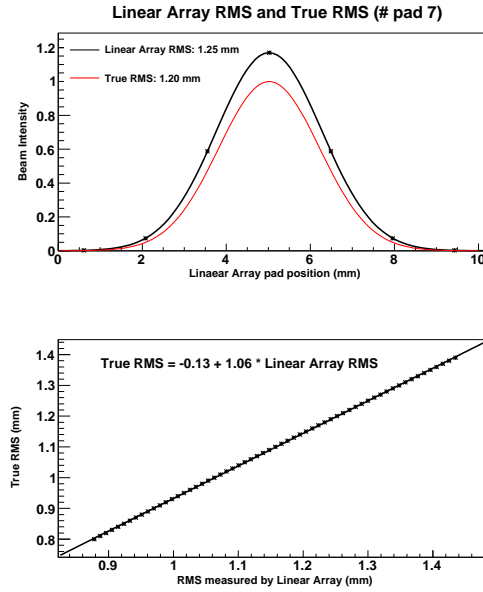
Figure C.2.2: These plots relate specifically to the LAPD detector configuration used during the source studies, with only 7 active pads. The first plot illustrates the differences between the true beam spot-size and the one measured by the LAPD detector. The second plot is a straight line fit of true beam spot-size against the one measured by the LAPD.

measurements.

The plots in Figure C.2.2 relate to the LAPD detector configuration, with only 7 active pads. The first plot illustrates the differences between the true beam spot-size and the one measured by the LAPD detector. These differences arise due to beam losses between the LAPD pads. The second plot is a straight line fit of true beam spot-size against the one measured by LAPD. The fit equation of this plot can be used to extract the true beam spot-size from the one measured by the LAPD as

$$y = -0.13 + 1.07x \tag{C.2.3}$$

where y is the true beam spot-size (RMS) and x is the RMS measured by the LAPD. This fit equation is specific to the LAPD detector configuration of 7 active pads. If

the number of active pads is varied, the fit equation's parameters changes as well.
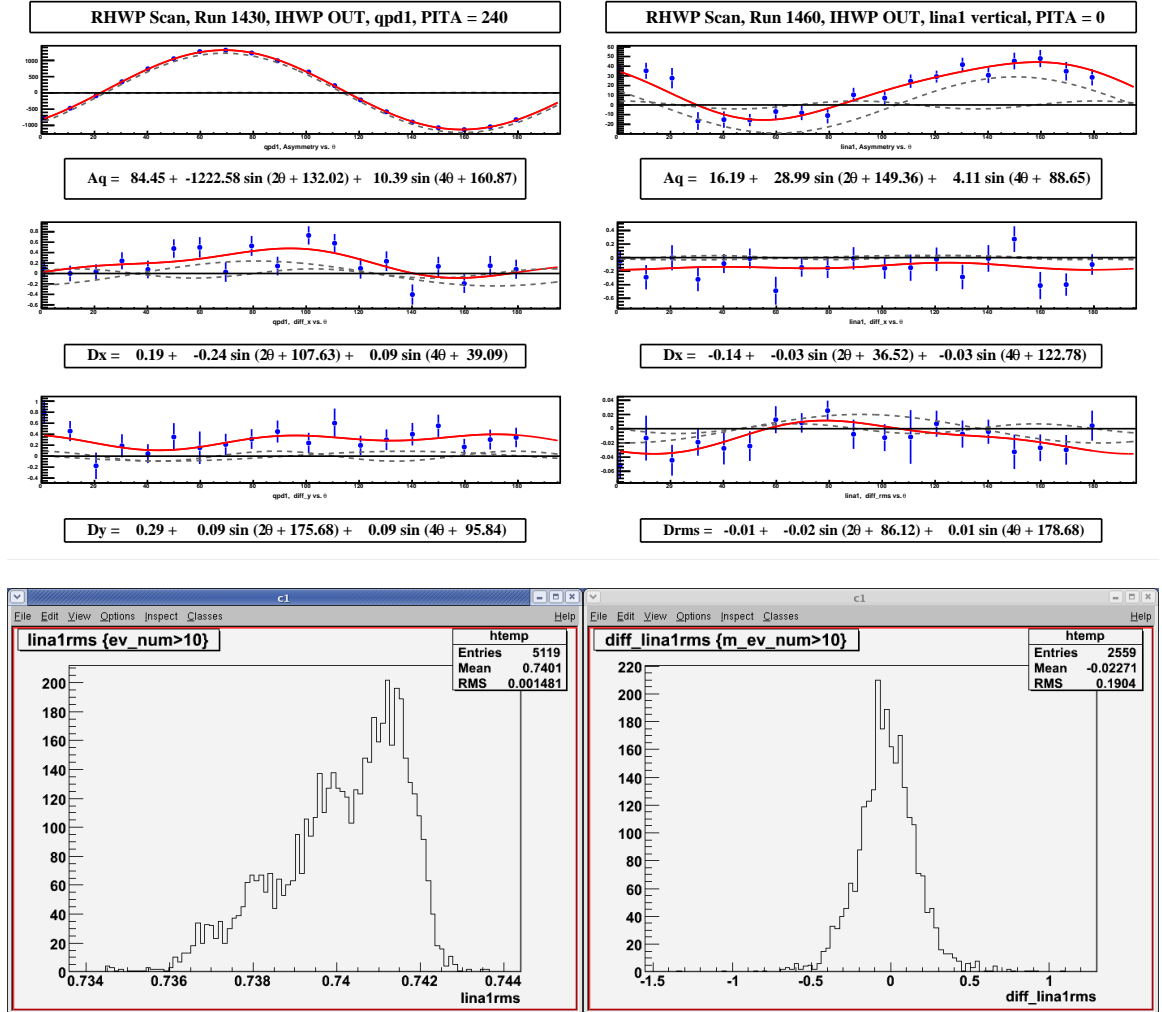
C.3   Pockels Cell (PC) Lensing Effects

Figure C.3.1: The top two plots represent data corresponding to RHWP scans acquired with the laser light *without* the analyzer on the laser's path in Figure 6.2.1. The top left plot was acquired on the QPD, and the rest on the LAPD detector oriented vertically. The bottom two plots correspond to the RHWP data of the top right. The bottom left plot indicates a beam spot-size of 0.74 mm, and the bottom right plot indicates a helicity-correlated (HC) spot-size difference of ~ 23 nm. This corresponds to a fractional variation of HC beam spot-size of $\sim 10^{-5}$.

The Pockels Cell (PC) "lensing effect", described in Section 6.3.1, is a *non-polarization* effect meaning that this effect is independent of the laser light polarization. The lensing effect arises because the PC is piezoelectric in nature, and the high-voltages (HVs) applied to the PC deforms its shape as illustrated in Figure 6.3.3. The PC lensing effects were characterized during the laser table source studies *without* the analyzer on the laser's path in Figure 6.2.1. In this setup, the non-polarization effects are dominated by the PC lensing effects. The characteristic rotating half-wave plate (RHWP) scan in this setup is presented in Figure C.3.1. In this figure, the top left is acquired on the QPD and the top right plots is acquired on the LAPD. In both these plots, the offset-, 2θ- and 4θ-terms are small, indicating that the PC lensing effects were small, with the exception being the 2θ-term of the RHWP scans acquired on the QPD. This large 2θ-term is due to large HC effects arising due to the RHWP itself, and not from the PC [1].

The bottom two plots of Figure C.3.1 characterize the PC lensing effects on the beam spot-size. The bottom left plot indicate a beam spot-size of 0.74 mm, and the bottom right plot indicate a HC spot-size differences of ~ 23 nm. This suggests a fractional variation of the HC beam spot-size of $\sim 10^{-5}$, which is well within the much stringent beam quality requirement of PREX.

C.4   Photocathode Analyzing Power

The analyzing power of the photocathode was determined by turning off the PC and performing a RHWP scan. The beam intensity maxima (I_{max}) and minima (I_{min}) of this scan, as shown in Figure C.4.1, were used to determine the photocathode

---

[1]The RHWP scan on the QPD was acquired at a PITA offset of 240 V. As a result, the Δ-phase effects arising from the PC might have coupled with the analyzing power of the RHWP leading to a large 2θ-term in this particular case.
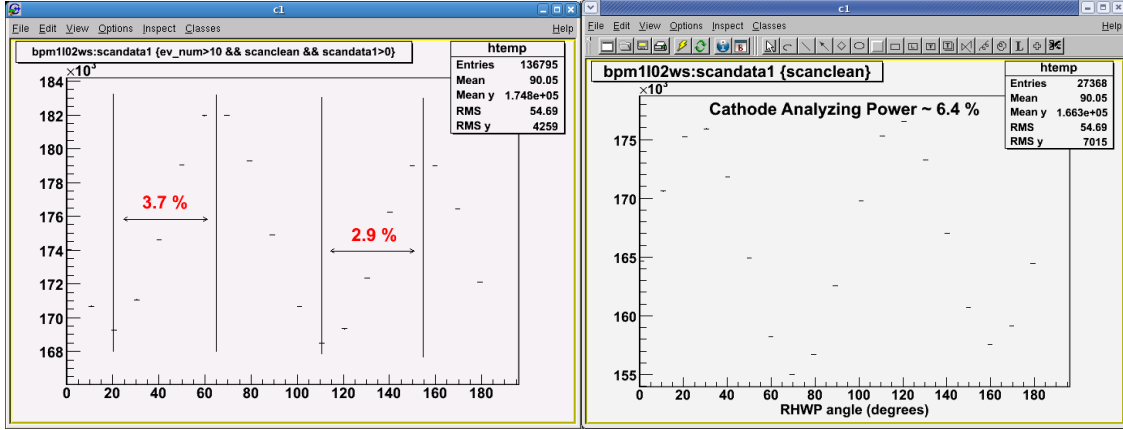
Figure C.4.1: The photocathode analyzing power was determined from the RHWP scans acquired with the PC turned off, and the beam position monitor (BPM) "gains" turned off. The left plot corresponds to the photocathode used during most of the source studies, and during HAPPEX-III and PREX. This plot suggests an analyzing power of $\sim 4\%$ for this photocathode. The plot on the right corresponds to the new photocathode. This photocathode had a crack on its surface and was used only for a couple of days during the source studies. The analyzing power of the photocathode is $\sim 6\%$ based on the right plot.

analyzing power as

$$\text{Analyzing Power} = \frac{I_{max} - I_{min}}{I_{max} + I_{min}}. \tag{C.4.1}$$

With the PC turned off, the laser light incident on the photocathode was almost entirely linear. As a result, the maxima and minima of the RHWP scan arose due to the photocathode's non-zero analyzing power, with these extrema determined by the size of the photocathode's analyzing power. The beam position monitor (BPM) "gains" were turned off during these RHWP scans because the "auto gain" setting at which the BPMs are normally operated, compensates any losses in the beam signal size with appropriate signal amplifications, washing out minima.
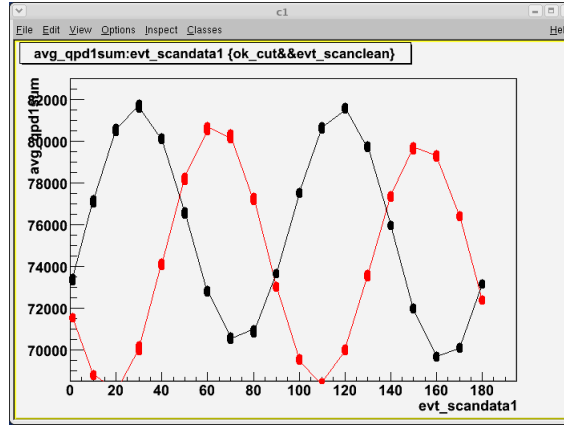
Figure C.5.1: The total intensity variation observed during typical RHWP scans acquired with IHWP IN and OUT is presented above. The black dots correspond to IHWP OUT and red dots to IHWP IN state. The laser intensity is minimum at RHWP of ~ 20 and $\sim 110°$ for IHWP IN, and is minimum at ~ 70 and $\sim 160°$ for IHWP OUT state. This suggests that the RHWP fast/slow-axis is either at ~ 20 or $\sim 110°$ to the horizontal.

C.5   RHWP fast/slow-axis

The fast/slow-axis of the rotatable half-wave plate (RHWP) was determined with the RHWP scan acquired with the analyzer on the laser's path in Figure 6.2.1 during the laser table source studies. The total intensity variation for typical such RHWP scans, for insertable half-wave plate (IHWP) states IN and OUT, with the RHWP rotated in the range of $\theta = [0, \pi]$ are presented in presented in Figure C.5.1. The red trace corresponds to the IHWP IN state, and the black trace to the IHWP OUT state. The laser intensity is minimum at RHWP of ~ 20 and $\sim 110°$ for IHWP IN, and is minimum at ~ 70 and $\sim 160°$ for IHWP OUT state. This suggests that the RHWP fast/slow-axis is either at ~ 20 or $\sim 110°$ to the horizontal.

C.6   Non-Gaussian Tails

Any non-Gaussian tails in the laser light significantly affect the helicity-correlated (HC) spot-size differences, and lead to significant systematic uncertainty in the HC asymmetry. Therefore, the laser light was characterized for the presence of any non-Gaussian tails, and its HC effects. This was done during the laser table source studies by translating the LAPD detector across the beam, and observing the agreement between the Gaussian and arithmetic HC position and spot-size variations. The arithmetic and Gaussian method of position and spot-size determination is described in Appendix C.2.1. A good agreement between the Gaussian and arithmetic HC parameters indicates a Gaussian beam intensity profile, without large tail effects. A large disparity between the Gaussian and arithmetic HC parameters suggests significant tail effects.

The plots in Figure C.6.1 correspond to data acquired with the LAPD oriented vertically (y) and translated along y. The data presented on the left column was acquired *without* the analyzer on the laser's path in Figure 6.2.1 and the data presented on the right column were acquired *with* the analyzer present on the laser's path. In each plot, the beam parameters evaluated using arithmetic and Gaussian methods are presented. Without the analyzer, the effects of non-Gaussian tails are suppressed, as is evident in the agreement of the arithmetic and Gaussian points on the left plots. However, with the analyzer, the arithmetic HC position and spot-size differences vary much more than the Gaussian counterparts as the LAPD position is scanned (right plots), suggesting large non-Gaussian tail effects. In the second plot of the right column, the Gaussian HC position differences are relatively constant, whereas the arithmetic HC position differences varies with the LAPD position. The beam position evaluated using the arithmetic method weights the beam tails by its
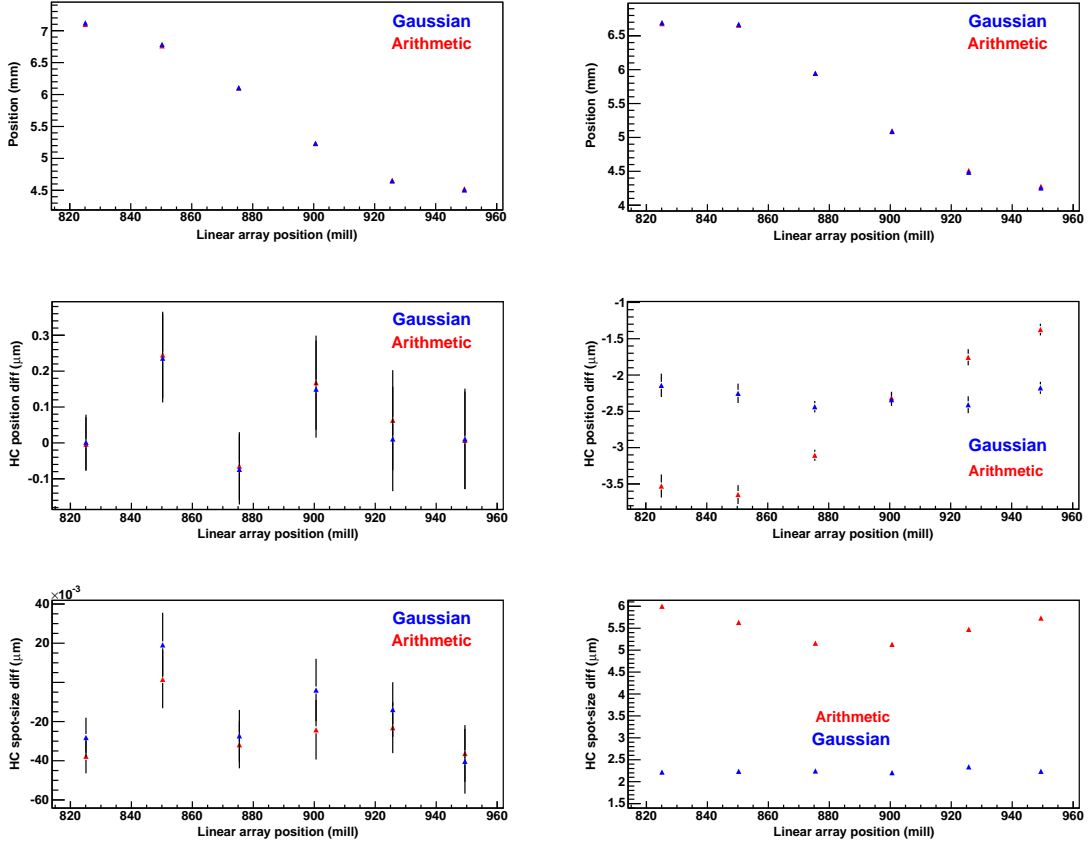
Figure C.6.1: The effect of non-Gaussian tails in the beam intensity profile is emphasized by comparing the helicity-correlated (HC) position differences, and the HC spot-size differences evaluated using the arithmetic and Gaussian method. These techniques are described in Appendix C.2.1. The plots on the left column correspond to data acquired *without* the analyzer on the laser's path in Figure 6.2.1 and the plots on the right column correspond to data acquired *with* the analyzer present on the laser's path. These data were acquired on the LAPD oriented vertically (y), and each point represents a different location of the LAPD along y. Without the analyzer, the effects of non-Gaussian tails are suppressed, as is evident in the agreement of the arithmetic and Gaussian points on the left plot. With the analyzer, however, the arithmetic HC position and spot-size differences vary much more than the Gaussian counterparts with the LAPD position in the right plots, suggesting large non-Gaussian tail effects.

intensity distribution, whereas that evaluated using the Gaussian method does not, as is described in Appendix C.2.1. Therefore, the dependence of the arithmetic HC
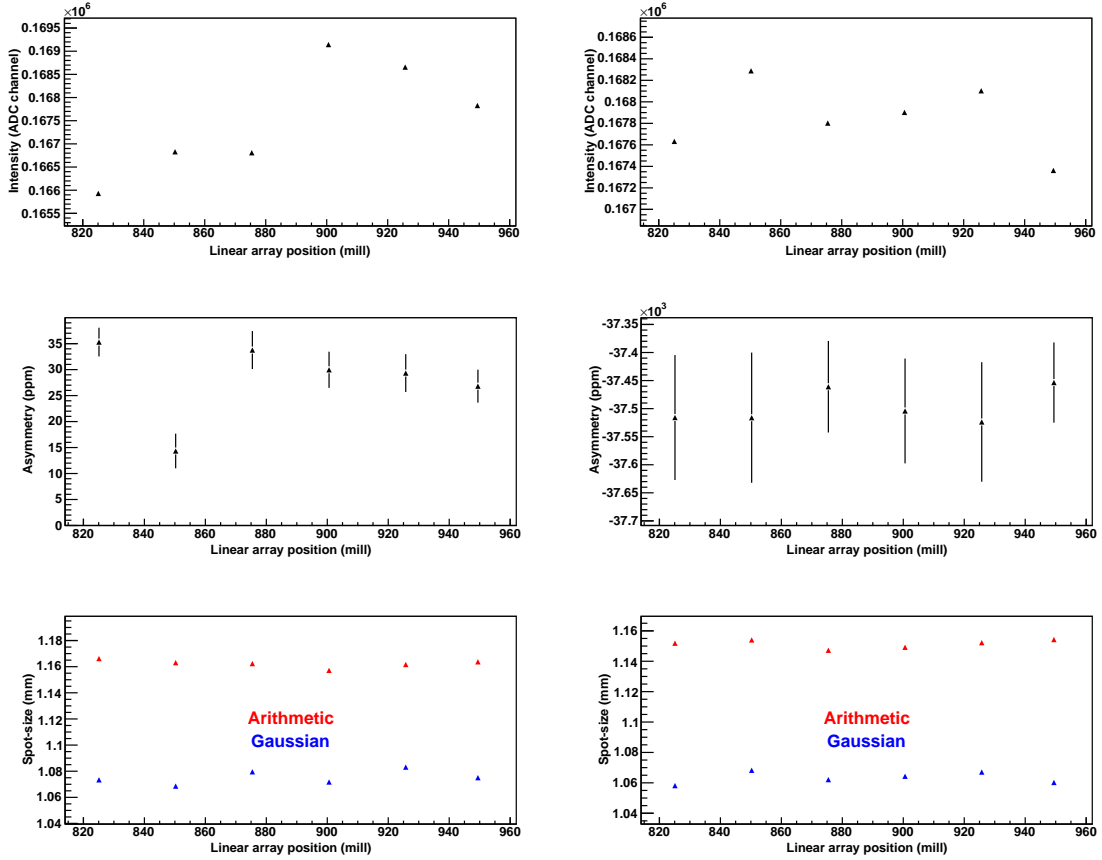
Figure C.6.2: The total beam intensity, asymmetry and the beam spot-size corresponding to the data presented in Figure C.6.1 are presented above. The data presented on the left column is acquired *without* the analyzer on the laser's path, while those presented on the right column is acquired *with* the analyzer on the laser's path. These data were acquired by translating the LAPD oriented vertically (y) along y.

position differences on the LAPD position suggests large non-Gaussian tails in the beam intensity profile. These tail effects are also observed in the HC spot-size differences: whereas the Gaussian HC spot-size differences remain relatively constant, the arithmetic HC spot-size differences are minimum when the beam is centered on the LAPD, and increases when it is not, as is evident in the bottom right plot of Figure C.6.1.

The total beam intensity, asymmetry and beam spot-size corresponding to the

data presented in Figure C.6.1 are presented in Figure C.6.2. As in Figure C.6.1, the data presented on the left column were acquired *without* the analyzer on the laser's path, while those presented on the right column were acquired *with* the analyzer on the laser's path.

The data presented in Figures C.6.1 and C.6.2 suggest that the size of the tail effects are about $\frac{\Delta\sigma}{\sigma} = 5 \times 10^{-3}$, when the analyzer (100% analyzing power) is present on the laser's path. During electron beam operation, this translates to tail effects of about $\frac{\Delta\sigma}{\sigma} = 5/25 \times 10^{-3} = 2 \times 10^{-4}$. This is because, the photocathode's analyzing power is $\sim 4\%$, a factor of ~ 25 less than that of the analyzer. Without the analyzer, the arithmetic and Gaussian HC parameters are in agreement, with the tail effects on the HC spot-size differences of about $\frac{\Delta\sigma}{\sigma} = 2 \times 10^{-5}$.

C.6.1   Slow-Helicity Reversal

The HC spot-size and shape differences, resulting from non-polarization effects do not reverse sign (as expected) during slow-helicity reversal, and as a consequence, can be canceled by using the technique of slow-helicity reversal. The technique of slow-helicity reversal is described in Section 5.6.2. The HC spot-size and shape differences corresponding to the data acquired with and without slow-helicity reversal are presented in Figure C.6.3. These data were acquired with a laser table setup *similar* to the one *without* the analyzer on the laser's path in Figure 6.2.1. The LAPD was used in the horizontal (x) orientation, and the insertable half-wave plate (IHWP) was used for slow-helicity reversal. $\lambda/2@45°$ corresponds to IHWP IN state and $\lambda/2@0°$ corresponds to IHWP OUT state. In the plot, the IHWP OUT data is presented by multiplying by -1, in order to emphasize that both the HC spot-size and shape differences are of similar *sign* and *magnitude* in both IHWP states. As a result, these data from the two IHWP states can be averaged to cancel the HC spot-size and shape
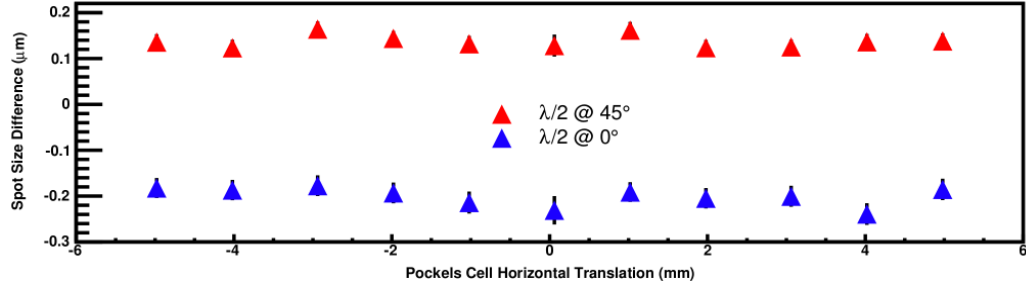
Figure C.6.3: The helicity-correlated (HC) spot-size and shape differences correspond-
ing to the data acquired with a laser table setup similar to the one *without* the ana-
lyzer on the laser's path in Figure 6.2.1 is presented above. The data was acquired
on the linear-array photodiode detector (LAPD) oriented horizontally (x), after care-
fully aligning the Pockels Cell (PC) for insertable half-wave plate (IHWP) states IN
($\lambda/2@45°$) and OUT ($\lambda/2@0°$). A +250 mm lens is used upstream of the LAPD
for point-to-point focusing. The IHWP OUT data is presented by multiplying by -1
above in order to emphasize that both the HC spot-size and shape differences are of
similar *sign* and *magnitude* in both IHWP states. As a result, the data from the two
IHWP states can be averaged to cancel the HC spot-size and shape differences. The
laser beam spot-size was about 0.5925 mm.

differences.

C.7   Point-to-Point Focusing

Point-to-point focusing can be used to suppress non-polarization effect, as is evident

in the data presented in Figure C.7.1. Point-to-point focusing is a technique in which

a converging lens (lens of +ve focal length) is used to focus the beam at the detector.

Figure C.7.1 presents data with (blue points) and without (red points) point-to-point

focusing. The suppression of HC position and spot-size and shape differences with

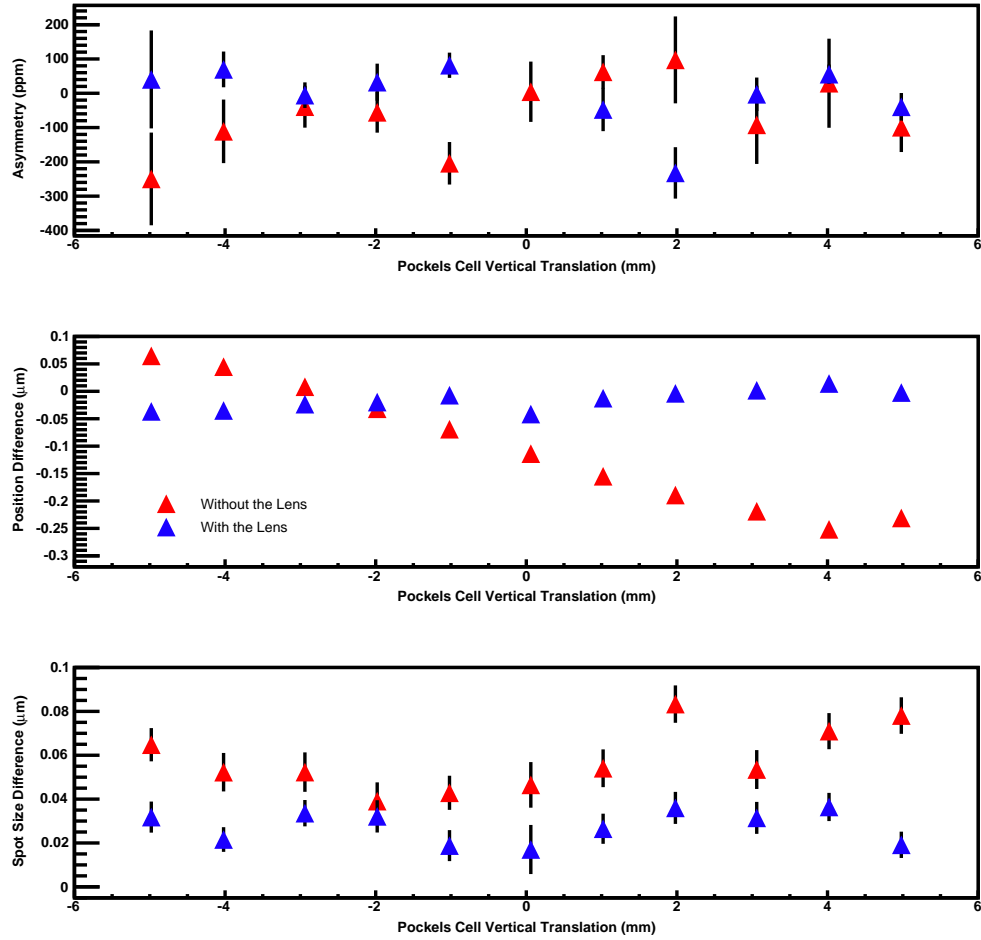point-to-point focusing is evident in Figure C.7.1.

Figure C.7.1: The suppression of helicity-correlated (HC) effects due to point-to-point focusing is observed in the data presented above. The data acquired with a +250 mm lens (for point-to-point focusing) are presented in blue, and the ones acquired without the lens are in red. These data were acquired on the linear-array photodiode detector (LAPD) oriented vertically (y). The LAPD was ~ 1 m downstream of the Pockels Cell (PC), and the lens was placed halfway between the PC and the LAPD for point-to-point focusing. The beam spot-size was 0.64 mm.

C.8   Photocathode Efficiency Non-uniformity

Continuous extraction of the electrons from the photocathode resulted in efficiency non-uniformities on the surface of the photocathode[1]. The photocathode also, inher-

---

[1]The incidence spot of the laser light on the photocathode was periodically moved both during HAPPEX-III and PREX, to mitigate the photocathode degradation.
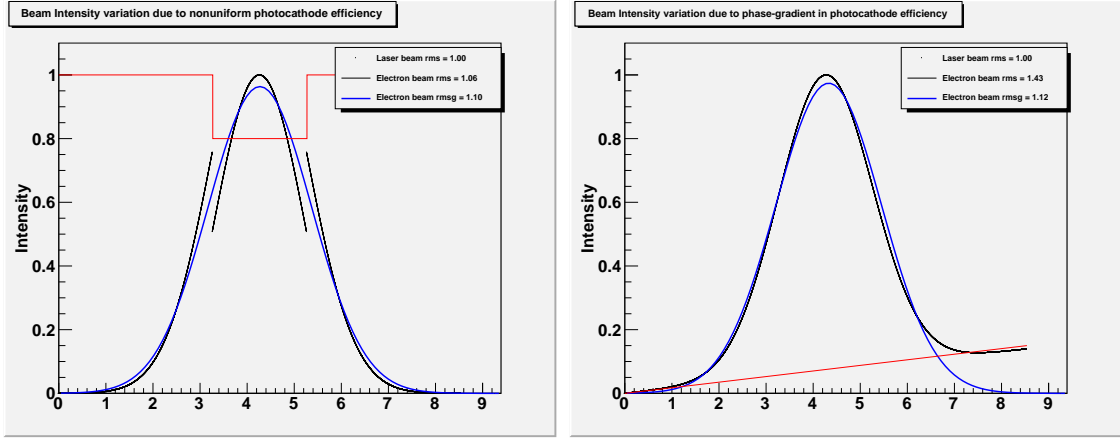
(a) The photocathode efficiency was modeled by a square well (red trace), with the bottom of the well indicating 80% efficiency and top indicating 100% efficiency. The width of the well was set to the laser light diameter (2σ) of 2 mm. A Gaussian laser light of $\sigma = 1$ mm incident about the center of the well on the photocathode resulted in electron beam (black trace) of $\sigma = 1.06$ mm. When fitted to a Gaussian (blue trace), the electron beam width was $\sigma = 1.10$ mm. The net effect of the photocathode efficiency degradation was electron beam width broadening.

(b) The photocathode phase-gradient was modeled by a straight line with a slope of 0.15 (red trace). Laser light of Gaussian profile and width of $\sigma = 1$ mm was incident on the photocathode. This generated electron beam of width $\sigma = 1.43$ mm (black trace). When fitted to a Gaussian profile, the electron beam width was $\sigma = 1.12$ mm. So, the net effect of the photocathode phase-gradient was to increase the beam spot-size.

Figure C.8.1: Simulation of the effects of the photocathode efficiency non-uniformity. Both the efficiency degradation and phase-gradients in the photocathode increased the electron beam spot-size.

ently, could have phase-gradients, that resulted in efficiency non-uniformities. The effects these non-uniformities on the electron beam spot-size are discussed below.

Figure C.8.1a presents the simulated results the photocathode efficiency degradation. The efficiency degradation was modeled by a square well (red trace), with the bottom of the well indicating 80% efficiency and top indicating 100% efficiency. The width of the well was set to the laser light diameter (2σ) of 2 mm. A Gaussian laser light of $\sigma = 1$ mm centered about the well extracted the electrons from the photocathode. This electron beam (black trace) had a width of $\sigma = 1.06$ mm. When fitted to a Gaussian (blue trace), the electron beam width was $\sigma = 1.10$ mm. So,

the net effect of the photocathode efficiency degradation was electron beam width broadening.

Figure C.8.1a presents the simulated results the photocathode phase-gradients. The photocathode phase-gradient was modeled by a straight line with a slope of 0.15 (red trace). Laser light of Gaussian profile and width of $\sigma = 1$ mm was incident on the photocathode. This generated electron beam of width $\sigma = 1.43$ mm (black trace). When fitted to a Gaussian profile, the electron beam width was $\sigma = 1.12$ mm. So, the net effect of the photocathode phase-gradient was to increase the beam spot-size.

In both cases, the electron beam width increased due to photocathode efficiency non-uniformities.

C.9 PC Translation Scan on Injector BPMs

The PC translation scan slopes and offsets measured on some of the BPMs at the injector are summarized in Table C.1. These numbers highlight the angular depen-dence of the HC parameters across the BPMs: the HC position differences and the PC translation slopes vary across the BPMs, fluctuating over a wide range.

Table C.1: The Pockels Cell (PC) translation slopes and offsets observed at some of the beam position monitors (BPMs) at the injector are summarized below. These numbers are presented to highlight the angular dependence of the HC parameters across the BPMs: the HC position differences and the PC translation slopes vary across the BPMs, fluctuating over a wide range.

		x-translation(nm/mill)	y-translation(nm/mill)	Offset(nm)
BPM1I02	Dx	5.1	12.5	-60
	Dy	15.2	-7.4	0
BPM1I04	Dx	-0.5	25.3	-230
	Dy	-19.1	2.2	-60
BPM1I06	Dx	-2.1	13.1	-130
	Dy	-29.0	6.3	-30
BPM0I01	Dx	2.8	-10.9	-70
	Dy	-0.1	1.5	-120
BPM0I01A	Dx	-7.8	2.2	-100
	Dy	-6.5	2.3	-70
BPM0I02	Dx	5.8	-33.7	-20
	Dy	29.1	-3.4	-180
BPM0I02A	Dx	8.5	-42.6	-60
	Dy	46.3	-6.5	-240
BPM0I05	Dx	-4.3	37.5	-300
	Dy	-52.9	14.4	250

Bibliography

[Ab12] S. Abrahamyan *et. al.* [PREX Collaboration], *Measurement of the Neutron Radius of ^{208}Pb Through Parity-Violation in Electron Scattering*, Phys. Rev. Lett. **108**, 112502 (2012). 2, 5, 6, 7, 249, 252, 253

[Ac07] A. Acha *et al.* [HAPPEX Collaboration], *Precision Measurements of the Nucleon Strange Form Factors at $Q^2 \sim 0.1$ GeV^2*, Phys. Rev. Lett. **98**, 032301 (2007). 2, 4, 5, 7, 131, 187, 256, 257, 267, 268, 272, 273, 278, 279

[Ac12] A. Acha *et. al.* [HAPPEX Collaboration], *Measurement of the Transverse Beam Asymmetry for Elastic Scattering for Selected Nuclei*, http://hallaweb.jlab.org/parity/prex/happex_transverse_v4.pdf (2012). 244

[Ah12] Z. Ahmed *et al.* [HAPPEX Collaboration], *New Precision Limit on the Strange Vector Form Factors of the Proton*, Phys. Rev. Lett. **108** 102001 (2012). 176, 278

[Al04] J. Alcorn *et al.*, Nucl. Instr. Methods Phys. Res. A **522**, 294-346 (2004). 30, 36, 37, 38, 41, 45, 46, 51, 58, 63, 64, 65, 66, 69, 76, 82, 229, 233, 283

[An04] K. A. Aniol *et al.* [HAPPEX Collaboration], *Parity violating electroweak asymmetry in polarized-e p scattering*, Phys. Rev. C **69**, 065501 (2004). 2, 4, 5, 31, 49, 56, 58, 207, 208, 209, 210, 255, 256, 267, 268, 272, 273, 278, 279

[An05] P. L. Anthony *et al.*, *Precision Measurement of the Weak Mixing Angle in Møller Scattering*, Phys. Rev. Lett. **95** 081601 (2005). 2, 6

[An10] D. Androic *et al.* [G0 Collaboration], *Strange Quark Contributions to Parity-Violating Asymmetries in the Backward Angle G0 Electron Scattering Experiment*, Phys. Rev. Lett. **104**, 012001 (2010). 2, 4, 264, 266, 267, 269, 272, 273, 274, 275, 276, 277, 278, 279

[AnH06] K. A. Aniol *et al.* [HAPPEX Collaboration], *Constraints on the nucleon strange form factors at $Q^2 \sim 0.1$ GeV^2*, Phys. Rev. Lett. **635**, 275-279 (2006). 2, 4, 5, 7, 131, 187, 256, 257, 267, 268, 272, 273, 278, 279

[AnHe06] K. A. Aniol *et al.* [HAPPEX Collaboration], *Parity-Violating Electron Scattering from* ^{4}He *and the Strange Electric Form Factor of the Nucleon*, Phys. Rev. Lett. **96**, 022003 (2006). 2, 4, 5, 7, 131, 256, 257, 267, 268, 272, 273, 278, 279

[Ar05] D. S. Armstrong *et al.* [G0 Collaboration], *Strange quark contributions to parity-violating asymmetries in the forward G0 electron proton scattering experiment*, Phys. Rev. Lett. **95**, 092001 (2005). 2, 4, 262, 263, 264, 267, 268, 272, 273, 274, 275, 276, 277, 278, 279

[Ar07] D. S. Armstrong *et al.*, *Precision measurement of the parity-violating asymmetry in deep inelastic scattering off deuterium using baseline 12 gev equipment in Hall C*, Proposal for Jefferson Lab PAC **32** (2007). 7, 280

[Arm07] D. S. Armstrong *et al.*, *The qweak experiment: "A search for new physics at the TeV scale via a measurement of the proton's weak charge"*, Spokespersons: R. D. Carlini, J. M. Finn, S. Kowalski, and S. A. Page, Proposal for Jefferson Lab PAC **33** (2007). 6

[As88] J. Ashman *et al.* [European Muon Collaboration], *A measurement of the spin asymmetry and determination of the structure function g(1) in deep inelastic muon proton scattering*, Phys. Lett. B **206**, 364 (1988). 4

[AS07] J. Arrington and I. Sick, *Precise determination of low-Q nucleon electromagnetic form factors and their impact on parity-violating e-p elastic scattering*, Phys. Rev. C **76**, 035201 (2007). 27, 237, 238

[Ba91] W. Barry, Nucl. Instr. Methods Phys. Res. A **301**, 407 (1991); T. Powers, L. Doolittle, R. Ursic, and J. Wagner, in Proceedings of the 7th Workshop on Beam Instrumentation, AIP Conf. Proc. No. 390, edited by A. Lumpkin and C. E. Eyberger (AIP, New York, 1997), JLAB-TN-96-021. 36, 38

[Ba95] A. O. Bazarko *et al.*, Z. Phys. C **65**, 189 (1995). 4

[Ba09] S. Baunack *et al.* [A4 Collaboration], *Measurement of Strange Quark Contributions to the Vector Form Factors of the Proton at* $Q^2 = 0.22(\text{GeV/c})^2$, Phys. Rev. Lett. **102**, 151803 (2009). 2, 4, 259, 260, 261, 267, 269, 272, 273, 274, 275, 279

[Be75] M. Beiner, H. Flocard, N. van Giai, P. Quentin, Nucl. Phys. A **238**, 29 (1975). 28

[Be05] E. J. Beise, M. L. Pitt and D. T.Spayde, *The SAMPLE measurement and weak nucleon structure*, Prog. Part. Nucl. Phys. **54**, 289-350 (2005). 2, 4, 257, 258, 259, 267, 269, 272, 273, 274, 275, 279

[Be08] J. Benesch *et al.*, *An ultra-precise measurement of the Weak Mixing Angle using Moller scattering*, Spokespersons: K. Kumar, Proposal for Jefferson Lab PAC **34** (2008). 7, 280

[BeF05] E. Beise, *The Axial Form Factor of the Nucleon*, http://arxiv.org/abs/nucl-ex/0501019 (2005). 18

[Bo08] A. Boehle, R. Michaels and J. Musson, *Low Current Cavity Monitor Tests*, http://hallaweb.jlab.org/parity/prex/lowi_cavity.pdf (2008). 76

[Bo09] P. Bosted *et al.*, *Precision measurement of parity-violation in deep inelastic scattering over a broad kinematic range*, Spokesperson: P. Souder, Proposal for Jefferson Lab PAC **35** (2009). 7, 280

[Bu03] H. Budd, A. Bodek and J. Arrington, *Modeling Quasi-elastic Form Factors for Electrons and Neutrino Scatterind*, arXiv:hep-ex/0308005 (2003). 18, 238

[BW64] M. Born and E. .Wolf, *Principles of Optics*, p.694-701 (1964). 137

[Ca89] G. D. Cates *et al.*, Nucl. Instr. Methods Phys. Res. A **278**,293 (1989). 118, 120

[Ch98] E. Chabanat, P. Bonche, P. Haensel, J. Meyer, R. Schaeffer, Nucl. Phys. A **635**, 231 (1998). 28

[Co05] E. Collett, *Field Guide to Polarization*, p.12-13 (2005). 139

[Do88] T. W. Donnelly *et al.*, Phys. Rev. C **37**, 2320-2325 (1988). 19

[Do89] T. W. Donnelly *et al.*, Nucl. Phys. A **503**, 589-631 (1989). 11

[Do09] T. Doi *et al.*, *Nucleon strangeness form factors from $N_f = 2+1$ clover fermion lattice QCD* Phys. Rev. D**80**, 094503 (2009). 274, 275, 276

[Es05] S. Escoffier *et al.*, *Accurate Measurement of the Electron Beam Polarization in JLab Hall A using Compton Polarimetry*, Nucl. Instr. Methods Phys. Res. A **551**, 563-574 (2005). 82

[Fi01] K. G. Fissum *et al.*, Nucl. Instr. Methods Phys. Res. A **474**, 108 (2001); *Vertical drift chambers for the hall a high resolution spectrometers at Jefferson Lab*, JLab-TN-00-016 (2000). 52

[Fl10] R. Flood, S. Higgins and R. Suleiman, *Helicity Control Board User's Guide (Draft 2)*, http://hallaweb.jlab.org/equipment/daq/HelicityUsersGuideFeb4.pdf (2010). 34

[Fr11] M. Friend *et al.*, Nucl. Instr. Methods Phys. Res. A, *Upgraded photon calorimeter with integrating readout for Hall A Compton Polarimeter at Jefferson Lab*, http://arxiv.org/abs/1108.3116 (2011). 65, 67

[Fr12] M. Lynn Friend, Ph. D. Thesis, Carnegie Mellon University (2012). 203

[Ga71] S. Galster *et al.*, Nucl. Phys. B **32**, 221 (1971). 18

[Gl61] S. L. Glashow, *Partial-Symmetries of Weak Interaction*, Nucl. Phys. **22**, 579-588 (1961). 1

[Go00] Y. Goto *et al.*, Phys. Rev. D **62**, 034017 (2000). 19

[Gr94] J. M. Grames, Ph. D. Thesis, University of Illinois at Urbana-Champaign (1994). 62, 63

[Ha73] F. J. Hasert *et al.*, Phys. Lett. B **46**, 138 (1973). 2

[HAMC] R. Michaels, *Hall A Monte Carlo*, http://hallaweb.jlab.org/parity/prex/hamc/. 211, 249

[He89] W. Heil *et al.*, *Improved Limits on the Weak, Neutral, Hadronic Axial Vector Coupling Constants from Quasielastic Scattering of Polarized Electrons*, Nucl. Phys. B **327**, 1-31 (1989). 2, 6

[Ho98] C. J. Horowitz, Phys. Rev. C **57**, 3430 (1998). 250

[Ho01] C. J. Horowitz, S. J. Pollock, P. A. Souder and R. Michaels, *Parity-Violating Measurements of Neutron Densities*, Phys. Rev. C **63**, 025501 (2001). 5, 28

[Ho12] C. J. Horowitz *et al.*, Weak charge Form Factors and radius of ^{208}Pb through Parity-Violation in Electron scattering, Phys. Rev. C **85**, 032501(R) (2012). 250, 251, 252, 253

[Hu03] T. B. Humensky, Ph. D. Thesis, Princeton University - Princeton (2003). 179, 180

[Hu04] T. B. Humensky *et al.*, *SLAC's polarized electron source laser system and minimization of electron beam helicity correlations for the E-158 parity violation experiment*, Nucl. Instr. Methods Phys. Res. A **521** (2004). 99, 112, 113, 114, 120, 122, 131, 135

[It04] T. M. Ito *et al.*, Phys. Rev. Lett. **92**, 102003 (2004). 2, 4, 257, 258, 267, 269, 274, 275, 279

[Ka07] Lisa Kaufman, Ph. D. Thesis, University of Massachusetts - Amherst (2007). 37, 102, 114

[Ke04] J. J. Kelly, Phys. Rev. C **70**, 068202 (2004). 264, 274, 275

[KM88] D. B. Kaplan and A. Manohar, Nucl. Phys. B **310** (1988). 4, 10, 22

[La97] H. L. Lai *et al.*, Phys. Rev. D **55**, 220 (1997). 4

[Lal97] G. A. Lalazissis, J. Konig, P. Ring, Phys. Rev. C **55**, 540 (1997). arXiv:9607039 [nucl-th]. 28

[Le01] C. W. Leemann *et al.*, *The Continuous Electron Beam Accelerator Facility:CEBAF at the Jefferson Laboratory*, Annu. Rev. Nucl. Part. Sci. **51**, 413-450 (2001). 29, 30, 34, 68

[Le05] D. Leinweber *et al.*, Phys. Rev. Lett. **94**, 212001 (2005); D. Leinweber *et al.*, Phys. Rev. Lett. **97**, 022001 (2006); P. Wang *et al.*, Phys. Rev. C **79**, 065202 (2009). 274, 275

[Li06] Jianglai Liu, Ph. D. Thesis, University of Maryland - College Park (2006). 19, 258, 260, 264, 265, 274, 275

[Li07] J. Liu, R. D. McKeown and M. J. Ramsey-Musolf, *Global Analysis of Nucleon Strange Form Factors at Low Q^2*, Phys. Rev. C **76**, 025202 (2007). 267, 268, 269, 270, 273, 278

[LY56] T. D. Lee and C. N. Yang, *Question of Parity Conservation in Weak Interactions*, Phys. Rev., **104**, 254-258 (1956). 1

[Ma04] F. E. Maas *et al.* [A4 Collaboration], *Measurement of strange quark contributions to the nucleon's form-factors at $Q^2 = 0.230(GeV/c)^2$*, Phys. Rev. Lett. **93**, 022002 (2004). 2, 4, 259, 261, 267, 268, 272, 274, 275, 279

[Ma05] F. E. Maas *et al.* [A4 Collaboration], *Evidence for strange quark contributions to the nucleon's form-factors at $q^2 = 0.108(GeV/c)^2$*, Phys. Rev. Lett. **94**, 152001 (2005). 2, 4, 20, 236, 259, 260, 261, 267, 268, 272, 273, 279

[Mc89] R. D. McKeown, *Sensitivity Of Polarized Elastic Electron Proton Scattering To The Anomalous Baryon Number Magnetic Moment*, Phys. Lett. B **219**, 140 (1989). 4

[Me09] D. Meekins, *Hall A Target Configuration (HAPPEX-III and PVDIS)*, https://jlabdoc.jlab.org/docushare/dsweb/View/Collection-9202, Private Communication (2009). 39

[Me12] Luis Mercado, Ph. D. Thesis, University of Massachusetts - Amherst (2012). 56, 81, 82, 88, 89, 247

[Mi98] G. A. Miller, Phys. Rev. C **57**, 1492 (1998). 15, 279

[Mi05] R. Michaels, Hall A Status Report - 2004, 41 (2005). 44, 86

[Mi10] R. Michaels, D. Meekins and P. Adderly, *Target Information for PREX*, Unpublished tech note. 062310, http://hallaweb.jlab.org/parity/prex/runinfo/PREX_Target_Info.doc (2010). 77

[Mo07] Bryan Moffit, Ph. D. Thesis, College of William and Mary (2007). 32, 52, 53, 186

[Mu94] M. J. Musolf *et al.*, *Intermediate-Energy Semileptonic Probes of the Hadronic Neutral Current*, Phys. Rep. **239**, No. 1 (1994). 8, 9, 10, 17, 21, 22, 237

[Na11] K. Nakamura *et al.* (Particle Data Group), J. Phys. G **37**, 075021 (2010) and 2011 partial update for the 2012 edition. (http://pdg.lbl.gov/). 19, 23, 24, 26, 237

[Ni01] Nilanga Liyanage, *Spectrometer constant determination for the Hall-A High Resolution Spectrometer pair*, Hall-A Technical Notes, Oct.12 (2001). 223, 291

[Ni02] Nilanga Liyanage, *Optics Calibration of the Hall A High Resolution Spectrometers using the new optimizer*, Hall-A Technical Notes, Jul.18 (2002). 219, 223, 290, 298, 300

[Pa07] K. D. Paschke, *Controlling helicity-correlated beam asymmetries in a polarized electron source*, Eur. Phys. J. A **32**, 549-553 (2007). 113, 115, 121

[Pa11] K. Paschke *et al.*, *Strange Vector Form-Factors from Parity-Violating Electron Scattering*, J. Phys: Conf. Ser. **299** (2011). 262

[PAN] R. S. Holmes, *The Parity Analyzer (PAN)*, http://www.phy.syr.edu/~rsholmes/happex/pan/html/index.html. 60, 107, 171, 306

[Pr78] C. Y. Prescott *et al.*, Phys. Lett. B **77**, 347 (1978). 2, 6

[Pa11] K. Paschke, K. Kumar, R. Michaels, P. A. Souder and G. M. Urciuoli, *PREX II: Precision Parity-Violating Measurement of the Neutron Skin of Lead*, http://hallaweb.jlab.org/parity/prex/prexII.pdf (2011). 84

[PREXWeb] R. Michaels, ^{208}Pb *Radius Experiment (PREX) Webpage*, http://hallaweb.jlab.org/parity/prex/. 73, 74, 77, 79

[Ra11] A. Rakhman, Ph. D. Thesis, Syracuse University - New York (2011). 83, 84

[RM] R. Michaels, *PREX Talks*, http://hallaweb.jlab.org/parity/prex/prextalks.html. 70

[RP05] B. G. Todd-Rutel and J. Piekarewicz, Phys. Rev. Lett. **95**, 122501 (2005). 28

[Ru01] G. A. Rutledge, Ph. D. Thesis, College of William and Mary (2001). 49

[Sa62] R. G. Sachs, Phys. Rev. **126**, 2256 (1962). 14

[Sa68] A. Salam, *Elementary Particle Theory, The Nobel Symposium no.8*, edited by N. Svartholm (Almqvist and Wiksell, Stockholm, 1968), 367-377. 1

[Sa11] O. Glamazdin, *Møller Polarimeter for PREX(Status Report)*, http://hallaweb.jlab.org/equipment/moller/Talks/PREX_Col_01_29_2011.pdf, Jan 29 (2011). 85

[Sa10] O. Glamazdin, *Hall A Møller Polarimeter after Upgrade*, http://hallaweb.jlab.org/equipment/moller/Talks/HAColab2010.pdf, June 10 (2010). 85

[SN10] Kiadtisak Saenboonruang, Nilanga Liyanage, *Pointing Analysis, HAPPEX III*, 2010. 211, 219, 223, 226, 229, 250, 290

[So90] P. A. Souder *et al.*, *Measurement of Parity Violation in the Elastic Scattering of Polarized Electrons from* ^{12}C, Phys. Rev. Lett. **65**, 694-697 (1990). 2, 6

[Sp04] D. T. Spayde *et al.* [SAMPLE Collaboration], *The Strange Quark Contribution to the Proton's Magnetic Moment*, Phys. Lett. B **583**,79-86, (2004). 2, 4, 257, 258, 267, 269, 272, 273, 279

[Un81] K. Unser, IEEE Trans. Nucl. Sci. **NS-28**, 2344 (1981) [SPIRES]; T. Powers, L. Doolittle, R. Ursic, and J. Wagner, in Proceedings of the 7th Workshop on Beam Instrumentation, AIP Conf. Proc. No. **390**, edited by A. Lumpkin and C. E. Eyberger (AIP, New York, 1997), JLAB-TN-96-021. 37, 282

[Va72] D. Vautherin, D. M. Brink, Phys. Rev. C **5**, 626 (1972). 28

[Vr87] H. de Vries, C. W. de Jager, C. de Vries, Atomic and Nuclear Data Tables, **36**, 496 (1987). 5

[Wa94] W. A. Watson *et al.*, *CODA: A Scalable, Distributed Data Acquisition System*, IEEE Trans. Nucl. Sci. **41**(1), 61 (1994); G. Heyes *et al.*, *The CEBAF Online Data Acquisition System*, in Proceedings of the CHEP Conference (1994), p. 122; D. J. Abbott *et al.*, *CODA Performance in the Real World*, 11th IEEE NPSS Real Time 1999 Conference, JLab-TN-99-12 (1999). 55

[Wh92] L. W. Whitlow *et al.*, Phys. Lett. B **282**, 475 (1992); Phys. Lett. B **250**, 193 (1990). 207

[We67] S. Weinberg, *A Model of Leptons*, Phys. Rev. Lett. **19**, 1264-1266 (1967). 1

[We12] J. Wexler, *PREX detector asymmetry summary*, http://ace.phys.virginia.edu/HAPPEX/120110_125526/dit_raw.pdf, Private Communication (2012). 242

[Wu57] C. S. Wu *et al.*, *Experimental Test of Parity Conservation in Beta Decay*, Phys. Rev. **105**, 1413-1415 (1957). 1

[Yo06] R. D. Young, J. Roche, R. D. Carlini, A. W. Thomas, *Extracting nucleon strange and anapole form factors from world data*, Phys. Rev. Lett. **97**, 102002 (2006). 273

[Ze59] Ya. B. Zel'dovich, *Parity Nonconservation in the First Order in the Weak-interaction constant in electron scattering and other effects.*, J. Exptl. Theoret. Phys. **36**, 964-966 (1959); Sov. Phys. JETP **9**, 682 (1959). 11, 236

[Zh00] S. L. Zhu, S. J. Puglia, B. R. Holstein, M. J. Ramsey-Musolf, *The Nucleon anapole moment and parity violating e p scattering*, Phys. Rev. D **62**, 033008 (2000). 22, 25, 26, 237, 274, 275